Rubidium Vapour-cell Frequency Standards : Metrology of Optical and Microwave Frequency References

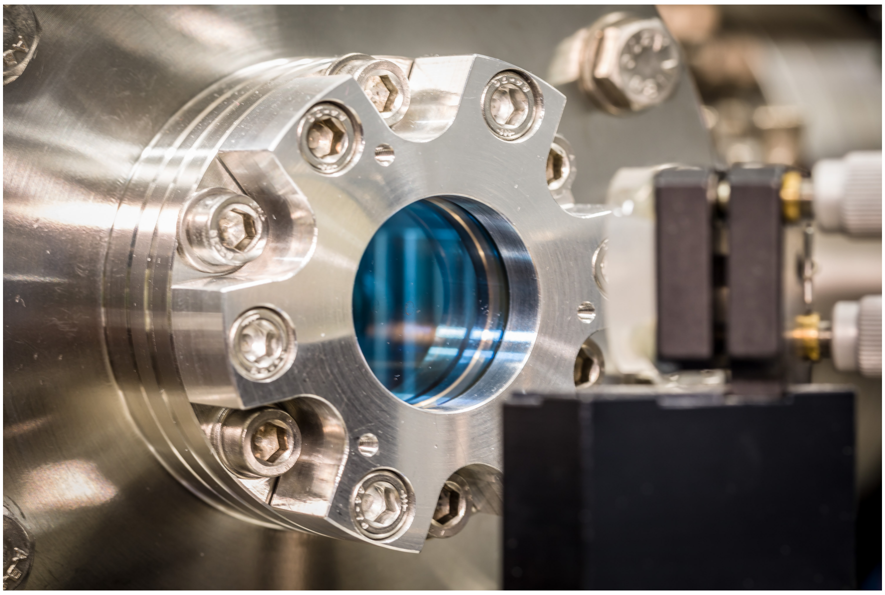

Thèse présentée à la Faculté des sciences de l'Université de Neuchâtel pour l'obtention du grade de

DOCTEUR ÈS SCIENCES
par :

WILLIAM MORENO
M.Sc. en Physique de l'Ecole Polytechnique Fédérale de Lausanne (EPFL), Suisse

Acceptée le 6 mai 2019 sur proposition du jury:

Prof. Dr. Gaetano MILETI, Université de Neuchâtel, Directeur de thèse
Prof. Dr. Jakob REICHEL, Sorbonne université, Paris, France, Rapporteur
Dr. Giorgio SANTARELLI, ParisTech, Institut d'optique, France, Rapporteur
Dr. Christoph AFFOLDERBACH, Université de Neuchâtel, Rapporteur
Dr. Arnaud LANDRAGIN, Observatoire de Paris (LNE-SYRTE), Paris, France, Examinateur

Neuchâtel, June 14, 2019

UNIVERSITÉ DE
NEUCHÂTEL

Faculté des Sciences
Secrétariat-décanat de Faculté
Rue Emile-Argand 11
2000 Neuchâtel – Suisse
Tél : + 41 (0)32 718 21 00
E-mail : secretariat.sciences@unine.ch

IMPRIMATUR POUR THESE DE DOCTORAT

La Faculté des sciences de l'Université de Neuchâtel autorise l'impression de la présente thèse soutenue par

Monsieur William MORENO

Titre:

"Rubidium Vapour-cell Frequency Standards : Metrology of Optical and Microwave Frequency References"

sur le rapport des membres du jury composé comme suit:

- Prof. associé Gaetano Mileti, directeur de thèse, Université de Neuchâtel, Suisse
- Dr Christoph Affolderbach, Université de Neuchâtel, Suisse
- Prof. Jakob Reichel, UPCM, Institut Universitaire de France, Paris
- Dr Giorgio Santarelli, Université de Bordeaux, France
- Dr Arnaud Landragin, SYRTE, Observatoire de Paris, France

Neuchâtel, le 13 juin 2019

Le Doyen, Prof. P. Felber

P. Fel

Abstract

This thesis concerns the development, study, and optimisation of compact and high-performance frequency references based on rubidium (Rb) vapour cells[1]. More specially, two Rb vapour-cell frequency references are studied: an optical-frequency reference at 1.5 μm and a double-resonance pulsed optically pumped (POP) atomic clock. The use of vapour cells allows compact frequency references (typically a volume of few litres) and with relative frequency stability (1) for a microwavve atomic clock at the level of $1 \cdot 10^{-14}$ at 1 day (equivalent to 1 ns/day) and (2) for the optical reference at the level of $1 \cdot 10^{-11}$ at 1 day (equivalent to $\approx$ 4 kHz/day). Such compact frequency references can be applied in industry, telecommunications, navigation, or as an on-board optical-frequency reference (e.g. LIDAR).

The first part of this thesis evaluates the medium- to long-term frequency stability of high-performance, compact POP atomic clocks. It evaluates the POP atomic clock frequency sensitivity to relevant quantities: laser frequency and intensity fluctuations (light-shift (LS) effects), microwave power (microwave-power shifts), and environmental effects (barometric effects, temperature). The impact of such perturbations are quantified using (1) a sensitivity coefficient, or shift coefficient, defined as the variation of the clock frequency with respect to the perturbing physical parameter (e.g. a power variation σ_p), $\Delta\nu_{\text{clock}}/\Delta \text{p}$; and (2) the amplitude of fluctuation of the perturbing physical parameter itself at various time scales, $\sigma_p(\tau)$. The sensitivity coefficients of the LS effect and the microwave-power shift are minimised, contributing to the clock's long-term frequency instability below 10^{-14} (relative frequency fluctuation).

A barometric effect is demonstrated in vapour-cell frequency standards. The natural fluctuation of the atmospheric pressure deforms the glass body of the vapour cell, which changes the internal gas pressure. It results in a coupling of the clock frequency with the atmospheric pressure. The phenomenon is characterised experimentally and theoretically, and the contribution of the barometric effect is reduced below 10^{-14}. By minimising the barometric effect, the microwave-power sensitivity, and the LS effect, a POP clock frequency stability of 1×10^{-14} (relative frequency fluctuation) at 10^4 seconds of integration time is demonstrated. More fundamental studies are carried out on the origin of the microwave-power shift in our POP clock prototype. The impact of the field inhomogeneity (light field and microwave fields) on the Ramsey signal and the clock frequency is studied numerically. Based on the simulated microwave-field amplitude distribution in the clock vapour cell, the measured Ramsey signal and its properties (contrast, the full width at half maximum (FWHM)) is reproduced by simulations.

The validation of the additive manufacturing (3D printing) for the fabrication of the complex microwave cavities is demonstrated. The POP clock setup and its possibilities (due to pulsed

---

[1] This work was conducted at the Laboratoire Temps-Fréquence at the University of Neuchâtel. This work was supported by the Swiss National Science Foundation (FNS): "Precision double-resonance spectroscopy and metrology with stabilised lasers and atomic vapours: applications for atomic clocks and magnetometers" no. 156621 (2015–2019).

interrogation) is used to evaluate the homogeneity and the distribution of the microwave field of the 3D-printed microwave cavity. Equivalent microwave-field distribution between the additive manufacturing cavity and the conventional-manufacturing cavity is demonstrated. Short-term frequency stability at the level of the state-of-the-art is presented.

The studies on microwave atomic clocks presented in this thesis constitute important steps towards a better understanding of double-resonance atomic clocks. The identification of the main source of long-term frequency instability and its reduction to below a relative frequency instability of 10^{-14} allows for our atomic clock prototype to be compared with state-of-the-art, compact, high-performance atomic clock. Moreover, this level of frequency instability allows for new studies on the physical phenomena to which the atomic clock is less sensitive to be conducted. The reported clock frequency stability with the additive manufacturing technology is an important step towards the commercialisation of high-performance double-resonance Rb atomic clocks.

The optical-frequency references studied in this thesis used an Rb vapour cell for the frequency stabilisation of lasers at 780 nm, 1560 nm and 1572 nm. A 1560 nm master laser was frequency stabilised to a Rb optical transition at 780 nm using frequency doubling. An optical-frequency comb generator was used to fill the gap of 12 nm between 1572 nm and the laser at 1560 nm. The laser system was designed to be an on-board frequency reference at 1572 nm for spaceborne CO2 LIDAR systems or optical pumping for Rb cell atomic clocks. The demonstrated frequency stability of the 1572 nm laser at 1572 nm is below $3 \cdot 10^{-11}$ (equivalent to 5.8 kHz at 1572 nm) at all time scales reaching $4 \cdot 10^{-12}$ (equivalent to 760 Hz at 1572 nm) in the long-term at the state-of-the-art level. In addition, the reproducibility and repeatability of the frequency stabilisation scheme of the master laser were evaluated. The degradation of the frequency noise and the relative intensity noise through the non-linear doubling process were also evaluated. The characterisation of the optical-frequency references identifies the basic elements for future evaluations of applications of optical pumping in atomic clocks or satellite LIDAR on-board frequency references.

Key words: atomic clock, rubidium vapour cell, double-resonance spectroscopy, pulsed optically pumped (POP) scheme, frequency instability, metrology, Optical frequency reference, LIDAR

Résumé

Cette thèse porte sur le développement, l'étude et l'optimisation de références de fréquence compactes de haute performances à base de cellules de vapeur de rubidium (Rb), [2] Plus particulièrement, deux références de fréquence à cellules à vapeur de Rb sont étudiées : une référence de fréquence optique à 1,5 μm et une horloge atomique à double résonance à pompage optique pulsé (POP). L'utilisation de cellules à vapeur permet de réaliser des références de fréquence compactes (i.e. dans un volume de quelques litres) ayant une stabilité de fréquence relative (1) pour une horloge atomique micro-onde au niveau de $1{\cdot}10^{-14}$ à 1 jour (équivalent à 1 ns/jour) et (2) pour la référence optique au niveau de $1 \cdot 10^{-11}$ à 1 jour (équivalent à environ 4 kHz/jour). Ces références de fréquence compactes peuvent être utilisées dans l'industrie, les télécommunications, la navigation ou comme référence de fréquence optique embarquée (par ex. LIDAR).

La première partie de cette thèse évalue la stabilité de fréquence à moyen et long terme d'une horloge atomique POP compacte de haute performance. Cela consiste à évaluer la sensibilité de la fréquence de l'horloge aux grandeurs pertinentes : fluctuations de fréquence et d'intensité du laser (effets de décalage de fréquence due à lumière (LS)), puissance micro-onde (décalages de fréquence due à la puissance micro-ondes), et effets environnementaux (effets barométriques, température). L'impact de telles perturbations est quantifié en utilisant (1) un coefficient de sensibilité, ou coefficient de décalage de fréquence, défini comme la variation de la fréquence d'horloge par rapport au paramètre physique perturbateur (par exemple une variation de puissance σ_p), $\Delta\nu_{\mathrm{clock}}/\Delta \mathrm{p}$; et (2) l'amplitude des fluctuations du paramètre physique perturbateur lui-même évalué à différentes échelles de temps, $\sigma_p(\tau)$. Les coefficients de sensibilité de l'effet LS et du décalage due à la puissance micro-onde sont minimisés, contribuant à l'instabilité de fréquence de l'horloge en dessous de 10^{-14} dans le long terme (fluctuation de fréquence relative). Un effet barométrique est démontré dans les étalons de fréquence à cellule de vapeur. La fluctuation naturelle de la pression atmosphérique déforme la cellule en verre, ce qui modifie la pression interne du gaz. Il en résulte un couplage de la fréquence de l'horloge avec la pression atmosphérique. Le phénomène est caractérisé expérimentalement et théoriquement, et la contribution de l'effet barométrique est réduite en dessous de 10^{-14}. En minimisant l'effet barométrique, la sensibilité à la puissance micro-ondes et l'effet LS, on démontre une stabilité de fréquence de notre prototype d'horloge POP de 1×10^{-14} (fluctuation de fréquence relative) à 10^4 secondes de temps d'intégration.

Des études plus fondamentales sont menées sur l'origine du décalage de fréquence dû à la puissance micro-onde pour notre prototype d'horloge POP. L'impact de l'inhomogénéité du champ (champ lumineux et champ micro-ondes) sur le signal de Ramsey et la fréquence de l'horloge est étudié numériquement. Sur la base de la distribution d'amplitude du champ micro-onde simulée dans

---

[2] Ces travaux ont été menés au Laboratoire Temps-Fréquence de l'Université de Neuchâtel. Ces travaux ont été soutenus par le Fonds national suisse de la recherche scientifique (FNS) : "Precision double-resonance spectroscopy and metrology with stabilised lasers and atomic vapours : applications for atomic clocks and magnetometers" n°. 156621 (2015-2019).

la cellule de l'horloge, le signal de Ramsey mesuré et ses propriétés (contraste, largeur totale à mi-hauteur (FWHM)) sont reproduits par simulations. La validation de la production additive (impression 3D) pour la fabrication des cavités micro-ondes complexes est démontrée. L'horloge POP et ses possibilités (grâce à l'interrogation pulsée) est utilisée pour évaluer l'homogénéité et la distribution du champ micro-onde de la cavité micro-onde. On démontre que la distribution du champ micro-onde de la cavité fabriqué par impression 3D est équivalente au champ micro-onde d'une cavité de fabrication conventionnelle. De plus, on présente une stabilité de fréquence horloge au niveau de l'état de l'art obtenu avec une horloge ayant une cavité micro-onde fabriquée par impression 3D.

Les études présentées dans cette thèse sont des étapes importantes vers une meilleure compréhension des horloges atomiques à double résonance. L'identification de la principale source d'instabilité de fréquence à long terme (l'effet barométrique) et sa réduction en dessous d'une instabilité de fréquence relative de 10^{-14} permet de comparer notre prototype d'horloge atomique avec l'état de l'art des horloges atomiques compactes et à haute performance. De plus, ce niveau d'instabilité de fréquence permet de mener de nouvelles études sur les phénomènes physiques auxquels l'horloge atomique est moins sensible. La stabilité de fréquence d'horloge obtenue avec l'horloge possédant une cavité fabriquée par impression 3D est une étape importante vers la commercialisation d'horloges atomiques Rb à double résonance.

La deuxième partie de cette thèse porte sur les références de fréquence optique utilisent une cellule à vapeur de Rb pour la stabilisation en fréquence des lasers à 780 nm, 1560 nm et 1572 nm. Un laser maître de 1560 nm a été stabilisé en fréquence sur une cellule de vapeur de Rb à 780 nm par doublement de fréquence. Un générateur de peigne de fréquence optique a été utilisé pour combler l'espace de 12 nm entre 1572 nm et le laser à 1560 nm. Le système laser a été conçu pour être une référence de fréquence embarquée à 1572 nm pour un système LIDAR spatial ou pour faire du pompage optique pour les horloges atomiques à cellules Rb. La stabilité de fréquence démontrée du laser à 1572 nm est inférieure à $3 \cdot 10^{-11}$ (équivalent à 5,8 kHz à 1572 nm) à toutes les échelles de temps et atteint $4 \cdot 10^{-12}$(équivalent à 760 Hz à 1572 nm) à long terme. En outre, la reproductibilité et la répétabilité du schéma de stabilisation de fréquence du laser maître ont été évaluées. La dégradation du bruit de fréquence et du bruit d'intensité par le processus de doublage de fréquence a également été évaluée. La caractérisation des références de fréquence optique permet d'identifier les futurs axes de recherche pour l'application de ces références optiques pour le pompage optique dans les horloges atomiques ou comme références de fréquence embarqué (LIDAR spatial).

Mots clefs : horloge atomique, cellule de vapeur de rubidium, spectroscopie à double résonnance, schéma de pompage optique pulsé (POP), instabilité de fréquence, métrologie, référence de fréquence optique, LIDAR

Exister, c’est sortir de soi
— Maurice Zundel

To my parents and my sister…

Acknowledgements

I would like to express my great appreciation to all the people that helped me during the last four years.

First, I would express my gratitude to my thesis adviser, Prof. Gaetano Mileti. He introduced me to the time and frequency domain, which is an exciting and living field of research. During the duration of my thesis, he trusted me when I was oscillating between experiments, numerical simulations, and theoretical calculation. His advice was precious at each level of my research, and he contributed largely to its success. Under his guidance, I learned the meaning, the advantages, and the constraints of conducting research. Finally, he encouraged me to pursue my career, helping me apply for an early postdoc. mobility project.

My second thank-you goes to Dr. Christoph Affolderbach, who accompanied this work carefully. He was always available for my short "physical" questions or my laboratory questions. I really appreciated our short and long exchanges about atomic physics and atomic clocks. I learned a lot from his meticulous reading of my work.

My third thank-you goes to Dr. Matthieu Pellaton. I would like to thank him for the challenge of his constructive and interesting criticisms. Our verbal jousting allowed me to step-up significantly.

I would like to thank Dr. Renaud Matthey-de-l'endroit, who followed my first work on the LIDAR-related project, and Dr. Stephan Schilt, who answered to all of my "naïve" questions related to noise theory. These two researchers have always been available for critical and constructive rereadings of my work. A special thanks goes to Prof. Thomas Südmeyer. His passion and motivation for physics inspired me, and our discussions helped me a lot.

I would like to thank all the jury members; Prof. Jakob Reichel, Dr. Giorgio Santarelli and Dr. Arnaud Landragin for their meticulous reading of this manuscript and for their comments that were very helpful to improve the quality of this manuscript.

I had the chance to complete my thesis at the same time as two of my colleagues: Nil Almat and Dr. Mohammadreza Gharavipour. They had to share the same open-space as me, which is proof of endless patience. Both of you helped me so much in the realisation of this thesis. I will never forget our days together and especially our conference weeks in Belgrade. Thank you for your spontaneous support at every important step of my thesis. I wish you the best for your future.

Florian Gruet: master of patience and kindness. I am sorry to have been so annoying over these last four years. Thank you very much for your foolproof support in the laboratory. I hope that one day I can payback all of your support.

Special thanks goes to Patrick Scherler. Patrick has always been available to help me on the clock, sometimes accompanying me under the optical table on hands and knees. His expertise has been a catalyst to this thesis. I would also like to thank Marc Durrenberger for his support for the electronics. I am sure you will be happy not to have me in your hair any more. From Patrick and Marc, I learned the definition of a job properly done. I would like to thank Daniel Varidel

and Dominique Schenker for their support. My special thanks are extended to the LTF secretariat: Natacha (God bless her), Joelle, Sévérine and Patricia. Thank you for all your helps.

I would like to thank our external colleagues from the time and frequency domain, including our colleagues from INRIM: Dr. Claudio Calosso, for building and providing the LO of our Rb-POP prototype, and Dr. Salvatore Micalizio, who shared his passion for the POP atomic clock and was always available to answer my questions. I am thankful for our collaboration with the DLR Institute and Dr. Andreas Fix, in particular, for his support of the LIDAR-related project. I would also like to thank our colleagues from Belgrade University: Prof. Brana Jelenkovic, Dr. Aleksandar Krmpot, and Ivan Radojicic. I really enjoyed our exchange.

During the four years of my thesis, I have the chance to share some time with past and present colleagues at the LTF. Thank you, François Labaye, for sharing your passion for power-lifting with me. Thank you, Loïc, for your help at some critical moments of my thesis. Sargis, you made my time at LTF a great moment; thank you for your endless positivity. I would like to thank all my colleagues who contributed to the fun atmosphere on the physics floor: Kutan, Nayara, Pierre, Hélène, Clément, Norbert, Maxime, Valentin, and the newcomers Jakub, Olga, Atif, and Julian. I would like to thank Célia Bergame for the good moment we spent together. To my teammates from the “Sentinelles d’argent”: thank you for having supported me and thank you for being a source of happiness and fun.

My biggest source of motivation and inspiration are the members of my family. There are no words to describe how grateful I am for having such a family. Thank your Mom, Dad, and Carène for standing behind me every day. I would not have obtained my PhD degree without you.

Neuchâtel, June 14, 2019 William Moreno

Contents

List of Figures

List of Tables

Author's contributions

Articles in peer-reviewed journals

1. W. Moreno, M. Pellaton, C. Affolderbach, N. Almat, M. Gharavipour, F. Gruet, G. Mileti, "*Impact of microwave-field inhomogeneity in an alkali vapour cell using Ramsey double-resonance spectroscopy,*" in Quantum Electronics, vol. 49, no. 3, pp. 293-297, Jan. 2019

2. W. Moreno, M. Pellaton, C. Affolderbach and G. Mileti, "*Barometric effect in vapor cell atomic clocks,*" in IEEE Transactions on Ultrasonics, Ferroelectrics, and Frequency Control, vol. 65, no. 8, pp. 1500-1503, Aug. 2018

3. N. Almat, M. Pellaton, W. Moreno, F. Gruet, C. Affolderbach, and G. Mileti, "*Rb vapor-cell clock demonstration with a frequency-doubled telecom laser,*" Applied Optics 57, 4707-4713 (2018)

4. (Editor's pick) C. Affolderbach, W. Moreno, A. E. Ivanov, T. Debogovic, M. Pellaton, A. K. Skrivervik, E. de Rijk, G. Mileti, "*Study of additive manufactured microwave cavities for pulsed optically pumped atomic clock applications,*" Applied Physics Letters 112, 113502, March 2018. (C. Affolderbach and W. Moreno contributed equally to this work)

5. N. Almat, W. Moreno, M. Pellaton, F. Gruet, C. Affolderbach, G. Mileti, "*Characterization of Frequency-Doubled 1.5-µm Lasers for High Performance Rb Clocks,*" in IEEE Transactions on Ultrasonics, Ferroelectrics, and Frequency Control, vol. 65, no. 6, pp. 919-926, June 2018

International conference with peer-reviewed proceedings

1. R. Matthey, W. Moreno, F. Gruet, P. Brochard, S. Schilt, G. Mileti, "*Rb-based stabilized laser at 1572 nm for CO2 monitoring,*" Journal of Physics: Conference Series 723 (2016) 012034 (poster presentation # D01 by R. Matthey)

International conferences with proceedings

1. W. Moreno, M. Pellaton, N. Almat, M. Gharavipour, C. Affolderbach and G. Mileti, *Investigations on microwave power shift in compact vapor-cell atomic clock*, 2019 Joint Conference of the European Frequency and Time Forum and IEEE International Frequency Control Symposium (EFTF/IFCS), Orlando, Florida, USA, 2019 (poster presentation TuPoS.26 by C. Affolderbach)

2. N. Almat, M. Gharavipour, W. Moreno, C. Affolderbach and G. Mileti, *Long-term stability analysis towards* $< 10^{-14}$ *level for a highly compact POP Rb cell atomic clock*, 2019 Joint Conference of the European Frequency and Time Forum and IEEE International Frequency

Control Symposium (EFTF/IFCS), Orlando, Florida, USA, 2019 (oral presentation MoAT2.5 and student poster competition finalist MoPoS.10 both by N. Almat)

3. S. Schilt, R. Matthey, W. Moreno, F. Gruet, K. Hey Tow, L. Thévenaz, G. Mileti, T. Südmeyer, *Frequency stabilized seed lasers for CO2 DIAL systems*, 2nd International workshop on space-based LIDAR remote sensing techniques and emerging technologies, Milos, Greece; June 4-8, 2018 (oral presentation by S.Schilt)

4. C. Affolderbach, N. Almat, M. Gharavipour, F. Gruet, W. Moreno, M. Pellaton and G. Mileti, *Selected studies on high performance laser-pumped Rubidium atomic clocks*, 2018 IEEE International Frequency Control Symposium, Olympic Valley, CA, USA, 2018 (oral presentation ThO2.3 by G. Mileti)

5. W. Moreno, C. Affolderbach, A. E. Ivanov, T. Debogovic, M. Pellaton, A. K. Skrivervik, E. de Rijk, G. Mileti, *Ramsey-mode Rb cell clock demonstration with a 3D-printed microwave cavity*, 2018 European Frequency and Time Forum (EFTF), Torino, Italy, 2018 (oral presentation C4L-B-4 by C. Affolderbach)

6. N. Almat, W. Moreno, M. Pellaton, M. Gharavipour, F. Gruet, C. Affolderbach, G. Mileti, *Cell-Based Stabilized Laser Sources and Light-Shifts in Pulsed Rb Atomic Clocks*, 2017 Joint Conference of the European Frequency and Time Forum and IEEE International Frequency Control Symposium (EFTF/IFCS), Besancon, 2017, pp. 63-65 (oral presentation A2P-D by W. Moreno and student poster competition finalist by N. Almat, poster # 1394)

7. W. Moreno, R. Matthey, F. Gruet, P. Brochard, S. Schilt, G. Mileti, *Rb-stabilized optical frequency reference at 1572 nm*, 2016 European Frequency and Time Forum (EFTF), York, 2016, pp. 1-4 (poster presentation # 1073 by R. Matthey)

8. W. Moreno, R. Matthey, F. Gruet, P. Brochard, S. Schilt, G. Mileti, *Rb-Stabilized Compact Optical Frequency Comb acting as a Versatile Wavelength Reference*, 2016 Conference on Lasers and Electro-Optics (CLEO), San Jose, CA, 2016, pp. 1-2 (oral presentation # SM2H.5 by W. Moreno)

9. W. Moreno, R. Matthey, F. Gruet, P. Brochard, S. Schilt, G. Mileti, *Rb-based optical frequency reference at 1572 nm*, 2016 IEEE International Frequency Control Symposium (IFCS), New Orleans, LA, 2016, pp. 1-2 (poster presentation # 3133 by W. Moreno)

Other conferences and presentations

1. N. Almat, W. Moreno, F. Gruet, C. Affolderbach and G. Mileti, *Long-term stability analysis at 10^{-14} level of a highly compact vapour-cell atomic clock for GNSS applications*, 7th international colloquium on scientific and fundamental aspects of GNSS, Zurich, Switzerland, September 4-6, 2019 (submitted for oral presentation)

2. C. Affolderbach, N. Almat, M. Gharavipour, F. Gruet, W. Moreno, M. Pellaton and G. Mileti, *Ramsey spectroscopy in vapour cells for compact high performance atomic clocks*, 8th International Symposium and School "Modern Problems of Laser Physics" (MPLP-2018), Novosibirsk, Russia; August 25-31, 2018 (oral presentation by G. Mileti)

3. C. Affolderbach, W. Moreno, A. E. Ivanov, T. Debogovic, M. Pellaton, A. K. Skrivervik, E. de Rijk, G. Mileti, *High-performance Rb atomic clock demonstration using additive manufactured*

microwave cavity, Swiss Physical Society Annual Meeting, Lausanne, Switzerland, August 28 – 31, 2018 (oral presentation by C. Affolderbach)

4. W. Moreno, M. Pellaton, M. Gharavipour, F. Gruet, C. Affolderbach, G. Mileti, *Light-shift in pulsed optically pumped Rubidium atomic clock*, oral # L.S.M.5 at Photonica, Belgrade, Serbia, August 28 - September 1, 2017 (oral presentation # L.S.M.5 by W. Moreno)
5. N. Almat, W. Moreno, M. Pellaton, F. Gruet, C. Affolderbach, G. Mileti, *Frequency-doubled laser sources stabilized to Rb-cell references*, Photonica, Belgrade, Serbia, August 28 - September 1, 2017 (poster presentation # L.S.M.10 by N. Almat)
6. (invited) C. Affolderbach, M. Gharavipour, F. Gruet, W. Moreno, M. Pellaton, G. Mileti, *Precision measurements for compact vapor-cell atomic clocks*, oral # L.4 at Photonica, Belgrade, Serbia, August 28 - September 1, 2017 (invited oral presentation # L.4 by C. Affolderbach)
7. (invited) C. Affolderbach, N. Almat, M. Gharavipour, F. Gruet, R. Matthey, W. Moreno, G. Mileti, *High performance and miniature laser-pumped vapour-cell frequency standards*, 3rd URSI Regional Conference on Radio Science, Tirupati, India, March 1-3, 2017. (invited plenary talk by G. Mileti)
8. (invited) C. Affolderbach, M. Gharavipour, F. Gruet, R. Matthey, W. Moreno, G. Mileti, *Double Resonance Spectroscopy in Rb Vapour Cells for High-Performance and Miniature Atomic Clocks*, invited oral presentation at 7th International Symposium and School "Modern Problems of Laser Physics" (MPLP-2017), Novosibirsk, Russia; August 22-28, 2016 (invited oral presentation by G. Mileti)
9. W. Moreno, F. Gruet, R. Matthey, G. Mileti, *Rb-based Stabilized Laser at 1572 nm for CO2 monitoring*, Joint Annual Meeting of the Austrian & Swiss Phys. Societies, Vienna, Austria, September 1-4, 2015 (poster presentation # 574 by W. Moreno)
10. W. Moreno, F. Gruet, R. Matthey, G. Mileti, *Rb-based Stabilized Laser at 1572 nm for CO2 monitoring*, Photonica - International School and Conference on Photonics, Belgrade, Serbia, August 24-28, 2015 (poster presentation # P.LS.2 by W. Moreno)

Physical Constants

Speed of Light[1]	c	299 792 458 [$m \cdot s^{-1}$]
Plank constant[1]	h	6.626 070 15 $\times 10^{-34}$ [J s]
Electron elementary charge[1]	e	1.602 176 634 $\times 10^{-19}$ [C]
Boltzman's Constant[1]	k_B	1.380 649 $\times 10^{-23}$ [JK^{-1}]
Free electron's Landé g-factor[2]	g_S	-2.002 0319 304 361 82(52)
Magnetic Constant[2]	μ_0	$4\pi \cdot 10^{-7}$ [NA^{-2}]
Electric Constant[2]	ϵ_0	8.854 187 817 $\ldots \times 10^{-12}$ [Fm^{-1}]
Bound electron's Landé g-factor ($5^2S_{1/2}$) [3]	g_J	2.002 331 13(20)
^{87}Rb Nucleus' Landé g-factor [3]	g_S	2.002 0319 304 361 53(53)
Bohr magneton $\frac{e\hbar}{2m_e}$[2]	ν_B	927.400 99 94 (57) $\times 10^{-26}$ [JT^{-1}]
Electron mass[2]	m_e	9.109 383 56(11) $\times 10^{-31}$ [Kg]
^{87}Rb atomic mass [3]	m_e	1.443 160 648(72) $\times 10^{-25}$ [Kg]

Abbreviations

AdM	**Ad**ditive **M**anufactured
AM	**A**mplitude **M**odulation
ALMA	**A**tacama **L**arge **M**illimeter **A**rray
AOM	**A**cousto-**O**ptic **M**odulator
BG	**B**uffer **G**as
CCE	**C**lock **C**ontrol **E**lectronic
CoM	**Co**nventional **M**anufactured
CPT	**C**oherent **P**opulation **T**rapping
Cs	**C**aesium
CW	**C**ontinuous **W**ave
DFB	**D**istributed **F**eed**B**ack
DR	**D**ouble **R**esonance
DWDM	**D**ense **W**avelength **D**ivision **M**ultiplexing
EPFL	**E**cole **P**olytechnique **F**édérale de **L**ausanne
ESA	**E**uropean **S**pace **A**gency
ETS	**E**nhanced **T**emperature **S**ensitivity
FEMTO-ST	**F**ranche-Comté **E**lectronique **M**écanique **T**hermique et **O**ptique – **S**ciences et **T**echnologie
FNS	**F**ond **N**ational **S**uisse
FOF	**F**ield **O**rientation **F**actor
FM	**F**requency **M**odulation
FN-PSD	**F**requency **N**oise **P**ower **S**pectral **D**ensity
FRU	**F**requency **R**eference **U**nit
FWHM	**F**ull **W**idth at **H**alf **M**aximum
GNSS	**G**lobal **N**avigation **S**atellite **S**ystems
GPS	**G**lobal **P**ositioning **S**ystem
H	**H**ydrogen
HC-PCF	**H**ollow-**C**ore **P**hotonic **C**rystal **F**iber
INRIM	**I**stituto **N**azionale di **Ri**cerca **M**etrologica
IPDA	**I**ntegrated-**P**ath **D**ifferential **A**bsorption
LEMA	**L**aboratory of **E**lectro**M**agnetics and **A**coustics
LGR	**L**oop-**G**ap-**R**esonnator
LH	**L**aser **H**ead
LIDAR	**Li**ght **D**etection **A**nd **R**anging
LIS	**Li**ght-**I**nduced **S**hift
LNE-SYRTE	**L**aboratoire **N**ational de Métrologie et d'**E**ssais - **Sy**stèmes de **R**éférence **T**emps-**E**space

LO	**L**ocal **O**scillator
LS	**L**ight **S**hift
LTF	**L**aboratoire **T**emps-**F**réquence
MPS	**M**icrowave **P**ower **S**hift
OFCG	**O**ptical **F**requency **C**omb **G**enerator
PD	**P**hoto **D**etector
PFS	**P**rimary **F**requency **S**tandard
PHM	**P**assive **H**ydrogen **M**aser
POP	**P**ulsed **O**ptically **P**umped
PP	**P**hysic **P**ackage
PPLN-WG	**P**eriodically-**P**oled **L**ithium **N**iobate **W**ave**g**uide
RAFS	**R**ubidium **A**tomic **F**requency **S**tandard
Rb	**R**ubidium
RCE	**R**esonator **C**ontrol **E**lectronics
RIN	**R**elative **I**ntensity **N**oise
SE	**S**pin **E**xchange
SIOM	**S**hanghai **I**nstitute of **O**ptics and Fine **M**echanics
SPHM	**S**pace **P**assive **H**ydrogen **M**aser
UNINE	**Uni**versité de **Ne**uchâtel
WMS	**W**avelength **M**odulation **S**pectroscopy

Introduction

According to the Oxford dictionary, time is [4]:

> *"The indefinite continued progress of existence and events in the past, present, and future regarded as a whole".*

The "measurement of time" consists of measuring the time interval T between two events. Generally, the unit of time is a specific time interval used to measure or express a general time interval. For example, the earth completes a rotation around the sun after $T \approx 365$ days or $T \approx 1$ years or $T \approx 52$ weeks. The units of time used here are "day", "year," or "week"; these can be used as the definition of a unit of time. The main problem with these units is that we know that the duration of a day varies in length, which means that the unit of time is not the same today as it was one hundred years ago. Moreover, it does not make sense to define a unit of time that is difficult to access at any point in the universe when it is not possible to observe our solar system over one year. The actual definition of the unit of time, in the International System of Units (SI) system, is the second; it is defined as the duration of 9'192'631'770 periods of the radiation between the ground-state hyperfine level of the caesium 133 atom [1]. The realisation of the SI second is made with hot-beam caesium clocks and primary frequency standards based on laser-cooled caesium fountains with a fractional uncertainty of about 10^{-16} [5], [6]. Nowadays, optical-frequency standards are surpassing primary frequency standards in the microwave regime in term of frequency stability and systematic uncertainty. Optical clocks based on different atomic species have reported fractional uncertainty in the range of 10^{-18} [7]. This has launched discussions about an eventual redefinition of the unit of time based on an optical transition [8].

The experimental realisation of the unit of time, from the past to today, is done using a frequency reference (regularly oscillating phenomenon) where the period T and the frequency f are related through the relation $f = 1/T$. Basically, a clock is composed by a frequency reference (for example, a pendulum) that is kept in motion by a source of energy (for example, a winding spring) that provides the proper amount of energy at the proper time and a read-out system counting and displaying the "tic-tac." In the case of an atomic clock, the atoms are "oscillating" between two states (the pendulum) by the action of a microwave or optical field (the spring). A frequency divider (the read-out system) is used to provide a 1-Hz, 10-Hz or 10-MHz signal. More generally, a stable frequency source is said to be a frequency standard if the instrument provides a stable oscillating signal with a known frequency. Here the terms "*stable*" and "*known*" can be quantified by numbers; the characterisation of the frequency standard determines these numbers. First, the term "*stable*" quantifies how well a frequency standard can reproduce the same frequency over a given time — also called the frequency stability or the frequency instability — which is characterised in terms of the Allan variance (see section 1.4). The term "*known*" means that the frequency of the frequency standard has been compared directly or indirectly to the frequency of a primary frequency standard, which is characterised in terms of accuracy. The most accurate frequency standards are the primary frequency standard, the frequency of which correspond to the definition of the second and does not need external calibration.

In atomic frequency standards, the frequency reference is realized by the atomic transition frequencies. However, the absolute atomic transition frequencies are frequency shifted from the unperturbed value of isolated atoms due to external perturbation, for example, electric and magnetic fields. The evaluation of these systematic frequency shifts allows for the output frequency of the frequency standard to be corrected. Exact knowledge of these frequency shifts is impossible; there will always be an error in these shifts. The second source of error in the output frequency is the frequency changed within a given time interval induced by stochastic or environmental-related frequency fluctuations. This second source of error is called the frequency instability of the frequency standards. The evaluation of the frequency instability determines the origin of the stochastic phenomena (generally by noise analysis) or identifies which environmental parameters are the most impactful sources of frequency instability (generally by observing time correlations).

Frequency standards are classified into two families: active and passive devices. An active frequency standard is based on the radiation emitted by a group of excited atoms. A passive frequency standard is based on the response of a physical system to an external perturbation at a given frequency. The response of the physical system is then used to frequency stabilise the frequency of the external perturbation; its basic principle is illustrated in Figure 1. Atomic frequency standards are based on atoms enclosed in a cm-scale or chip-scale vapour cell, ultra-cold atoms confined in optical lattices or a radio-frequency trap, or beams of hot or cold atoms. This thesis is devoted to compact frequency standards based on an alkali vapour cell. Alkali atoms (such as caesium and rubidium) and hydrogen have been used to build atomic frequency standard in the GHz range (atomic clock) and the THz range (optical-frequency reference in the near infra-red).

The work presented in this thesis is dedicated to (1) the evaluation of the frequency instability of a microwave and 1.5-μm optical-frequency standards based on a rubidium (Rb) vapour cell using the Allan variance to quantify the degree of frequency instability, and (2) the measurement of the optical frequency of 1.5-μm optical-frequency standards frequency stabilised using a Rb vapour cell with an emphasis on the reproducibility and repeatability of the optical frequency of the 1.5-μm optical-frequency standards.

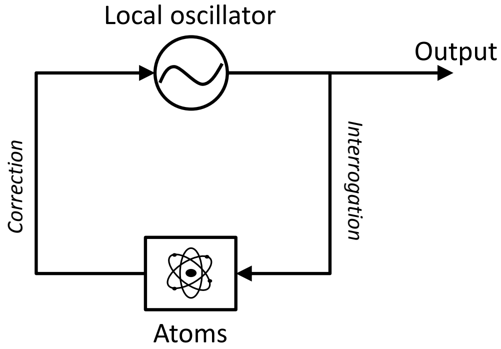

Figure 1 – *Schematic of a passive atomic frequency standards.*

Compact and high-performance atomic clock

Compact and high-performance atomic clocks [9][10][11], which combine compactness (few litres) with high-frequency stability performance, apply to large industrial fields, including global navigation satellite systems (GNSS), telecommunication synchronisation, defence, and astrometry.

These clocks probe the hyperfine ground-state frequency of atoms like Rb, caesium (Cs), and hydrogen (H). This type of product is commercialised: common compact atomic clocks include the Cs beam standard [12] [13], the passive hydrogen maser (PHM) [14] [15], and the Rb atomic frequency standard (RAFS) [16] [17]. The most common laboratory prototype clocks are the continuous-wave (CW)[9],[18],[10] and pulsed optically pumped (POP)[19],[20],[21] double-resonance (DR) clocks, the CW [22] or pulsed clocks [23],[11],[24] coherent population trapping (CPT) clocks, and the compact cold caesium atom clock [25].

The status of the frequency stability performances of the best compact atomic clocks - at the beginning of this thesis in 2015 [3] - are shown in Figure 2. Most recent laboratory atomic clock prototypes have reached frequency stabilities at 1 second on the range $2-4\times10^{-13}$, which is better than the short-term frequency instabilities of most commercial compact atomic clocks. However, most of the laboratory prototypes present medium- to long-term frequency instabilities of 10^{-14} for integration times higher than 10^4 seconds. Today, the long-term frequency stability of commercial compact atomic clocks outperforms the long-term frequency stability of the laboratory prototypes. However, the compact atomic clock laboratory prototypes have the potential to presents better frequency stability than their commercial counterparts if their long-term frequency instability is enhanced. The main identified effects limiting the long-term stability of laboratory prototypes are clock sensitivities to (1) light sources properties (LS effects), (2) microwave power and (3) environmental properties (temperature, pressure, humidity).

This thesis focuses on the DR Rb atomic clock. In the DR atomic clock, the alkali ground-state hyperfine frequency ν_0 is probed using two external fields: a light field and a microwave field. The light field is in resonance with one optical transition of the atom (in the THz range) and is used to pump the atoms into one of the ground states. The light field can be generated by a discharge lamp [17],[16] or a laser diode[19][26]. The microwave field is in resonance with ν_0 (in the GHz range) and is used to probe the atomic frequency, depopulating the optically pumped ground state. The microwave field is applied to the atoms using a microwave cavity. Finally, the ground state depopulated by the microwave field is probed using the light field and a photodiode; if the microwave frequency is exactly at the hyperfine ground-state frequency, the absorption of light along the vapour cell is maximal; otherwise, the absorption light is lower. The photodiode after the vapour cell transforms the transmitted light into a proportional voltage. Figure 3 presents a schematic of a DR atomic clock.

Two different schemes can be implemented to build an Rb DR atomic clock: a continuous-wave DR (CW-DR) atomic clock and a POP atomic clock. The first scheme applies the light field and the microwave field to the vapour cell continuously. The atoms can be seen as a three-level system during the microwave interaction. The main limitation of the CW-DR scheme is the coupling between the optical coherence created with the light field and the clock frequency probed by the microwave via the AC-Stark shift effect. The POP scheme consists of a series of pulses: a strong first optical pump pulse used to optically pump the atoms in one ground-state level, followed

---

[3] The status of the frequency stability performances of the best compact atomic clocks in 2019 at the end of the thesis is presented in figure 4

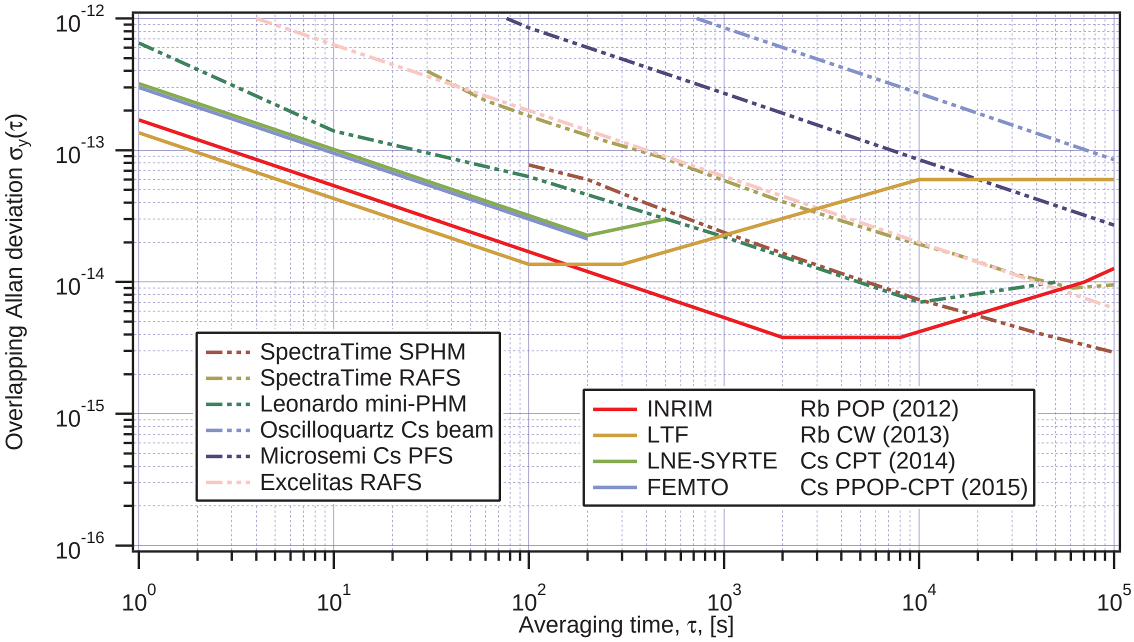

Figure 2 – *State of the art of laboratory compact atomic clocks in 2015 : INRIM Rb-POP [19]; UNINE Rb-CW [26]; LNE-SYRTE Cs CPT [27]; FEMTO PPOP Cs CPT [28]. Industrial atomic clocks : SpectraTime SPHM [14] and RAFS [16]; Oscilloquartz Cs beam [12]; Leonardo mini-PHM [15]; Microsemi Cs PFS [29]; Excelitas RAFS [17].*

by a microwave interrogation (Ramsey spectroscopy) composed of two microwave pulses and a weak optical-detection pulse used to detect the change in absorption. The advantage of the fields' separation is being able to consider the atoms as a two-level system during the microwave interrogation, uncoupling the light field and the clock frequency. This approach helps achieve better long-term stability.

The Time and Frequency Laboratory (LTF) at University of Neuchâtel has developed a compact atomic clock prototype based on a 2.5 cm long Rb vapour cell and a magnetron-type microwave cavity [30][10][20]. The clock prototype is described in Chapter 2. Previous studies on the clock prototype have demonstrated a short-term stability $1.4 \cdot 10^{-13}\tau^{-1/2}$ [10] when the clock is operated in the CW-DR scheme and $2.1 \cdot 10^{-13}\tau^{-1/2}$ when it is operated in POP scheme [20][31]. However, for both schemes, the measured and estimated medium- to long-term relative frequency instability is in the high 10^{-14} at 10^{4} second of integration time [31]. The present study is devoted to the analysis of the main source of frequency instability in the medium- to long-term when the clock is operated in POP mode and extends the analysis performed by Gharavipour in his thesis [31]. The main sources of frequency instability — the LS, microwave-power shift, and barometric shift — are studied in Chapter 3. A comparison between frequency instability budgets (short and medium- to long-term) and frequency instability measurement is presented in the same chapter.

On-board optical-frequency reference

Compact and robust optical-frequency references in the 1.5 μm and 780 nm optical spectral region have numerous applications, including in the areas of telecommunication (for example, in dense wavelength division multiplexing (DWDM)), coherent optical communications [32], high-accuracy optical measurement [33], spaceborne CO_2 spectroscopy [34][35][36][37], time synchronisation

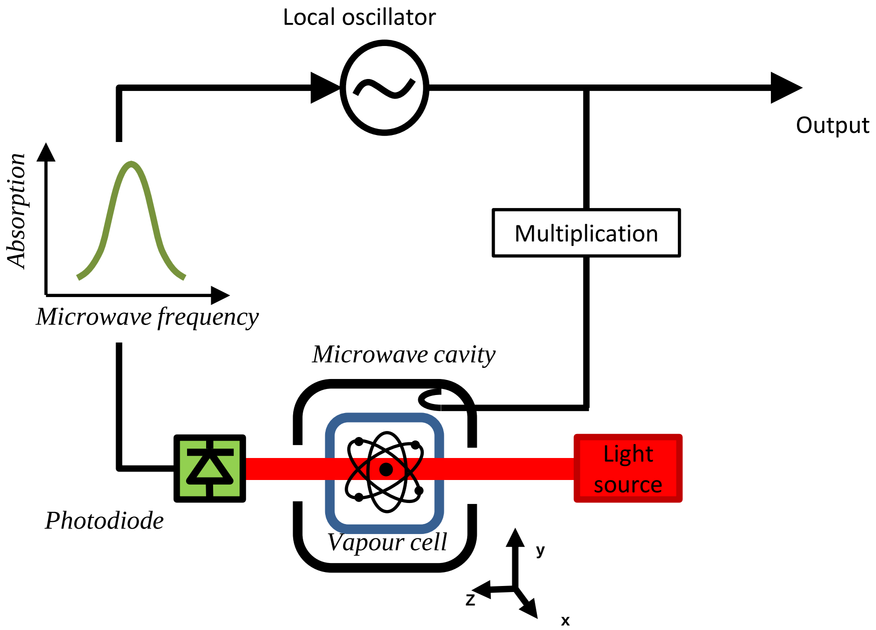

Figure 3 – *Schematic of a double resonance atomic frequency standard.*

in large-area radio-telescope arrays (like the Atacama Large Millimeter Array (ALMA)) [38], and for optical pumping in atomic clocks [39], atomic physics instrumentation [40],[41],[42] and atom interferometry [43].

In the case of spaceborne CO_2 spectroscopy, space agencies are considering the feasibility of measuring atmospheric CO_2 using a satellite-borne, CO_2 integrated-path differential absorption LIDAR (IPDA) system [34][44]. To achieve this scientific goal, feasibility studies [45][34] defined the requirements for the LIDAR laser transmitter frequency stability. At 1572 nm, a required frequency stability — in terms of Allan deviation — better than 200 kHz at 7 s and below 20 kHz ($<10^{-10}$ fractional stability) for integration times between 700 s to the envisaged three-year operational lifetime of the mission was determined [36].

Frequency-stable laser sources at 1.5 μm have been developed through stabilisation to acetylene transitions in the spectral range of 1510 to 1550 nm, using a bulk reference gas cell [46][47] or a gas-filled hollow-core photonic crystal fibre (HC-PCF) [48][49][50]. Alternative approaches to produce frequency standards in the optical telecommunications spectral region (C-Band: 1530 to 1565 nm) have used the second harmonic of a 1.5 μm laser locked to the Rb two-photon transition at 778 nm [51][52][53][54][55] or to the D2 line at 780 nm [56][57][58][59][60][61][62][63]. The advantage of this approach is the ability to use a cm-scale or a micro-fabricated Rb cell (compared to the tens of centimetres of the acetylene glass cell [47]), while benefiting from the large variety of telecom-grade semiconductor lasers. A frequency-doubled, fibre-coupled 1560 nm laser stabilised to an Rb gas cell provides a stable optical frequency at 1560 nm, 780 nm, or at both wavelengths simultaneously. Sub-Doppler absorption spectroscopy in conjunction with wavelength modulation spectroscopy (WMS) is a common and simple method to lock the frequency of a laser to an atomic transition. By retro-reflecting the laser beam through a Rb cell, narrow Lamb dips showing a Lorentzian profile with a typical FWHM of about 10 MHz can be obtained and superimposed to the Doppler-broadened (≈500 MHz) Gaussian absorption background.

At the LTF, an optical-frequency reference at 1572 nm was developed. It uses one Rb vapour cell for frequency stabilisation of lasers at 780 nm, 1560 nm, and 1572 nm [64][65]. A 1560 nm master laser is frequency stabilised to the Rb vapour cell at 780 nm using frequency doubling. An optical-frequency-comb generator is used to fill the gap of 12 nm between 1572 nm and the laser at 1560 nm. In Chapter 6, the frequency stability performance of the laser system is presented. A frequency instability at 1572 nm at the level of 10^{-11} at all time scales is demonstrated.

Thesis outline

The contents of this thesis are arranged in chapters as follows:

Chapter 1

This chapter reviews the theory of the Rb vapour-cell frequency standard. First, the Rb hyperfine structure is briefly presented. Second, the theory associated with optical-frequency reference is presented with an emphasis on sub-Doppler absorption spectroscopy. Third, the theory describing the response of the atoms to a DR perturbation in the semi-classic approach based on the calculation performed by Godone et al. [66] is reviewed. This approach allows for atomic responses to be described using the Bloch sphere representation. Using this representation, the main properties of the atomic signal are presented. The fourth section of this chapter presents the basics of determining the clock's frequency instability in terms of overlapping Allan deviation. An overview of the underlying noise processes is also given. Finally, the relevant perturbations of high-performance vapour-cell Rb frequency standards are discussed in detail.

Chapter 2

This chapter presents the experimental realisation of the vapour-cell frequency reference prototypes used in this thesis work. First, compact Rb vapour-cell laser head are described in detail. The second part of the chapter is devoted to the experimental description of the compact atomic clock prototype based on a 2.5 cm long Rb vapour cell and a magnetron-type microwave cavity. The laser system based on a cm-scale vapour cell is described, and the performance in terms of frequency noises and frequency stability is presented. The microwave cavity, the local oscillator, and the vapour cell are described.

Chapter 3

This chapter is devoted to the stability optimisation and evaluation of the microwave-frequency standard. It presents measurements of the sensitivity coefficients and the fluctuations of the main sources of instabilities. A configuration of the clock parameters (light intensity, microwave power, atmospheric pressure) is identified such that the impact of the LS and the microwave shift is reduced. The barometric effect is also described, analysed, and reduced. The chapter presents measurements of the medium- to long-term stability of the Rb clock prototype. The short-term and medium- to long-term frequency instability budget is compared with the measured frequency instabilities. The chapter concludes with a discussion of the comparison and the identification of the source of frequency instabilities.

Chapter 4

This chapter concerns the use of an additive manufactured (3D-printed) microwave cavity inside the Rb clock prototype. The Ramsey and Zeeman spectra are presented as well as the Rabi oscillation. A short-term frequency stability at the state-of-the-art level is demonstrated.

Chapter 5

The final chapter describes the use of the Rb vapour cell to build an onboard optical-frequency reference at 1572 nm. The system is a laser system based on the frequency doubling of a 1560-nm laser and the generation of an optical comb with a span of 40 nm around 1560 nm. The frequency instability at 780 nm, 1560 nm, and 1572 nm is presented. The sub-system composed of the frequency-doubling stage and the compact frequency reference unit is analysed in detail. The impact of the frequency doubling on the frequency and intensity noise at 780 nm and 1560 nm is presented. The reproducibility and repeatability of the absolute laser frequency at 780 nm and 1560 nm is also evaluated.

Personal contributions

The first aspect of my contribution concerned the evaluation of the medium- to long-term frequency stability of our POP-DR Rb atomic clock prototype. It consisted of evaluating the clock frequency sensitivity to relevant quantities: laser frequency and intensity fluctuations (light-shift effects), microwave power (microwave-power shift), and environmental effects (barometric effect, temperature). For each of these effects, the sensitivity coefficients as well as the parameter fluctuations were measured. It resulted to identify the natural fluctuation of atmospheric pressure as the most important source of frequency instability for our POP-DR Rb atomic clock prototype. In addition, I carried out numerical simulations evaluating the impact of vapour cell inhomogeneity (temperature, light intensity, microwave power, and so forth) on the clock frequency. This resulted in a deeper understanding of the microwave power shift and a pedagogical tool (based on the Bloch sphere representation) used to explain the working principle of a POP atomic clock. Finally, my contribution concluded in the demonstration of clock frequency stability to the level of $1{\cdot}10^{-14}$ (relative frequency fluctuation) at 10^4 seconds of integration time. In parallel, I experimentally characterized microwave cavities made by additive manufacturing (3D-printing). The homogeneity and distribution of the microwave field inside the 3D-printed microwave cavity are characterized using the POP atomic clock. Short-term frequency stability at state-of-the-art level was demonstrated.

The second aspect of my contribution concerns optical frequency reference at 1572 nm. The optical frequency reference is a laser system based on a single rubidium vapour cell for frequency stabilization of lasers at 780 nm, 1560 nm, and 1572 nm. My work consisted of demonstrating that the frequency stability of light at 780 nm, 1560 nm, and 1572 nm is identical and comparable with the frequency stability of state of the art optical frequency reference laser heads at 780 nm. It has been done by identifying and reducing the main source of frequency instability especially in the short- and medium- term. An optimisation of the laser frequency stability was also performed. Moreover, the measured frequency stability at 1572 nm represents the state of the art in frequency stabilization at 1572 nm. Subsequently, I focused my research on the characterization of the frequency-stabilised master laser at 1560 nm and 780 nm, with emphasis on its application in high performance atomic clocks.

1 Vapour-cell frequency standard theory

Frequency standards are instruments that provide a stable oscillating signal with a known frequency. They are generally based on an oscillating phenomenon as the oscillations of a pendulum, the oscillations of a quartz crystal, or an atom oscillating between two atomic states. The advantage of using atoms as a frequency reference is that two atoms of the same species share the same properties (e.g. the atomic structure), which allows duplication with a high level of fidelity of the frequency standards. Moreover, the atomic transitions allows to use the high atomic transition frequencies which gives high an atomic quality factor resulting into a higher frequency stability [67].

Atomic frequency standards are based on the transition of an atom between two energy states (E_1, E_2) by the absorption or the emission of a photon of frequency:

$$\nu_B = \frac{E_2 - E_1}{h}, \tag{1.1}$$

where ν_B is the Bohr frequency, and h is the Planck constant. Based on this phenomenon, we can build a frequency standard by stabilisation of the frequency of an external oscillator to the Bohr frequency of a specific transition, as illustrated in Figure 1. In particular, alkali atoms have an energy structure with two ground states with a Bohr frequency in the GHz range. The difference between the first energy states and the ground states is in the near infra-red optical domain. Spectroscopy allows for these Bohr frequencies to be interrogated and an atomic signal that can be used to stabilise the external local oscillator to be extracted. Light spectroscopy allows for the absorption spectrum of the Bohr optical frequency to be measured, whereas DR spectroscopy (light plus microwave) allows for the Bohr microwave frequency to be interrogated.

This chapter briefly reviews the theory behind the optical and the DR spectroscopy techniques used in this thesis. First, the energy structure of the Rb atoms and perturbations of the energy structure are reviewed. The energy structure allows for the optical and the microwave-frequency references and their associated spectroscopy notation used in this thesis to be identified. Second, the two spectroscopy methods are presented. The sub-Doppler technique is presented using a simple two-level model. This model is used for a qualitative discussion on the properties of the sub-Doppler signal. The working principle of the POP scheme is described based on the calculation performed by Godone et al. [66] that makes use of the three-level approximation of the ^{87}Rb D_2 line. This theoretical review is used in the analysis of the experimental studies in Chapter 3 and 4. Finally, the most important clock frequency shifts and the achievable clock frequency instability are presented.

1.1 Alkali atoms and atomic structure

The atomic energy structure can be ordered using quantum numbers. The choice of quantum numbers depends on the atomic species and the strength of the interactions inside the atom. Alkali atoms are hydrogen-like. These atoms consist of a nucleus, $Z-1$ filled subshells, and the outermost electron in a s-orbital. The description of the alkali atom energy structure is based on the hydrogen energy structure.

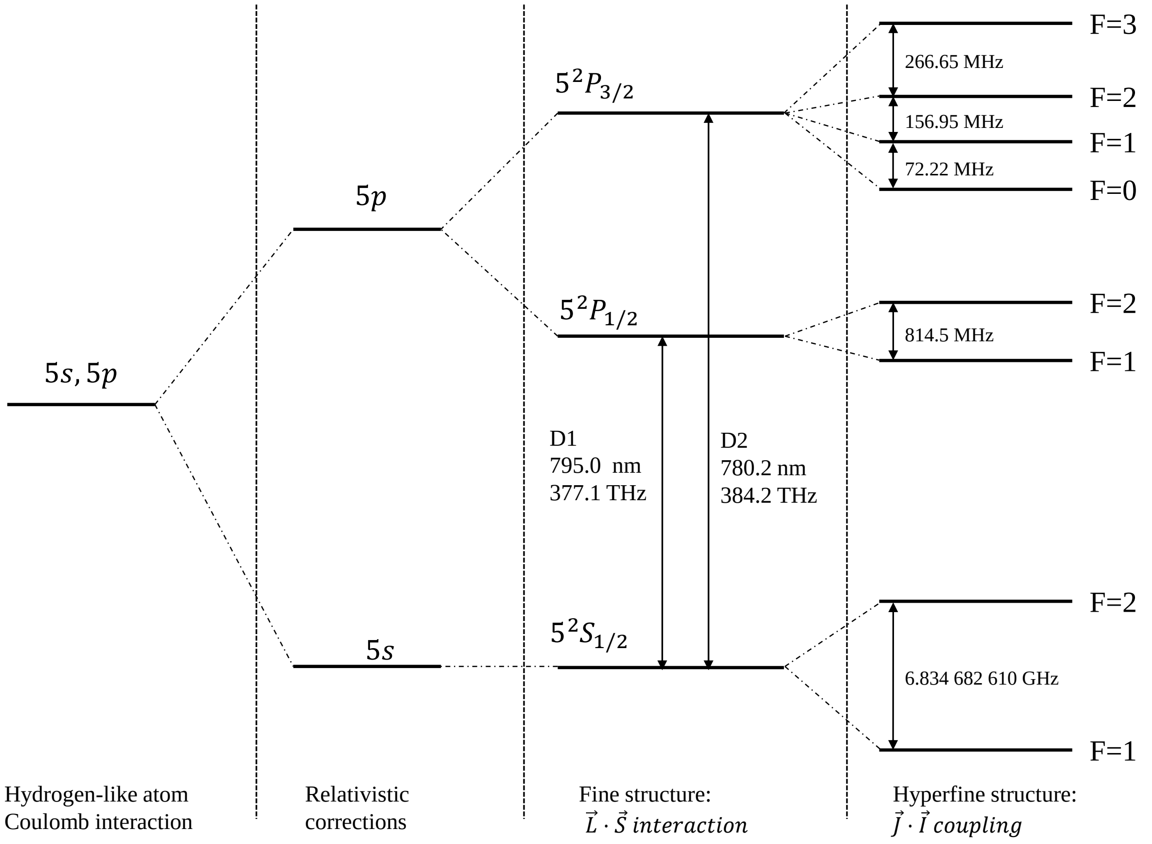

Figure 1.1 – *Energy structure of* ^{87}*Rb for* $n = 5$. *The nucleus atomic spin is* $I = 3/2$.

1.1.1 Hyperfine Hamiltonian: Alkali atom hyperfine structure

The Hamiltonian describing the energy structure of alkali atom is given as[1]:

$$\widehat{H}_0 = \widehat{H}_c + \widehat{H}_{re} + \widehat{H}_{so} + \widehat{H}_{hyp}. \tag{1.2}$$

The first term $\widehat{H}_c$ represents the coulomb interaction between the nucleus plus the $Z-1$ filled subshells with the outermost electron. The second term $\widehat{H}_{re}$ contains relativistic correction independent of the electron spin $\widehat{\mathbf{S}}$. The third term is the spin-orbit Hamiltonian $\widehat{H}_{so} = \alpha \cdot \widehat{\mathbf{L}} \cdot \widehat{\mathbf{S}}$. It couples the electron angular momentum $\widehat{\mathbf{L}}$ and the electron spin $\widehat{\mathbf{S}}$ and is responsible for the fine structure. The last term is hyperfine coupling $\widehat{H}_{hyp} = \beta \cdot \widehat{\mathbf{I}} \cdot \widehat{\mathbf{J}}$. It couples the nucleus spin $\widehat{\mathbf{I}}$ with the total angular momentum $\widehat{\mathbf{J}} = \widehat{\mathbf{L}} + \widehat{\mathbf{S}}$ of the electron. It gives the hyperfine structure. The energy structure E and

---

[1] The bold font is used to represent a vector, and the widehat is used to represent a quantum operator.

the eigenstates Ψ of the total Hamiltonian $\widehat{H}_0$ are the solution of:

$$\widehat{H}_0\Psi = E\Psi. \tag{1.3}$$

The solution of equation (1.3) can be parametrised in terms of quantum numbers. The quantum numbers are usually representative of the symmetry of the system and are eigenvalues of conserved operators. The two first interactions $\widehat{H}_c + \widehat{H}_{re}$ conserve $\widehat{\mathbf{L}}^2$ and $\widehat{L}_z$. The Hamiltonian $\widehat{H}_c + \widehat{H}_{re}$ can be diagonalised in the basis $|L, m_L\rangle$ defined by:

$$\begin{aligned} \widehat{\mathbf{L}}^2\,|L, m_L\rangle &= \hbar^2 L(L+1)\,|L, m_L\rangle \\ \widehat{L}_z\,|L, m_L\rangle &= \hbar m_L\,|L, m_L\rangle\,, \end{aligned} \tag{1.4}$$

with $L = 0, 1, 2\ldots$ and $m_L = -L, -L+1, \ldots, L-1, L$. The energy levels of the Hamiltonian $\widehat{H}_c + \widehat{H}_{re}$ depend on the principal quantum number n. The eigenstates can be described in the basis $|n, L, m_L\rangle$. The basis is usually indicated nL, where the conventional notation replaces values of $L = 0, 1, 2, 3, \ldots$ with letters $s, p, d, f, \ldots$.

Considering the spin-orbit interaction, the Hamiltonian $\widehat{H}_c + \widehat{H}_{re} + \widehat{H}_{so}$ conserves $\widehat{\mathbf{L}}^2$ and the total angular momentum $\widehat{\mathbf{J}}^2$. The electron total angular momentum $\widehat{\mathbf{J}}$ verifies the same equations (1.4). The Hamiltonian $\widehat{H}_c + \widehat{H}_{re} + \widehat{H}_{so}$ is then diagonal in the basis $|n, J, m_J, L\rangle$. The quantum number J lies in the range $|L-S| \leq J \leq L+S$. The fine structure induced by the spin-orbit interaction is usually represented by the spectroscopy notation:

$$n^{2s+1}L_J. \tag{1.5}$$

Finally, the total Hamiltonian $\widehat{H}_0$ conserves the total angular momentum $\widehat{\mathbf{F}} = \widehat{\mathbf{J}} + \widehat{\mathbf{I}}$. The Hamiltonian is then diagonal in the basis $|n, J, L, F, m_F\rangle$ where the quantum number F takes value in the range $|J-I| \leq F \leq J+I$. The total angular momentum $\widehat{\mathbf{F}}$ verifies the same equations (1.4). The hyperfine structure induced by the Hamiltonian (1.2) is usually represented as:

$$|n^{2S+1}L_J, F\rangle\,. \tag{1.6}$$

The energy structure induced by the Hamiltonian (1.2) and for $n = 5$ is presented in Figure (1.1) in the case of ^{87}Rb. The electron structure of ^{87}Rb is $(1s^2, 2s^2, 2p^6, 3s^2, 3p^6, 4s^2, 3d^{10}, 4p^6, 5s^1)$, where the outermost electron occupies the states $|5^2S_{1/2}, F, m_F\rangle$ in the thermal equilibrium. We called these states *ground states*. The optical transitions $5^2S_{1/2} \to 5^2P_{1/2}$ and $5^2S_{1/2} \to 5^2P_{3/2}$ are called the D_1 line (at 795 nm or 377.1 THz) and D_2 line (at 780.2 nm or 384.2 THz), respectively. In this thesis, the D_2 line is the optical-frequency reference transition, and the microwave transition $|5^2S_{1/2}, F=1\rangle \to |5^2S_{1/2}, F=2\rangle$ is the microwave-frequency reference (at 6.834 GHz).

1.2 Sub-Doppler absorption spectroscopy

In this section, a simple theoretical model is used to illustrate the difference between basic and sub-Doppler absorption spectroscopy. Ordinary laser spectroscopy uses one laser beam; the absorption of this beam is measured when the laser frequency is scanned across the resonance optical frequency. In a two-level system, the absorption of the light intensity through the vapour cell is described by the Beer-Lambert law:

$$\frac{dI}{dz} = -\alpha I, \tag{1.7}$$

where α is the absorption coefficient, which is given by:

$$d\alpha = \sigma(P_g - P_e)dn, \tag{1.8}$$

where σ is the absorption cross-section, dn is the fraction of atoms participating in the absorption, and P_g,P_e are the fraction of atoms in the ground state or the exited state. The term P_g - P_e is a consequence of the equilibrium between stimulated emission and absorption of photons and P_g - P_e = 1 in the case of a single beam with low intensity. The absorption coefficient possesses a Lorentzian profile with the natural linewidth Γ:

$$\sigma(\nu,\nu_0) = \sigma_0 \frac{1}{1+4(\nu-\nu_0)^2/\Gamma^2}. \tag{1.9}$$

Equation 1.9 shows that the absorption is not described by a Dirac function $\delta(\nu-\nu_0)$, where only one frequency is absorbed by the vapour, but by a broad profile where a group of laser frequencies is absorbed. In the case of equation 1.9, the linewidth of the absorption is given by Γ, which represents the best possible resolution of an optical transition[2]. For the D_2 optical transition, Γ is about 6 MHz [3].

In the case of an atomic vapour of temperature T, the fraction of atoms dn in the velocity group v and $v + dv$ participating in the absorption is given by the Boltzmann distribution:

$$dn = n_0 \sqrt{\frac{m}{2\pi k_B T}} e^{-mv_z^2/2k_B T} dv_z. \tag{1.10}$$

where k_B is the Boltzmann constant, T is the absolute temperature, m is the Rb mass, $n_0 = N/V$ is the atomic density, and v_z is the longitudinal velocity (parallel to the light beam). Due to the Doppler effect, the atoms with a velocity v_z are probed by a Doppler-shifted light frequency, i.e. $\nu - v_z/c$. Finally, one obtains:

$$\alpha(\nu) = \sigma_0 n_0 \sqrt{\frac{m}{2\pi k_B T}} \int_{\infty}^{\infty} \frac{e^{-mv_z^2/2k_B T}}{1+4(\nu - v_z/c - \nu_0)^2/\Gamma^2} dv_z \tag{1.11}$$

Equation 1.11 describes how the vapour absorbs a group of laser frequency described by a Gaussian profile induced by the Doppler effect. It results in an increase in the optical transition ν_0 resolution due to the Doppler effect, which is about $\Delta\nu_{Dop} = \sqrt{\frac{8k_B T ln2}{mc^2}}\nu_0 \approx 500$ MHz at 315 K for the D_2 transition.

The sub-Doppler absorption spectroscopy is a method that represents the optical transitions with a resolution that can reach the level of the natural linewidth. Sub-Doppler spectroscopy is based on two counter-propagating beams with the same frequency but different intensities. The most intense

---

[2] The natural linewidth Γ is the result of the Heisenberg uncertainty principle and represents the intrinsic limit of the measurement of the energy of one atomic state.

[3] in an evacuated Rb cell only.

beam is used as a pump beam, and the weaker one is used as a probe beam. Each beam interacts with a different group of atoms that possess different longitudinal velocities due to the Doppler effect. If the group velocities are different, the absorption of the probe beam is not perturbed by the pump beam, and the problem is reduced to ordinary linear spectroscopy. If the group velocities are the same, i.e. for a zero longitudinal velocity $v_z = 0$, the same group of atoms absorbs the pump and the probe light. The pump light depopulates the number of atoms participating in the absorption of the probe light, which results in a decrease of the probe absorption [68]. In the case of a closed two-level system, the impact of the pump light on the ground state and excited state population is described by [69]:

$$P_g - P_e = \frac{1}{1+2\frac{I}{I_{sat}}}, \tag{1.12}$$

where I_{sat} is the saturation intensity and I is the pump light intensity. Figure 1.2 presents the absorption coefficient α obtained by integration over the velocity of equation (1.11) considering equation (1.12).

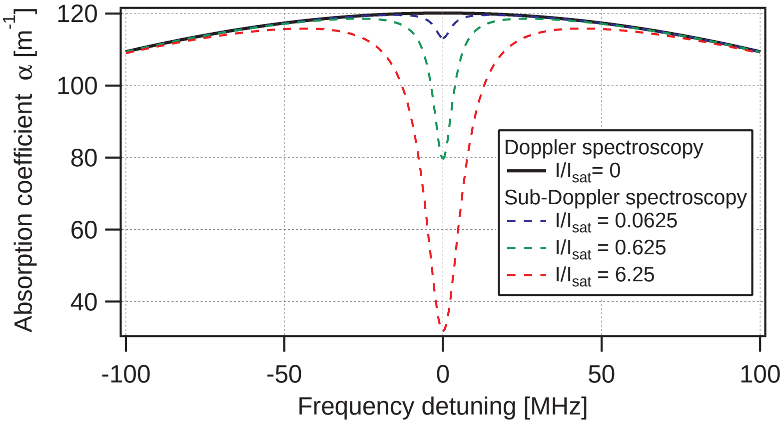

Figure 1.2 – *Probe beam absorption coefficient α calculated in a simple two level model (equations (1.11 and 1.12) in the case of Doppler spectroscopy (black curve) and sub-Doppler spectroscopy (colored dashed curves).*

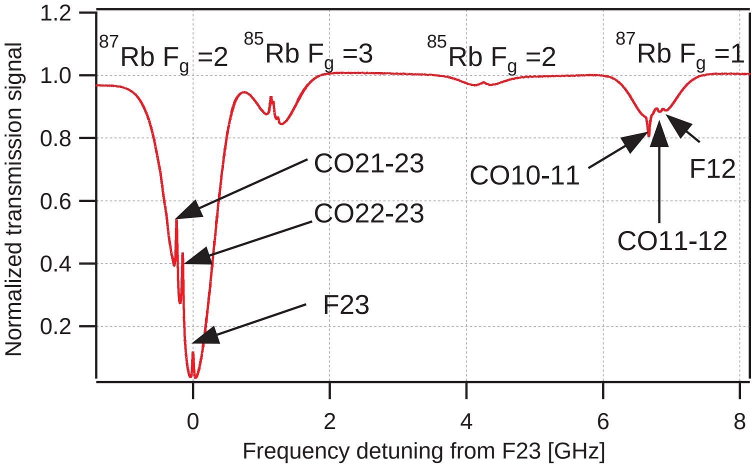

Figure 1.3 – *Sub-Doppler absorption spectrum measured using one home-made Rb AOM-integrated laser head (see chapter 2) containing an enriched ^{87}Rb vapour cell.*

The impact of the pump beam on the probe absorption results in dips in the absorption spectrum called *Lamb dips* [69]. These dips are at the optical transition frequencies. The FWHM of the *Lamb dip* is about $\Delta\nu_{Lamp} = \gamma\sqrt{1+\frac{I}{I_{\text{sat}}}}$ [69], where γ is the natural linewidth (for ^{87}Rb $\gamma \approx 6$ MHz) and I is the pump intensity. The amplitude of the *Lamb dip* is in about $\frac{I}{I_{\text{sat}}}$. For the typical optical intensity of 12 mW/cm^2 used in our home-made Rb-stabilised laser head, the FWHM of the *Lamb dip* is 17.3 MHz.

Another group of velocities can be detected by the sub-Doppler method. Consider an atom with two different optical-frequency transitions (ν_1 and ν_2) sharing one common level (for example, the same ground state) and a group of atoms having a longitudinal velocity $-v_z$ with respect to the pump beam and $+v_z$ with respect to the probe beam. In the frame of the atoms, the pump and the probe beam are frequency shifted by the Doppler effect. A saturation dip results at a laser frequency such that the pump beam is absorbed by the first optical transition $\nu_1 = \nu_{\text{laser}}(1+\frac{v_z}{c})$ and the probe beam absorbed by the second optical transition $\nu_2 = \nu_{\text{laser}}(1-\frac{v_z}{c})$ which is simply given by:

$$\nu_{Laser} = \frac{\nu_1+\nu_2}{2}. \tag{1.13}$$

Symmetrically, the other group of atoms with a longitudinal velocity $+v_z$ with respect to the pump beam and $-v_z$ with respect to the probe beam is also detected at the same frequency given by equation (1.13). This results in a dip in the absorption spectrum at this frequency. We identify these dips *cross-over* with the following symbol CO. Figure 1.3 presents a typical measured sub-Doppler transmission spectrum with the sub-Doppler dips highlighted. For the transitions of interest in this work, Table 1.1 presents the optical transitions associated with each sub-Doppler dip. The spectroscopic notation introduced in Table 1.1 is used extensively in all chapters of this document.

Symbol		Spectroscopy notation	Frequency detuning from F23 [MHz]
F=1	F12	$\lvert 5^2S_{1/2}, F=1\rangle \leftrightarrow \lvert 5^2S_{1/2}, F=2\rangle$	6'568.03
	CO11-12	$\lvert 5^2S_{1/2}, F=1\rangle \leftrightarrow \lvert 5^2S_{1/2}, F=1/F=2\rangle$	6'489.56
	CO10-11	$\lvert 5^2S_{1/2}, F=1\rangle \leftrightarrow \lvert 5^2S_{1/2}, F=0/F=1\rangle$	6'374.97
F=2	F23	$\lvert 5^2S_{1/2}, F=2\rangle \leftrightarrow \lvert 5^2S_{1/2}, F=3\rangle$	0
	CO22-23	$\lvert 5^2S_{1/2}, F=2\rangle \leftrightarrow \lvert 5^2S_{1/2}, F=2/F=3\rangle$	-133.33
	CO21-23	$\lvert 5^2S_{1/2}, F=2\rangle \leftrightarrow \lvert 5^2S_{1/2}, F=1/F=3\rangle$	-211.79

Table 1.1 – *Symbol, Spectroscopy notation and frequency detuning [70] for the sub-Dopper dips used in this works and presentend on Figure 1.3.*

1.3 Working principle of a DR atomic clock

In this section, the working principle of a DR atomic clock and, in particular, the case of a POP scheme, is reviewed. For this purpose, we follow the theoretical approach used by Godone et al. [71],[66] and Vanier et al. [67] based on the three-level approximation.

The three-level approximation allows for the complete set of equations describing the time evolution of the density matrix, where the density matrix describes statistically the atomic density in the vapour cell, to be written. The well-known Bloch sphere representation is based on this set of equations. From these equations, atomic response can be simulated in the POP scheme with homogeneous interaction fields (light and microwave fields). The simulation is used to introduce and study the main properties of the signal (contrast and FWHM).

1.3.1 Perturbation Hamiltonian: DR interaction

Rubidium DR atomic clocks are based on the interaction between Rb atoms and two types of electromagnetic fields: a light field and a magnetic field. In the semi-classical approach, these interactions are treated as a perturbation $\widehat{W}$:

$$\widehat{H} = \widehat{H}_0 + \widehat{W}, \tag{1.14}$$

where $\widehat{H}_0$ is the non-perturbed Hamiltonian given by (1.2) with eigenvalues and eigenvectors solutions of:

$$\widehat{H}_0 \left| i \right\rangle = E_i \left| i \right\rangle, \tag{1.15}$$

where the eigenvector $\left| i \right\rangle$ represents one of the states (1.6).

1.3.1.1 Light interaction

For the transition of interest, the light field interaction is mainly dominated by the interaction of the oscillating electric light field. The coupling of the oscillating magnetic light field with the electron is a tiny perturbation in the atomic system, and it is neglected here. We write the oscillating electric light field in the form:

$$\mathbf{E}(r,t) \quad = \quad \mathbf{e}(\lambda)E(r,t)\frac{1}{2}e^{i\omega_L t-\mathbf{k}\cdot\mathbf{r}} + c.c. \tag{1.16}$$

where $E(r,t)$ is the slowly varying light amplitude, **e** is the polarisation vector, ω_L is the laser angular frequency, **k** is the wave vector, and **r** is the position vector. Under the dipole approximation [4], the light field interaction is described by the following Hamiltonian:

$$\begin{aligned} \widehat{H}_E &= -q\widehat{\mathbf{r}}\cdot\widehat{\mathbf{E}} \\ &= -\widehat{d}E(\widehat{r},t)\frac{1}{2}e^{\omega_L t} + c.c. \end{aligned} \tag{1.17}$$

---

[4] The dipole approximation consists of neglecting the term $e^{-\mathbf{k}\cdot\mathbf{r}}$. In the case of ^{87}Rb, the product $\mathbf{k}\cdot\mathbf{r}$ is about 10^{-3} and $e^{-\mathbf{k}\cdot\mathbf{r}} \approx 1-\mathbf{k}\cdot\mathbf{r} \approx 1$.

where $\widehat{d} = q\widehat{\mathbf{r}}\cdot\widehat{\mathbf{e}}$ is the dipole moment. The laser interaction can be represented by the optical Rabi frequency $\omega_R(r,t) = \langle j|\widehat{d}|i\rangle\frac{E(r,t)}{\hbar}$ where $\langle j|\widehat{d}|i\rangle$ is the matrix element of the dipole moment associated with the atomic transition $|i\rangle \to |j\rangle$. We assume that the optical Rabi frequency is a real number, i.e. $\omega_R(r,t) = \omega_R(r,t)^*$.

1.3.1.2 Magnetic interaction

In the case of an interaction with a magnetic field $\mathbf{B}$, the Hamiltonian is given as:

$$\widehat{H}_B = -\widehat{\boldsymbol{\mu}}\cdot\widehat{\mathbf{B}}, \tag{1.18}$$

where $\widehat{\mu}$ is the magnetic moment operator of the atom, given as $\widehat{\boldsymbol{\mu}} = -\mu_B(\widehat{\mathbf{L}} + g_J\widehat{\mathbf{J}} - g_I\widehat{\mathbf{I}})$.

For an oscillating magnetic field $\widehat{\mathbf{B}}(r,t)$ aligned along the z-axis of the clock (see Figure 3), we assumed that the oscillating magnetic field is in the form:

$$\mathbf{B}(r,t) = \mathbf{z}B_z(r,t)\frac{1}{2}e^{i\omega_m t + i\phi t} + c.c. \tag{1.19}$$

where $B_z(r,t)$ is the slowly varying magnetic-field amplitude, ω_m is the microwave angular frequency, and ϕ a phase term. The Hamiltonian of the interaction can be written:

$$\begin{aligned}\widehat{H}_B &= -\widehat{\mu}\cdot\widehat{\mathbf{B}}\\ &= -\widehat{\mu}_z B_z(r,t)\frac{1}{2}e^{i\omega_m t + i\phi t} + c.c.\end{aligned} \tag{1.20}$$

The interaction with an oscillating magnetic field can be represented by the Rabi frequency $b = \langle j|\mu_z|i\rangle\frac{B_z(r,t)}{\hbar}$ where $\langle j|\mu_z|i\rangle$ is the matrix element of the magnetic moment associated with the transition $|i\rangle \to |j\rangle$. We assume that the Rabi frequency b is a real number, i.e. $b(r,t) = b(r,t)^*$.

In the case of a static magnetic field $\widehat{\mathbf{B}}(r)$ aligned along the z-direction, equation (1.18) is reduced to:

$$\widehat{H}_B = \mu_B(\widehat{L}_z + g_J\widehat{J}_z - g_I\widehat{I}_z)B_z \tag{1.21}$$

In a DR atomic clock, the analysis of the interaction with the static magnetic field is focussed on the ground states $|5^2S_{1/2}, F=1\rangle$ and $|5^2S_{1/2}, F=2\rangle$ for which $L=0$. In this case, the total Hamiltonian is reduced to:

$$\widehat{H}_0 + \widehat{H}_B = \alpha_{L=0}\widehat{\mathbf{I}}\cdot\widehat{\mathbf{S}} + \mu_B(g_J\widehat{S}_z - g_I\widehat{I}_z)B_z \tag{1.22}$$

The eigenvalues of the Hamiltonian (1.22) in the basis (1.6) are given by the Breit-Rabi formula [72],[67]. In the case of ^{87}Rb with $I = 3/2$, one obtains:

$$E(F,m_F) = -\frac{E_{HFS}}{8} - g_I\mu_B B_z m_F \pm \frac{1}{2}E_{HFS}\left(1 + m_F x + x^2\right)^{1/2} \tag{1.23}$$

where the plus sign applies for $F=2$ and the minus sign for $F=1$. In (1.23), $x = (g_J + g_I)\mu_B B_z/E_{HFS}$ and $E_{HFS}/h = 2\alpha_{L=0}/h = 6834682610.90429(9)$ Hz [73].

For low static magnetic field and for magnetic dipole transitions defined by $\Delta m_F = 0, \pm 1$, the hyperfine energy difference between the ground states is given by [67][74]:

$$E(F=2, m_F) - E(F=1, m_F) \quad = \quad E_{HFS} + (m_{F=1} + m_{F=2}) \frac{g_J \mu_B}{4} B_z + \frac{(g_J \mu_B)^2}{2E_{HFS}} B_z^2 \tag{1.24}$$

The dependence of the hyperfine splitting on the static magnetic field is reduced to a linear and a quadratic dependence. The hyperfine frequency splitting can then be written as:

$$\begin{aligned} \nu_{21} &\equiv \frac{E(F=2, m_F) - E(F=1, m_F)}{h} \\ &= \nu_{HFS} + (m_F^{F=1} + m_F^{F=2}) \frac{g_J \mu_B}{4h} B_z + \frac{(g_J \mu_B)^2}{2E_{HFS} h} B_z^2 \end{aligned} \tag{1.25}$$

The linear coefficient is $(m_F^{F=1} + m_F^{F=2}) 0.7 \frac{MHz}{G}$ and the quadratic coefficient is $575.14 \frac{Hz}{G^2}$. The hyperfine transition $|5^2 S_{1/2}, F=1, m_F=0\rangle \leftrightarrow |5^2 S_{1/2}, F=2, m_F=0\rangle$ is insensitive to the static magnetic field at the first order. This first-order insensitivity makes the hyperfine transition $|5^2 S_{1/2}, F=1, m_F=0\rangle \leftrightarrow |5^2 S_{1/2}, F=2, m_F=0\rangle$ the clock transition with the following static magnetic-field sensitivity:

$$\nu_{21} \quad = \quad \nu_{HFS} + \frac{(g_J \mu_B)^2}{2E_{HFS} h} B_z^2 \tag{1.26}$$

1.3.2 Life time of the atomic state and buffer-gas broadening

Under the interaction of external fields, the population distribution of atomic energy levels is out of thermal equilibrium. The atoms tend to return to the equilibrium by spontaneous emission. The lifetime of the exited state is denoted τ and the de-excitation rate is $\Gamma^* = \frac{1}{\tau}$. The finite lifetime of the energy state induces a broadening of the energy level.

In the present study, we consider ^{87} Rb vapour confined in a glass cell. The Rb atoms are confined with a mixture of the buffer gases (BGs) argon and nitrogen, which prevent the Rb atom from colliding with the cell wall. The nitrogen is used as a quenching gas, which avoids fluorescence, whereas the argon is used to decrease the temperature coefficient of the nitrogen (see section 1.4.5.2). For buffer gas used in our vapour cell (N_2 and Ar), the collisions cause an increase in the de-excitation rate of the exited states by ≈ 13.5 MHz/hPa (≈ 18 MHz/Torr) [26]. The buffer-gas de-excitation rate is $\Gamma^*/(2\pi) \approx 405$ MHz for a buffer-gas pressure of 30 hPa.

In the ground states, relaxation to the thermal equilibrium is a result of wall collisions, Rb–Rb collisions, and Rb–BG collisions. These collisions impact the wave function of the outermost electron of the Rb atom by changing the coulomb interaction $\widehat{H}_C$. The relaxation of observable quantities, such as the population and the coherence of the ground states, is denoted γ_1 (also called the longitudinal relaxation rate), and the coherence relaxation rate is γ_2 (also called the transverse relaxation rate), respectively. The ground-state relaxation rate in our Rb vapour cell is about $\gamma_1^{-1} \approx \gamma_2^{-1} \approx 4.5$ ms [31].

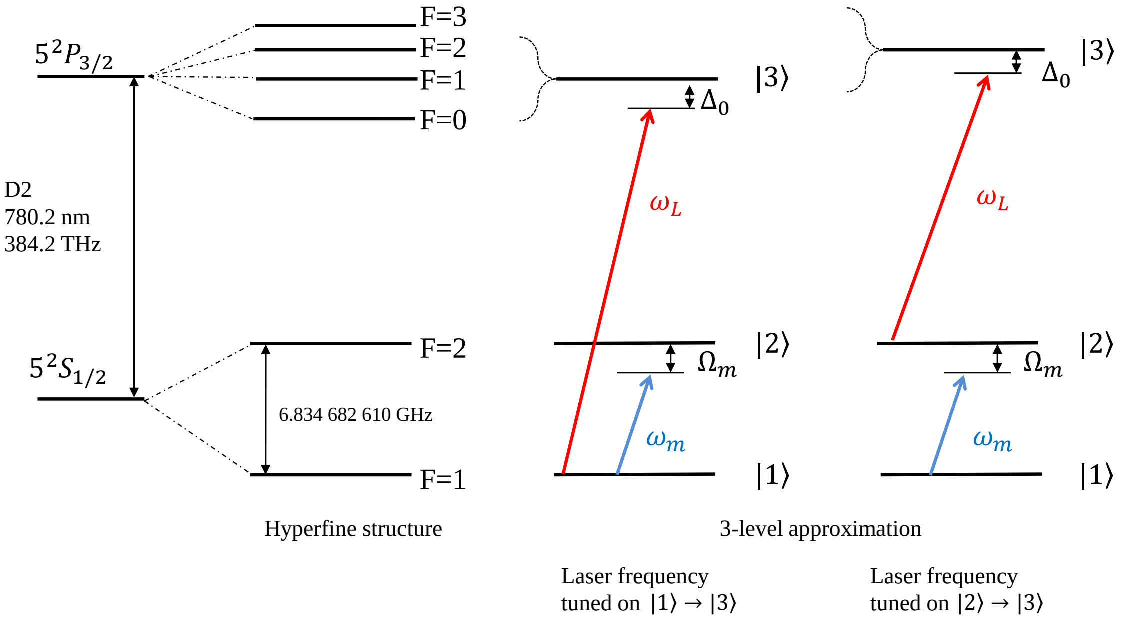

Figure 1.4 – *Comparison between the hyperfine structure of* ^{87}*Rb and the 3-level model. The light field interaction is represented by the red arrow and the microwave magnetic field interaction is represented by the blue arrow. Depending on the laser frequency, the level* $|3\rangle$ *is defined as* $|3\rangle = |5^2P_{3/2}, F = \{0,1,2\}, m_F\rangle$ *if the laser is frequency tuned on* $|1\rangle \rightarrow |3\rangle$ *or* $|3\rangle = |5^2P_{3/2}, F = \{1,2,3\}, m_F\rangle$ *if the laser is frequency tuned on* $|2\rangle \rightarrow |3\rangle$.

1.3.3 Density matrix equations in the three-level approximation

The hyperfine transition $|5^2S_{1/2}, F = 1, m_F = 0\rangle \leftrightarrow |5^2S_{1/2}, F = 2, m_F = 0\rangle$ is the clock transition. The interrogation of the clock transition is done through the interaction of the atoms with an optical field and an magnetic field. The impact of these interactions on the clock signal can be analysed using a simple energy structure model where the hyperfine structure of Figure 1.1 is approximated by a three-level system. This approximation is motivated by the frequency splitting (hundreds of MHz) between the states $|5^2P_{3/2}, F = 1\rangle$ to $|5^2P_{3/2}, F = 3\rangle$ or between the states $|5^2P_{3/2}, F = 0\rangle$ to $|5^2P_{3/2}, F = 2\rangle$ compared to the hyperfine frequency splitting (6.8 GHz) of the clock transition. Figure 1.4 presents the three-level approximation. The three-level system is described by three states $|1\rangle, |2\rangle, |3\rangle$ where:

$$\begin{aligned}
|1\rangle &\equiv |5^2S_{1/2}, F = 1, m_F = 0\rangle \\
|2\rangle &\equiv |5^2S_{1/2}, F = 2, m_F = 0\rangle \\
|3\rangle &\equiv |5^2P_{3/2}, F = \{0,1,2\}, m_F\rangle \, \text{or} \, |5^2P_{3/2}, F = \{1,2,3\}, m_F\rangle \, .
\end{aligned} \tag{1.27}$$

The states (1.27) verify $\widehat{H}_0 |i\rangle = \hbar\omega_i |i\rangle$ where $\widehat{H}_0$ is given by equation (1.2). In the basis $\{|1\rangle, |2\rangle, |3\rangle\}$, the optical Rabi frequency of the light field is $\omega_{R_1} = d_{31}\frac{E_1(r,t)}{\hbar}$ if the laser frequency is tuned to $|1\rangle \rightarrow |3\rangle$, or $\omega_{R_2} = d_{32}\frac{E_2(r,t)}{\hbar}$ if the laser frequency is tuned to $|2\rangle \rightarrow |3\rangle$. In the basis (1.27), the total

Hamiltonian $\widehat{H}_0 + \widehat{H}_E(r,t) + \widehat{H}_B(r,t)^5$ is given by:

$$\widehat{H}(r,t) = \frac{\hbar}{2}\begin{bmatrix} \omega_1 & -be^{i\omega_m t} & -\omega_{R_1}e^{i\omega_{L_1}t} \\ -be^{i\omega_m t} & \omega_2 & 0 \\ -\omega_{R_1}e^{i\omega_{L_1}t} & 0 & \omega_3 \end{bmatrix} + c.c. \tag{1.28}$$

for the light frequency on $|1\rangle \rightarrow |3\rangle$, and for the light frequency on $|2\rangle \rightarrow |3\rangle$:

$$\widehat{H}(r,t) = \frac{\hbar}{2}\begin{bmatrix} \omega_1 & -be^{i\omega_m t} & 0 \\ -be^{i\omega_m t} & \omega_2 & -\omega_{R_2}e^{i\omega_{L_2}t} \\ 0 & -\omega_{R_2}e^{i\omega_{L_2}t} & \omega_3 \end{bmatrix} + c.c. \tag{1.29}$$

The density matrix $\widehat{\rho}$ describes an ensemble of atoms statistically. In the case of mixed quantum states, the diagonal elements ρ_{mm} give the probability of occupying the quantum state $|m\rangle$, and the off-diagonal elements ρ_{mn} describe the coherent superposition of states $|n\rangle$,$|m\rangle$ and are called **coherences**. The time evolution of the density matrix is given by the quantum Liouville equation:

$$\frac{\partial\widehat{\rho}}{\partial t} + \widehat{\Gamma}_{rel}(t) = -\frac{i}{\hbar}[\widehat{H},\widehat{\rho}] + \widehat{\Gamma}_{exc}(t), \tag{1.30}$$

where the square bracket denotes the commutator. The terms $\widehat{\Gamma}_{rel}(t)$ and $\widehat{\Gamma}_{exc}(t)$ are relaxation and excitation processes not induced in the external fields [71]. In order to simplify the analysis of the time solution of equation (1.30), we neglect the cavity feedback, i.e. the spontaneous radiation emitted by the atoms. This approximation is valid for the type of microwave cavity used in this study because of its high loses (low-quality factor, see Chapter 3). The Hamiltonian $\widehat{H}$ is the Hamiltonian driving the system. The Liouville equation (1.30) gives six coupled equations for the diagonal elements (ρ_{ii}) and for the off-diagonal elements ($\rho_{ij}, i \neq j$). We assume that the solutions for the off-diagonal elements are of the form:

$$\begin{aligned} \rho_{12} &= \delta_{12}e^{i\omega_m t} \\ \rho_{13} &= \delta_{13}e^{i\omega_{L_1}t} \\ \rho_{23} &= \delta_{23}e^{i(\omega_{L_1}-\omega_m)t} \end{aligned} \tag{1.31}$$

for the light frequency on $|1\rangle \rightarrow |3\rangle$, and for the light frequency on $|2\rangle \rightarrow |3\rangle$:

$$\begin{aligned} \rho_{12} &= \delta_{12}e^{i\omega_m t} \\ \rho_{13} &= \delta_{13}e^{i(\omega_{L_2}+\omega_m)t} \\ \rho_{23} &= \delta_{23}e^{i\omega_{L_2}t} \end{aligned} \tag{1.32}$$

where the δ_{ij} are complex, slowly varying functions. Expanding equation (1.30) using the identities

---

[5] In this development, we first write the equations containing both optical and microwave interactions. Latter on, the equations are restricted to the optical pump pulse only or to the microwave interaction only, respectively.

(1.31) and (1.32), we obtain [71]:

$$
\begin{aligned}
\dot{\rho}_{11}+\frac{\gamma_1}{2}(\rho_{11}-\rho_{22}) &= b\mathrm{Im}\big(\delta_{12}e^{-i\phi}\big)+\omega_{R_1}\mathrm{Im}\big(\delta_{13}\big)+\frac{\Gamma^*}{2}\rho_{33}\\
\dot{\rho}_{22}+\frac{\gamma_1}{2}(\rho_{22}-\rho_{11}) &= -b\mathrm{Im}\big(\delta_{12}e^{-i\phi}\big)+\omega_{R_2}\mathrm{Im}\big(\delta_{23}\big)+\frac{\Gamma^*}{2}\rho_{33}\\
\dot{\rho}_{33}+\Gamma^*\rho_{33} &= -\omega_{R_1}\mathrm{Im}\big(\delta_{13}\big)-\omega_{R_2}\mathrm{Im}\big(\delta_{23}\big)\\
\dot{\delta}_{12}+i(\Omega_m-i\gamma_2) &= i\frac{b}{2}e^{i\phi}(\rho_{22}-\rho_{11})+i\frac{\omega_{R_1}}{2}\delta_{32}-i\frac{\omega_{R_2}}{2}\delta_{13}\\
\dot{\delta}_{13}+i\Big(\Delta_0+\Omega_m-i\frac{\Gamma^*}{2}\Big)\delta_{13} &= i\frac{b}{2}e^{i\phi}\delta_{23}-i\frac{\omega_{R_1}}{2}(\rho_{11}-\rho_{33})-i\frac{\omega_{R_2}}{2}\delta_{12}\\
\dot{\delta}_{23}+i\Big(\Delta_0-\Omega_m-i\frac{\Gamma^*}{2}\Big)\delta_{23} &= i\frac{b}{2}e^{-i\phi}\delta_{23}-i\frac{\omega_{R_2}}{2}(\rho_{22}-\rho_{33})-i\frac{\omega_{R_1}}{2}\delta_{12}^*,
\end{aligned}
\tag{1.33}
$$

where the blue (contains ωR_1) and red (contains ωR_2) terms are present only in the case of the light frequency on $|1\rangle \rightarrow |3\rangle$, respectively $|2\rangle \rightarrow |3\rangle$. In equation (1.33), Δ_0 is the laser detuning define by $\Delta_0 = (\omega_3 - \omega_i) - \omega_{L_i}$ and Ω_m is the microwave angular frequency detuning defined by $\Omega_m = (\omega_2 - \omega_1) - \omega_m$. It is possible to simplify the six coupled equations (1.33) using the following assumptions [71]:

- A1: We assume a high excited-state decay: $\Gamma^*/(2\pi) \gg \gamma_1, \gamma_2$
- A2: We assume a small optic and magnetic fields interaction: $\omega_R \ll \Gamma^*$ and $b \ll \Gamma^*$, respectively
- A3: We assume a small microwave detuning $\Omega_m \ll \Gamma^*$
- A4: We assume that the optical coherences (ρ_{13},ρ_{23}) evolve at the typical time scale of $1/\Gamma^* \propto 1$ ns, which is faster than the ground-state microwave coherence (ρ_{12}) that evolves with the typical time scale of $1/\gamma_2 \propto 1$ ms. Results show that the optical coherences rapidly reach their stationary values and follow the ground-state evolution adiabatically.
- A5: We assume a homogeneous field distribution in the vapour cell, and $B_z(r,t)$ and $E(r,t)$ vary slowly enough that they can be considered time-independent during one interrogation cycle, i.e. $\omega_{R_i} \neq \omega_{R_i}(\mathbf{r},t)$ and $b \neq b(\mathbf{r},t)$. This assumption is equivalent to consider the case of a single localised atom, or, alternatively, to a cell with a fully homogeneous field distribution.

Under these assumptions, equations (1.33) can be written in the form (with $\Delta = \rho_{22} - \rho_{11}$ and $\phi = \pi/2$)[71][66]:

$$
\begin{aligned}
\dot{\Delta}+\Big(\gamma_1+\frac{\Gamma_{R_i}}{1+\delta_0^2}\Big)\Delta &= 2b\mathrm{Re}(\delta_{12})\pm\frac{\Gamma_{R_i}}{1+\delta_0^2}\\
\dot{\delta}_{12}+\left(\gamma_2+\frac{\Gamma_{R_i}}{1+\delta_0^2}+i\Big(\Omega_m\pm\frac{\Gamma_{R_i}\delta_0}{1+\delta_0^2}\Big)\right)\delta_{12} &= i\frac{b}{2}\Delta,
\end{aligned}
\tag{1.34}
$$

where the plus sign corresponds to ω_{R_1} and the minus sign to ω_{R_2}. We have redefined the normalised laser frequency detuning $\delta_0 = \frac{2\Delta_0}{\Gamma^*}$ and the optical pumping rate $\Gamma_{R_i} = \frac{\omega_{R_i}^2}{2\Gamma^*}$. The coupled equations (1.34) describe the time evolution of the population difference (Δ) and the coherence (δ_{12}) of the ground state when the atoms are interacting with an optical field (ω_{R_i}) and a microwave magnetic field (b) simultaneously.

In a POP operation, the light fields interactions (states preparation and detection) and the microwave interrogation are separated in time such that the atoms behave as a simple two-level system during the microwave interaction. A typical POP timing is presented in Figure (1.5). The POP clock is operated by repeating the POP timing with a frequency of $f_C = \frac{1}{T_C}$ where T_C is the total cycle time. Based on the timing sequence in Figure (1.5), the set of equations (1.34) can be solved for each interaction's phase [66].

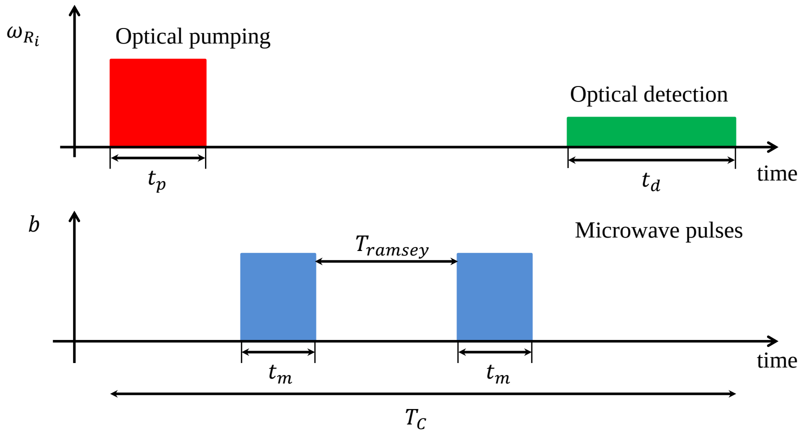

Figure 1.5 – *Pulsed optically pumped (POP) timing sequence. t_p, optical pumping duration; t_m microwave pulse duration; T_{ramsey} free evolution duration (Ramsey time);t_d detection pulse duration. Each pulse is separated by dead times to avoid overlapping between different pulses.*

1.3.3.1 Pumping phase

The pumping phase is used to optically pump all the atoms in one of the ground states $|1\rangle$ or $|2\rangle$ using an intense light interaction. During the pumping phase, equations (1.34) are:

$$\begin{aligned} \dot{\Delta} + \gamma_1'\Delta &= \pm\frac{\Gamma_{R_i}}{1+\delta_0^2} \\ \dot{\delta}_{12} + \left(\gamma_2' + i\Omega_m'\right)\delta_{12} &= 0. \end{aligned} \tag{1.35}$$

where $\gamma_1' = \gamma_1 + \frac{\Gamma_{R_i}}{1+\delta_0^2}$,$\gamma_2' = \gamma_2 + \frac{\Gamma_{R_i}}{1+\delta_0^2}$ and $\Omega_m' = \Omega_m \pm \frac{\Gamma_{R_i}\delta_0}{1+\delta_0^2}$. The solutions of these differentials equations are:

$$\begin{aligned} \Delta(t) &= \Delta(t=0)e^{-\gamma_1' t} \pm \frac{\Gamma_{R_i}}{\gamma_1'(1+\delta_0^2)}\left(1-e^{-\gamma_1' t}\right) \\ \delta_{12}(t) &= \delta_{12}(t=0)e^{-\gamma_2' t}e^{i\Omega_m' t}. \end{aligned} \tag{1.36}$$

where $\Delta(t=0)$ is the population difference at the beginning of the pump pulse and $\delta_{12}(t=0)$ is the ground-state coherence at the beginning of the pump pulse. The figures (1.6) and (1.7) present the dynamic evolution of the population inversion $\Delta(t)$ and the ground-state coherence $\delta_{12}(t)$ in typical experimental conditions.

To create a ground-state population difference $\Delta = \pm 1$ from an equi-distributed ground state $\Delta = 0$, the typical time scale is about 0.1 ms to 1 ms. From an initial ground-state coherence of $\delta_{12} = 1 + i$, the coherence is attenuated by one order of magnitude at the same time scale of 0.1 ms to 1 ms.

Considering the sub-states $|5^2S_{1/2}, F=1, m_F\rangle$ and $|5^2S_{1/2}, F=2, m_F\rangle$, the population inversion at the end of the pumping phase can take two different values depending on the pump laser frequency. If the pump laser frequency is tuned to the optical transition $|5^2S_{1/2}, F=1\rangle \rightarrow |5^2P_{3/2}\rangle$ and for perfect optical pumping, the atoms are equi-distributed along the five sub-states $|5^2S_{1/2}, F=2, m_F=\{-2,-1,0,1,2\}\rangle$. At the end of the pumping phase, the population inversion is then $\Delta_i = \rho_{22} - \rho_{11} = 1/5$. The same logic applies to the other optical transition $|5^2S_{1/2}, F=2\rangle \rightarrow |5^2P_{3/2}\rangle$, leading to $\Delta_i = -1/3$.

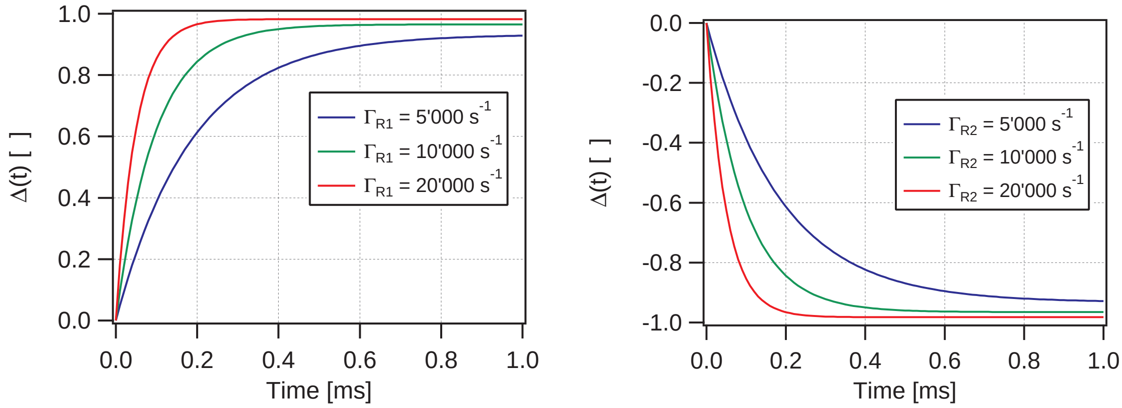

(a) The laser is frequency tuned to $|1\rangle \rightarrow |3\rangle$.

(b) The laser is frequency tuned to $|2\rangle \rightarrow |3\rangle$.

Figure 1.6 – *Time evolution of the population inversion* $\Delta(t)$ *for different optical pumping rates and for the two laser frequencies. We used* $\Delta(t=0)=0$, $\delta_0=0$ *and* $\gamma_1=\gamma_2=238\ s^{-1}$.

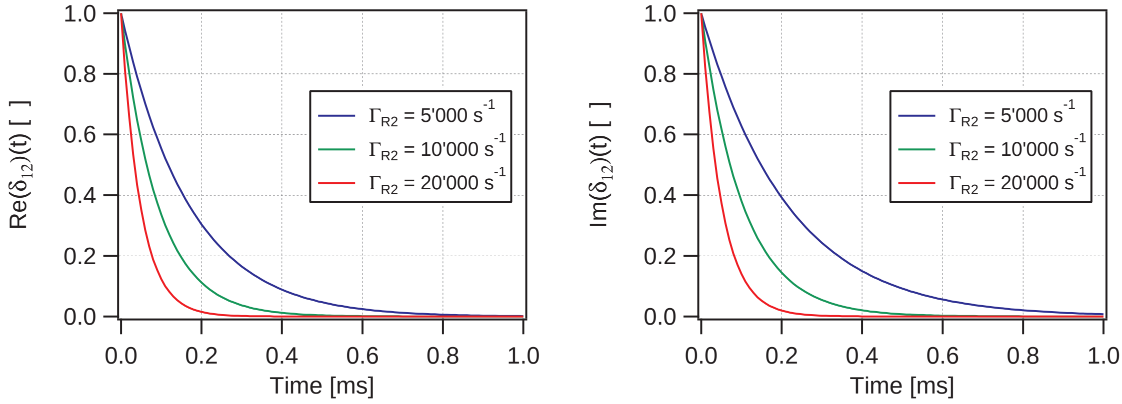

(a) Real part of $\delta_{12}(t)$.

(b) Imaginary part of $\delta_{12}(t)$.

Figure 1.7 – *Time evolution of the ground state coherence* $\delta_{12}(t)$ *for different optical pumping rate and for the laser frequency tuned on* $F=2$. *We used* $\delta_{12}(t=0)=1+i$, $\delta_0=0$ *and* $\gamma_1=\gamma_2=238\ s^{-1}$.

1.3.3.2 Microwave interrogation

After pumping the atoms in one of the ground states, a microwave pulse is used to create a coherence between the two ground states. At the end of the first microwave pulse, the coherence evolves freely during a duration T_R (without any interaction with external fields). During T_R, the coherence accumulates a phase that depends on the microwave frequency. Finally, a second microwave pulse is used to project the atoms in the opposite ground state for optical detection. The signal obtained at the end of the second microwave pulse can be deduced from equations (1.34). During the microwave interrogation, the equations (1.34) become:

$$\begin{aligned} \dot{\Delta} &= 2b\mathrm{Re}(\delta_{12}) \\ \dot{\delta}_{12} + i\Omega_m \delta_{12} &= i\frac{b}{2}\Delta, \end{aligned} \tag{1.37}$$

where we have neglected the decay rate during the microwave interrogation: $t_m \ll \gamma_i^{-1}$. During the free evolution, the equations (1.34) become:

$$\begin{aligned} \dot{\Delta} + \gamma_1 \Delta &= 0 \\ \dot{\delta}_{12} + (\gamma_2 + i\Omega_m)\delta_{12} &= 0. \end{aligned} \tag{1.38}$$

1.3.3.3 Bloch vector representation

A physical interpretation to the solution of the set of equations (1.37) and (1.38) can be obtained using Bloch vector representation. Bloch vector **R** is introduced with the following notation:

$$\mathbf{R} = \begin{bmatrix} R_1 \\ R_2 \\ R_3 \end{bmatrix} = \begin{bmatrix} 2\mathrm{Re}(\delta_{12}) \\ 2\mathrm{Im}(\delta_{12}) \\ \Delta \end{bmatrix}, \tag{1.39}$$

the solution of equation (1.37) and (1.38) can be expressed as follows [66]:

$$\mathbf{R}(t) = M(t)\mathbf{R}(0), \tag{1.40}$$

where **R**(0) describes the ground states at the beginning of the microwave pulse or at the beginning of the free evolution. The matrix $M(t)$ describes the transformation of the vector **R**. During the microwave interaction, the matrix $M(t)$ is given by [67],[66]:

$$M_m(t) = \begin{pmatrix} \cos(\xi t) & \frac{\Omega_m}{\xi}\sin(\xi t) & -\frac{b}{\xi}\sin(\xi t) \\ -\frac{\Omega_m}{\xi}\sin(\xi t) & \frac{b^2+\Omega_m^2\cos(\xi t)}{\xi^2} & \frac{\Omega_m b}{\xi^2}(1-\cos(\xi t)) \\ \frac{b}{\xi}\sin(\xi t) & \frac{\Omega_m b}{\xi^2}(1-\cos(\xi t)) & \frac{\Omega_m^2+b^2\cos(\xi t)}{\xi^2} \end{pmatrix}, \tag{1.41}$$

where $\xi = \sqrt{b^2+\Omega_m^2}$. In the case of zero microwave detuning $\Omega_m = 0$, the matrix (1.41) reduces to a rotation matrix along the y-axis by an angle of $\theta = b \cdot t_m$. During the free evolution, the matrix $M(t)$ is given by [67],[66]:

$$M_R(t) = \begin{pmatrix} e^{-\gamma_2 t}\cos(\Omega_m t) & e^{-\gamma_2 t}\sin(\Omega_m t) & 0 \\ -e^{-\gamma_2 t}\sin(\Omega_m t) & e^{-\gamma_2 t}\cos(\Omega_m t) & 0 \\ 0 & 0 & e^{-\gamma_1 t} \end{pmatrix}. \tag{1.42}$$

Finally, the POP sequence can be represented by a product of the matrix:

$$\mathbf{R}(t) = M_m(t_m) \cdot M_R(T_R) \cdot M_m(t_m)\mathbf{R}(0), \tag{1.43}$$

where t_m is the duration of the microwave pulse, T_R is the duration of the free-evolution time, and $\mathbf{R}(0)$ is the Bloch vector at the end of the pump pulse ($\mathbf{R}(0)$ solution of equation (1.35)). Equation (1.43) can be represented graphically. Indeed, the transformations given by the matrix $M_m(t)$ and $M_R(t)$ correspond to rotations in a xyz-space. The x-axis and the y-axis correspond to the real part and the imaginary part of the ground-state coherence, respectively. The z-axis represents the population difference in the ground states. Figure 1.8 presents the time evolution of the Bloch vector—equation (1.43)—with different configurations of microwave pulse area and microwave detuning.

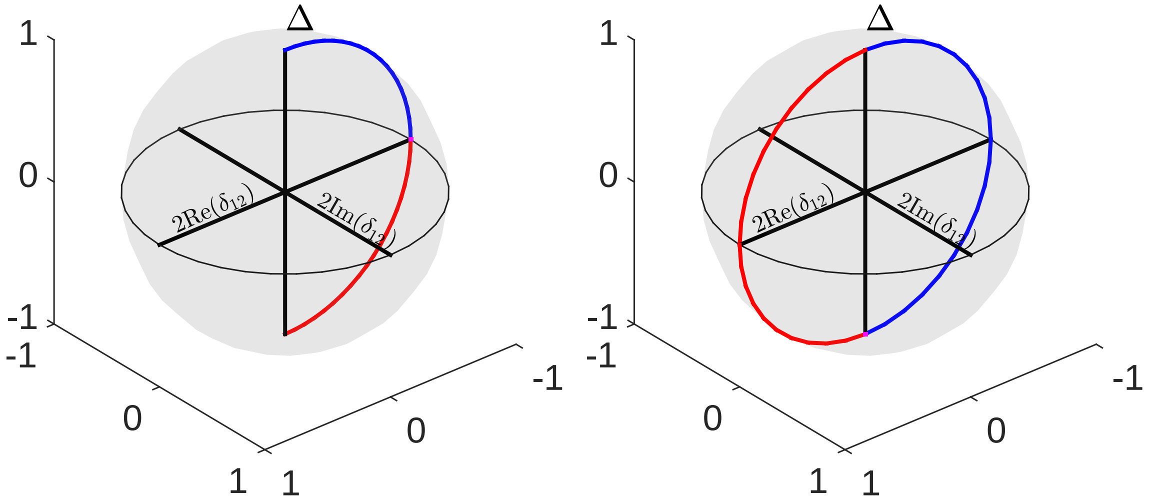

(a) $b \cdot t_m = \pi/2$, $t_m = 0.3$ ms, $\Omega_m = 2\pi \cdot 0$ Hz.   **(b)** $b \cdot t_m = \pi$, $t_m = 0.3$ ms, $\Omega_m = 2\pi \cdot 0$ Hz.

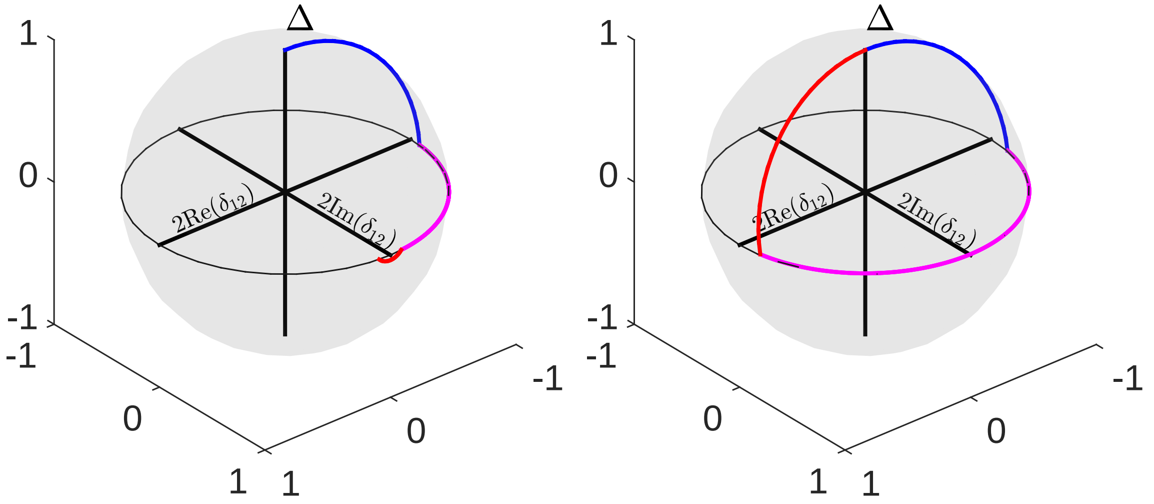

(c) $b \cdot t_m = \pi/2$, $t_m = 0.3$ ms, $\Omega_m = 2\pi \cdot 74$ Hz.   **(d)** $b \cdot t_m = \pi/2$, $t_m = 0.3$ ms, $\Omega_m = 2\pi \cdot 148$ Hz.

Figure 1.8 – *Time evolution of the Bloch vector* $\mathbf{R}$ *simulated using equation (1.43); blue curve: first microwave pulse; magenta curve: free-evolution time; red curve: second microwave pulse. The initial condition are* $\Delta(0) = 1$ *and* $\delta_{12}(0) = 0 + i0$. *We used* $\delta_0 = 0$ *and* $\gamma_1 = \gamma_2 = 238\ s^{-1}$.

1.3.4 Ramsey spectrum and properties

For a DR atomic clock with optical detection, the state of the atoms after the microwave interrogation is obtained through optical detection. The optical signal is proportional to the number of atoms in one of the ground states (depending on the detection light frequency). The absorption of the detection light in the vapour cell is the solution to the Beer-Lambert law:

$$I(\mathbf{r},t) = I(0,t)e^{-N_0 \cdot L_{cell} \cdot \sigma_{13} n_1(\mathbf{r},t)}, \tag{1.44}$$

where $I(0,t)$ is the light intensity at the entrance of the vapour cell, $N_0 = N_0(T_{cell})$ is the ^{87}Rb density, L_{cell} is the vapour cell length, σ_{13} is the absorption cross-section of the optical transition $|1\rangle \rightarrow |3\rangle$, and $n_1(\mathbf{r})$ is the number of atoms in the state $|1\rangle$. In the three-level approximations, the number of atoms in $|1\rangle$ is given by:

$$n_1(\mathbf{r},t) = \frac{1}{2} - \frac{\Delta(\mathbf{r},t)}{2} \tag{1.45}$$

where $\Delta(\mathbf{r},t)$ can be obtained from equation (1.43). Considering the hyperfine structure of the ground states and the laser frequency tuned to the transition $|1\rangle \rightarrow |3\rangle$, the effective number of atoms absorbing the light during the detection phase is:

$$n_1(\mathbf{r},t) = \frac{3}{8} - \frac{\Delta(\mathbf{r},t)}{2} \tag{1.46}$$

Figure (1.9) represents the calculated light intensity at the end of the vapour cell $I(L_{cell})$ according to equations (1.44) and (1.46) after one cycle of the microwave interrogation defined by equation (1.43). The Ramsey spectrum is normalised to the intensity at the end of the vapour cell if no microwave interrogation occurs (i.e. $b = 0$). It means that the Ramsey spectrum is normalised with respect to an atomic state described by $\Delta_0 e^{-\gamma_1 T_R}$ which is a mixed state and not a pure state (see Appendix D). It explains why the normalised Ramsey spectrum can reach value higher than 1. The normalised Ramsey spectrum displayed in Figure (1.9) is a typical clock signal of a POP-DR atomic

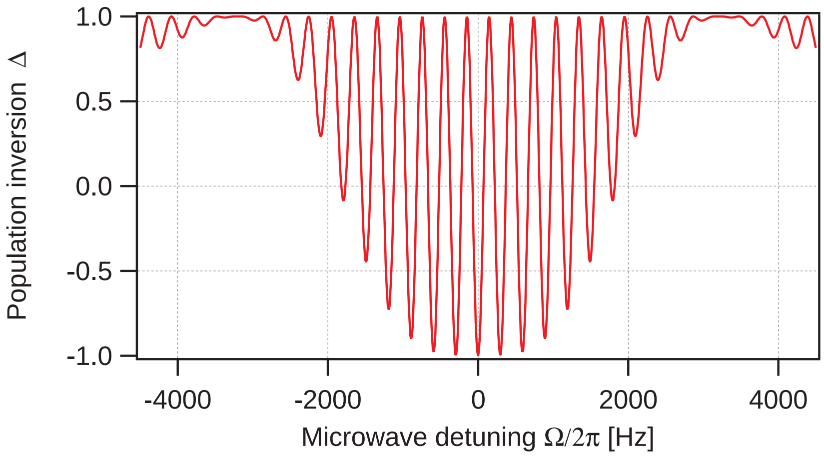

Figure 1.9 – *Light intensity at the end of the vapour cell calculated with equations (1.44), (1.46) and with 1 iteration of equation (1.43). The simulation conditions are:* $\Delta(0) = 1$, $\delta_{12} = 0 + i0$, $\theta = \pi/2$, $t_m = 0.3$ *ms,* $T_{ramsey} = 3$ *ms,* $\sigma_{13} = 1.3 \cdot 10^{-15} m^2$, $\gamma_1 = 360\ s^{-1}$ *and* $\gamma_2 = 340\ s^{-1}$.

clock.

The central fringe is used to frequency lock the quartz. The central fringe of Figure (1.9) has a cosine line-shape [75] characterised by three quantities: the contrast (C), the FWHM, and the central frequency (ω_{clock}). Experimentally, these properties of the central fringe are accessed by fitting the central fringe of Figure 1.9 with a cosine function [75]:

$$f(\omega) \quad = \quad a_1 \cdot \cos(\omega \cdot a_2) + a_4 \cdot \cos(2\omega \cdot a_2) + a_3. \tag{1.47}$$

where the contrast is obtained by $C = \frac{2(a_1+a_4)}{(-a_1-a_4+a_3)}$ and the FWHM $= 0.5/a_2$. The next two sections are focused on the relation between the contrast and the FWHM with the microwave pulse area $b \cdot t_m$ and how these properties can be understood using the Bloch sphere representation.

1.3.4.1 Contrast and Rabi oscillations

The variation of the contrast with the microwave Rabi frequency b is known as the Rabi oscillation. It corresponds to the oscillation of the population in the ground state as a function of the microwave Rabi frequency b. Experimentally, we detected the change of the central fringe contrast as a function of the microwave Rabi frequency b, where the contrast is defined as the relative change in the absorption [20]:

$$R = 1 - \frac{I(bt_m, \Omega_m = 0)}{I(bt_m = 0, \Omega_m = 0)}. \tag{1.48}$$

Please note that generally, the Rabi oscillations are represented as function of the pulse area of one pulse in a Rabi scheme, or as a function of one or both pulses in a Ramsey scheme. In this thesis, the Rabi oscillations determined are represented as functions of the pulse area of one microwave pulse in the Ramsey scheme, i.e. half of the pulse area value in the Rabi scheme.

The variation of the contrast as a function of the product $b \cdot t_m$ at zero microwave detuning is shown in Figure (1.10). The contrast is maximum for $b \cdot t_m = \pi/2 + n\pi$ and minimum for $b \cdot t_m = n\pi$ where n is a positive integer. The Bloch sphere representation can explain this behaviour. In the case of two

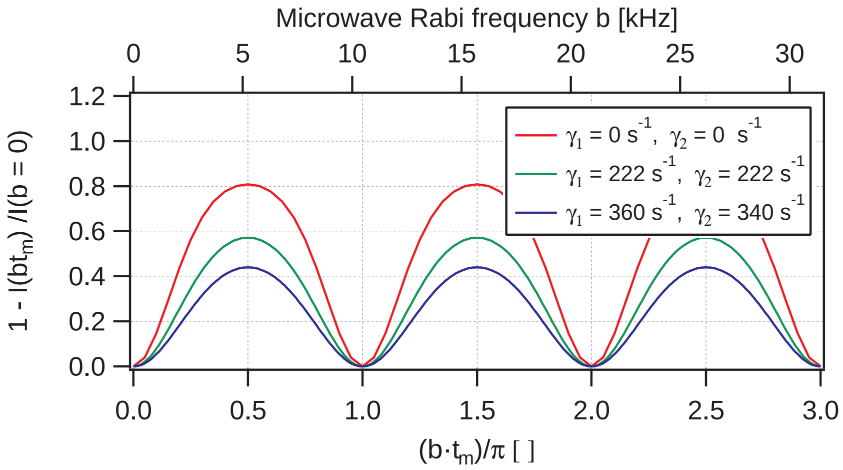

Figure 1.10 – *Rabi oscilliation calculated when the Rabi frequency b is varied for different relaxations rates* γ_1 *and* γ_2. *The simulation conditions are:* $t_m = 0.3ms$, $\Omega_m = 2\pi \cdot 0$ *Hz.*

microwave $\pi/2 + n\pi$ pulses and at zero microwave detuning, the Bloch vector rotates by an angle of $\pi/2 + n\pi$ around the y-axis and, after the second microwave pulse, is aligned along $-z$ direction for all n; all the atoms are in the state $|1\rangle$. In the case of two microwave $n\pi$ pulses and at zero microwave detuning, the Bloch vector rotates twice by an angle of $n\pi$ around the y-axis and is aligned along the $+z$ direction for all n; all atoms are in the state $|2\rangle$. The number of atoms in the final state is reduced by the relaxation process described by γ_1 and γ_2, occurring during the interrogation, as illustrated in Figure (1.10). The comparison between the theoretical prediction and the experimental value for the contrast is conducted in Chapter 3. The impact of the microwave-field inhomogeneity on the contrast is also discussed in Chapter 3.

1.3.4.2 Full width at half maximum as a function of the microwave pulse area

In this section, the FWHM of the central fringe as a function of the microwave pulse area is estimated.

Assuming a symmetrical central fringe, the FWHM can be written as $\omega_{\text{FWHM}} = 2 \cdot \omega_{\text{HWHM}}$. The condition on ω_{HWHM} is that $\Delta = 0$ at the end of the second microwave pulse corresponding to the condition $R_3(t) = 0$ where $R_3(t)$ is the third component of the vector solution of equation 1.43. From the matrix (1.41) and (1.42) and in condition of perfect optical pumping, the condition $R_3(t) = 0$ gives the following condition (the demonstration is presented in Appendix A):

$$\omega_{\text{HWHM}} T_R + 2\phi_0(b, \omega_{\text{HWHM}}) = \frac{\pi}{2}, \tag{1.49}$$

with

$$\phi_0(b, \Omega_m) = \arctan\Big(\frac{\Omega_m}{\sqrt{b^2 + \Omega_m^2}} \frac{1 - \cos(\xi t_m)}{\sin(\xi t_m)}\Big). \tag{1.50}$$

The condition (1.49) can be solved numerically, and the solution is shown in Figure 1.11. To confirm this result, the central Ramsey fringe is simulated for different microwave pulse areas using the equations (1.44), (1.46) and with one iteration of equation (1.43). For each of the simulated central fringes, the cosine fit function (1.47) is applied in order to extract the FWHM. The result is shown in Figure 1.11. The FWHM obtained with the cosine fit function (1.47), which agrees with the FWHM obtained from the condition (1.49). In particular, in the following three cases: $\theta = \pi/2$, $\theta = 3\pi/2$ and $\theta = 2\pi$, equation 1.50 becomes (with $\Omega_m \gg b$):

$$\phi_0(\theta = \pi/2, \omega_{\text{HWHM}}) \approx \arctan\Big(\frac{\omega_{\text{HWHM}}}{b} \cdot 1\Big) \approx \frac{\omega_{\text{HWHM}}}{b} \tag{1.51}$$

$$\phi_0(\theta = 3\pi/2, \omega_{\text{HWHM}}) \approx \arctan\Big(\frac{\omega_{\text{HWHM}}}{b} \cdot (-1)\Big) \approx -\frac{\omega_{\text{HWHM}}}{b} \tag{1.52}$$

$$\phi_0(\theta = 2\pi, \omega_{\text{HWHM}}) \approx \arctan\Big(\frac{\omega_{\text{HWHM}}}{b} \cdot 0\Big) \approx 0 \tag{1.53}$$

which results in :

$$f_{\text{FWHM}}(\theta = \pi/2) \approx \frac{1}{2\left(T_R + \frac{4t_m}{\pi}\right)} \tag{1.54}$$

$$f_{\text{FWHM}}(\theta = 3\pi/2) \approx \frac{1}{2\left(T_R - \frac{4t_m}{\pi}\right)} \tag{1.55}$$

$$f_{\text{FWHM}}(\theta = 2\pi) \approx \frac{1}{2T_R} \tag{1.56}$$

The variation of the FWHM with respect to $b \cdot t_m$ obtained from the simulation is not defined for $b \cdot t_m = n \cdot \pi$ with n a positive integer because of the absence of the central Ramsey fringe (see the simulated Rabi oscillations). Moreover, the simulation and the analytical FWHM presents a divergence at $b \cdot t_m = \pi$, the origin of which is not understood. However, in Chapter 3, we see that this divergence is removed when considering microwave magnetic-field inhomogeneity inside the vapour cell. Moreover, Chapter 3 presents the experimental FWHM, which does not present this divergence.

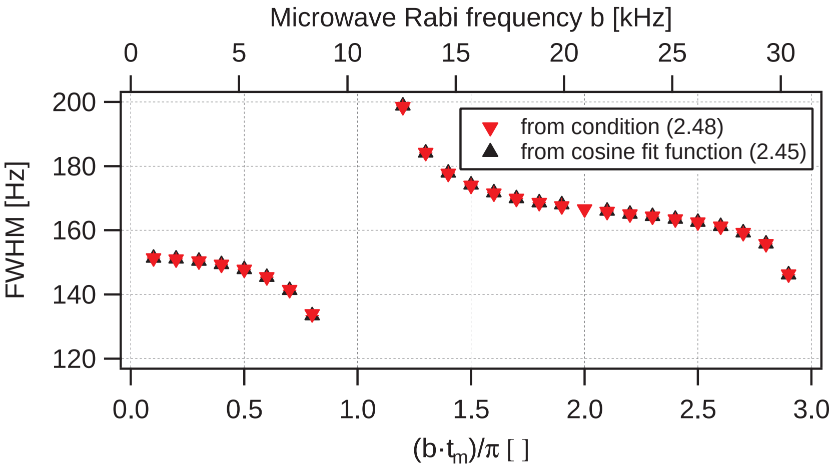

Figure 1.11 – *FWHM of the central Ramsey fringe when the Rabi frequency b is varied in the conditions:* $t_m = 0.3ms$, $\gamma_1 = 360\ s^{-1}$ *and* $\gamma_2 = 340\ s^{-1}$.

1.4 Frequency standards characterisation

As mentioned before, the frequency instability of the frequency standards characterises how well a frequency standard can reproduce the same frequency over a given time. The frequency instability is characterised in terms of the Allan deviation.

In this section, the Allan deviation and the overlapping Allan deviation are first presented. Then, the general requirements of the atomic signal are reviewed. The formula approximating the short-term frequency instability is introduced. This formula is used to characterise the short-term frequency instability of the optical-frequency reference. The second part of this section is focused on the main sources of frequency instability encountered in a vapour-cell atomic clock. This second part begins by reviewing the sources of instability impacting the short-term frequency instability (τ = 0.1 s to 100 s). It is followed by a list of all the common frequency shifts that impact the medium- to long-term frequency instability ($\tau = 10^4$ s) in an POP-DR Rb atomic clock. A sensitivity coefficient to the related physical parameters is estimated for each frequency shift. Finally, a table summarises the frequency sensitivity estimated with our POP-DR Rb clock prototype. The table allows us to build a frequency instability budget for the medium- to long-term. The preliminary budget is used to identify the perturbations contributing the most to the clock frequency fluctuations.

1.4.1 Allan variance

For statistical frequency fluctuations, it is common to write the instantaneous frequency in the form:

$$f(t) = f_0 \cdot (1+\epsilon+y(t)), \tag{1.57}$$

where f_0 is the unperturbed atomic frequency, ϵ is the systematic fractional frequency bias, and $y(t)$ is the time-dependent fractional frequency shift:

$$y(t) = \frac{f(t) - f_0 \cdot (1+\epsilon)}{f_0}. \tag{1.58}$$

The noise performance of the frequency standards is obtained by measuring the fractional frequency difference $y(t)$ averaged on an averaging time τ. Let divide the time t into equal time intervals $\tau = t_{i+1} - t_i$, the relative clock frequency $y(t)$ averaged over the time τ is defined:

$$\bar{y}_n = \frac{1}{\tau}\int_0^\tau y(t_n+s)ds. \tag{1.59}$$

The Allan deviation is a two-sample variance that identifies noise processes. From a set of N frequency samples $\bar{y}_n$ over time intervals τ, the Allan deviation is defined as [76]:

$$\sigma_y(\tau) = \sqrt{\frac{1}{2(N-1)}\sum_{i=1}^{N-1}(\bar{y}_{i+1}-\bar{y}_i)^2}. \tag{1.60}$$

The estimation (1.60) can be improved (can provide better confidence) by the use of the overlapping Allan deviation defined as [76]:

$$\sigma_y(\tau) = \sqrt{\frac{1}{2m^2(N-2m+1)} \sum_{j=1}^{N-2m+1} \left(\sum_{i=j}^{j+m-1} \bar{y}_{i+m} - \bar{y}_i \right)}, \tag{1.61}$$

where the relative clock frequency $y(t)$ is averaged over a duration of $m\tau$. The quantity $\sigma_y(\tau)$ is a measure of the frequency instability of the frequency standards. The Allan variance is generally represented on a log–log plot where three regions are identified according to the averaging time scales: the short-term stability (τ between 0.1 s and 100 s), the medium stability (τ between 100 s and 10'000 s), and the long-term stability (τ between 10'000 s and 100'000 s and above). Generally, the short-term stability is dominated by frequency white noise, which corresponds to an averaging of the frequencies. For a longer integration time, these processes impact the frequency stability less ($\sigma_y(\tau)$ decreases) because the white noise averages down as τ^{-1} (for white phase noise) or as $\tau^{-1/2}$ (for white frequency noise). Whereas, the medium and long-term stability are degraded by random or "slow" phenomena and frequency drift. Systematic frequency shifts tend to fluctuate over long-time scale (from the minute to the day or longer), which results in an increase in the frequency instability. The impact of these fluctuations is quantified via two quantities: a sensitivity coefficient, or shift coefficient, defined as the variation of the frequency standard with respect to the perturbing physical parameter (e.g. a power variation ΔP), $\frac{\Delta f}{\Delta P}$; and the amplitude of the fluctuations of the perturbing physical parameter itself at various time scales, $\sigma_P(\tau)$.

1.4.2 Signal requirements

In order to frequency stabilise the local oscillator frequency to the atomic frequency (see Figure 1), the atom is used as a frequency discriminator. The atoms transform the frequency fluctuation of the local oscillator into a signal V. The discriminator is given by $\frac{\partial V}{\partial f}$. We denote ΔV as the fluctuation of the measured signal V. At the first order, the corresponding fractional frequency error Δy of the local oscillator is given by:

$$\Delta y = \frac{\Delta f}{f_0} = \frac{\Delta V}{f_0 \cdot \frac{\partial V}{\partial f}}, \tag{1.62}$$

The discriminator slope $\frac{\partial V}{\partial f}$ depends on the signal shape and the modulation parameters of the interrogation scheme. In the case of a sine modulation of the interrogative frequency and close to the line centre, the optimum modulation amplitude is $\frac{\Gamma/2}{\sqrt{2}}$ [67], which results in a discriminator slope of $\sqrt{2}\frac{2A}{\Gamma}$. In the case of white frequency noise, a good approximation of the short-term frequency instabilities can be obtained [77]:

$$\sigma_y(\tau) = \frac{N}{\sqrt{2} \cdot D \cdot \nu_0} \tau^{-1/2}, \tag{1.63}$$

where N is the total noise power, D is the discriminator approximated by $\frac{2A}{\Gamma}$ and ν_0 is the interrogation frequency. In general, in order to reach a better frequency stability, the amplitude A of the signal must be as high as possible, and the linewidth Γ must be as low as possible.

1.4.3 Stability measurements

This thesis was realised in the Time and Frequency Laboratory (LTF) at University of Neuchâtel. The LTF is a unique university laboratory in Switzerland that possess all the instruments required for such research. Indeed, in order to characterise the relative frequency instability of an atomic clock at the level of 10^{-14}, it is necessary to use a second frequency reference with the same or better relative frequency instability. At LTF, a hydrogen maser (iMaser3000 [78]) referenced to GNSS is used as a timing reference for the entire laboratory. The GNSS reference is used to control and correct the long-term frequency fluctuation of the hydrogen maser. The timing reference provided by the hydrogen maser is distributed to all parts of the laboratory using a frequency distribution system and phase comparators for frequency instability measurements. Finally, optical-frequency references are characterised using an optical-frequency comb (FC1500 from MenloSystems), which allows absolute optical-frequency measurements at 1.5 μm and 780 nm as well as frequency instability measurements because the optical comb is reference to the hydrogen maser [79].

1.4.4 Clock short-term instability

1.4.4.1 Shot-noise limit

The short-term frequency instability refers the frequency instability over a time interval between 0.1 s and 100 s. In the case of our vapour-cell atomic clock, the short-term frequency instability fundamental limit is the detection noise induced by the shot-noise phenomenon, which is a consequence of the discrete nature of light. The shot-noise limit represents the lowest frequency instability realisable in our case. In a POP atomic clock, the contribution of the shot noise to $\sigma_y^{\text{det}}(\tau)$ can be estimated as follows [20]:

$$\sigma_y^{\text{shot-noise}}(\tau) = \frac{1}{\pi}\frac{1}{C\cdot Q_a}\left(\sum_{n=1}^{\infty}\text{sinc}(\pi\cdot nf_c\cdot t_d)^2\frac{2h\nu}{\eta P_0}\right)^{1/2}\sqrt{\frac{T_C}{t_d}}\frac{1}{\sqrt{\tau}}, \tag{1.64}$$

where C is the contrast of the central fringe of the Ramsey spectrum (see Figure 1.12), Q_a is the atomic quality factor defined as the ratio between the ground-state hyperfine frequency and the FWHM of the central fringe $Q_a = \frac{\nu_{12}}{FWHM}$, $f_c = \frac{1}{T_C}$ is the cycle operation frequency (T_C is the cycle duration), t_d is the duration of the optical-detection pulse, ν and P_0 are the detection light frequency and power, respectively, and η is the quantum efficiency of the photodiode. In our POP-DR Rb atomic clock prototype, the shot-noise limit is about $5\cdot10^{-14}\tau^{-1/2}$.

1.4.4.2 Detection noise

Generally, the relative intensity noise (RIN) of the light is the dominant source of detection noise (which occurs during the detection pulse in POP atomic clock). The RIN measured during the detection pulse is mainly composed by the laser amplitude noise (laser AM) and the FM-to-AM conversion of the laser frequency noise into amplitude noise. An estimation of the instability induced by the RIN during the detection pulse is given by [20]:

$$\sigma_y^{\text{det}}(\tau) = \frac{1}{\pi}\frac{1}{C\cdot Q_a}\left(\sum_{n=1}^{\infty}\text{sinc}(\pi\cdot nf_c\cdot t_d)^2 S_{RIN}^{det}(nf_c)\right)^{1/2}\sqrt{\frac{T_C}{t_d}}\frac{1}{\sqrt{\tau}}, \tag{1.65}$$

where S_{RIN} is the power spectral density of the RIN for the optical-detection signal expressed in the unit of $\frac{1}{Hz}$. In our POP-DR Rb atomic clock prototype, the detection-noise limit is about $2.2 \cdot 10^{-13} \tau^{-1/2}$[31].

1.4.4.3 Dick effect

The phase noise of the microwave source is transferred to the clock frequency through the Dick effect [80]. The contribution to the short-term instability can be estimated using the formula [80]:

$$\sigma_y^{\text{Dick}}(\tau) = \left(\sum_{m=1}^{\infty} \left(\frac{g_m^{c2}}{g_0^2} + \frac{g_m^{s2}}{g_0^2} \right) S_y^{LO}(m f_c) \right)^{1/2} \frac{1}{\sqrt{\tau}}, \tag{1.66}$$

where S_y^{LO} is the one-sided power spectral density of the microwave fractional frequency fluctuations expressed in the unit of $\frac{1}{Hz}$. The parameters g_m^c, g_m^s, and g_0 are defined by [80]:

$$\begin{pmatrix} g_m^s \\ g_m^c \\ g_0 \end{pmatrix} = \frac{1}{T_C} \int_0^{T_c} g(\xi) \begin{pmatrix} \sin(2\pi m \xi) \\ \cos(2\pi m \xi) \\ 1 \end{pmatrix} d\xi, \tag{1.67}$$

where m is a positive integer and $g(t)$ is the sensitivity function to the frequency fluctuation of the microwave-frequency fluctuations. In the case of the Ramsey interrogation, $g(t)$ is given by [80]:

$$g(t) = \begin{cases} a \sin(bt) & 0 \leq t \leq t_m \\ a \sin(b t_m) & t_m \leq t \leq T_{\text{ramsey}} + t_m \\ a \sin\big(b(T_{\text{ramsey}} + 2t_m - t)\big) & T_{\text{ramsey}} + t_m \leq t \leq T_{\text{ramsey}} + 2t_m \\ 0 & T_{\text{ramsey}} + 2t_m \leq t \leq T_c \end{cases} \tag{1.68}$$

where $a = -\sin\big(\Omega_0 T_{\text{ramsey}}\big) \sin(b t_m)$ and Ω_0 is the modulation amplitude. In our POP-DR Rb atomic clock prototype, the Dick effect limit is about $7.5 \cdot 10^{-14} \tau^{-1/2}$[31].

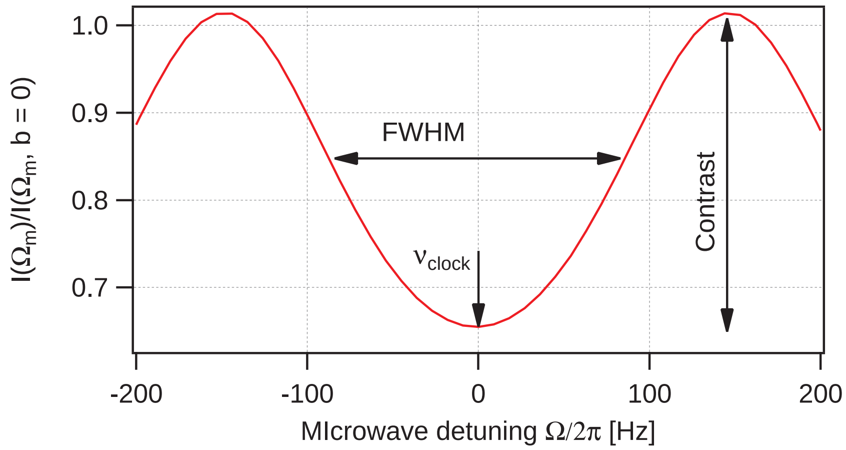

Figure 1.12 – *Representation of the contrast C and the FWHM of the central Ramsey fringe.*

1.4.4.4 Total short-term

Finally, the short-term frequency instability is given by the quadratic sum of all these noises in terms of Allan variance. In the condition of operation of the POP-DR Rb atomic clock presented by Gharavipour in his thesis [31], the short-term frequency instability is given by:

$$\sigma_y(\tau) = \sqrt{\left(\sigma_y^{\text{det}}(\tau)\right)^2 + \left(\sigma_y^{\text{Dick}}(\tau)\right)^2} \approx 2.2 \cdot 10^{-13} \tau^{-1/2} [31]. \tag{1.69}$$

In the following section, other sources of frequency stability are reviewed. The frequency instabilities induced by other physical parameters such as the cell temperature, laser frequency, and intensity, are generally lower than the shot-noise limit $5 \cdot 10^{-14}$ at 1 second, and they are not considered in equation (1.69). Below, we list the main sources of frequency shifts in Rb vapour-cell atomic clocks that are relevant to the long-term frequency instability of our POP-DR Rb clock prototype.

1.4.5 Clock medium- to long-term frequency instability

The clock frequency shifts are characterised using a sensitivity coefficient of the clock frequency to a physical parameter (e.g. a power variation ΔP), $\frac{\Delta f}{\Delta P}$, and the amplitude of the fluctuations of the perturbing physical parameter itself at various time scales, $\sigma_P(\tau)$.

1.4.5.1 Second-order Zeeman shift

As previously discussed in section 1.3.1.2, the static magnetic field inside the vapour cell aligned along the z-axis induces a frequency shift given by:

$$\Delta\nu_{\text{Zeeman}} = C_{\text{Zeeman}} \cdot B_z^2, \tag{1.70}$$

where $C_{\text{Zeeman}} = 575.14 \cdot 10^8 \frac{Hz}{T^2}$ and B_z is the static magnetic field. In our compact Rb atomic clock prototype [31][20], the static magnetic field is generated by a solenoid surrounding the vapour cell, which creates a static magnetic field of $1.07 \cdot 10^{-5}$ T (more details are provided in Chapter 3). The absolute frequency shift induced by the second-order Zeeman shift is $\Delta\nu_{\text{Zeeman}} \approx 6.58$ Hz at $B_z = 1.07 \cdot 10^{-5}$ T, and the second-order Zeeman sensitivity coefficient is:

$$\frac{\partial\nu_{\text{Zeeman}}}{\partial B_z} = 2 \cdot C_{\text{Zeeman}} \cdot B_z. \tag{1.71}$$

The second-order Zeeman shift and its sensitivity coefficients areW given in Table 1.2.

$\Delta\nu_{\text{Zeeman}}$	$\partial\nu_{\text{Zeeman}}/\partial B_z$	$\partial(\nu_{\text{Zeeman}}/\nu_0)/\partial B_z$
6.58 Hz	1.23 MHz/T	$1.8 \cdot 10^{-4}$/T

Table 1.2 – *2^{nd}-order Zeeman shift and its sensitivity coefficients.*

A magnetic shield strongly attenuates the environmental magnetic field; however, a residual magnetic field B_r remains. Moreover, the magnetic-field shields induce a field noise B_n. The total contribution to the cock instabilities of B_z,B_r, and B_n is given by:

$$\sigma_y(\tau) = \left|\frac{\partial \nu_{\text{Zeeman}}}{\partial B_z}\right| \sqrt{\sigma_{B_z}(\tau)^2 + \sigma_{B_n}(\tau)^2 + \sigma_{B_r}(\tau)^2} \tag{1.72}$$

1.4.5.2 Buffer-gas density shift

The hyperfine ground state frequency is frequency shifted by the collisions between the Rb atoms and the buffer gas. The collisions depend on the temperature of the vapour and the density of the buffer gas. The clock offset frequency due to the collision shifts is described by [67]:

$$\Delta\nu_{\text{Buffer-gas}} = P(\beta' + \delta'\Delta T + \gamma'\Delta T^2), \tag{1.73}$$

where ν_0 is the unperturbed clock frequency, P is the total buffer-gas pressure, β', δ', and γ' are coefficients for the gas mixture, and $\Delta T = T - T_0$ is the temperature difference between the vapour temperature and a reference temperature T_0 for which the coefficients are given. For a two-gas mixture with a partial pressure ratio $r = P_{\text{Ar}}/P_{N_2}$, these coefficients can be written as [81]:

$$\begin{aligned} \beta' &= \frac{\beta_{N_2} + r\beta_{Ar}}{1+r} \\ \delta' &= \frac{\delta_{N_2} + r\delta_{Ar}}{1+r} \\ \gamma' &= \frac{\gamma_{N_2} + r\gamma_{Ar}}{1+r}. \end{aligned} \tag{1.74}$$

Table 1.3 presents the value of these coefficients obtained from [81] and the corresponding coefficient calculated for the cell buffer-gas mixture used in our Rb clock prototype (see Chapter 3). The first-order temperature coefficient is:

$$\frac{\partial\Delta\nu_{\text{Buffer-gas}}}{\partial T} = P(\delta' + 2\gamma'(T - T_0)), \tag{1.75}$$

Equation (1.75) cancels for a vapour temperature of $T_i = T_0 - \frac{\delta'}{2\gamma'}$. For our buffer-gas mixture, the inversion temperature is approximately $T_i \approx 62.15$ °C. However, experimentally, a residual first-order coefficient remains at the inversion temperature. Previous analyses of our POP-DR Rb clock prototype have measured a coefficient of about 15.1 mHz/K (equivalent to $2.2 \cdot 10^{-12}$/K) [31]. The second-order temperature coefficient is:

$$\frac{\partial^2\Delta\nu_{\text{Buffer-gas}}}{\partial T^2} = 2P\gamma'. \tag{1.76}$$

The frequency shift due to collisional shift and its sensitivity coefficients are given in Table 1.4. The clock frequency sensitivity to the internal buffer-gas pressure can be deduced from equation (1.73) for a fixed cell temperature $T_{\text{cell}} = 62.2 \pm 0.2$ °C [6] (see Table 1.4 for the numerical value):

$$\frac{\partial\Delta\nu_{\text{Buffer-gas}}}{\partial P} = \beta' + \delta'\Delta T + \gamma'\Delta T^2. \tag{1.77}$$

---

[6] The temperature uncertainty of ±0.2 °C come from the uncertainty of the NTCs reported the datasheet.

The clock vapour cell is formed by a core glass cylinder plus a glass stem. The stem is used as a cold point. It is used to prevent condensation of the Rb vapour on the vapour-cell windows. Moreover, the vapour Rb density inside the cell core is controlled via the stem temperature. However, it induces a coupling between the clock frequency and the stem temperature. The stem temperature sensitivity is generally different from the cell-temperature sensitivity. The typical order of magnitude of the stem temperature sensitivity is [82](see Table 1.4 for the numerical value):

$$\frac{\partial \nu_{\text{Clock}}}{\partial T_{\text{stem}}} = P_s \beta' \frac{v_s}{T_{\text{stem}}}. \tag{1.78}$$

where T_{stem} is the stem temperature and $v_s = V_{\text{stem}}/V_{\text{total}}$ is the normalised stem volume. The presence of the stem induces a change of the inversion temperature T_i as described by Calosso et al. [82].

	$\beta \left[\frac{\text{Hz}}{\text{hPa}}\right]$	$\delta \left[\frac{\text{Hz}}{\text{hPa K}}\right]$	$\gamma \left[\frac{\text{Hz}}{\text{hPa K}^2}\right]$
Nitrogen	410.95	0.39	-9.75·10^{-4}
Argon	-44.78	-0.24	-2.6·10^{-4}
Mixture	$\beta' \left[\frac{\text{Hz}}{\text{hPa}}\right]$	$\delta' \left[\frac{\text{Hz}}{\text{hPa K}}\right]$	$\gamma' \left[\frac{\text{Hz}}{\text{hPa K}^2}\right]$
$P_{\text{Ar}}/P_{N_2} = 1.6$	130.82	2.3·10^{-3}	-5.4·10^{-4}

Table 1.3 – *Buffer gas shift coefficients for* ^{87}*Rb in argon and nitrogen gases [81].*

$\Delta\nu_{\text{Buffer-gas}}$	$\partial\nu_{\text{Buffer-gas}}/\partial T$	$\partial(\nu_{\text{Buffer-gas}}/\nu_0)/\partial T$
4’254.55 Hz	15.1 mHz/K [31]	2.2·10^{-12}/K [31]
	$\partial\nu_{\text{Buffer-gas}}/\partial T^2$	$\partial(\nu_{\text{Buffer-gas}}/\nu_0)/\partial T^2$
	-35 mHz/K^2	-5.12·10^{-12}/K^2
	$\partial\nu_{\text{Buffer-gas}}/\partial P$	$\partial(\nu_{\text{Buffer-gas}}/\nu_0)/\partial P$
	130.51 Hz/hPa	1.92·10^{-8}/hPa
	$\partial\nu_{\text{Clock}}/\partial T_{\text{stem}}$	$\partial(\nu_{\text{Clock}}/\nu_0)/\partial T_{\text{stem}}$
	7.6 mHz/K[31]	1.1·10^{-12}/K [31]

Table 1.4 – *The clock offset frequency due to collisional shift and its second order sensitivity coefficients for the buffer-gas vapour cell of our POP-DR Rb atomic clock prototype [31], for a cell with a 5 mm*^{3} *stem volume (see section 2.3.2).*

1.4.5.3 Spin-exchange shift

The Rb–Rb collisions are an important source of frequency shift in Rb atomic frequency standards. When the alkali atoms get too close to one another, the two outermost electrons of the alkali atoms can be described using one wave function. Due to Pauli's principle, the wave function describing the two electrons is antisymmetric under permutation. It can be shown that the collision produces a phase shift in the ground-state coherence δ_{12} [67],[83]. If the collision happens during the free-evolution time, it induces a frequency shift of the clock frequency (see equation (1.38)). The spin-exchange shift can be estimated using [83],[84]:

$$\Delta\nu_{\mathrm{SE}} = -\frac{1}{8\pi} n\bar{v}\lambda_{SE}\langle\Delta\rangle_{T_R}, \tag{1.79}$$

where $n \approx 2.9\cdot10^{17} m^{-3}$ is the Rb density, $\bar{v}$ is the average relative velocity of two colliding atoms at temperature T, $\lambda_{SE} \approx 6.9\cdot10^{-15} cm^2$ [83] is the spin-exchange cross-section characterising the frequency shift, and $\langle\Delta\rangle_{T_R}$ is the average population inversion during the free-evolution time. The population inversion during the free-evolution time is mainly impacted by the relaxation γ_1 and by the cavity feedback characterised by the number of microwave photons emitted by one atom in 1 s defined as:

$$k = \frac{\mu_0\mu_B^2\eta' Q_L n}{\hbar(2I+1)} \approx 1.9\ s^{-1}, \tag{1.80}$$

where η' is the cavity filling factor, Q_L is the loaded cavity quality factor (a complete discussion of the microwave-cavity properties can be found in Chapter 3), and I is the nuclear spin. Considering the feedback of the cavity, the inversion population during the free-evolution time is [66][83], at $b\cdot t_m = \pi/2$:

$$\Delta(t) = -e^{-\gamma_1 t}\tanh\Big(\frac{k}{\gamma_1}(1-e^{-\gamma_1 t})\Big), \tag{1.81}$$

which gives $\langle\Delta\rangle_{T_R} \approx -1.1\cdot10^{-3}$. The Rb density $n(T)$ is defined as [67]:

$$n(T) = \frac{9.656\cdot10^{18}}{T}\cdot10^{7.43-\frac{4215}{T}}. \tag{1.82}$$

For an absolute change in the temperature by ΔT = 1 K at 62 °C, the relative change in the Rb density is $\Delta n/n \approx 10$ %. The spin-exchange coefficient for a change of ΔT = 1 K is then given by:

$$\frac{\Delta\nu_{\mathrm{SE}}}{\Delta T} = -\frac{1}{8\pi}\frac{\Delta n}{\Delta T}\bar{v}\lambda_{SE}\langle\Delta\rangle_{T_R}. \tag{1.83}$$

The absolute frequency shift induced by the spin exchange and its sensitivity coefficients are shown in Table 1.5.

1.4.5.4 Cavity pulling

The vapour cell is enclosed in a microwave cavity that enhances the microwave radiation amplitude and defines the field geometry. The resonant frequency of the microwave cavity is generally different from the hyperfine ground-state frequency. We denote the cavity detuning $\Delta\nu_{\mathrm{cav}}$. The hyperfine

$\Delta\nu_{\mathrm{SE}}$	$\Delta\nu_{\mathrm{SE}}/\Delta T$	$(\Delta\nu_{\mathrm{SE}}/\nu_0)/\Delta T$
4.7 mHz	0.16 mHz/K	$2.3\cdot10^{-14}$/K

Table 1.5 – *Spin-exchange shift and its sensitivity coefficients.*

ground-state frequency is "pulled" by the resonance frequency of the microwave cavity. It induces a coupling between the clock frequency and physical parameters of the cavity—temperature, humidity, and pressure—where these parameters impact the cavity detuning. The cavity-pulling shift in the POP clock and in the three-level approximation is given by [66]:

$$\Delta\nu_{\text{cavity-pulling}} = -\frac{4}{\pi}\frac{Q_L}{Q_a}\Delta\nu_{\mathrm{cav}}\ln\left[\cosh(A) - \mathrm{sgn}(\Delta_i)\cos(b\cdot t_m)\sinh(A)\right], \tag{1.84}$$

where Q_L is the loaded quality factor, Q_a is the atomic quality factor, Δ_i is the population inversion at the end of the pumping phase (which depends on the optical pumping scheme), and $A = \frac{k}{\gamma_2}|\Delta_i|(1-e^{-\gamma_2 T_R})$. Figure 1.13 shows the cavity-pulling shifts $\Delta\nu_{\text{cavity-pulling}}$ as functions of the microwave pulse area $b\cdot t_m$ for two different Δ_i in the standard conditions of our Rb atomic clock prototype and for $\Omega_m = 2\pi\cdot 0$ Hz.

The cavity-pulling shift sensitivity coefficient to the microwave power can be deduced using ($b\cdot t_m = \theta$):

$$\frac{\partial\Delta\nu_{\text{cavitiy-pulling}}}{\partial\theta} = -\frac{4}{\pi}\frac{Q_L}{Q_a}\Delta\nu_{\mathrm{cav}}\frac{\mathrm{sgn}(\Delta_i)\sin(\theta)\sinh(A(T))}{\cosh(A(T)) - \mathrm{sgn}(\Delta_i)\cos(\theta)\sinh(A(T))} \tag{1.85}$$

Using the fact that $\Delta\theta/\theta = \frac{1}{2}\Delta P_\mu/P_\mu$ with P_μ is the microwave power, one can rewrite:

$$\frac{\Delta\nu_{\text{cavitiy-pulling}}}{\Delta P_\mu} = \frac{\Delta\nu_{\text{cavitiy-pulling}}}{(\Delta\theta/\theta)}\cdot\frac{1}{2P_\mu} \tag{1.86}$$

The cavity-pulling shift sensitivity coefficients are presented in Table 1.7. The cavity-pulling shifts sensitivity to temperature, humidity, and pressure comes from the sensitivity of the cavity detuning $\Delta\nu_{\mathrm{cav}}$ to these parameters. The temperature sensitivity comes from thermal dilatation of the microwave cavity used in our Rb atomic clock prototype. The temperature sensitivity of the cavity detuning was measured as $\partial(\Delta\nu_{\mathrm{cav}})/\partial T \approx -40$ kHz/K at 62 °C [31]. The humidity and pressure sensitivity come from the air dielectric constant change inside the cavity. The microwave-cavity resonance frequency sensitivity to the air pressure and humidity are calculated in Appendix B and are given by $\partial(\Delta\nu_{\mathrm{cav}})/\partial P \approx -16$ Hz/Pa and $\partial(\Delta\nu_{\mathrm{cav}})/\partial h \approx -37.5$ kHz/(g/m^3). Table 1.7 summarises the sensitivity coefficients of $\Delta\nu_{\text{cavity-pulling}}$ to the temperature, pressure, and humidity for the pump laser frequency stabilised on $|5^2S_{1/2}, F=1\rangle \rightarrow |5^2P_{3/2}\rangle$ (F=1) and $|5^2S_{1/2}, F=2\rangle \rightarrow |5^2P_{3/2}\rangle$ (F=2) and $\theta = \pi/2$. For standard atmospheric conditions, the sensitivity coefficients listed in Table 1.7 impact the clock frequency instabilities at the level of $10^{-17} - 10^{-16}$ for time scales around one day, well below our target frequency instabilities of 10^{-14} at 10^4s of integration time.

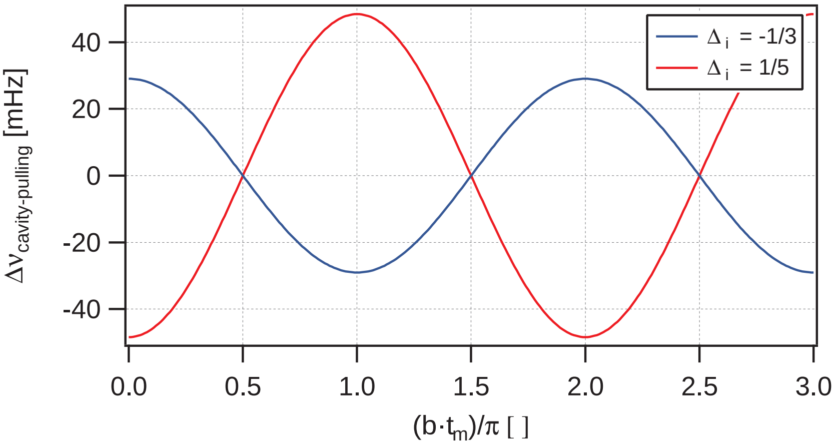

Figure 1.13 – *Cavity pulling shifts* $\Delta\nu_{cavity\text{-}pulling}$ *as a function of the microwave pulse area* $b\cdot t_m$ *for* $\Delta_i = -1/3$ *and* $\Delta_i = 1/5$ *in the conditions* $k = 1.9s^{-1}$, $\gamma_1 = 360\ s^{-1}$ $\gamma_2 = 340\ s^{-1}$, $Q_L = 185$, $Q_a = 4.63\cdot 10^7$, $\Delta\nu_{cav} = 1.6$ *MHz and* $T_R = 3$ *ms.*

Parameters x		$\partial(\Delta\nu_{\text{cavity-pulling}})/\partial x$	$\partial(\Delta\nu_{\text{cavity-pulling}}/\nu_0)/\partial x$
θ	F=1	0.11 mHz/%	$1.6\cdot 10^{-14}$/%
	F=2	-0.07 mHz/%	$-9.6\cdot 10^{-15}$/%
P_μ	F=1	0.28 mHz/μW	$4\cdot 10^{-14}/\mu$W
	F=2	-0.17 mHz/μW	$-2.4\cdot 10^{-14}/\mu$W

Table 1.6 – *Cavity-pulling shift sensitivity coefficients to microwave power and the induced clock sensitivities for* $\theta = \pi/2$.

Environmental parameters x		$\partial(\Delta\nu_{\text{cav}})/\partial x$	$\partial(\Delta\nu_{\text{cavity-pulling}})/\partial x$	$\partial(\Delta\nu_{\text{cavity-pulling}}/\nu_0)/\partial x$
Temperature	F=1	- 40 kHz/K	0.14 μHz/K	$2\cdot 10^{-17}$/K
	F=2		0.05 μHz/K	$8\cdot 10^{-18}$/K
Pressure	F=1	- 1.6 kHz/hPa	5.5 nHz/hPa	$8\cdot 10^{-19}$/hPa
	F=2		1.9 nHz/hPa	$3\cdot 10^{-19}$/hPa
Humidity	F=1	- 37.5 kHz/(g/m^3)	0.13 μHz/(g/m^3)	$2\cdot 10^{-17}$/(g/m^3)
	F=2		0.05 μHz/(g/m^3)	$7\cdot 10^{-18}$/(g/m^3)

Table 1.7 – *Cavity-pulling shift sensitivity coefficients to environmental parameters and the induced clock sensitivities for* $\theta = \pi/2$.

1.4.5.5 Light-induced shifts

Light-induced shifts (LIS) describe the clock frequency sensitivity to the laser frequency and the laser intensity. In a CW-DR Rb atomic clock, the coupling between the clock frequency and the laser frequency and intensity is performed through the AC-Stark shift [85]. The AC-Stark shift changes the hyperfine energy structure of the atoms by coupling the light field and the induced dipole moment [67]. In a CW-DR Rb clock, the light field and the microwave field are applied simultaneously, and the AC-Stark shift induces a clock frequency shift. However, in POP operation, the light field and the microwave field are applied separately in time, which strongly reduces the impact of the AC-Stark shift on the clock frequency. Recent studies [19],[20] [86] have presented a residual coupling between the clock frequency and the light frequency and intensity. Section 3.2.1 is devoted to the experimental analysis of the LIS in our POP-DR Rb prototype. Here we give some of the key elements used to analyse the POP LS.

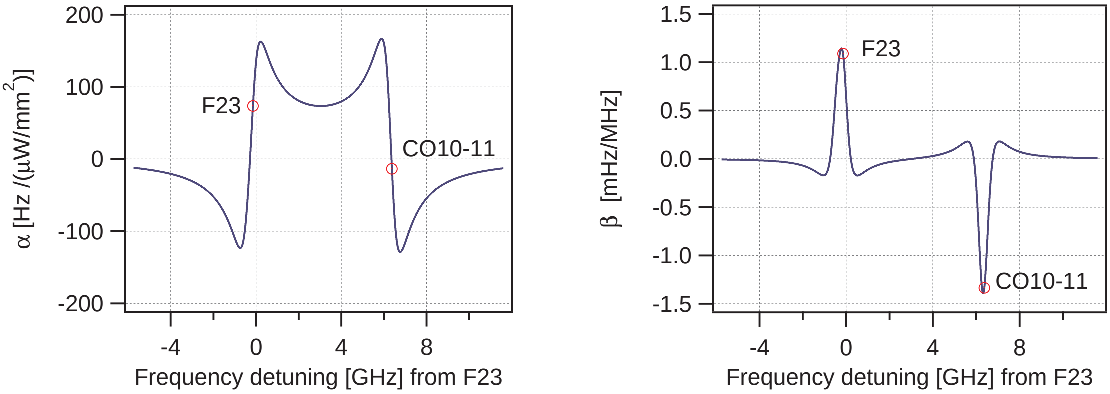

(a) *Intensity LS coefficient α as a function of the laser frequency detuning.*

(b) *Frequency LS coefficient β as a function of the laser frequency detuning and for a light intensity of 0.0021 μW/mm^2.*

Figure 1.14 – *Intensity and frequency light-induced shift coefficients calculated according to [87],[67], [74]. The red dots correspond to a laser frequency tuned to F23 and CO10-11 (see Table 1.1 for the defintion of these spectroscopic notations defintion.).*

One source of LIS in POP Rb clocks is due to leakage light during the Ramsey time [31]. In our Rb atomic clock prototype, the light pulses (pump and detection), as well as the sequence without light (microwave interrogations and Ramsey time), are made using an acousto-optic modulator (AOM) as an optical switch. The light attenuation of the AOM is 34 dB in our Rb atomic clock prototype, which results in a typical leakage light intensity of about 0.0021 μW/mm^2 at the entrance of the vapour cell. According to the theory developed in [87],[67],[74], the AC-Stark shift at the light intensity 0.0021 μW/mm^2 is about 0.16 Hz for the laser frequency tuned to $|5^2S_{1/2}, F=2\rangle \rightarrow |5^2P_{3/2}, F=3\rangle$, see Figure 1.14. The order of magnitude for the LS coefficients are given in Table 1.8(see Figure 1.14).

Another identified source of LS is the residual coherence at the end of the optical pump pulse [66][88]. Figure 1.7 shows that for a low pumping rate (for example, 10'000 Hz) or for a short pump duration (for example, 0.2 ms), an initial real and imaginary part of the ground-state coherence is present at the beginning of the microwave interrogation. The initial coherence depends on the laser frequency and intensity as illustrated in equation (1.36). The impact of an initial coherence on the Ramsey spectrum can be understood using the Bloch sphere. An initial imaginary coherence

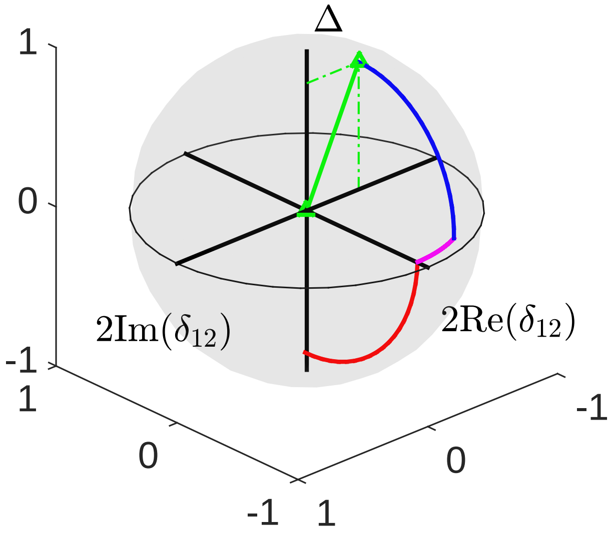

(a) *Time evolution of itinial conditions* $\Delta(0) = 0.8$ *and* $\delta_{12}(0) = 0 - i0.2$ *(green vector) with* $\Omega_m = 2\pi \cdot 22$ *Hz.*

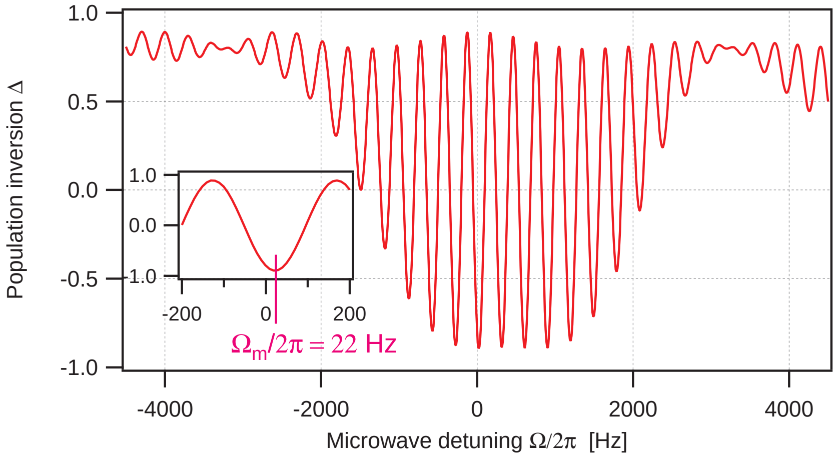

(b) *Ramsey fringes. Inset: zoom on the central fringe.*

Figure 1.15 – *Numerical study of the impact of an initial coherence* $\delta_{12}(0) = 0 - i0.2$ *on the Ramsey spectrum under the conditions of* $\pi/2$*-pulse,* $\delta_0 = 0$ *and* $\gamma_1 = \gamma_2 = 0\ s^{-1}$.

Laser parameter x		$\partial \Delta\nu_{\text{clock}} / \partial x$	$\partial(\Delta\nu_{\text{clock}}/\nu_0)/\partial x$
Laser intensity I_L	F23	74 Hz/ (μW/mm^2)	$1.1{\cdot}10^{-8}$/(μW/mm^2)
	CO10-11	-13.5 Hz/ (μW/mm^2)	$-2{\cdot}10^{-9}$/(μW/mm^2)
Laser frequency f_L	F23	1.1 mHz/ MHz	$1.6{\cdot}10^{-13}$/MHz
	CO10-11	-1.3 mHz/ MHz	$-2{\cdot}10^{-13}$/MHz

Table 1.8 – *AC-Stark shifts coefficients calculated for a light intensity of 0.0021* μ*W/mm*^{2} *according to the theory presented in [74].*

induces an initial phase during the free evolution, as illustrated in Figure 1.15a. For an initial coherence of $\delta_{12}(0) = 0 - i0.2$, a microwave-frequency detuning $\Omega_m = 2\pi \cdot 22$ Hz is necessary to reach the highest population inversion (see inset of Figure 1.15b).

We generally define a global intensity LIS coefficient (or α-coefficient) as:

$$\alpha \equiv \left.\frac{\Delta\nu}{(\Delta I_L)/I_L}\right|_{\text{fixed } \nu_L} \left[\frac{\text{Hz}}{\%}\right], \tag{1.87}$$

for a fixed laser frequency ν_L. The global frequency LS coefficient (or β-coefficient) is defined as:

$$\beta \equiv \left.\frac{\Delta\nu}{\Delta\nu_L}\right|_{\text{fixed } I_L} \left[\frac{\text{Hz}}{\text{MHz}}\right], \tag{1.88}$$

for a fixed light intensity I_L. These definitions of the sensitivity coefficients consider all the phenomena that couple the clock frequency and the light frequency and intensity. In an Rb-POP atomic clock, an experimental intensity LIS coefficient in the range of $\alpha \approx (0.2 - 0.6)$ mHz/% and a frequency LIS coefficient in the range of $\beta \approx (0.1 - 3)$mHz/MHz were reported [86],[19].

1.4.5.6 Barometric shifts

The impact of atmospheric pressure variations on the clock's frequency—environmental pressure shift—results from three mechanisms. The first mechanism is the temperature changes around the clock induced by conductive and convective heat flows that can modify the temperatures of all the clock parts [89],[90]. The second mechanism is called the barometric effect: the external pressure variations deform the resonance cell's dimension and change the internal buffer-gas density [89],[91]. The third mechanism is the change of the air dielectric constant that modifies the microwave-cavity resonance frequency and impacts the clock frequency through the cavity-pulling effect [92],[84]. The total sensitivity of the clock frequency with the change in the environmental pressure was reported to be in the range of 10^{-13}/hPa [89][93].

The impact of the environmental pressure on the clock frequency was not present in the frequency instability budget of our previous compact CW-DR atomic clock prototype [26] and the previous evaluations of our POP-DR Rb atomic clock prototype [31][20]. The reason is because other effects - as light-induced shifts or stem temperature coefficient - were contributing to the long-term frequency instability at the level of 10^{-13}. Part of the work presented in this thesis allowed to identify the Barometric effect as one of the most dominant sources of frequency instability in our POP-DR Rb atomic clock prototype. Section 3.3 contains an experimental and theoretical analysis of the barometric effect on our atomic clock prototype.

1.4.5.7 Position shift

The *position-shift* effect refers to a relation between the rubidium resonant frequency and the position of the atoms inside the vapour cell [94][95][96][97]. This effect is mostly present in atomic clock based on vapours cells with buffer-gas, where the atoms are spatially localized during one iteration cycle. When the atoms are quickly moving through the interaction zone (for example for coated vapour cell without a buffer gas), the atom's velocity is such that during one interrogation cycle the atoms average the fields inhomogeneities (electrical and magnetic fields). It results that during one interrogation cycle, the atoms experience a spatial average of these fields.

Light intensity inhomogeneity induces an inhomogeneity in the optical pumping of the atoms. It impacts the initial conditions before the microwave interrogation, which leads to a spatial dependence of $\Delta(t = 0, \mathbf{r})$ and $\delta_{12}(t = 0, \mathbf{r})$. As illustrated in 1.14, an atom with an initial coherence generates a Ramsey spectrum that is slightly frequency shifted. Each atom in the vapour cell produces a Ramsey spectrum frequency shifted depending on the position of the atom in the cell. The signal detected on the photodiode, after the vapour cell, is the average of all the Ramsey spectra. As a consequence, in a buffer-gas cell where atoms are efficiently localized on the time-scales of the Ramsey sequence, this average is inhomogeneous and can result in a frequency shift when the microwave power is varied. However, in the case of a wall-coated cell, every single atom individually averages over all possible clock frequencies during its free flight through the cell; therefore in this case the averaging is homogeneous and in general does not result in a frequency shift [96]. The other sources of the spatial distribution of the atomic hyperfine frequency are the inhomogeneity of the static magnetic field (2^{nd} Zeeman shifts), the microwave inhomogeneity (via the cavity-pulling shift), and the temperature gradient inside the cell [94].

The inhomogeneity of the microwave amplitude result in a spatial dependence of the microwave Rabi frequency $b(\mathbf{r})$. The microwave Rabi frequency acts as a weight for the central fringe of the Ramsey spectrum of a single atom that undergoes Rabi oscillation (see Figure 1.10) [94]. A spatial distribution of b induces a spatial distribution of the weight. The clock frequency is then a weighted average of the hyperfine frequency of the atoms. If the microwave Rabi frequency changes, the value of the weight changes, changing the clock frequency. The position shift is a coupling between the clock frequency and the spatial distributions of the atomic hyperfine frequency and the microwave Rabi frequency. We describe the global position shift by the sensitivity of the clock frequency to the microwave power injected into the cavity:

$$\frac{\partial \Delta \nu_{\text{clock}}}{\partial P_{\mu}} \left[\frac{\text{Hz}}{\mu\text{W}}\right], \tag{1.89}$$

where P_{μ} is the microwave power. The typical order of magnitude of the microwave-shift coefficient is $12.3 \cdot 10^{-3} \left[\frac{\text{Hz}}{\mu\text{W}}\right]$ [86]. Additional experimental and numerical analysis on the position shift will be provided in Chapter 4.

1.4.6 Clock preliminary medium- to long-term instability budget

The analysis presented in this section can be used to establish a preliminary medium- to long-term instability budget. The estimated instability induced by a phenomenon is obtained from:

$$\sigma_y(\tau) = \left|\frac{\partial(\nu_{clock}/\nu_0)}{\partial x}\right| \sigma_x(\tau), \tag{1.90}$$

where x is a physical parameter (temperature, pressure, ...) and $\frac{\partial \nu_{clock}}{\partial x}$ is the clock frequency sensitivity to x. If the clock frequency instabilities are composed by a number N of uncorrelated frequency instabilities sources, the clock frequency instability is given by:

$$\sigma_y(\tau)^2 = \sum_{i=1}^{N} \left(\left|\frac{\partial(\nu_{clock}/\nu_0)}{\partial x_i}\right| \sigma_{x_i}(\tau)\right)^2. \tag{1.91}$$

In this study, we are interested in the medium- to long-term (at $\tau = 10^4$ s to $\tau = 10^5$ s) instability of our Rb-POP atomic clock prototype. Table 1.9 summarises the source frequency instabilities and the associated clock frequency-sensitivity coefficient evaluated in this chapter. In order to establish a preliminary medium- to long-term instability budget, the sensitivity coefficients presented throughout this chapter are combined with the variance of the physical quantities $\sigma_{x_i}(\tau)$ reported in the previous study on our Rb atomic clock prototype [10],[26],[31] and on similar POP atomic clocks [84]. As shown in Table 1.9, we obtain an estimated frequency instability about $1.2 \cdot 10^{-13}$ at $\tau = 10^4$ s. The main source of long-term frequency instability is the microwave-power shift at the level of $2 \cdot 10^{-14}$, the stem temperature sensitivity at $6 \cdot 10^{-15}$, and the barometric effect at $1 \cdot 10^{-13}$.

Physical effect	Physical parameter	Frequency shift	Absolute coefficient	Relative coefficient	Physical fluctuation $\sigma_{x_i}(\tau)$	Relative instab. at 10^4 s
Zeeman effect	C-field	6.6 Hz	1.23 MHz/T	$1.8 \cdot 10^{-4}$ /T	$4.1{\cdot}10^{-11}$ T$^{a)}$	$7.4 \cdot 10^{-15}$
Density shift (1^{st})	T_{cell}	4’255 Hz	15.1 mHz/K^2	$2.2 \cdot 10^{-12}$/K	2.5 mK $^{a)}$	$1.1 \cdot 10^{-14}$
Density shift (2^{nd})	T_{cell}	N.A	-35 mHz/K^2	$5.2 \cdot 10^{-12}$/K^2	2.5 mK^2 $^{a)}$	$1.3 \cdot 10^{-16}$
Stem TC	T_{stem}	N.A.	7.6 mHz/K	$1.1 \cdot 10^{-12}$/K	5 mK $^{a)}$	$5.5 \cdot 10^{-15}$
Spin-Exchange	T_{cell}	5 mHz	0.16 mHz/K	$2.3 \cdot 10^{-14}$/K	5 mK $^{a)}$	$1.2 \cdot 10^{-16}$
Cavity-pulling	$P_{\mu W}$	< 50 mHz	0.28 mHz/μW	$4 \cdot 10^{-14}$/μW	$1 \cdot 10^{-2}$$\mu$W $^{b)}$	$4.0 \cdot 10^{-16}$
	T_{cav}		0.14 μHz/K	$2 \cdot 10^{-17}$/K	5 mK $^{a)}$	$1 \cdot 10^{-19}$
	Pressure		5.5 nHz/hPa	$8 \cdot 10^{-19}$ /hPa	1 hPa $^{c)}$	$8 \cdot 10^{-17}$
	Humidity		0.13 μHz/(g/m^3)	$2 \cdot 10^{-17}$ /(g/m^3)	0.2 (g/m^3) $^{e)}$	$3.8 \cdot 10^{-18}$
Microwave shift	$P_{\mu W}$	N.A.	1.3 mHz/μW	$1.8 \cdot 10^{-12}$/μW	$1 \cdot 10^{-2}$$\mu$W$^{b)}$	$1.8 \cdot 10^{-14}$
Light shift	I_{Laser}	N.A.	0.41 mHz/%	$2.1 \cdot 10^{-14}$/%	0.1 %$^{d)}$	$2.1 \cdot 10^{-15}$
Light shift	f_{Laser}	N.A.	3.2 mHz/MHz	$4.6 \cdot 10^{-13}$/MHz	3 kHz$^{d)}$	$1.4 \cdot 10^{-15}$
Barometric effect	Pressure	N.A.	$6.9 \cdot 10^{-4}$ Hz/hPa	$1 \cdot 10^{-13}$/hPa[98]	1 hPa $^{c)}$	$1 \cdot 10^{-13}$

Total approx. freq. shift	4263 Hz	Total estimated contribution at 10^4s	$1.1 \cdot 10^{-13}$

Table 1.9 – *Preliminary instabilities budget at $\tau = 10^4$ s according to the sensitivity coefficients presented in this chaper. The variance of the physical parameter fluctuations $\sigma_{x_i}(\tau)$ are typical values measured in previous LTF atomic clock prototypes or for compact atomic clock similar to the one evaluated in this thesis : a) [10], b) [26], c) [84], d) [31], e) typical environmental data*

1.5 Conclusion

This chapter reviewed the theoretical basis necessary to understand the working principle of the Rb vapour-cell frequency reference presented in the following chapters.

First, the sub-Doppler spectroscopy technique is presented. The technique is based on two counter-propagating beams inside a vapour cell. The technique helps obtain a MHz-linewidth signal that can be used to frequency stabilise the probe frequency. The sub-Doppler spectroscopy is a key element of the optical-frequency references presented in this thesis: for two different home-made laser heads emitting at 780 nm (see Chapter 2) and a frequency-doubled 1560 nm laser (see Chapter 5).

Second, we reviewed the theoretical model used to explain the basic properties of an Rb-POP atomic clock. In the three-level approximation, the time evolution of the density matrix is represented using a matrix product (see equation (1.43)) using the Bloch sphere representation. This representation is a powerful tool to understand the POP clock signal (Ramsey spectrum) and its properties (Contrast, FWHM). The calculation performed in this chapter serves as a basis for the numerical analysis of the experimental studies of the chapter 3 where the impact of field inhomogeneities on the signal properties are analysed. The most dominant sources of coupling between the clock frequency and the physical parameters are introduced. Each source of coupling is characterised by a sensitivity coefficient, coupling the clock frequency with one physical parameter. Some of these coefficients can be calculated and others can only be measured. Table 1.9 presents the coefficients calculated in this chapter and the typical measured coefficients found in the literature. The table is completed with the typical fluctuations of the physical parameters for an Rb atomic clock similar to our prototype clock. The table provides a simple tool to evaluate the main source of frequency instabilities. According to the established preliminary budget in Table 1.9, the potential main sources of limitation are the barometric effect, the temperature sensitivity of the cell, and the microwave shift. These clock frequency sensitivities will be experimentally evaluated in Chapter 3.

The next chapter details optical and microwave-frequency references based on the cm-scale Rb vapour cell used in this thesis.

2 Compact Rb vapour-cell frequency standard prototypes

In this chapter, we provide the details of the two frequency standards used in this thesis. The first part of this chapter is dedicated to the presentation of two Rb vapour-cell optical-frequency references at 780 nm (D_2 line of ^{87}Rb): a frequency reference unit (FRU) and laser heads (LHs). We will distinguish two type of LH: a standard LH and an AOM integrated LH used in the atomic clock prototype. The optical-frequency references contain a cm-scale ^{87}Rb-enriched vapour-cell and a sub-Doppler absorption spectroscopy scheme. They are described in detail in section 2.2. The second part of this chapter presents the compact vapour-cell atomic clock. The atomic clock is composed of three main parts: the laser system, the physics package containing the vapour cell and the microwave cavity, and the local oscillator. Each of these parts is described in detail in section 2.3.

2.1 Vapour cells

The vapour cell is the heart of the atomic clock. The vapour cells used in this work were fabricated at LTF. More details can be found in [74]. The vapour cell is a borosilicate cylindrical glass cell with two end windows that are flat to avoid any lensing effect with the light propagating through the cell. Two different vapour cells are used in our frequency reference: 10 mm diameter and 19 mm long used in the optical-frequency references, and 25 mm diameter and 25 mm long used in the atomic clock. They are shown in Figure 2.1.

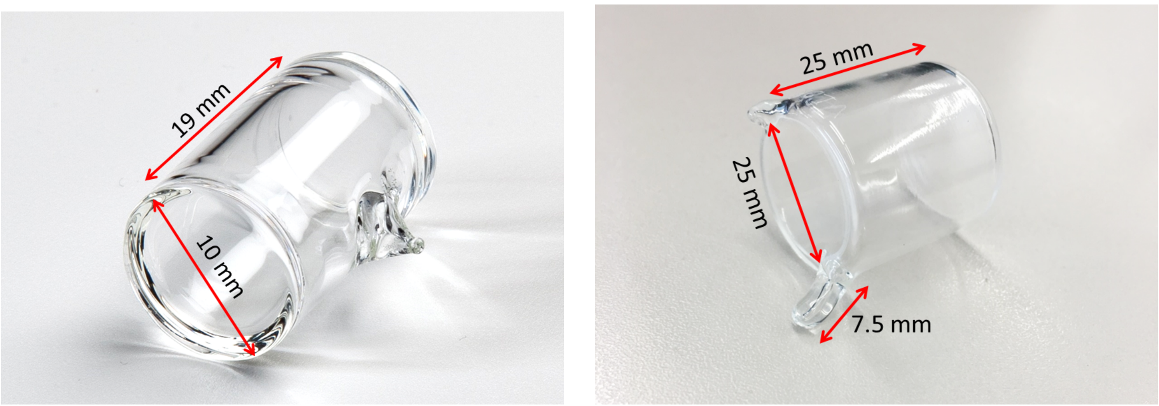

(a) *Vapour cell used in the laser heads and FRU.*

(b) *Clock vapour cell. ID : 3301*

Figure 2.1 – *Photography of the two type of vapour cell used in this work.*

2.2 Compact vapour-cell optical frequency standards

Gaetano Mileti's group at LTF has developed several compact and high-performance optical-frequency references based on cm-scale vapour cell [99][100][101]. Home-made Rb vapour-cell LHs were developed to be used for optical pumping in compact Rb atomic clocks [100][101]. Details about these LHs can be found in previous LTF theses [102],[26],[74],[31]. In this section, we review the different LHs as well as the optical-FRU with a focus on the properties of interest for the work presented in this thesis: relative frequency instability and relative intensity instability.

2.2.1 Frequency reference unit

The frequency reference unit (FRU), shown in Figure 2.2, has a similar design to the LHs built at the LTF [101] but with the purpose of being incorporated into fibred laser systems. All the elements are mounted on a thermally controlled baseplate. The FRU contains only the vapour cell and the optics necessary for sub-Doppler absorption spectroscopy. The light is introduced into the FRU by a non-PM mono-mode optical fibre, which prevents the optics from being realigned. At the output of the fibre, the light is guided to the sub-Doppler spectroscopy part. The vapour cell is fabricated at the LTF [74]. The vapour cell is 10 mm large and 19 mm long and is filled with enriched ^{87}Rb vapour. The vapour cell is mounted to a temperature control and is thermalised at 40°C. The cell is surrounded by two magnetic shields. The FRU has three photodetectors: One is situated at the entrance of the vapour cell and is used to measure the optical power. The second is situated after the vapour cell and can be used for Doppler absorption spectroscopy. The third is used for sub-Doppler spectroscopy. The FRU contains the photodetectors pre-amplifications electronics.

The FRU occupies a volume of 0.77 dm^3 (dimensions 160 x 80 x 60 mm^3). Chapter 5 presents the frequency noise, the RIN, and the frequency stability of a frequency-doubled 1560 nm laser frequency stabilised using the FRU.

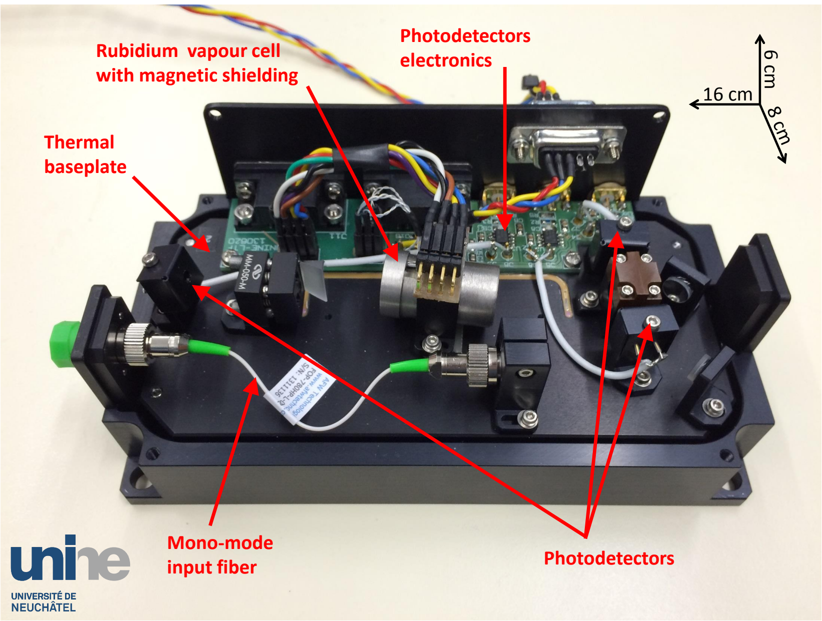

Figure 2.2 – *Photography of the home-made frequency reference unit without the outer covering.*

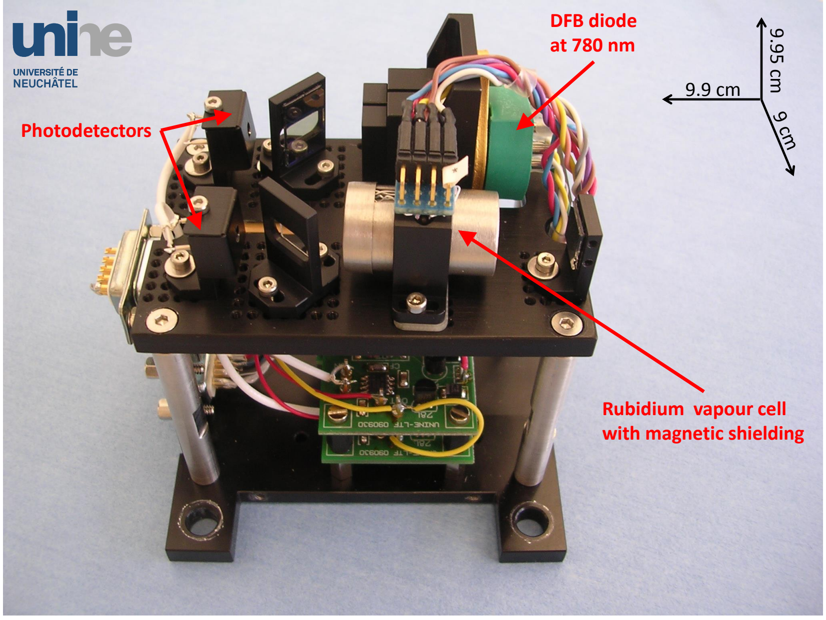

Figure 2.3 – *Photography of the home-made standard laser head.*

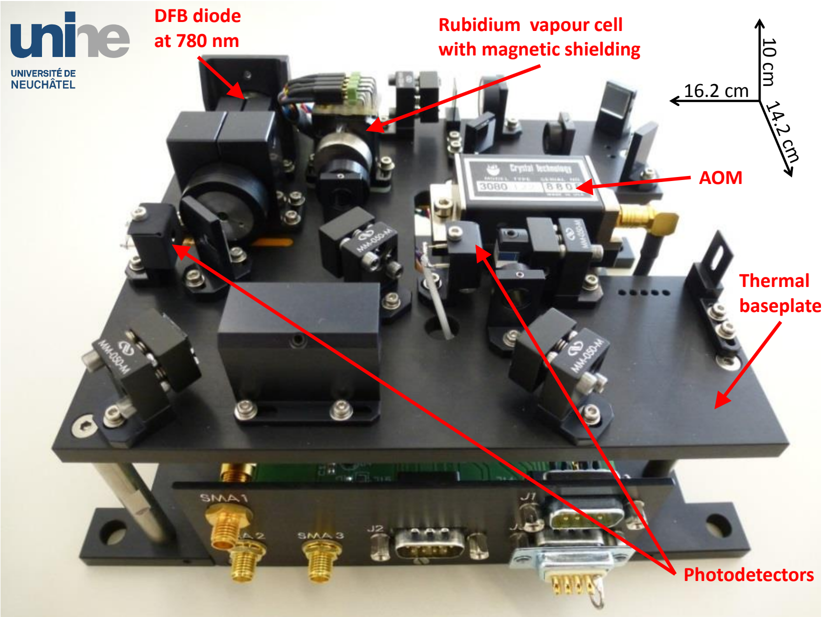

Figure 2.4 – *Photography of the home-made AOM laser head.*

2.2.2 Laser head

2.2.2.1 Description

The standard LH is shown in Figure 2.3. The standard LH has a design similar to the FRU except for the presence of a light source. The laser is a 780 nm DFB diode from Eagleyard photonics GmbH. The output of the laser is separated into two parts: the first part of the light is sent through a photodetector for direct optical-power measurement, while the second part is further separated into two parts. The first part of this second division is sent to the sub-Doppler absorption scheme for frequency stabilisation of the diode, and the second part is used as the LH output. The laser diode, the optics, the vapour-cell, and the electronics are enclosed in a volume of 0.89 dm^3 (dimensions 90 x 99 x 99.5 mm^3). As for the FRU, the vapour cell and the baseplate are thermalised at 40°C and 27°C, respectively. The LH is used as an optical-frequency reference in Chapter 5.

The acousto-optic modulator–integrated LH (AOM-LH) is shown in Figure 2.4. The AOM-LH is an upgraded version of the standard LH. The AOM-LH has a free-space AOM with the associated free-space optics. The AOM is operated in a double pass: the light goes through the AOM twice. The AOM free-space optics are aligned such that the second-order is obtained after the second pass of the light through the AOM. The AOM is fed with a 75 MHz radio-frequency (RF), which induces a frequency shift of the AOM-LH light output by -150 MHz. Further details can be found in [101] and [26]. The AOM-LH is the laser system used in the atomic clock prototype. The AOM serves as an optical switch in order to create optical pulses and to frequency shift the light frequency. The AOM is fed with a 75 MHz RF signal obtained from a synthetiser (Agilent E8257D) reference to the H-maser. The RF power sent to the AOM is ≈ 1 W during the optical pumping pulse and about 50 to 80 mW during the detection pulse. The optical power during the pump pulse is ≈ 12 mW; the optical power during the detection pulse is about 100μW. The ON/OFF ratio was measured at 40 dB [103][31] with a rise/fall time of about 4.5 μs [31] [1] .

---

[1] not limited by the RF switch with a typically 10 ns of rise/fall times.

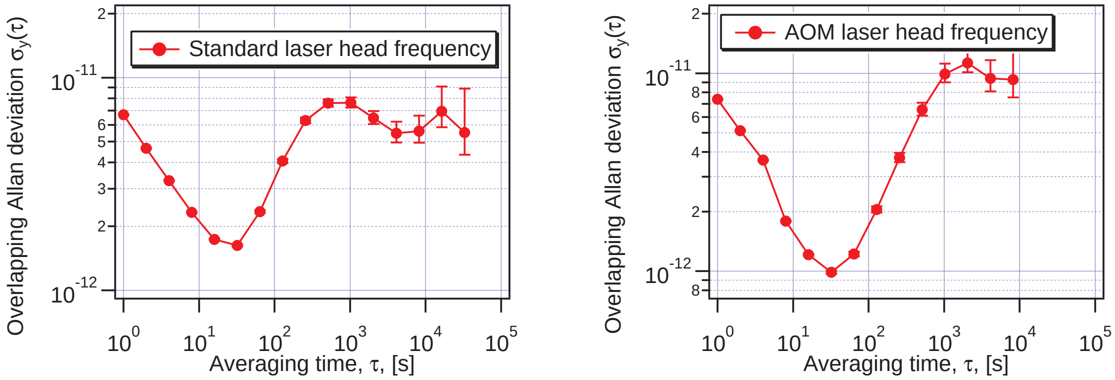

(a) *Standard laser head frequency instability.* **(b)** *AOM laser head frequency instability.*

Figure 2.5 – *Relative frequency instability of optical references obtained by the frequency stabilization of two different laser heads. Obtained from a beat note at 780-nm of the laser head heterodyned with a fully-stabilized commercial Er-fiber frequency comb referenced to an H-maser.*

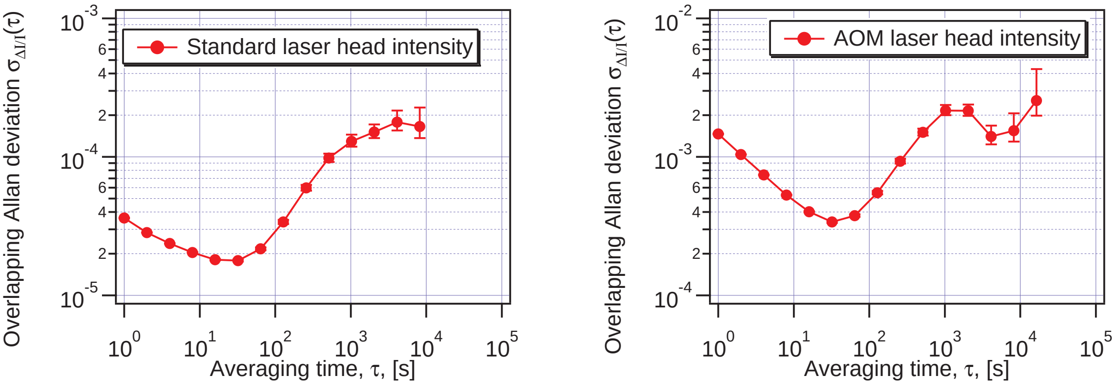

(a) *Standard laser head intensity instability.* **(b)** *AOM laser head intensity instability.*

Figure 2.6 – *Relative intensity instability of optical references.*

2.2.2.2 Characterisation

These LHs have been extensively characterised and their basics properties can be found in [101],[26] and [31]. This section presents the characteristics that are important to the work presented in this thesis. As mentioned in section 1.4.6, the quantities of interest for the establishment of a medium- to long-term frequency instability budget are the frequency stability, the relative intensity stability, the RIN, and the frequency noise (FM). The frequency stability of the standard LH and the AOM-LH are measured from heterodyne beat measurements with a fully-stabilised commercial Er-fibre optical-frequency comb (Menlo Systems) referenced to an H-maser. The overlapping Allan deviation of the beat-note for the standard and AOM LH are shown in Figure 2.5. Both LHs present a relative frequency instability below or equal to 10^{-11} at all time scale which corresponds to absolute frequency fluctuation below or equal to 4 kHz at 780 nm. Both frequency instabilities present a bump around 10^3 seconds corresponding to the laboratory air conditioning fluctuation cycle. The LHs intensity stability is presented in Figure 2.6. The relative intensity of the standard LH reaches 0.02 % at 10^4 second and the relative intensity of the AOM-LH is at a level of 0.2 % at 10^4. The degradation of the laser intensity is mainly attributed to the AOM, which is a source of intensity instabilities in our compact LH setup.

The impact of the RIN and the FM of the AOM-LH on the short-term frequency stability of the atomic clock is described by equation 1.63 when the clock is operated in CW-DR or 1.65 when the clock is operated in POP. The quantity of interest is the optical-detection noise. The optical-detection noise is composed of the AOM-LH amplitude modulation (AM) noise and the frequency modulation (FM) noise converted into AM noise inside the vapour cell [104]. For our POP-DR Rb clock prototype, the AM noise added by the integrated AOM and the FM-to-AM noise conversion contribute at the same level [20] and contribute to the clock short-term frequency instability at the level of $1 \cdot 10^{-13}$. Detailed analysis and discussion on the optical-detection noise for compact Rb clocks similar to the one used in this study can be found in [20] and [105][106][31]. The detection noise of our POP-DR Rb clock prototype is presented in Chapter 3.

2.2.3 Frequency stabilisation scheme

The sub-Doppler signal is used to frequency stabilise the laser frequency to one sub-Doppler dip. The laser is frequency-modulated by applying a 50 kHz sinusoidal signal with a modulation depth of ≈1 MHz to its injection current. The detected modulated sub-Doppler signal is injected into a pre-amplifier circuit, which amplifies and filters the signal at 50 kHz. An error signal is generated by demodulating the signal at 50 kHz by multiplying it with a 50-kHz reference signal using a phase-sensitive synchronous detection. The demodulation results in the generation of the first derivative of the sub-Doppler signal, as shown in Figure 2.7. The zero voltage of the error signal defines the frequency stabilisation point. A feedback signal processed by a proportional-integrator servo-controller is applied to the laser injection current for frequency stabilisation of any sub-Doppler dips.

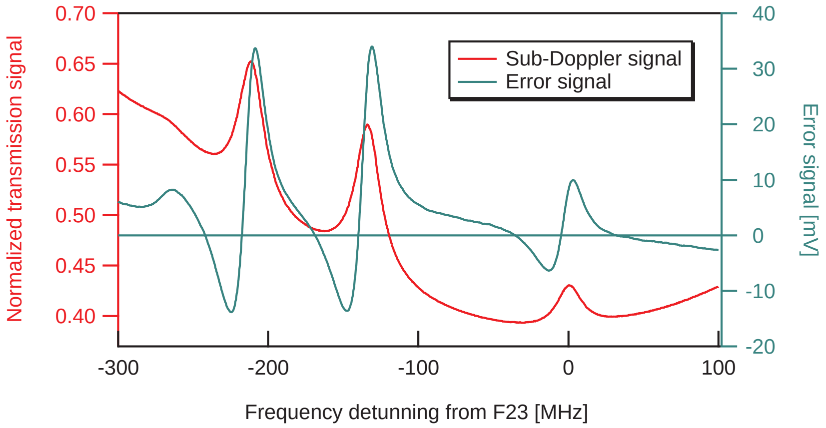

Figure 2.7 – *Typical sub-Doppler absorption spectrum of the F23 transitions and the two closest cross-over CO21-23 and CO22-23 (see Table 1.1) and the associated error signal obtained with the FRU.*

2.3 Compact vapour-cell atomic clock

2.3.1 Schematic

The schematic of the POP-DR Rb atomic clock prototype is presented in Figure 2.8. The atomic clock is composed of three parts: the laser system, the physics package (PP), and the local oscillator (LO). The laser system is the AOM-LH previously described.

The PP contains the Rb vapour cell and the microwave cavity. A solenoid is disposed around the microwave cavity which generates a static magnetic field inside the vapour cell. Thermal protections, regulation steps and magnetic shields surround the PP. The magnetic shields consist of two layers of a high permeability alloy (mu-metal). The input light is expanded using a telescope. The light beam inside the vapour cell has a 19 mm diameter. The light beam is refocused into a photodetector using a collimating lens. The signal of the photodetector passes through a pre-amplifier system.

The LO is an oven-controlled crystal oscillator (OCXO) enclosed in an instrument developed by the Dr. Calosso, INRIM [107]. In the framework of this thesis, the instrument developed by Dr. Calosso is named clock control electronic (CCE). The CCE possesses three functions: use of a microwave synthesis chain to generate 6.835 GHz from the OCXO, control of the POP timing sequence and frequency stabilisation of the OCXO to the atomic resonance frequency. The main part of the clock is described below.

2.3.2 Vapour cell

2.3.2.1 Description

The clock vapour cell (see Figure 2.1b) contains enriched ^{87}Rb and buffer gas (argon and nitrogen). The cell dimensions are: 25 mm diameter and 25 mm long. Figure 2.9 presents a typical absorption spectrum obtained with the PP vapour cell. The broadening of the optical transitions is mainly due to the collision process between the rubidium atoms and the buffer gas. The buffer-gas mixture has the ratio $\mathrm{Ar}/\mathrm{N}_2 = 1.6$ with a total pressure of 32.5 hPa. The vapour cell has a stem reservoir ($V_{\mathrm{stem}} = 5$ mm^2) used to control the vapour density of the atoms in the cell core. The volume of the stem is lower than previous vapour cells by a factor of three [26]. Calosso et al. demonstrated how the stem induces a coupling between the clock frequency and the stem temperature fluctuation through a change in the buffer-gas density, called the enhanced temperature sensitivity (ETS) [82]. The ETS sensitivity coefficient is given by [82]:

$$\frac{\partial \nu_{\mathrm{clock}}}{\partial T_{\mathrm{Stem}}} \approx P_s \beta' \frac{v_s}{T_{\mathrm{Stem}}}, \tag{2.1}$$

where, T_{Stem} is the stem temperature, $v_s = V_{\mathrm{Stem}}/V$ and β' is the pressure coefficient of equation 1.74. The stem temperature sensitivity was measured at the level of $1.2 \cdot 10^{-11}$/K [26] for a 25 mm long stem ($V_{\mathrm{stem}} \approx 5$ mm^2) and at the level of $1.2 \cdot 10^{-12}$/K [31] when using a shorter stem ($V_{\mathrm{stem}} \approx 5$ mm^2).

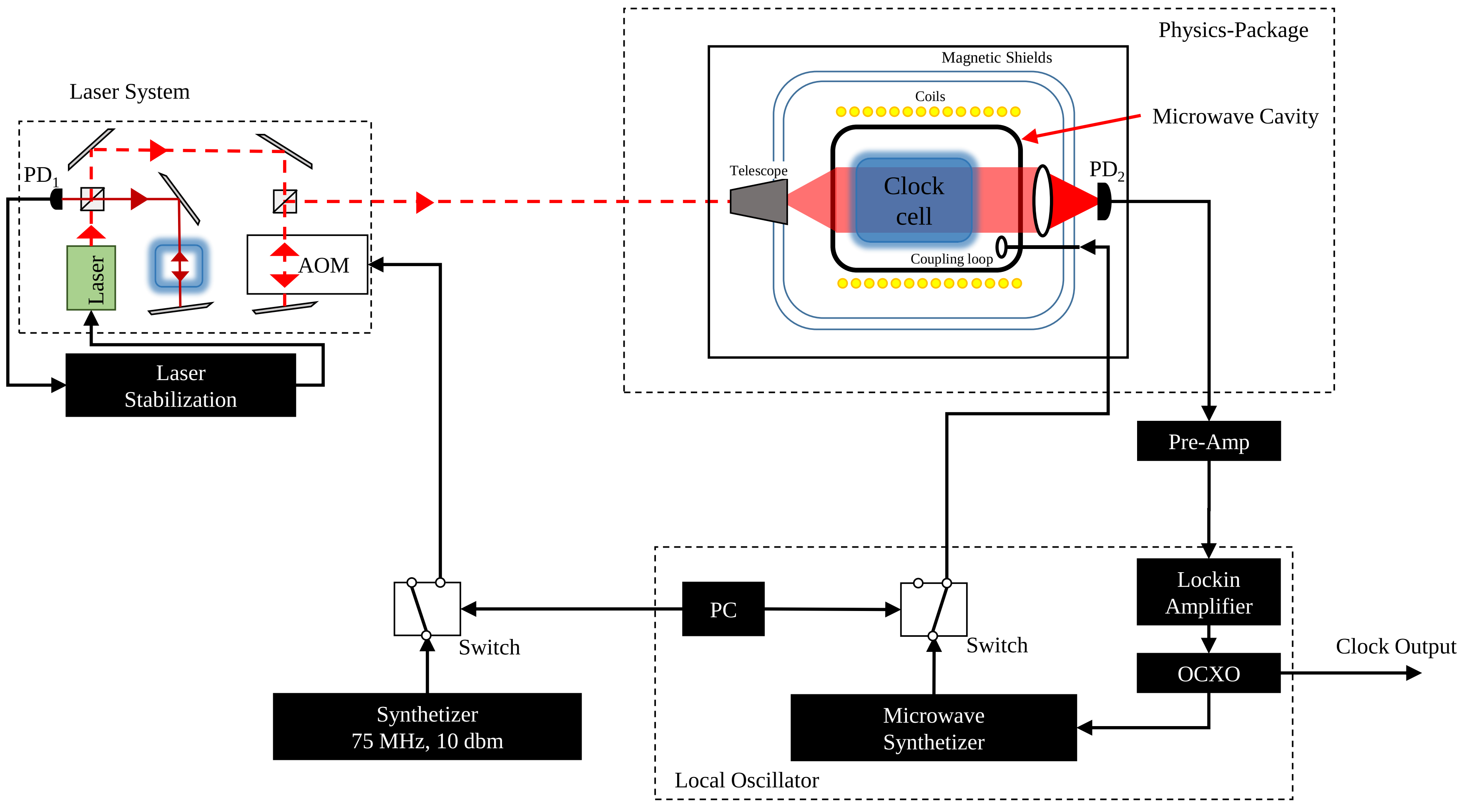

Figure 2.8 – *Schematic of the atomic clock prototype. The clock is composed by three main parts: Laser system (LH), Physics Package (PP), Local Oscillator (LO).*

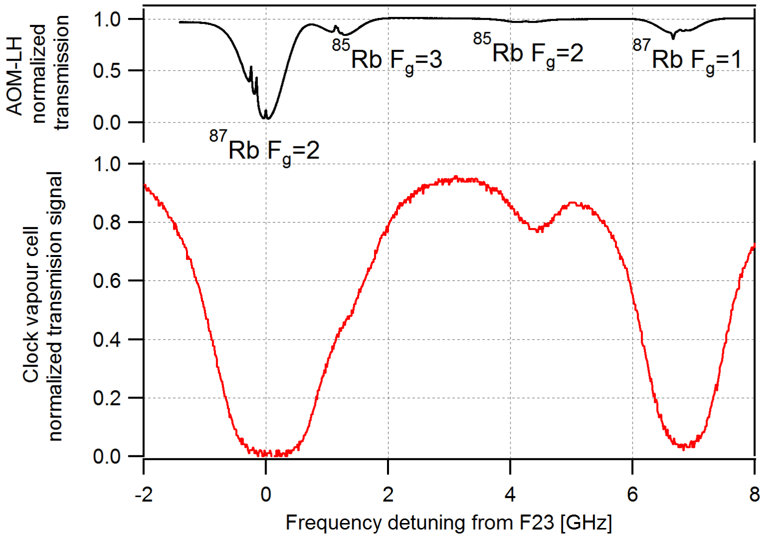

Figure 2.9 – *(top) Typical sub-Doppler absorption spectrum of the AOM-LH. (bottom) Typical Doppler absorption spectrum of the clock vapour cell. The cell is at* 62.7 ± 0.2 *°C and the optical power is* 120 *μW. The bumps in the absorption at a laser frequency detuning ≈ + 1.3 GHz and +4.5 GHz corresponds to the Doppler absorption of the residual* ^{85}*Rb.*

2.3.3 Microwave cavity

2.3.3.1 Description

In an Rb vapour-cell atomic clock, the clock transition $|5^2S_{1/2}, F=1, m_F=0\rangle \leftrightarrow |5^2S_{1/2}, F=2, m_F=0\rangle$ is isolated from the other m_F Zeeman transitions by applying an external static magnetic field. The static magnetic field defines the quantisation axis. In a DR atomic clock, a microwave signal is obtained by multiplication of a quartz frequency. The microwave signal is applied to the atoms using a microwave cavity surrounding the atoms. The microwave cavity generates a microwave field H. In order to obtain a strong clock signal, the microwave magnetic field H must be as perfectly parallel as possible to the static magnetic field throughout the vapour cell. Another requirement of H is that the atoms experience the same μw field amplitude throughout the cell such that a maximum number of atoms undergo an ideal $\pi/2$ pulse.

The μw cavities used in this thesis are based on the so-called loop-gap resonator (LGR), also known as magnetron-type cavity [30][108]. The LGR consists of a metallic slotted loop inside a cylindrical shield. The resonant mode corresponding to the clock transition has the electric field concentrated in the gaps; the resonant magnetic field is confined within the loop and aligned along the axial direction. This mode is called TE_{011}-like mode in analogy with simple cylindrical microwave cavities [92]. The cavity used in the atomic clock prototype has an internal shield diameter of 36 mm and an inner loop diameter of 25.5 mm. The length of cavity is approximately 35 mm, which gives the cavity an inner volume of 36 cm^2. In comparison, a simple cylindrical cavity would have a volume of 105 cm^3 [19][92].

Two different magnetron-type cavities are used in this thesis: one conventional manufactured cavity (CoM cavity) and one cavity made by additive manufacturing (AdM cavity; this process is commonly known as 3D-printing), see Figure 2.10. Generally, conventional cavities are manufactured by subtractive precision machining of metals, often followed by assembly steps requiring precise positioning or alignment of the cavity components. The AdM technology allows microwave cavities

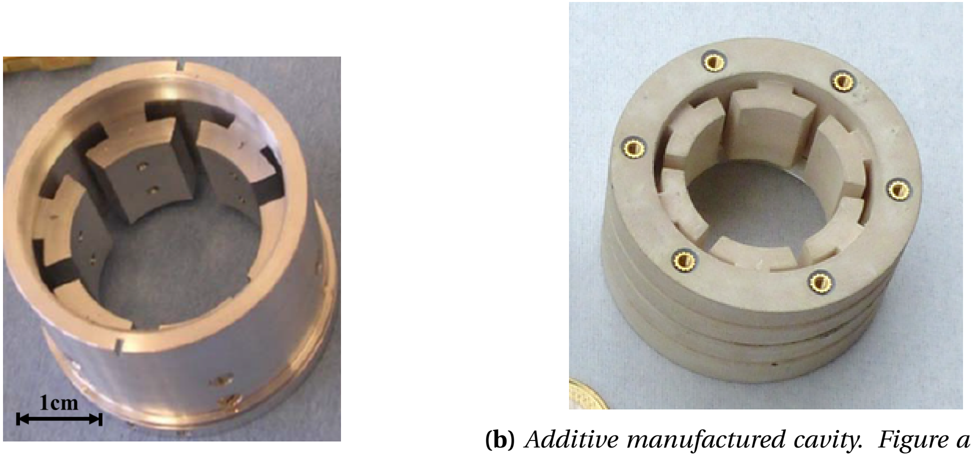

(a) *Conventional manufactured cavity.*

(b) *Additive manufactured cavity. Figure adapted from [109].*

Figure 2.10 – *Photography of the two microwave cavities used in this work.*

made from one piece to be created. The CoM cavity is used in the Rb atomic clock prototype that is characterised in Chapter 3. The properties of the AdM cavity are experimentally studied and a demonstration of a high-performance Rb atomic clock based on an AdM cavity is conducted in Chapter 4.

2.3.3.2 Characterisation

For a microwave cavity, the most important parameters are the cavity resonance frequency and the unloaded and loaded quality factor Q_i,Q_l. The quality factor represents the ratio between the mean energy stored in the microwave cavity with respect to all the power lost (for example, in the walls of the cavity, in the cell body, or in the coupling loop). The unloaded or loaded quality factor corresponds to the case with and without the vapour cell, respectively. The microwave magnetic field can be characterised by two parameters: the filling factor η' and the field orientation factor (FOF) ξ. The filling factor is defined as [67]:

$$\eta' = \frac{V_{cavity}}{V_{cell}} \cdot \frac{\left(\int_{V_{cell}} H_z dV\right)^2}{\int_{V_{cavity}} |H|^2 dV}, \tag{2.2}$$

Parameter	Symbol	CoM Cavity	AdM Cavity
Resonant frequency [GHz]	ν_r	6.831	6.835
Filling factor	η'	0.136	-
Field orientation factor	ξ	0.877	0.9
Volume (dm^3)	V_{cavity}	0.044	0.044
Q-factor (unloaded)	Q_i	488	360
Q-factor (loaded)	Q_l	185	150

Table 2.1 – *Simulated microwave performance of the two magnetron-type cavities (CoM [26]),(AdM [109]).*

where V_{cell} is the volume of the clock cell occupied by Rb atoms without the stem, and V_{cavity} is the total volume of the cavity. The z-axis is parallel to the static magnetic field.The filling factor is a measure of the efficiency of the cavity to couple energy to the atoms stored in the vapour cell. In order to quantify the homogeneity of the H-field orientation across the vapour cell only, we define the FOF ξ as [30]:

$$\xi = \frac{\int_{V_{cell}} H_z^2 dV}{\int_{V_{cell}} |H|^2 dV}. \tag{2.3}$$

Experimentally, the FOF is obtained using the equation [30]:

$$\xi_{exp} = \frac{\int S_\pi dv}{\int S_\pi dv + \int S_\sigma dv}, \tag{2.4}$$

where $\int S_\pi dv$ and $\int S_\sigma dv$ are the transmission signal strengths obtained in a CW-DR integrated over the Zeeman peaks for $\Delta m_F = 0$ (π) and $\Delta m_F = \pm 1$ (σ). The Zeeman spectrum obtained using the conventional cavity is shown in Figure 2.11. Table 2.1 contains the parameters of the two microwave cavities obtained from numerical simulation, details about these simulations can be found in [26].

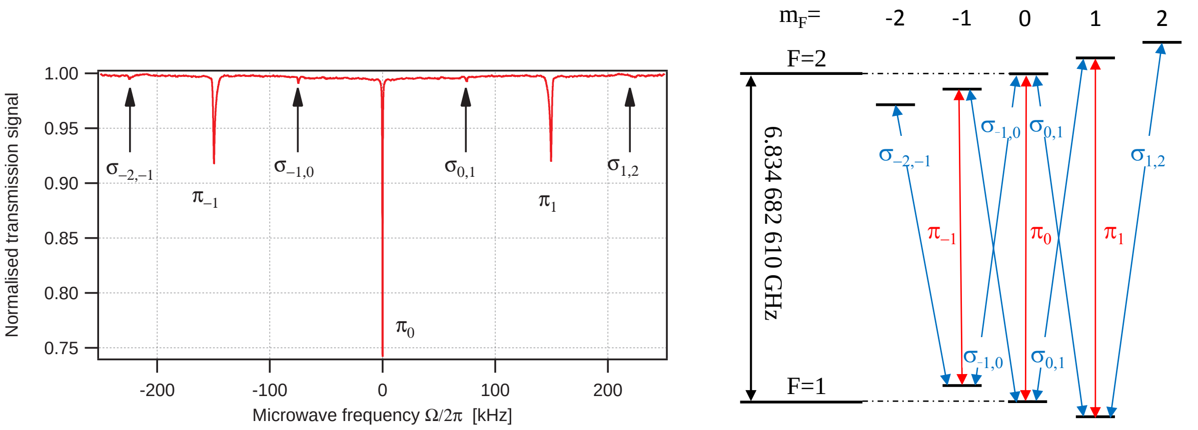

(a) *Measured Zeeman spectrum over a span of 500 kHz.*

(b) *Zeeman transitions for correspoding peaks in 2.11a.*

Figure 2.11 – *CoM Cavity measured Zeeman transitions between the ground state* $|5^2S_{1/2}, F=1\rangle \leftrightarrow |5^2S_{1/2}, F=2\rangle$.

2.3.4 Clock control electronic

2.3.4.1 Microwave source

The clock control electronic (CCE) produces 6.834 GHz from the 10 MHz quartz using a multiplication chain [107]. The multiplication chain is based on the generation of three signals—5.3 MHz, 180 MHz, and 7020 MHz—and their frequency mixing. The heart of the LO is an oven-controlled crystal oscillator (OCXO), which generates a 10 MHz signal. One part of the OCXO signal is used as a clock output and the other is sent to the multiplication chain. The first stage of the multiplication chain obtains a 5.3 MHz and a 180 MHz signal. The second stage uses the 180 MHz to generate a microwave comb where the thirty-ninth harmonic at 7020 MHz is selected. Finally, the LO output frequency at 6.8347 GHz is obtained by subtracting the 185.3 MHz from the 7020 MHz.

Figure 2.12 presents the measured phase noise of the 6.834 GHz signal expressed in dBc/Hz. The phase noise is measured by cross-correlation using two reference synthesisers. The details of the measurement can be found in [26]. The impact of the phase noise on the short-term stability can be obtained by applying equation 1.66. The estimated impact of the LO to the short-term stability is then equal to or lower than $1.73 \cdot 10^{-13} \frac{1}{\sqrt{\tau}}$.[2]

The power stability of the microwave source is measured using a power detector (ZX47-60-S+ Mini-Circuit). The power detector is thermally protected from the laboratory's natural temperature fluctuations. The microwave power is measured at 20 μW. The temperature of the power detector and the microwave power are recorded using a high-resolution data acquisition system. The relative fluctuation of the microwave power is shown in Figure 2.13. A relative power fluctuation below 0.01% is obtained at 10^4 s. The sensitivity of the clock frequency with respect to the microwave power (microwave-power shift) is studied in detail in Chapter 4.

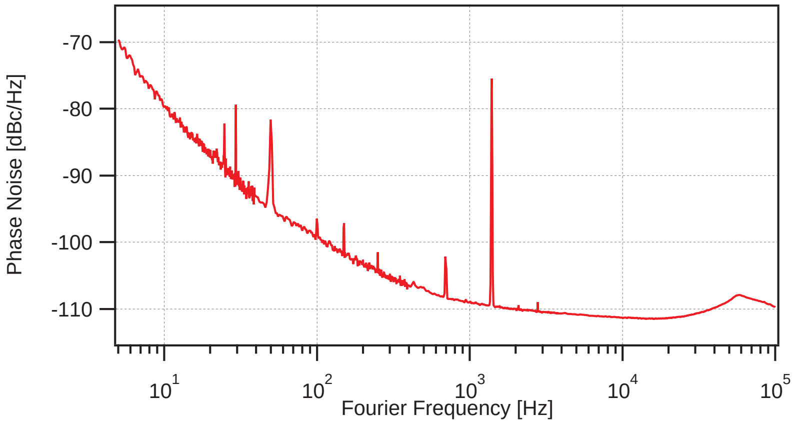

Figure 2.12 – *Phase noise measured at 6.834 GHz carrier frequency [10]. The origin of the noise pic at 1.405 kHz is unknown but probably come from the noise measurement setup. However, the frequency at 1.405 kHz does not contribute to the clock short-term frequency instability only harmonics of the cycle frequency contribute where the closest are 1.266 kHz (m = 6) and 1.477 kHz (m = 7).*

2.3.4.2 Pulsed optically pumped timing sequence

Another function of the CCE is to control the timing sequence of the POP interrogation. The CCE generates the pattern used in the POP scheme: an optically pump phase, two microwave pulses separated by the Ramsey time, and the optical-detection phase. Figure 2.14 presents a typical POP pattern generated by the CCE.

2.3.5 Static magnetic field

A static magnetic field is generated by a solenoid surrounding the microwave cavity. The static magnetic field is aligned parallel to the laser beam inside the vapour cell. The solenoid has 284

---

[2] The origin of noise peak at ≈ 1400 Hz (with a linewidth of 35 Hz) is unknown. However, it does not contribute to the short-term frequency instability because it doesn't overlap any harmonic of the cycle frequency f_c (f_c = 210.97 Hz, see Table 3.11)

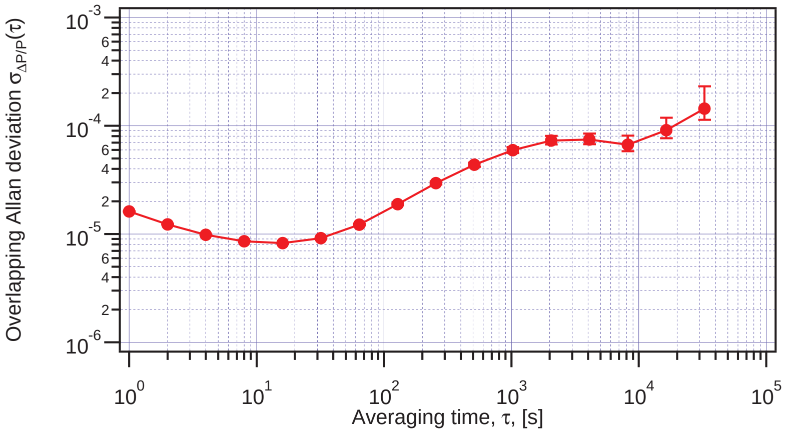

Figure 2.13 – *Power stability of the microwave source.*

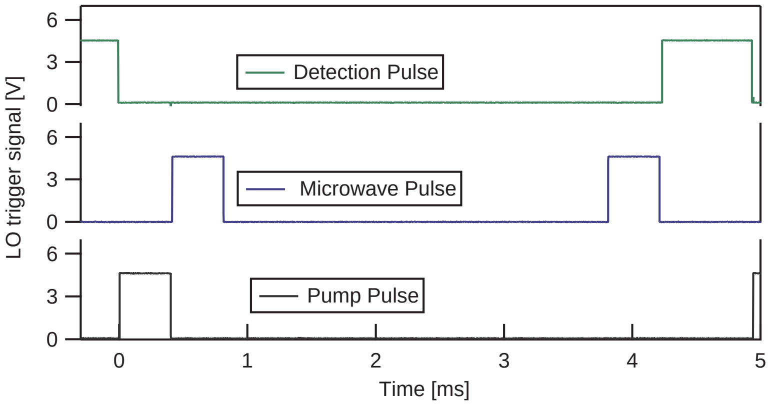

Figure 2.14 – *POP pattern generated by the LO. Pump duration : 0.4 ms, microwave pulse duration : 0.4 ms, Ramsey time : 3 ms, detection duration : 0.7 ms.*

turns and is 4.8 cm long. The value of the static magnetic field inside the vapour cell as a function of the C-field current was measured by Gharavipour [31] at 0.00672 T/A. The C-field current is 1.6 mA, which gives a static magnetic field of $B_z = 1.07 \cdot 10^{-5}$ T. As mentioned in section 1.4.5.1, the PP is surrounded by two magnetic shields. The inner shield is 44 mm width, 52 mm long, and has a thickness of 0.8 m. The second shield is 49 mm large, 100 mm long, and has a thickness of 0.8 mm. The longitudinal shielding factor is 3067, corresponding to an attenuation of 70 dB [26].

2.3.6 Setup breadboard

A picture of the clock breadboard is shown in Figure 2.15. The PP temperatures (vapour cell temperature and stem temperature) and the LH temperatures (baseplate and vapour cell) are controlled by resonator-controlled electronics (RCEs). The neutral density filter wheel is used to vary the optical power in the LS studies in Chapter 4. The photodector and the flip mirror at the entrance of the PP are used to measure the optical power. In this configuration, measuring optical power and clock frequency simultaneously is not possible.

The Figure 2.16 shows the clock breadboard where the PP is enclosed inside a pressure-controlled (PC) chamber. The PC chamber is used as a damper that reduces the atmospheric pressure fluctuation around the PP. This clock setup is used in section 3.3.2.2 and 3.5.

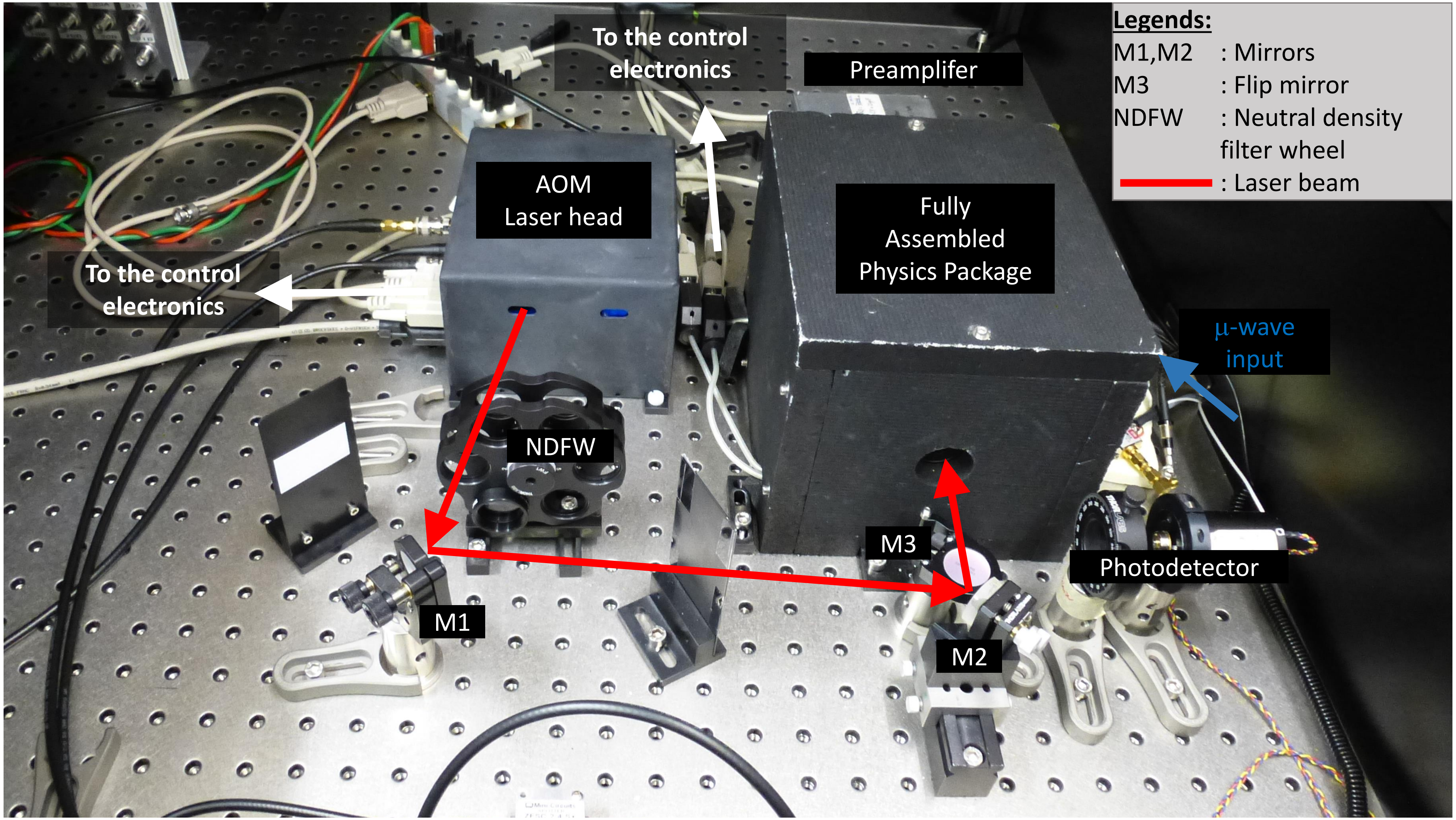

Figure 2.15 – *Experimental breadboard of our POP-DR Rb atomic clock prototype showing the Physics Package and the AOM laser head. This setup corresponds to the block scheme presented in Figure 2.8. The neutral density filter wheel is used to vary the optical power in the light-shift studies of Chapter 4. The photodector and the flip mirror at the entrance of the PP are used to measure the optical power.*

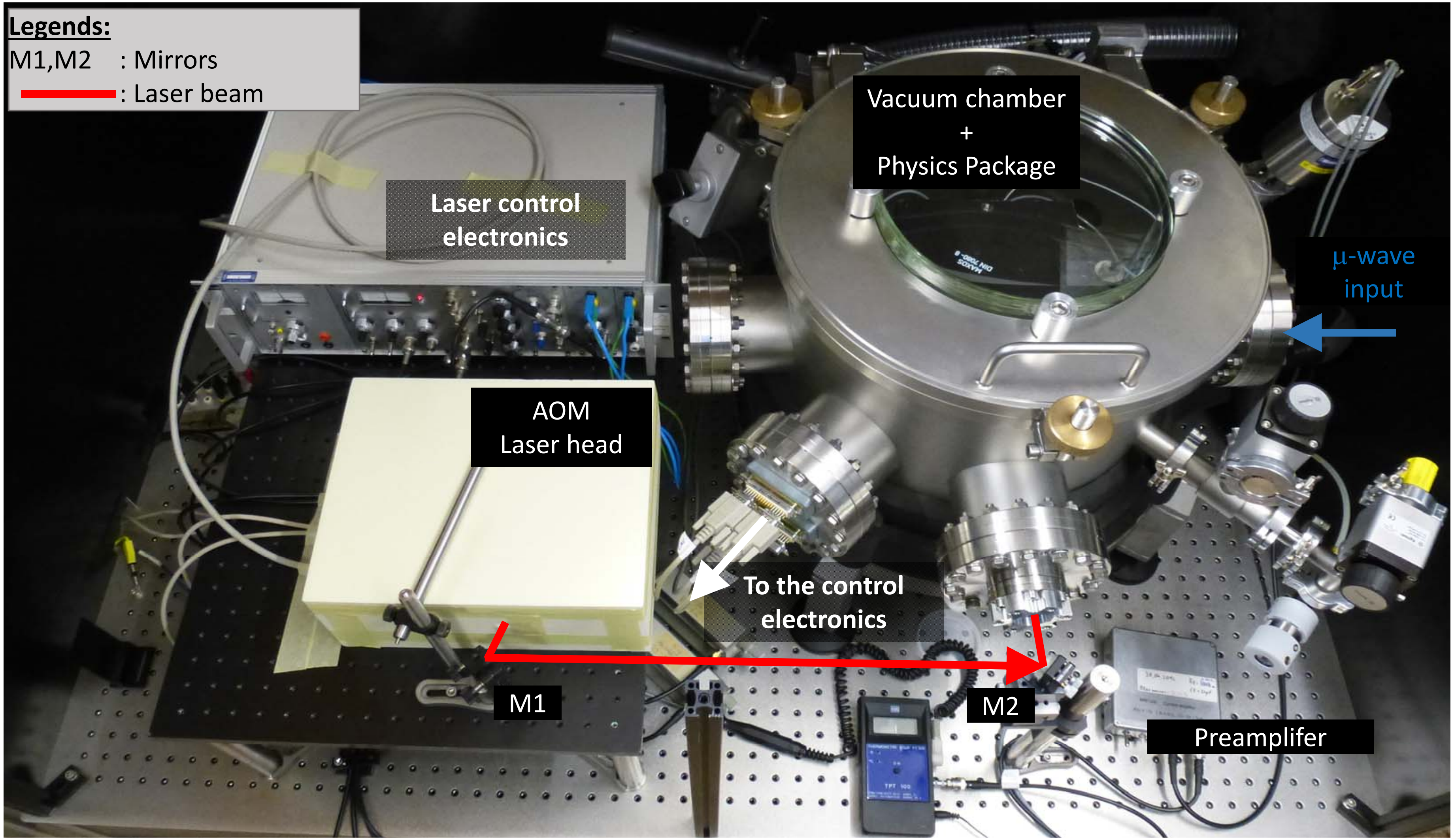

Figure 2.16 – *Experimental breadboard of our POP-DR Rb atomic clock prototype showing the Physics Package inside a pressure-controlled chamber and the AOM laser head. This setup corresponds to the block scheme presented in Figure 2.8. The pressure-controlled chamber is used as a damper that reduces the atmopsheric pressure fluctuation around the PP.*

2.4 Conclusion

This chapter reviewed the two frequency standards used in this thesis. The first frequency standard is based on a 10 mm large and 19 mm long vapour cell with enriched ^{87}Rb. It is used to build compact optical-frequency standards used at 780 nm (FRU, standard LH, AOM-LH) and at 1560 nm (FRU). The second frequency standard is based on a 25 mm large and 25 mm long vapour cell with enriched ^{87}Rb mixed with a mixture of buffer gas (Ar,N_2). It is used to build a POP-DR Rb atomic clock. The atomic clock and the AOM-LH are used in the experimental studies described in Chapter 3 and Chapter 4. The FRU and the standard LH are used in Chapter 5.

3 Microwave-frequency standard: Pulsed rubidium clock

In Chapter 1, we reviewed the most common sources of frequency instabilities for POP-DR Rb clocks. An instability budget is elaborated for our POP-DR Rb clock prototype mainly based on the analyses of Gharavipour [31] and Kang et al.[20]. From this preliminary budget, we identify the microwave-power shift, the cell and stem temperature sensitivity, and the barometric effect as the main sources of medium- to long-term frequency instabilities. This chapter is dedicated to the experimental characterisation and optimisation of the Rb vapour-cell microwave-frequency reference described in Chapter 2 operating in the POP scheme.

First, the main source of frequency sensitivity of our POP-DR Rb clock is reviewed with the presentation of an experimental study on microwave-power sensitivity, LIS effects, and the barometric effect. These experimental studies are completed with a brief review of other frequency shifts (cell and stem temperature, Zeeman effect). In order to reduce the frequency sensitivity of our POP-DR Rb clock at all time scales, the operating points (pulse durations, microwave power, and light intensity) are chosen such that the sensitivity coefficients are minimised. Table 3.1 summarises the standard operation points of our POP-DR Rb clock [31]. These parameters are used in each study of this chapter unless indicated otherwise.

Second, based on these experimental studies, the short-term and medium- to long-term frequency instability budgets are presented. Finally, a relative frequency instability of 10^{-14} at 10^4s of integration time is demonstrated.

Ramsey scheme	Duration [ms]	Input power
Optical pumping	$t_p = 0.4$	13 [mW]
Microwave pulses (2 × $\pi/2$-pulses)	$t_m = 0.3$	15 [μW]
Ramsey time	$t_R = 3$	-
Optical detection	$t_d = 0.7$	120 [μW]

Table 3.1 – *Standard durations and input powers for three phases of optical pumping, microwave interrogation and optical detection in our POP-DR Rb clock. These parameters are used to each studies of this chapter unless indicated otherwise.*

3.1 Microwave power shift studies

The microwave-power shift (MPS) is an important source of frequency instabilities in DR atomic clocks [96]. In a POP-DR Rb clock, the origin of the clock frequency sensitivity to the microwave power was identified as the result of two mechanisms. The first mechanism is the cavity-pulling effect, which is related to the frequency difference between the Rb ground-state frequency and the microwave-cavity resonance frequency [66][19]. The second mechanism is the position-shift effect. The resonance frequency of a group of Rb atoms will be different from another group of atoms in the vapour cell with buffer gas because of inhomogeneous electric, magnetic, and electromagnetic (EM) fields. The measured clock frequency is a weighted average of the resonance frequencies of each group of atoms. Any change in the microwave power will modify the weighting inside the vapour cell, which results in a clock frequency change [96][97]. Note that this description is valid only for buffer-gas cells in which the change of position of each atom during a Ramsey cycle may be considered negligible.

In this section, we experimentally evaluate the MPS sensitivity coefficient (i.e $\frac{\partial \Delta \nu_{\text{clock}}}{\partial P_{\mu}}$) of our POP-DR Rb clock prototype. The coefficient is determined for various operating points. Then, we demonstrate that the MPS of our POP-DR Rb clock is originated from the position shift. We show that the MPS of our POP-DR Rb clock can be reproduced by the presence of two inhomogeneities: microwave-field amplitude inhomogeneity and atomic ground-state resonant-frequency inhomogeneity. The demonstration is based on numerical calculations that generalise the model presented in section 1.3 (valid in the case of homogeneous field distribution) for the case of inhomogeneous field distributions. Finally, several origins of the atomic ground-state resonant-frequency inhomogeneity are discussed.

3.1.1 Microwave-power shifts measurement

First, the MPS is measured by frequency stabilising the clock quartz on the central fringe of the Ramsey spectrum and varying the microwave power $P_{\mu W}$ at constant pulse duration t_m [31]. The measurement is performed when the laser is frequency stabilised onto the six sub-Doppler transitions (see Table 1.1). The results are shown in Figure 3.1. Second, the microwave-power shift is measured simultaneously with the contrast of the central fringe, see Figure 3.2. The microwave Rabi frequency is proportional to the square root of the microwave power, i.e. $\theta = b \cdot t_m \propto \sqrt{P_{\mu W}} \cdot t_m$. Figure 3.2 allows the product $\sqrt{P_{\mu W}} \cdot t_m$ to normalise such that the first maximum of the Rabi oscillation occurs at $b \cdot t_m = \pi/2$.

From the measurement of Figure 3.1, we obtain the microwave-power sensitivity coefficients at $P_{\mu W} = 15$ μW (corresponding to $b \cdot t_m = \pi/2$). The coefficients are obtained from a linear fit of the data when the laser is tuned on $|5^2S_{1/2}, F=1\rangle \leftrightarrow |5^2S_{1/2}, F'\rangle$ transitions and from a quadratic fit when the laser is tuned on $|5^2S_{1/2}, F=2\rangle \leftrightarrow |5^2S_{1/2}, F'\rangle$ transitions. In the latter case, the MPS coefficients are also determined at the inversion point for $P_{\mu W} = 20$ μW (corresponding to $b \cdot t_m = 0.57 \cdot \pi$) where the coefficient is minimum. Table 3.2 presents the microwave-power sensitivity coefficient obtained at $P_{\mu W} = 15$ μW and $P_{\mu W} = 20$ μW for each laser frequency.

The MPS coefficients measured when the laser is tuned on $|5^2S_{1/2}, F=2\rangle \leftrightarrow |5^2S_{1/2}, F'\rangle$ transitions at $P_{\mu W} \approx 20$ μW (the inversion points) are one order of magnitude lower than the MPS coefficients measured at $P_{\mu W} = 15$ for all the laser frequencies.

Operating the POP clock with $b \cdot t_m \neq \pi/2$ impacts (1) the contrast and the FWHM of the central fringe (see Figure 1.10 and 1.11) and (2) the cavity-pulling shift. In the case of $P_{\mu W} \approx 20\mu$W, the contrast is 41% and the FWHM is 146.1 Hz, making this change negligible. Changing the microwave power changes the cavity-pulling shift as illustrated in Figure 1.13 and described by equation 1.84. Table 3.3 presents the cavity-pulling shift and the cavity-pulling shift sensitivity to microwave power and environmental parameters calculated using equation 1.84 at the three-inversion microwave power for the $|5^2S_{1/2}, F = 2\rangle \leftrightarrow |5^2S_{1/2}, F'\rangle$ transitions. The cavity-pulling shift sensitivity to environmental parameters at $P_{\mu W} \approx 20\mu$W is higher than the one calculated at $P_{\mu W} = 15\mu$W (see Table 1.7); however, the sensitivities are still negligible. According to the calculation in Table 3.3, operating the clock in the condition laser on CO21-23 and $P_{\mu W} \approx 20.1\mu$W minimises the MPS coefficient and the cavity-pulling shift sensitivities.

According to calculation performed in section 1.4.5.4 and in Table 3.3, the measured MPS of Figure 3.1 and the MPS coefficient are not reproduced by the cavity-pulling effect. In the next section, we demonstrate that the measured MPS can be reproduced by considering the position-shift effect.

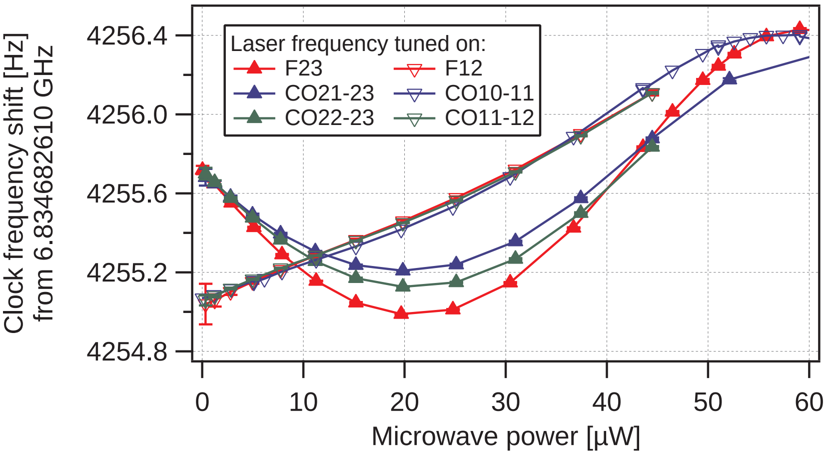

Figure 3.1 – *Clock frequency shift as a function of the microwave power.*

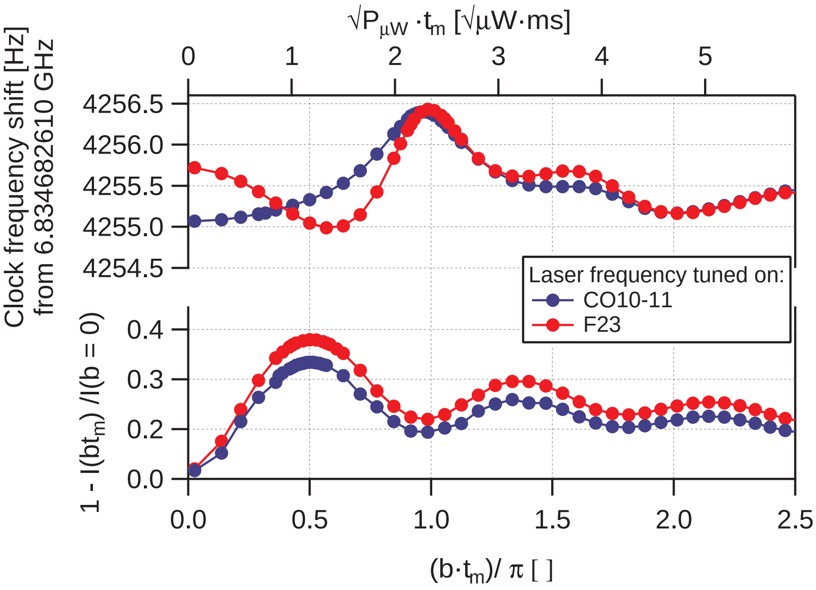

Figure 3.2 – *Clock frequency shift and contrast of the central fringe as a function of the microwave power.*

Laser frequency	MPS coefficient $\left[\frac{1}{\mu\mathrm{W}}\right]$	
tuned on:	$P_{\mu W} = 15\ \mu$W	at inversion point
F23	$(-3.2 \pm 0.2) \cdot 10^{-12}$	$\leq 2 \cdot 10^{-13}$ at $P_{\mu W} = 21\ \mu$W
CO21-23	$(-1.8 \pm 0.2) \cdot 10^{-12}$	$\leq 2 \cdot 10^{-13}$ at $P_{\mu W} = 20.1\ \mu$W
CO22-23	$(-2.4 \pm 0.2) \cdot 10^{-12}$	$\leq 2 \cdot 10^{-13}$ at $P_{\mu W} = 20.9\ \mu$W
F12	$(3.0 \pm 0.2) \cdot 10^{-12}$	-
CO10-11	$(2.7 \pm 0.1) \cdot 10^{-12}$	-
CO11-12	$(2.81 \pm 0.05) \cdot 10^{-12}$	-

Table 3.2 – *MPS coefficients from data of Figure 3.1 for two different microwave powers corresponding to* $\theta = \pi/2$ *(*$P_{\mu W} = 15\ \mu W$*) and* $\theta = 1.14\pi/2$ *(*$P_{\mu W} = 20\ \mu W$*).*

Laser transitions	$P_{\mu W}$ [μW]	$\Delta\nu_{CP}$ [mHz]	$\frac{\partial(\Delta\nu_{CP})}{\partial T}$ [/K]	$\frac{\partial(\Delta\nu_{CP})}{\partial P}$ [/Pa]	$\frac{\partial(\Delta\nu_{CP})}{\partial h}$ [/(g/m^3)]	$\frac{\partial(\Delta\nu_{CP})}{\partial W}$ [/μW]
F23	21	-1.18	$5.8 \cdot 10^{-15}$	$2.3 \cdot 10^{-18}$	$5.5 \cdot 10^{-15}$	$-2.6 \cdot 10^{-14}$
CO21-23	20.1	-1.02	$5.0 \cdot 10^{-15}$	$2.0 \cdot 10^{-18}$	$4.7 \cdot 10^{-15}$	$-2.7 \cdot 10^{-14}$
CO22-23	20.9	-1.17	$5.7 \cdot 10^{-15}$	$2.3 \cdot 10^{-18}$	$5.4 \cdot 10^{-15}$	$-2.6 \cdot 10^{-14}$

Table 3.3 – *Cavity-pulling (CP) shift sensitivity coefficients calculated according to equation (1.84) in the case of microwave power of Table 3.2.*

3.1.2 Microwave-field amplitude inhomogeneity simulation

In this section, the role of the microwave-field amplitude inhomogeneity on the MPS is evaluated numerically using a numerical model. The numerical model is based on the theoretical model presented in section 1.3. As this model is valid for homogeneous field distributions, the vapour cell is decomposed into a mesh where each point of the mesh has a different value of the microwave-field amplitude $B_z(\vec{r})$. Here, the following hypotheses are assumed:

- A1: No microwave-field phase inhomogeneity is considered. We consider that the two microwave pulses have the same phases $\phi = 0$.
- A2: No microwave-field direction inhomogeneity is considered. In this case, we consider only the π_0 microwave transition between the two clock states [74].
- A3: Only microwave-field amplitude inhomogeneity is considered.

3.1.2.1 Note on the microwave-field phase

In the study presented in this section, the phase of the microwave field is considered homogeneous (the hypothesis A1). However, phase variations exist due to microwave-field power losses in the cavity. In the case of inhomogeneous microwave-field phase distribution, the moving rubidium atoms are affected by a different microwave-field phase during one interrogation cycle. This phenomenon is well known in caesium beam atomic clocks [110] and atomic fountains where the atomic flux passes trough the microwave cavity two times [111][112][113]. For atomic clocks based on buffer-gas vapour cell, the rubidium atoms are localized in a space region due to the buffer-gas collisions. For our POP-DR Rb atomic clock, the mean free path is of the order of $\approx 5\ \mu$m [114] and the mean distance travelled during one microwave interaction ($T_c \approx 5$ ms) is 0.5 mm. A phase gradient across the vapour cell at the order 0.1 radian was simulated for a microwave cavity with a similar design as the one used in this thesis [115]. For an atom sbuject to a phase gradient during the Ramsey interrogation, the phase gradient $\Delta\phi$ can be seen - in the Bloch vector representation - as an initial phase in the coherence plan resulting in a clock frequency shift. However, in order to impact the clock frequency instability, the microwave-field phase gradient would need to vary over long time scales (time scale of the day). As discussed by Godone et al. [116], possible long-time scale variations of the phase gradient in vapour-cell clocks can originate from non-uniformity of the atomic medium density. Further numerical and experimental evaluations are need in order to better characterise this effect.

3.1.2.2 Numerical model

The microwave-field amplitude distribution of our magnetron-type cavity is obtained from numerical simulation performed at the Laboratory of Electromagnetics and Acoustics (LEMA-EPFL). The normalised distribution $B_z^n(\vec{r})$ ($B_z^n(\vec{r}) \leq 1, \forall \vec{r} \in V_{\text{cell}}$) is presented in Figure 3.4. The normalised distribution is used to define a local microwave pulse area $\theta(\vec{r})$ with $\theta(\vec{r}) = B_z^n(\vec{r})\theta_{\text{max}}$ where θ_{max} is the maximum microwave pulse area inside the vapour cell. Based on the microwave pulse area distribution, the population inversion $\Delta(\vec{r})$ at the end of the Ramsey sequence is computed locally at each point of the mesh using the matrix product 1.42. The light intensity at the cell output is then computed according to the Beer-Lamber law:

$$I_i(z = L_{cell}) = I_0 \cdot e^{-\sigma_{i3} n_0 \sum_j \rho_{ii}(z_j)\Delta z}, \tag{3.1}$$

where I_0 is the detection light intensity at the entrance of the vapour cell, the subscript i is one of the two ground states, σ_{i3} is the optical absorption cross-section for the transition $|i\rangle \rightarrow |3\rangle$, n_0 is the Rb density, Δz is the z-axis integration step, and $\rho_{ii}(z_j)$ is the population density of atoms in one of the ground-state levels at the point z_i. Considering the hyperfine structure of the state $|i\rangle$, the population density of atoms at the end of the optical pumping is given by $\rho_{11} = 3/8–\Delta/2$ or $\rho_{22} = 5/8 + \Delta/2$. In this study, the population density of atoms $\bar{\rho}_{ii}(z_j)$ is obtained by summing the contributions of the plan perpendicular to the light propagation vector:

$$\bar{\rho}_{ii}(z_j) = \frac{1}{n_x \cdot n_y} \sum_{x_n, y_m}^{x_n^2 + y_m^2 < R_{cell}^2} \rho_{ii}(x_n, y_m, z_j), \tag{3.2}$$

where n_x and n_y are the number of subdivisions of the mesh along the x- and y-axes, respectively. In this section, a perfect optical pumping is assumed: all the atoms are perfectly optically pumped in one of the ground states. Hence, the Bloch vector at the beginning of the first microwave interaction (t=0) is given by $R_1(0)$ = (0,0,1/5) for the pumping light frequency tuned to $|1\rangle \rightarrow |3\rangle$ and by $R_2(0)$ = (0,0,-1/3) for the pumping light frequency tuned to $|2\rangle \rightarrow |3\rangle$, see Figure 3.3. The parameters used in the numerical calculation are summarised in Table 3.4.

In the next sections, the impact of the microwave amplitude inhomogeneity and its weighting of the atomic resonant frequencies distributed within the cell on the properties of the central Ramsey fringe is presented with an emphasis on its (1) contrast, (2) FWHM, and (3) central fringe central frequency (CFCF) detuning. A large part of the results presented in this section were published in [117].

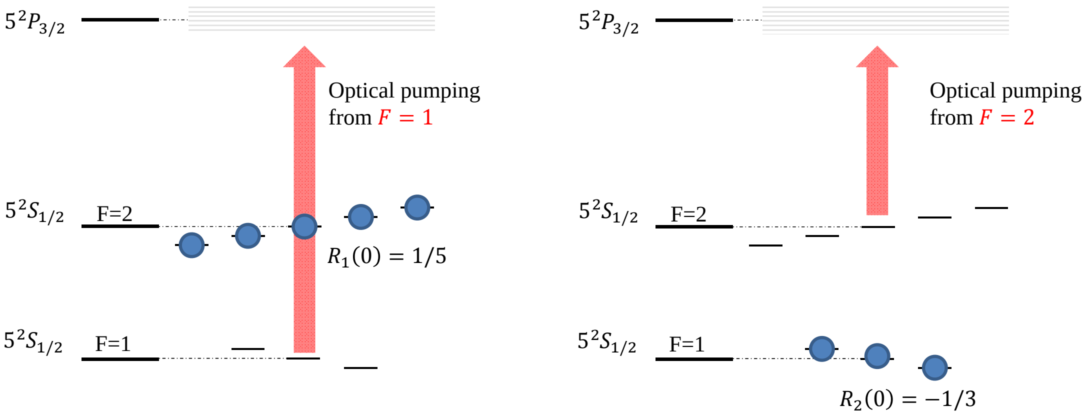

Figure 3.3 – *Optical pumping scheme and atomic ground-state Zeeman levels populations in the case of ideal optical pumping. The size of the blue circle indicates the atomic population level.*

3.1.2.3 Microwave power normalisation

For the simulated and measured Ramsey spectra, the atoms undergo a local microwave pulse area $\theta(\vec{r})$. The value of this local microwave pulse area depends on θ_m for the simulated spectrum or on $P_{\mu W}$ for the measured spectra. In the next sections, we want to compare the simulated spectrum and the measured spectrum. However, we encounter the following issues:

Size of the absorption cell (diameter, length)	25 mm, 25 mm
Size of the subdivisions (Δx,Δy,Δz)	2 mm, 2 mm, 1 mm
Optical absorption cross section (σ_{13},σ_{23})	$1.3 \cdot 10^{-15}$ m^2, $1.6 \cdot 10^{-15}$ m^2
Rubidium density n_0	$2.89 \cdot 10^{17}$ m^3
Theoretical linewidth of the optical transition D_2	$\Gamma = 2\pi \cdot 405$ MHz
Population and coherence relaxation rates (γ_1,γ_2)	360 s^{-1}, 340 s^{-1}

Table 3.4 – *Parameters used in the numerical simulation.*

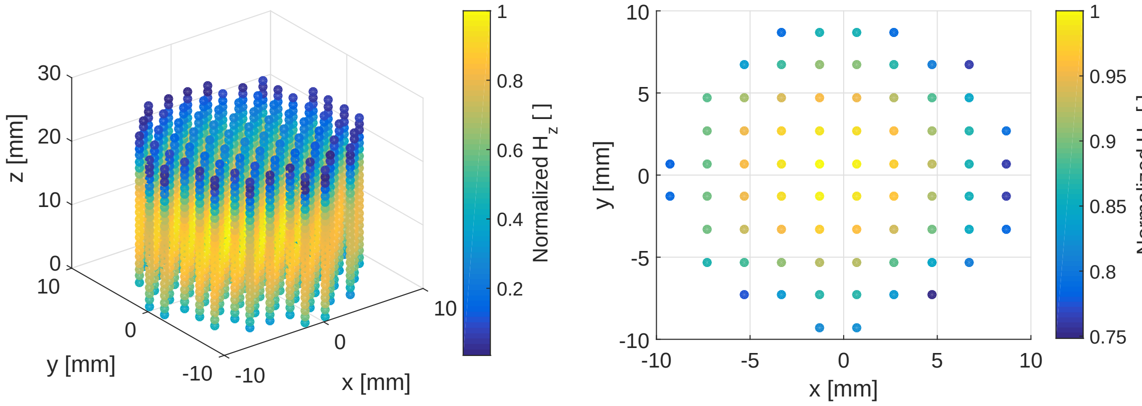

(a) *Overall distribution* **(b)** *Transverse distribution at z = 9 mm.*

Figure 3.4 – *Normalized simulated magnetic field amplitude B_z^n distribution inside the vapour cell. The simulation is performed at the Laboratory of Electromagnetics and Acoustics (LEMA-EPFL). Figure adapted from [117].*

1. The microwave-field amplitude distribution in Figure 3.4 is an approximation of the real distribution inside the vapour cell.
2. The microwave power injected into the microwave cavity is not precisely known. Indeed, the microwave power is measured before the cavity, and the power losses induced by the coupling loop are unknown.
3. For a fixed simulation parameter $\theta_{\max}$, the corresponding experimental $P_{\mu W}$ is also unknown.

In order to solve these issues, the Rabi oscillations are used as a comparison tool. For the simulation and measurement, the first maximum of the Rabi oscillation occurs when most of the atoms in the vapour cell undergo two $\pi/2$ pulses. To compare the two sets of data, we associate a single measurement with a fixed microwave pulse area θ_n; the microwave pulse area θ_{sim} ($\theta_{sim} = \theta_{\max}$) and θ_{meas} ($\theta_{meas} \propto \sqrt{P_{\mu W}} \cdot t_m$) are normalised such that the first maximum of the simulated and measured Rabi oscillations occurs at $\theta_n = \pi/2$ [1].

3.1.2.4 Ramsey spectra

The simulated light intensity at the end of the vapour cell I(z = L$_{\text{cell}}$) as a function of the microwave-frequency detuning Ω_m is obtained according to equation (3.1) after one cycle of microwave

---

[1] In this thesis θ applies to one single microwave pulse and the POP scheme is composed of two identical θ_n pulses.

interrogation described by the matrix product (1.43) in the conditions indicated in Table 3.4. Figure 3.5 presents the Ramsey spectra simulated for different normalised microwave pulse areas θ_n in the case of the inhomogeneous microwave amplitude distribution in Figure 3.4. Figure 3.5 also presents the measured Ramsey spectra at the corresponding normalised microwave pulse, and they are measured for a pump optical power of 12.8 mW, a detection power of 148 μW, and the LH frequency stabilised to the cross-over CO10-11. All the Ramsey spectra are normalised to the light intensity detected at the end of the vapour cell in the absence of any microwave interrogation (i.e. $P_{\mu W} = 0$).

The simulated Ramsey fringes agree with the measured Ramsey fringes over the frequency span. However, Figure 3.5 shows a small central fringe mismatch for microwave pulse area π and $1.5 \cdot \pi$. The origin of this mismatch is unknown, but it is suspected to come from (1) the simulation parameters (Table 3.4), not corresponding to the experimental reality (especially, the relaxation rates γ_1 and γ_2 were empirically fixed); or (2) the uncertainty on the microwave power $P_{\mu W}$ coupled into the microwave cavity. Nevertheless, the simulated Ramsey fringes still reproduce the experimental data much better than the homogeneous field case. This is especially true in the case of $\theta_n = \pi$.

3.1.2.5 Contrast and full width at half maximum

The central Ramsey fringe is simulated and measured for microwave pulse area θ_n ranging from 0 to $\approx 3\pi$. Each of the central fringes is fitted with the cosine fit function (1.47) from which the contrast and the FWHM is obtained. Figure 3.6 and Figure 3.7 present the variation of the contrast (defined by equation (1.48)) and the FWHM as a function of the normalised microwave pulse area θ_n, respectively. The measurement data are well reproduced by the simulation for microwave pulses between 0 and 2.3π.

The behaviour of the contrast and the FWHM as functions of the microwave power can be easily understood. In the case of a homogeneous microwave-field amplitude distribution, all the atoms in the vapour cell undergo the same microwave pulse. All the groups of atoms produce the same Ramsey spectrum and, consequently, are identical to the output Ramsey spectrum. The central Ramsey fringe contrast is maximal for $\pi/2$-pulse and is zero for π pulse. For a π pulse, no fringes are observed, and the FWHM cannot be defined, which explains the discontinuity of the FWHM at $\theta_n = \pi$ in Figure 3.7.

For inhomogeneous microwave-field amplitude distribution, different groups of atoms in the vapour cell undergo slightly different microwave pulses. This means that the output Ramsey spectrum is an average of each Ramsey spectrum generated inside the cell. The consequence is that a residual central fringe at $\theta_n = \pi$ is always present. Thus, a non-zero contrast (Figure 3.6) and the FWHM (Figure 3.7) can be determined for $\theta_n = \pi$.

Figure 3.8 presents simulated Ramsey spectra in 2D plots: the x-axis is the microwave pulse area, the y-axis is the microwave-frequency detuning, and the z-axis (the coloured scale) represents the normalised intensity.

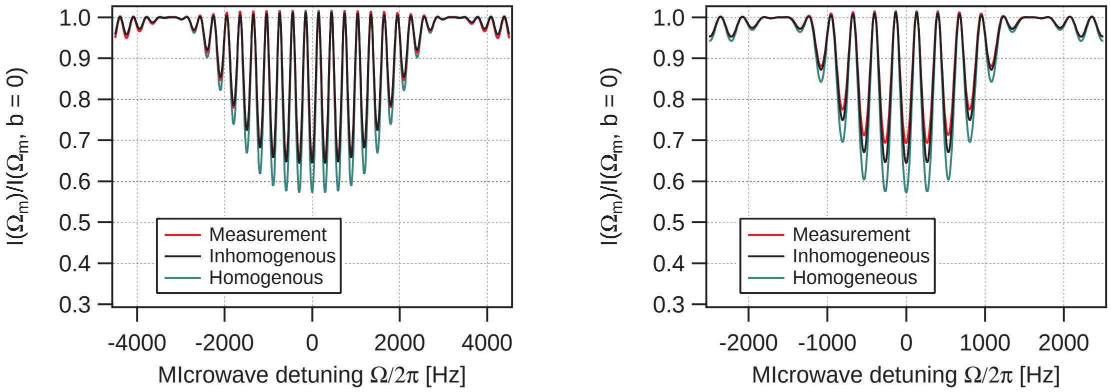

(a) $\theta_n = 0.5\cdot\pi$ *and* $t_m = 0.3$ *ms.* **(b)** $\theta_n = 0.5\cdot\pi$ *and* $t_m = 0.6$ *ms.*

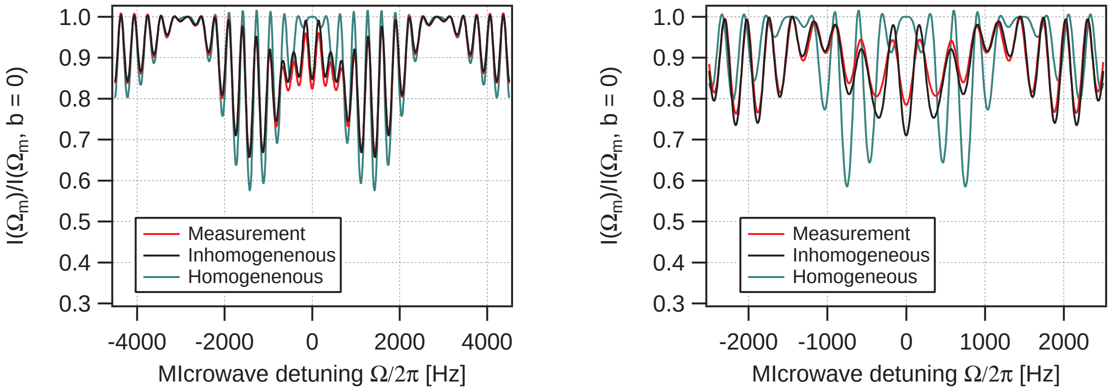

(c) $\theta_n = \pi$ *and* $t_m = 0.3$ *ms.* **(d)** $\theta_n = \pi$ *and* $t_m = 0.6$ *ms.*

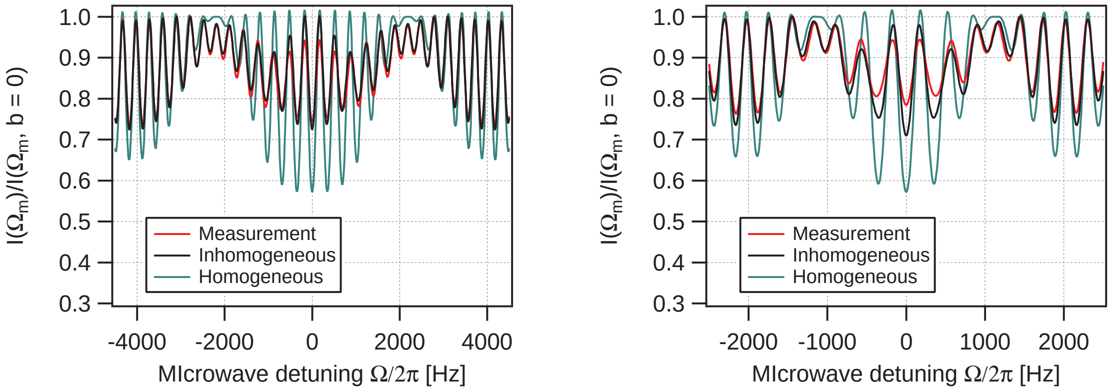

(e) $\theta_n = 1.5\cdot\pi$ *and* $t_m = 0.3$ *ms.* **(f)** $\theta_n = 1.5\cdot\pi$ *and* $t_m = 0.6$ *ms.*

Figure 3.5 – *Measured and simulated Ramsey spectra for different microwave pulse area.*

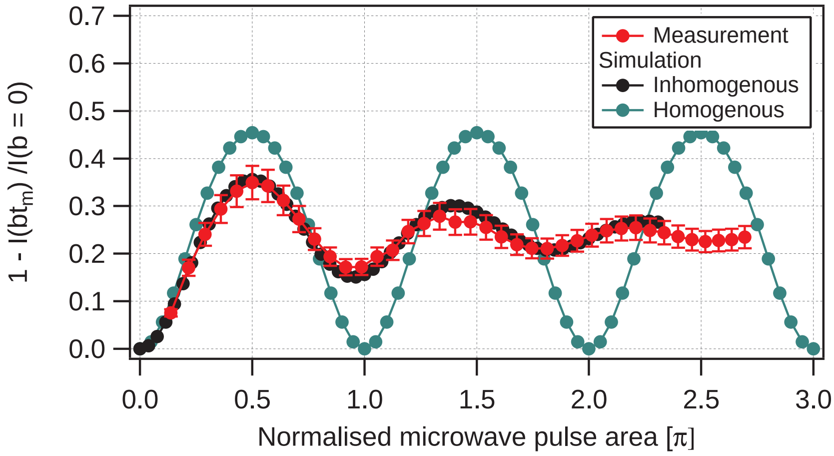

Figure 3.6 – *Measured and simulated Rabi oscillations for zero microwave detuning as functions of the normalized microwave pulse area* θ_n*. The horizontal axis is normalized such that the first maximum occurs at* $\theta = \pi/2$*. Figure adapted from [117]. The uncertainty on the measurement was not evaluated in detail, however the errors bars on the measurement correspond to a relative error of 10%.*

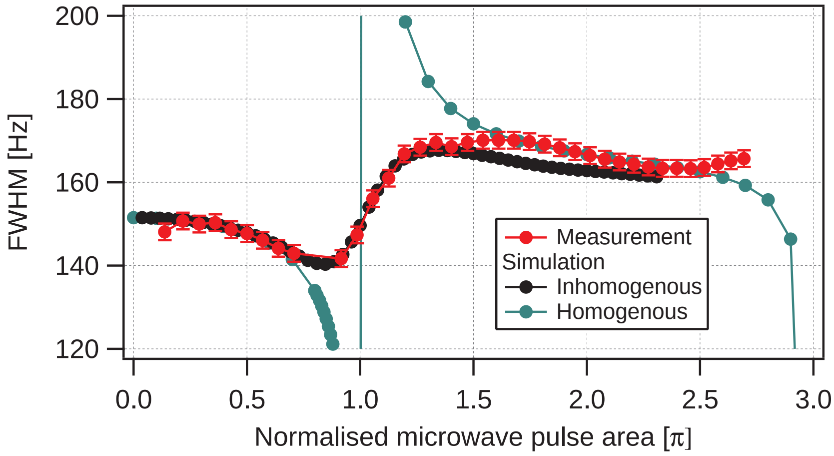

Figure 3.7 – *Measured and simulated central Ramsey fringe linewidth as functions of the normalized microwave pulse area* θ_n*. Figure adapted from [117]. The uncertainty on the measurement was not evaluated in detail, however the errors bars on the measurement correspond to a relative error of 2 Hz, according to [31].*

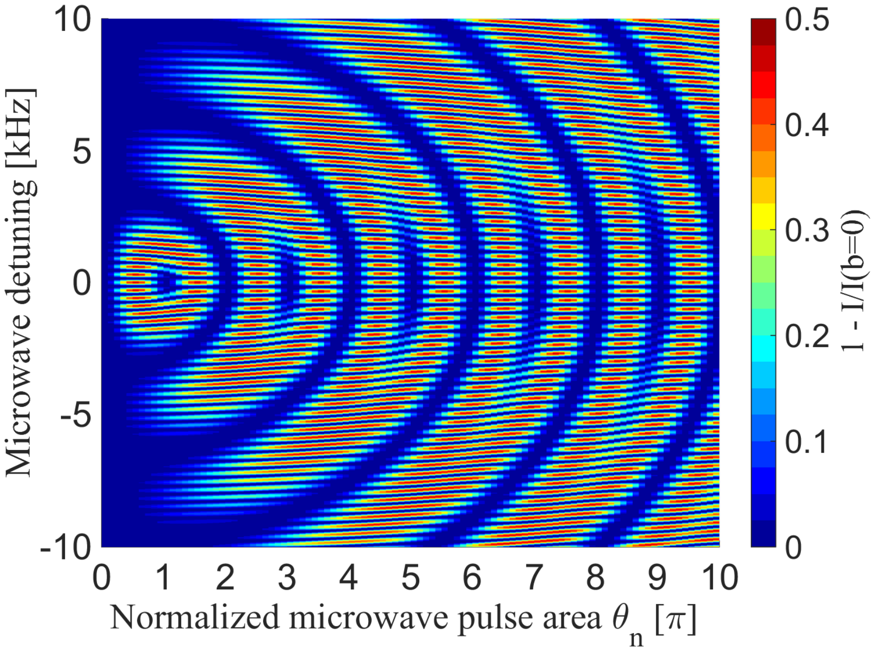

(a) *Homogeneous microwave field amplitude.*

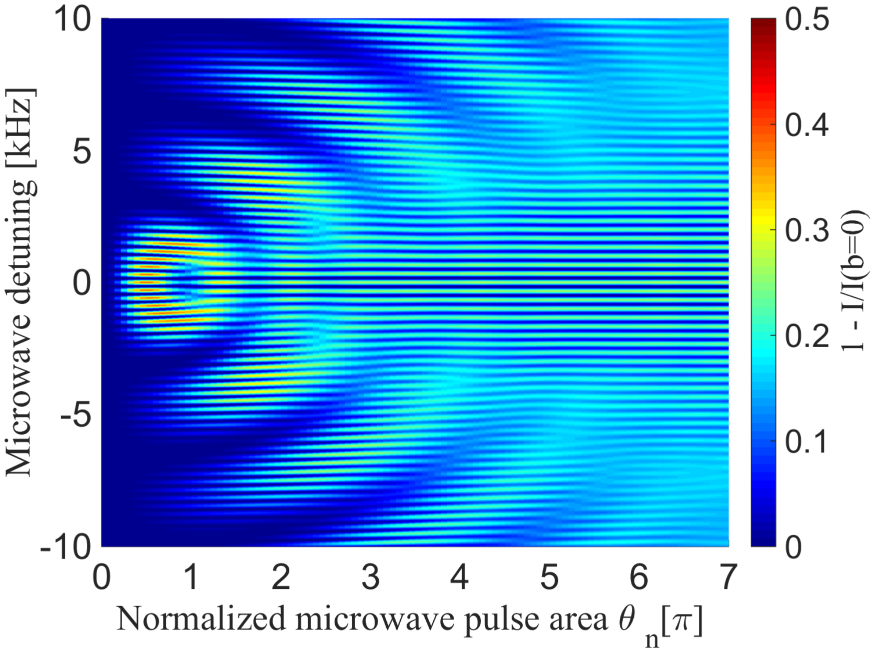

(b) *Inhomogeneous microwave field amplitude.*

Figure 3.8 – *Simulated Ramsey spectra in a 2D-plots : the x-axis is the normalized microwave pulse area θ_n, the y-axis is the microwave frequency detuning and z-axis (the colored scale) represents the normalized intensity.*

3.1.2.6 Microwave-power shift

In this section, the position-shift effect induced by the microwave-field amplitude inhomogeneity is simulated by considering two inhomogeneities: (1) microwave-field amplitude inhomogeneity (given by Figure 3.4) and (2) an estimated ground-state resonant-frequency shift distribution. The latter corresponds to the frequency shift between the unperturbed ground-state resonant-frequency ν_{HFS} and the local ground-state resonant-frequency $\nu(x, y, z)$ with $\Delta\nu(x, y, z) = \nu(x, y, z) - \nu_{\text{HFS}}$. The aim of this approach is determine which ground-state resonant-frequency shift distribution can be at the origin of the observed microwave power shift of our POP-DR Rb Rb clock prototype (see Figure 3.1). This is done numerically using the numerical model and a ground-state frequency shift distribution of the most important frequency shifts of our POP-DR Rb Rb clock prototype. According to Chapter 2, the most important frequency shifts $\Delta\nu(x, y, z)$ are the 2^{nd}-order Zeeman shift, the cavity-pulling shift, the residual AC-Stark shift induced by the leakage light, and the density shift induced by a temperature gradient.

In the following section, first a ground-state resonant-frequency shift distribution for each of the most probable phenomena is deduced, and the impact of each of these distributions on the simulated central frequency of the central fringe (CFCF) is presented. Second, the results are compared and discussed.

In order to compare the numerical results (the CFCF versus the normalised microwave pulse area) with the experimental microwave-power shift of Figure 3.1, the following points are used for comparison:

P1: The frequency difference $\nu_{\text{CFCF}}(\theta_n = \pi) - \nu_{\text{CFCF}}(\theta_n = 0) \equiv \Delta\nu^{\pi-0}_{\text{CFCF}}$, which corresponds to the biggest frequency difference when applied to the experimental data (see Figure 3.2).

P2: The sensitivity coefficient $\partial\nu_{\text{CFCF}}/\partial\theta_n$ [2] is obtained via a linear fit at $\pi/2$.

These two points, P1 and P2, will be given for each simulation case and summarised at the end. When applied to the data in Figure 3.1, one obtains in the case of (1) a laser detuning F=1 a frequency difference $\Delta f^{\pi-0}_{\text{CFCF}} = +1.34$ Hz and a sensitivity coefficient $\partial\nu_{\text{CFCF}}/\partial\theta_n = 9 \cdot 10^{-13}/\%$ and (2) a laser detuning F=2 a frequency difference $\Delta f^{\pi-0}_{\text{CFCF}} = +0.7$ Hz and a sensitivity coefficient $\partial\nu_{\text{CFCF}}/\partial\theta_n = -6 \cdot 10^{-13}/\%$.

Homogeneous shift

First, we consider a homogeneous frequency shift distribution:

$$\Delta\nu_{\text{Homogeneous}}(x, y, z) = C \tag{3.3}$$

where C is a constant. Figure 3.9 presents the simulated microwave-power sensitivity of the CFCF for C = 0 Hz and C = ± 1 Hz. As expected, weighting has no effect due to the absence of position shift. Therefore, we do not see any microwave power shift.

---

[2] The sensitivity coefficient is expressed in the unit of Hz/% of nominal microwave power using $\frac{\partial\nu_{\text{CFCF}}}{\partial\theta_n} \cdot \frac{\pi/2}{100}$.

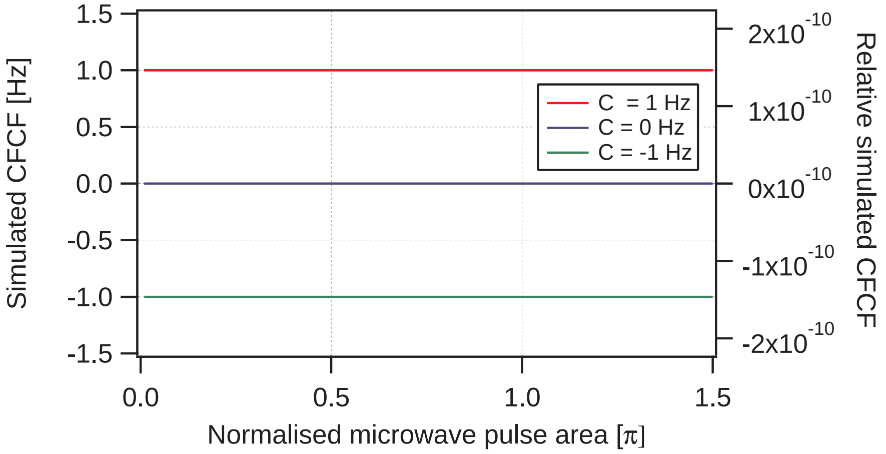

Figure 3.9 – *Simulated central fringe central frequency as a function of the normalized microwave pulse area* θ_n *taking into acount a homogenoeous frequency shift.*

Second-order Zeeman shift

The frequency shift induced by the second-order Zeeman effect is given by equation 1.70:

$$\Delta\nu_{2^{nd}\text{-order Zeeman}}(x,y,z) = C\cdot B_z(x,y,z)^2, \tag{3.4}$$

with $C = 575.14\cdot 10^8$ Hz/T^2. The distribution of the static magnetic field B_z inside the vapour cell due to the solenoid used in the PP is approximated by:

$$\begin{aligned} B_z(x,y,z) &= B_0\cdot f(x,y)\cdot g(z) && (3.5)\\ &= B_0\cdot(1+a_2(x^2+y^2)+a_4(x^2+y^2)^2)\cdot(b_2(z-z_0)^2+1) && (3.6)\end{aligned}$$

where $B_0 = \left(\frac{\mu_0 IN}{L}\right)$, where I is the current, N the number of turns, and L the length of the coil. The distribution is composed of two parts. The first term is a transverse profile with $a_2 = 94.267$ T/m^2 and $a_4 = -5.209\cdot 10^5$ T/m^4. This transverse profile guarantees a variation of 0.4% of B$_z$ from the centre of the cell to the edge of the cell on the z-axis, in agreement with reported DC magnetic-field measurements performed on a vapour-cell Rb clock [114]. The second term is a longitudinal quadratic profile with $b_2 = 113.42$ T/m^2 and $z_0 = L_{\text{cell}}/2$. This longitudinal profile guarantees a DC field inhomogeneity of about 1.92 % over the entire vapour cell [3], in agreement with the measurement reported for our POP-DR Rb clock prototype performed by Gharavipour in his thesis [31]. Figure 3.10 presents the CFCF, considering the local frequency shift $\Delta\nu_{2^{nd}\text{-order Zeeman}}(x,y,z)$. The two cases correspond to a B_z inhomogeneity of 1.92 % and 3.45 % over the entire vapour cell.

When applying the two comparison points on the simulated CFCF, one obtains, in the case of a C-field total inhomogeneity of 1.92 %, a frequency difference $\Delta f^{\pi-0}_{\text{CFCF}} = -0.07$ Hz and a sensitivity coefficient $\partial\nu_{\text{CFCF}}/\partial\theta_n = -4.3\cdot 10^{-14}$/%. In the case of a C-field total inhomogeneity of 3.45 %, one obtains a frequency difference $\Delta f^{\pi-0}_{\text{CFCF}} = -0.15$ Hz and a sensitivity coefficient $\partial\nu_{\text{CFCF}}/\partial\theta_n = -9.1\cdot 10^{-14}$/%. The value of these two comparisons points is one order of magnitude lower than the one extracted from the experimental data. Therefore, the C-field inhomogeneity in addition to the

---

[3] In this study, the global value of the inhomogeneity over the entire vapour cell is estimated as $\frac{\max(B_z(x,y,z))-\min(B_z(x,y,z))}{\text{mean}(B_z(x,y,z))}$

microwave field inhomogeneity cannot be the origin of the observed microwave power shift of our POP-DR Rb clock prototype.

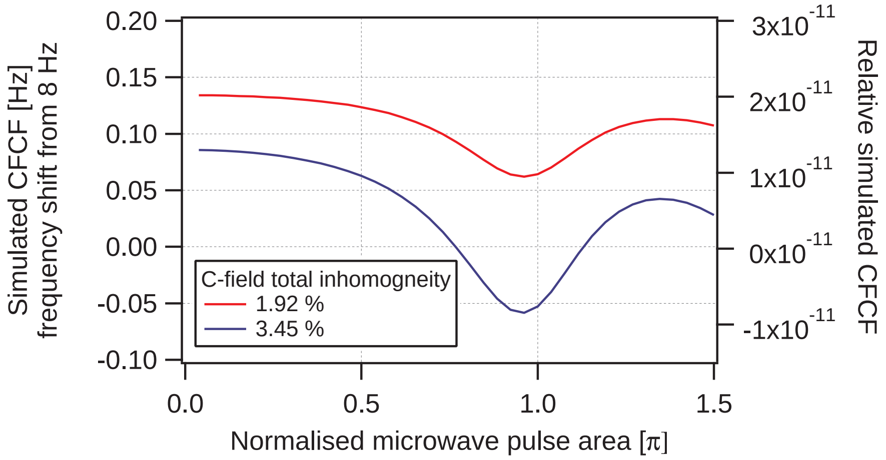

Figure 3.10 – *Simulated central fringe central frequency as a function of the normalized microwave pulse area θ_n taking into acount a spatial distribution of the 2^{nd}-order Zeeman shift.*

Cavity-pulling shift

The frequency shift induced by the cavity-pulling is given by equation 1.84. The distribution of the cavity-pulling shift follows the distribution of the microwave-field amplitude in the cavity. One obtains (see equation 1.84):

$$\Delta\nu_{\text{cavity-pulling}}(x,y,z) = -\frac{4}{\pi}\frac{Q_L}{Q_a}\Delta\nu_{\text{cav}}\ln\left[\cosh(A(T_R)) - \text{sgn}(\Delta_i)\cos\big(\theta(x,y,z)\big)\sinh(A(T_R))\right]. \quad (3.7)$$

For simplicity, only a spatial inhomogeneity of θ is considered and Δ_i is assumed homogeneous. Figure 3.11 presents the CFCF considering the local frequency shift $\Delta\nu_{\text{cavity-pulling}}(x,y,z)$. The three cases correspond to hypothetical cavity frequency detuning $\Delta\nu_{\text{cav}}$ of 1.2 MHz (the most probable case), 12 MHz, and a massively detuned cavity by 120 MHz.

When applying the two comparisons points to the simulated CFCF, one obtains, in the case of (1) a cavity frequency detuning $\Delta\nu_{\text{cav}}$=1.2 MHz: a frequency difference $\Delta f^{\pi-0}_{\text{CFCF}} < 0.01$ Hz and a sensitivity coefficient $\partial\nu_{\text{CFCF}}/\partial\theta_n = -5.5\cdot10^{-15}/\%$ (2) a cavity frequency detuning $\Delta\nu_{\text{cav}}$=12 MHz: a frequency difference $\Delta f^{\pi-0}_{\text{CFCF}} = -0.04$ Hz and a sensitivity coefficient $\partial\nu_{\text{CFCF}}/\partial\theta_n = -5.5\cdot10^{-14}/\%$ (3) a cavity frequency detuning $\Delta\nu_{\text{cav}}$=120 MHz: a frequency difference $\Delta f^{\pi-0}_{\text{CFCF}} = -0.4$ Hz and a sensitivity coefficient $\partial\nu_{\text{CFCF}}/\partial\theta_n = -5.5\cdot10^{-13}/\%$. In these three cases, the frequency difference $\Delta f^{\pi-0}_{\text{CFCF}}$ is smaller than the value obtained from the experimental data. However, in the case of $\Delta\nu_{\text{cav}}$=120 MHz, the simulated sensitivity coefficient is of the order of magnitude of the experimental sensitivity coefficient measured for F=2. However, the case $\Delta\nu_{\text{cav}}$=120 MHz is not representative of the reality because our microwave-cavity detuning is measured at about 1.2 MHz.

Therefore, the cavity-pulling shift inhomogeneity in addition to the microwave field inhomogeneity cannot be the origin of the observed microwave power shift of our POP-DR Rb clock prototype.

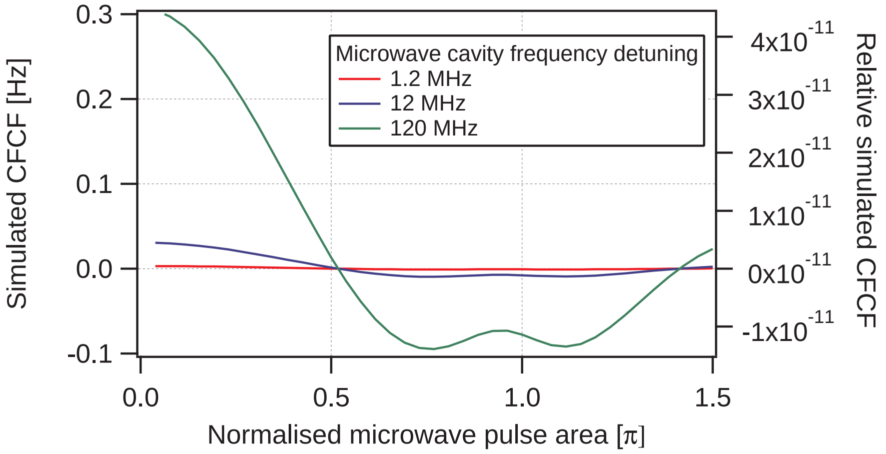

Figure 3.11 – *Simulated central fringe central frequency as a function of the normalized microwave pulse area θ_n taking into acount a spatial distribution of the cavity-pulling shift.*

Temperature gradient

Another source of frequency shift is the density-shift gradient induced by a potential temperature gradient across the vapour cell. In our POP-DR Rb clock prototype, the temperature gradient is suspected of coming from two sources. The first source is the temperature difference between the stem volume and the cell volume. The second source is the difference between the local temperature around the heater and temperature control NTC and the rest of the volume. In order to simplify the discussion, a linear longitudinal temperature profile along the z-axis is assumed. The induced density-shift profile is then given by:

$$\begin{aligned} \Delta\nu_{\text{density}}(x,y,z) &= c_T + b_T\cdot(T(x,y,z)-T_0) + a_T\cdot(T(x,y,z)-T_0)^2 && (3.8)\\ T(x,y,z) &= T_0 + \Delta T\cdot(z/L_{cell}-0.5), && (3.9)\end{aligned}$$

where $c_T = 4255.194$ Hz, $b_T = 0.132$ Hz/K, $a_T = -0.0249$ Hz/K^2 and $T_0 = 62.65$ K is the inversion temperature (see section 3.4.1). ΔT is the temperature gradient across the vapour cell. As the exact temperature gradient in our POP-DR Rb clock cell is unknown, a wide range of temperature gradients is considered : $\Delta T = 1$ K, $\Delta T = 5$ K, and $\Delta T = 10$ K. These temperatures gradients are rather over-estimated values.

Figure 3.12 presents the simulated CFCF considering the local frequency shift $\Delta\nu_{\text{density}}(x,y,z)$ in the three cases of temperature gradient. The simulated CFCF is, in the case of (1) a temperature gradient $\Delta T = 1$ K: a frequency difference $\Delta f^{0-\pi}_{\text{CFCF}} = 0.03$ Hz and a sensitivity coefficient $\partial\nu_{\text{CFCF}}/\partial\theta_n = 1.1\cdot10^{-14}/\%$ (2) a temperature gradient $\Delta T = 5$ K: a frequency difference $\Delta f^{0-\pi}_{\text{CFCF}} = 0.10$ Hz and a sensitivity coefficient $\partial\nu_{\text{CFCF}}/\partial\theta_n = 2.67\cdot10^{-14}/\%$ (3) a temperature gradient $\Delta T = 10$ K: a frequency difference $\Delta f^{0-\pi}_{\text{CFCF}} = 0.13$ Hz and a sensitivity coefficient $\partial\nu_{\text{CFCF}}/\partial\theta_n = -8.8\cdot10^{-15}/\%$. The value of these two comparisons points is one order of magnitude lower than the one extracted from the experimental data.

Therefore, realistic temperature gradients across the cell in addition to the microwave field inhomogeneity cannot be the origin of the observed microwave power shift of our POP-DR Rb clock prototype.

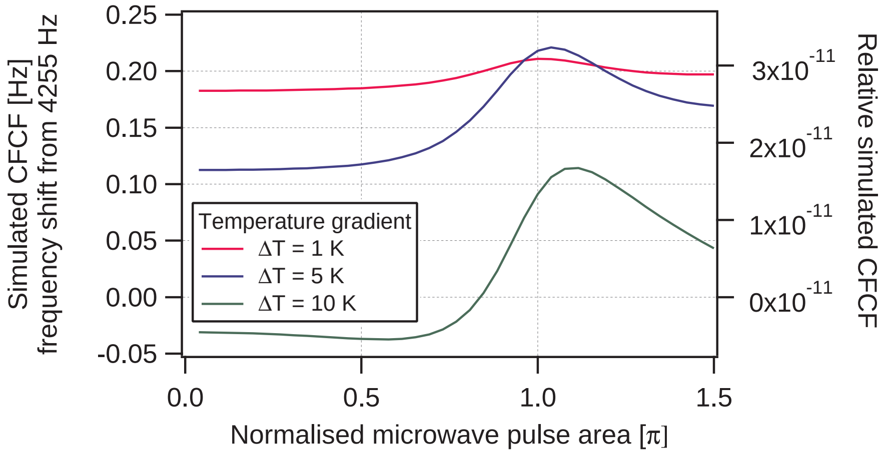

Figure 3.12 – *Simulated central fringe central frequency as a function of the normalized microwave pulse area θ_n taking into acount a spatial distribution of the density shift.*

Residual light shift

As previously mentioned, earlier studies have demonstrated that a residual LS is present in our POP-DR Rb clock prototype [31]. This residual LS is a consequence of AOM-LH leakage light during the Ramsey interrogation, which shifts the ground-state frequency resonance due to the AC-Stark shift. Typical leakage optical power measured in front of the PP is 0.6 μW. The propagation of this light through the vapour cell is inhomogeneous. The transverse profile is assumed to be described by a Gaussian profile, and the longitudinal profile follows the Beer-Lambert law. It follows:

$$I_{\text{leakage}}(x,y,z) = I_0 \cdot e^{-2(x^2+y^2)/w(z)^2} \cdot e^{-L_{\text{cell}}\cdot\sigma_{i3}n_0\rho_{ii}(z)}, \tag{3.10}$$

with $w(z) = w_0\sqrt{1+(z/z_r)^2}$ [4], $w_0 = R_{\text{cell}}$ [69] and $z_r = \pi w_0^2/\lambda$ where $\lambda = 780.24$ nm. The ground-state resonant-frequency shift distribution is then given by:

$$\Delta\nu_{\text{LS}}(x,y,z) = \alpha_{\text{AC-Stark}} \cdot I_{\text{leakage}}(x,y,z). \tag{3.11}$$

with $\alpha_{\text{AC-Stark}}$ is the AC-Stark α-LS coefficient. As the exact light profile of the residual light inside the vapour cell is unknown, three different beam profiles are considered : $w_0 = R_{\text{cell}}$, $w_0 = 5R_{\text{cell}}$, and $w_0 = 10R_{\text{cell}}$.

Figure 3.13 presents the simulated CFCF, taking into account the local frequency shift $\Delta\nu_{\text{LS}}(x,y,z)$ in the case of $\alpha_{\text{AC-Stark}} = -13.43$ Hz mm/μW (CO10-11) and three different beam profiles. The simulated CFCF is, in the case of (1) a beam profile $w_0 = R_{\text{cell}}$: a frequency difference $\Delta f^{0-\pi}_{\text{CFCF}} < 0.01$ Hz and a sensitivity coefficient $\partial\nu_{\text{CFCF}}/\partial\theta_n = -2.2\cdot10^{-16}/\%$ (2) a beam profile $w_0 = 5R_{\text{cell}}$: a frequency difference $\Delta f^{0-\pi}_{\text{CFCF}} < 0.01$ Hz and a sensitivity coefficient $\partial\nu_{\text{CFCF}}/\partial\theta_n = 8.9\cdot10^{-16}/\%$ (3) a beam profile $w_0 = 10R_{\text{cell}}$: a frequency difference $\Delta f^{0-\pi}_{\text{CFCF}} < 0.01$ Hz and a sensitivity coefficient $\partial\nu_{\text{CFCF}}/\partial\theta_n = 9.6\cdot10^{-16}/\%$. The value of these two comparisons points is two orders of magnitude lower than the one extracted from the experimental data.

Therefore, the residual light shift in addition to the microwave field inhomogeneity cannot be the

---

[4] where $w(z)$ is the beam radius defined as the distance from the beam axis where the intensity drops by a ratio of $1/e^2$ from the maximal value [69].

origin of the observed microwave power shift of our POP-DR Rb clock prototype.

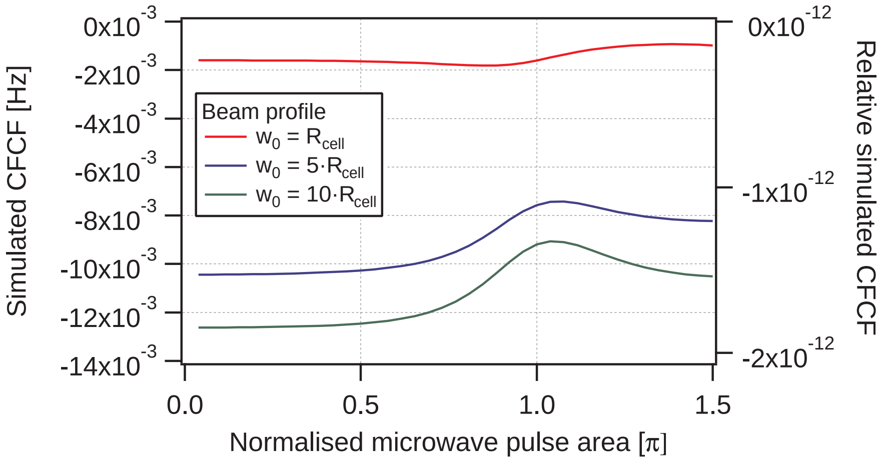

Figure 3.13 – *Simulated central fringe central frequency as a function of the normalized microwave pulse area θ_n taking into acount a spatial distribution of the residual AC-Stark shift.*

Residual coherence

Finally, a residual coherence at the beginning of the Ramsey interrogation gives rise to a frequency shift of the Ramsey spectrum (see section 1.4.5.5). The origin of the residual coherence at the beginning of the microwave interaction is due to an incomplete optical pumping that does not suppress all the coherence present at the beginning of the pump pulse. The residual coherence inhomogeneity results from the inhomogeneity of the pumping optical light during the pump pulse. The coherence at the end of the pump pulse is given by equation (1.36):

$$\delta_{12}(t_p) \quad = \quad \delta_{12}(t=0)e^{-\left(\gamma_2+\frac{\Gamma_p(x,y,z)}{1+\delta_0^2}\right)t_p} e^{i\left(\frac{\Gamma_p(x,y,z)\delta_0}{1+\delta_0^2}\right)t_p}. \tag{3.12}$$

In the analysis, the inhomogeneity of the pumping optical light induces an inhomogeneity in the pumping rate Γ_p(x,y,z) and the initial coherence $\delta_{12}(t=0)$. However, in order to solve the problem of the residual coherence correctly, one has to solve two problems: (1) the time and space evolution of the pumping rate Γ_p(x,y,z) that obeys the Maxwell equations [88][66] and (2) the initial coherence $\delta_{12}(t=0)$ on the number of previous cycles. In order to avoid solving several coupled equations in space and in time, an empirical frequency distribution that mimics the residual coherence is proposed. As illustrated in Figure 1.15a, only the imaginary part of equation (3.12) will induce a frequency shift. Based on this observation, one has:

$$\Delta\nu_{\text{res. coh.}}(x,y,z) = d_1 \cdot e^{-\left(\gamma_2+\frac{\Gamma_p(x,y,z)}{1+\delta_0^2}\right)t_p} \cdot \sin\left(\frac{\Gamma_p(x,y,z)\delta_0}{1+\delta_0^2} \cdot t_p\right), \tag{3.13}$$

where $d_1 = -18.75$ is an empirical constant. As previously mentioned, $\Gamma_p(x,y,z)$ is the optical pumping rate, and it can be defined as $\Gamma_p(x,y,z) = 3.5 \cdot 10^3 I_{\text{pump}}(x,y,z)$ according to the analysis reported in [74]. The spatial profile of $I_{\text{pump}}(x,y,z)$ is defined according to equation 3.10 with $w_0 = 3R_{\text{cell}}$. Figure 3.14 presents the CFCF considering the local frequency shift $\Delta\nu_{\text{res. coh.}}(x,y,z)$ in three cases of laser detuning: $\Delta_L = -300$ MHz, $\Delta_L = 0$ MHz, and $\Delta_L = +100$ MHz.

The simulated CFCF is, in the case of (1) a laser detuning $\Delta_L = 100$ MHz: a frequency difference $\Delta f^{0-\pi}_{\mathrm{CFCF}} = -0.69$ Hz and a sensitivity coefficient $\partial \nu_{\mathrm{CFCF}}/\partial\theta_n = -4.8 \cdot 10^{-13}/\%$ (2) a laser detuning $\Delta_L = 0$ MHz: a frequency difference $\Delta f^{0-\pi}_{\mathrm{CFCF}} = 0$ Hz and a sensitivity coefficient $\partial \nu_{\mathrm{CFCF}}/\partial\theta_n = 0/\%$ (3) a laser detuning $\Delta_L = -300$ MHz: a frequency difference $\Delta f^{0-\pi}_{\mathrm{CFCF}} = 1.34$ Hz and a sensitivity coefficient $\partial \nu_{\mathrm{CFCF}}/\partial\theta_n = 9.2 \cdot 10^{-13}/\%$. In the latter case ($\Delta_L = -300$ MHz), good agreement with the experimental data for F=1 was found.

Therefore, the shift distribution 3.12 in addition to the microwave field inhomogeneity can reproduce and explain the experimental microwave power sensitivity of our POP-DR Rb clock prototype in the case of F = 1 and $\Delta_L = -300$ MHz.

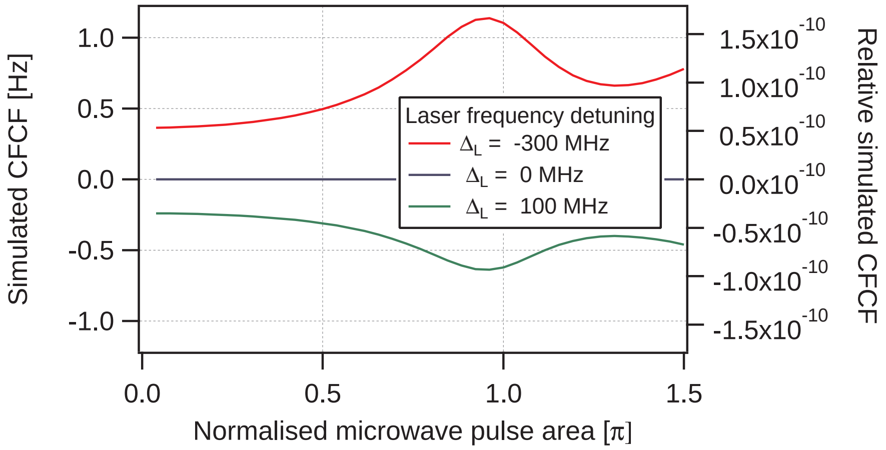

Figure 3.14 – *Simulated central fringe central frequency as a function of the normalized microwave pulse area θ_n taking into acount a spatial distribution of $\Delta\nu_{res.\ coh.}(x,y,z)$. Figure adapted from [117].*

3.1.2.7 Discussion on the simulation results

The MPS of the CFCF can be numerically reproduced by considering two inhomogeneities: Rb ground-state resonant-frequency shift distribution and microwave-field amplitude distribution. Since the output Ramsey spectrum is an average of the Ramsey spectrum generated from each group of atoms in the vapour cell,each group of atoms contributes depending on the microwave pulses that they undergo. However, for a homogeneous resonance frequency shift distribution, each group of atoms contributes with a different weight but with the same frequency shift, which explains the absence of MPS in the CFCF. In the case of an inhomogeneous resonant-frequency shift distribution, the inhomogeneous microwave field weights these various local shifts. When changing the microwave power ($\theta = b \cdot t_m \propto \sqrt{P_{\mu W}} \cdot t_m$), the weight distribution changes, which gives rise to the MPS of the CFCF.

In this study, different ground-state resonant-frequency shift distributions were considered. The comparison between the numerical calculation and the experiment focuses on the form of a curve with two aspects: $\Delta f^{0-\pi}_{\mathrm{CFCF}}$ and the sensitivity coefficient obtained at $\pi/2$. Table 3.5 summarises the two comparisons points, P1 and P2, evaluated for each simulation result based on different ground-state resonant-frequency shift distributions. Based on Table 3.5 and the general shape of the simulated CFCF, the case considering a frequency shift inhomogeneity induced by the residual coherence with a laser detuning of $\Delta_L = -300$ MHz reproduced the most the experimental data, whereas the other position shifts give negligible contributions.

Inhomogeneity	Parameter	$\Delta f^{\pi-0}_{\text{CFCF}}$	$\partial \nu_{\text{CFCF}} / \partial \theta_n \big\|_{\pi/2}$
2^{nd}-order Zeeman shift	C-field total inhomogeneity of 1.92 %	-0.07 Hz	-4.23 $\cdot 10^{-14}$/%
	C-field total inhomogeneity of 3.45 %	-0.15 Hz	-9.1 $\cdot 10^{-14}$/%
Cavity-pulling shift	$\Delta\nu_{\text{cav}}$=1.2 MHz	<0.01 Hz	-5.5 $\cdot 10^{-15}$/%
	$\Delta\nu_{\text{cav}}$=12 MHz	-0.04 Hz	-5.5 $\cdot 10^{-14}$/%
	$\Delta\nu_{\text{cav}}$=120 MHz	-0.39 Hz	-5.5 $\cdot 10^{-13}$/%
Temperature gradient	$\Delta T = 1$ K	+0.03 Hz	1.1 $\cdot 10^{-14}$/%
	$\Delta T = 5$ K	+0.10 Hz	2.67 $\cdot 10^{-14}$/%
	$\Delta T = 10$ K	+0.13 Hz	-8.8 $\cdot 10^{-15}$/%
Residual light-shift	beam profile $w_0 = R_{\text{cell}}$	<0.01 Hz	-2.2 $\cdot 10^{-16}$/%
	beam profile $w_0 = 5R_{\text{cell}}$	<0.01 Hz	8.9 $\cdot 10^{-16}$/%
	beam profile $w_0 = 10R_{\text{cell}}$	<0.01 Hz	9.6 $\cdot 10^{-16}$/%
Residual coherence	laser detuning $\Delta_L = 100$ MHz	-0.69 Hz	-4.8 $\cdot 10^{-13}$/%
	laser detuning $\Delta_L = 0$ MHz	0 Hz	0 /%
	laser detuning $\Delta_L = -300$ MHz	1.34 Hz	9.2 $\cdot 10^{-13}$/%
Experiment (Figure 3.1)	F=1	+1.34 Hz	9 $\cdot 10^{-13}$/%
	F=2	+0.7 Hz	-6 $\cdot 10^{-13}$/%

Table 3.5 – *Comparison between the simulated CFCF obtained considering different ground-state resonant frequency shift distributions and the microwave field amplitude inhomongeneity. The comparison is based on the comparison points P1 and P2 of section 3.1.2.6.*

Moreover, the frequency distribution given by the residual coherence (equation 3.13) can be determined more exactly. Indeed, based on equation 1.36 in Chapter 1, the impact of the pump pulse on the Bloch vector can be calculated (then simulated) as well at each point of the cell mesh. It allows a more exact solution of the residual coherence at the end of the pump pulse at each point of the cell mesh to be determined. The residual coherence distribution will be mainly impacted by the distribution of the pump light in the cell. However, to reproduce more precisely what happened in the experiment, one must consider the succession of an infinite number of interrogation cycles (pump pulse plus microwave interrogation) where the microwave frequency jumps between the left and the right of the central fringe, represented in Figure 3.15. It corresponds to the square modulation amplitude of the clock stabilisation loop, which is ± 80 Hz in our clock prototype. This approach consists of a potential next step towards a more exact determination of the CFCF microwave sensitivity.

Another approach would be to repeat the calculation performed by Micalizio et al. [88], where the complete set of coupled differential equations describing the time evolution of the density matrix (equations 1.33 in Chapter 1) are solved numerically simultaneously. Moreover, Micalizio et al. considered the Zeeman structure of the two ground-state levels, which could be interesting in our case because it could be the origin of the different shapes of the experimental MPS obtained for

F=1 and F=2.

Finally, the analysis performed in this section aims to evaluate only the impact of the inhomogeneity of the microwave-field amplitude and the Rb ground-state resonant-frequency shift. However, the exact description of the Rb ground-state resonant-frequency shift distribution is not possible using the approach of this study. Indeed, certain physical parameters are considered homogeneous over the vapour cell as γ_1, γ_2, Γ^*, etc., which is not fully correct. A possibly more complete approach is provided by Mesoscopic physics [118].

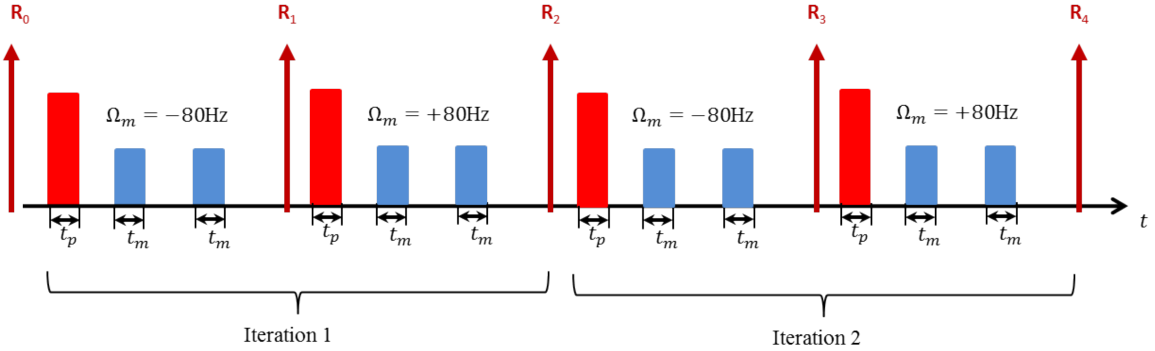

Figure 3.15 – *Proposition of timing sequence for evaluating the impact of the residual coherence. Each iteration is composed of two interrogation cycles where each interrogation cycle is composed by a pump pulse (red rectangle) and the microwave interrogation (blue rectangle). Red vectors R_i are the Bloch vector at the end of one cycle and are used as initial vector for the following new cycle.*

3.1.3 Conclusion

The experimental data in Figure 3.1 shows that a clock operation point exists that reduces the microwave-power sensitivity coefficient in our POP-DR Rb clock. This occurs when the laser frequency is tuned on the CO21-23 transition and for $b \cdot t_m = 0.57 \cdot \pi$ microwave pulse. In this condition, we measure an MPS coefficient at the level of $2 \cdot 10^{-13}/\mu$W, which is one order of magnitude lower than the previously reported coefficient [86]. Considering a microwave-power fluctuation ≤ 0.01% at 20 μW (see Figure 2.13), the clock instability arising from the MPS of our clock prototype is estimated at the level of $4 \cdot 10^{-16}$ at 10^4 s of integration time.

Based on the position-shift effect, the experimental MPS for F=1 is reproduced by considering two inhomogeneities: Rb ground-state resonant-frequency shift distribution and microwave-field amplitude distribution. However, the exact description of the Rb ground-state resonant-frequency shift distribution is not possible using the approach of this study because the calculations are based on simple frequency shift along the vapour cell where most of the distribution is based on empiric parameters and due to the limitation from the simple 3-level model considered in our numerical model. Another important source of limitation comes from the approximation of the impact of the residual coherence on the CFCF frequency. A more exact approach would be to calculate the evolution of the Bloch vector through the pump pulse and repeating the POP scheme over several iterations.

Nevertheless, the simple three-level models of section 1.3, combined with the microwave-field amplitude distribution of our microwave cavity, can reproduce the Rabi oscillation as well as the FWHM of the central Ramsey fringe. Moreover, we would be able to see that the microwave sensitivity of the CFCF does not result from the cavity-pulling shift but more likely from the presence of the ground-sate frequency shift combined with microwave-field amplitude inhomogeneities.

3.2 Light-induced shift studies

A light-shift (LS) effect is a physical effect that describes the frequency shifts of the atomic levels induced by virtual transitions (AC-Stark shifts) [87]. The consequence of the LS effect is a frequency shift of the clock frequency as a function of the light properties (e.g. frequency, intensity). In a DR-CW atomic clock, the AC-Stark shift [85] is the dominant source of LS because the light field and the microwave field are applied simultaneously. However, in a POP operation, the light and the microwave field are separate in time, which strongly reduces the light during the microwave interaction. However, previous studies on our POP-DR Rb clock prototype performed by Gharavipour in his thesis [31] have demonstrated that a residual light is present. The residual light originates from the AOM-LH; it corresponds to the light passing through the AOM when it is switched off. The presence of residual light during the Ramsey time induces an AC-Stark shift. The same study [31] demonstrated that the α-LS coefficient calculated using the AC-Stark shift theory agrees with the measured α-LS coefficients. However, the study does not explain the opposite sign between the measured frequency LS coefficients (β-LS) and the predicted AC-Stark frequency LS coefficients. Moreover, the study does not address a potential LS induced by the pump light and the detection light.

In the present study, the LS in our POP-DR Rb clock prototype is completed by other light-induced shifts (LIS): the LIS is decomposed into contributions arising separately during the pump pulse, the detection pulse, and the Ramsey time. In this section, four LISs are considered:

- *global LIS* refers to intensity and frequency LIS measurements when the light intensity is varied during the whole POP scheme with the same ratio.
- *pump LIS* refers to intensity and frequency LIS measurements when only the pump light intensity is varied.
- *detection LIS* refers to intensity and frequency LIS measurements when only the detection light intensity is varied.
- *residual LS* refers to intensity and frequency LSs arising from the residual light during the Ramsey scheme as described by [31].

In addition to the AC-Stark shift, the residual coherence at the end of the optical pump pulse significantly limits the performances of our clock. Finally, the origins of these separated LIS are discussed.

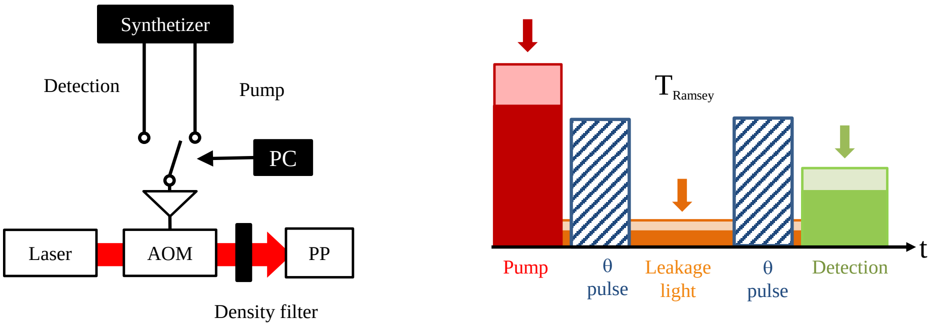

Figure 3.16 – *Global light-induced shift measurement scheme. Left: the light intensity is varied during the entire scheme by the used of a density filter at the entrance of the PP. Right: the light intensity is changed with the same ratio during the entier scheme.*

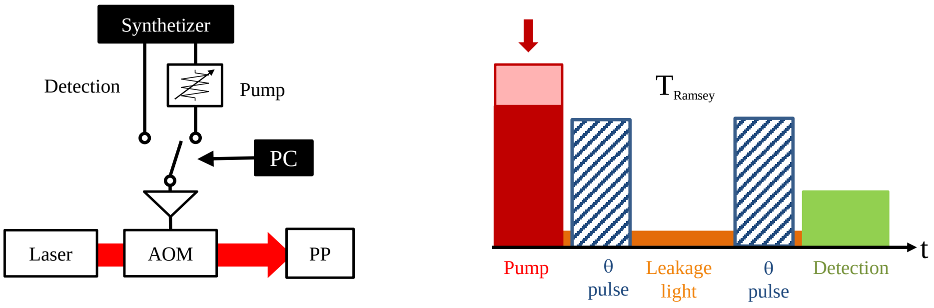

Figure 3.17 – *Pump light-induced shift measurement scheme. Left: the light intensity is varied during the pump pulse by the used of a variable attenuator at ouptut of the synthesizer. Right: the light intensity is changed only during the pump pulse.*

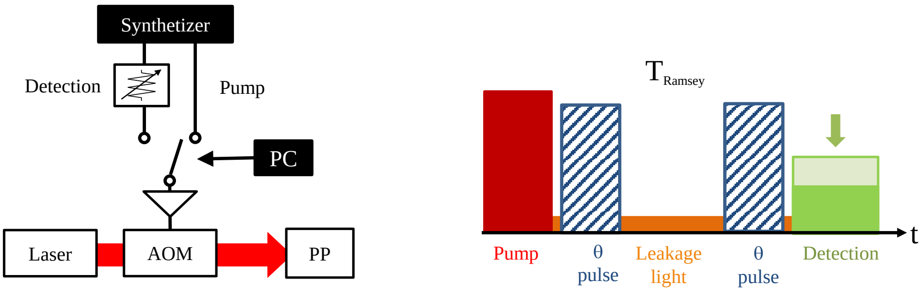

Figure 3.18 – *Detection light-induced shift measurement scheme. Left: the light intensity is varied during the detection pulse by the used of a variable attenuator at ouptut of the synthesizer. Right: the light intensity is changed only during the detection pulse.*

3.2.1 Light-induced shift measurement

The global LIS coefficients (α_{global},β_{global}) are obtained by measuring the clock frequency shift when the laser optical power is varied during the entire scheme (see Figure 3.16). The light intensity is varied using an optical density filter situated in front of the PP, see Figure 3.16. It guarantees that the pump, detection, and residual light are varied with the same relative percentage. The measurement is repeated when the AOM-LH is frequency stabilised on the six sub-Doppler transitions (see Table 1.1 for the spectroscopy notations). The measurements are performed for a pump pulse duration of 0.4 ms, a detection pulse duration of 0.7 ms, and for two $\pi/2$ microwave pulses durations of 0.4 ms. Figure 3.19 presents the results. The α_{global} and β_{global} coefficients are shown in Table 3.6 and Table 3.7, respectively. The intensity LIS coefficients are determined from a linear fit at $P_{\text{pump}} = 11$ mW. The frequency LIS coefficients are determined using equation (1.88) from Figure 3.19 where, for a fixed intensity, the clock frequency shifts are given for six laser frequencies and use the known optical-frequency difference between these transitions. It results in a β-LIS coefficient determined for F=1 or F=2 (see Table 3.7).

The α_{global} coefficient is lowest when the AOM-LH is frequency stabilised on CO21-23 where $\alpha_{\text{global}} \leq 3 \cdot 10^{-14}/\%$. For a relative intensity fluctuation $\leq 0.3\%$ (see Figure 2.6b), the estimated impact of the LIS on the medium- to long-term frequency stability of our Rb clock prototype is $\leq 9 \cdot 10^{-15}$, in agreement with previously reported values [31].

The pump and detection intensity LIS coefficients α_{pump} and $\alpha_{\text{detection}}$, respectively, are measured by varying only the pump or the detection optical power. The optical power is varied during the pump or the detection pulse, acting on the RF power sent to the AOM-LH using a variable attenuator, as shown in Figure 3.17 and Figure 3.18. In the standard configuration, the RF power sent to the AOM is $P \approx 1$ W during the pump pulse and $P \approx 0.035$ W during the detection pulse. The RF frequency is 75 MHz; however, we use the negative second-order output beam optically shifted by $-2 \cdot 75$ MHz.

Figure 3.20 presents the pump LIS measurement, and Figure 3.21 presents the detection LIS measurement. The intensity LIS coefficients α_{pump} and $\alpha_{\text{detection}}$ are determined from a linear fit at $P_{\text{pump}} = 11$ mW and $P_{\text{det}} = 93.5\mu$W, respectively. These coefficients are shown in Table 3.6. With our measurement setup, it is not possible to measure the frequency LIS coefficients β_{pump} and $\beta_{\text{detection}}$ because the laser frequency cannot be varied during a specific optical pulse. However, we can extract the global β-LS coefficients from these measurements. The global β-LS coefficients are determined from Figure 3.20 and Figure 3.21 using equation 1.88 (see Table 3.7). The frequency LIS coefficients are determined at $P_{\text{pump}} = 11$ mW and $P_{\text{det}} = 93.5\mu$W. As expected, the frequency LIS coefficients of Table 3.7 agree with one another, considering the error bars.

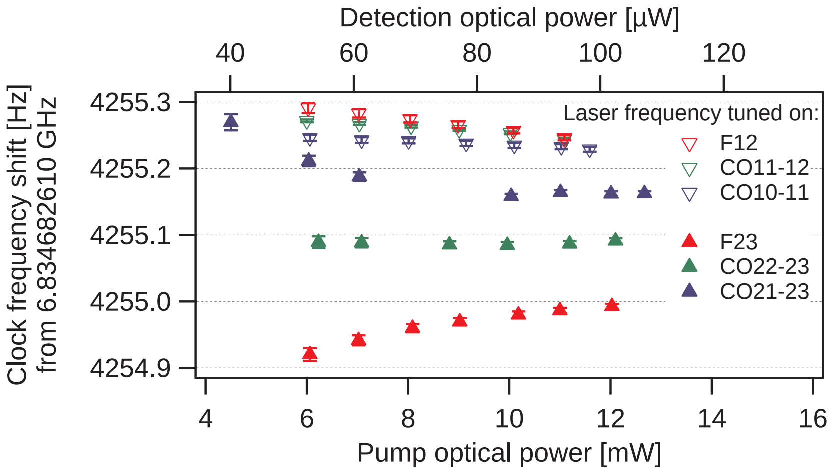

Figure 3.19 – *Global intensity light-shift measurements.*

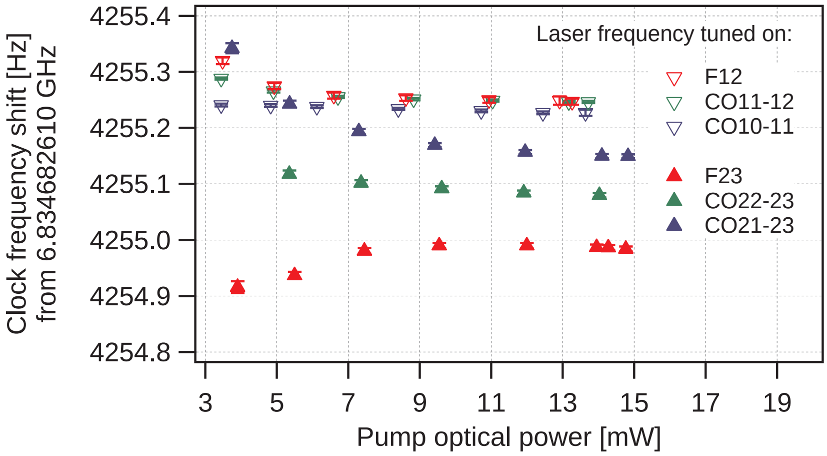

Figure 3.20 – *Pump intensity light-shift measurements. Figure adapted from [119].*

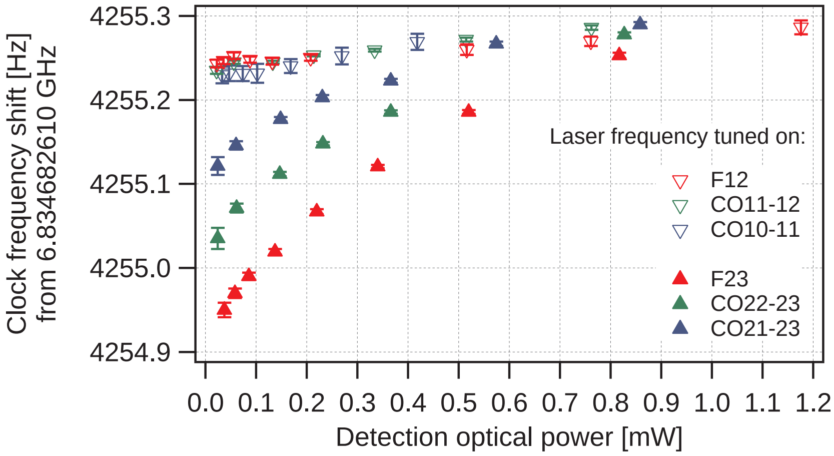

Figure 3.21 – *Detection intensity light-shift measurements. Figure adapted from [105].*

Laser frequency tuned on	$\alpha_{\text{global}}\left[\frac{1}{\%}\right]$ from Figure 3.19	$\alpha_{\text{pump}}\left[\frac{1}{\%}\right]$ from Figure 3.20	$\alpha_{\text{detection}}\left[\frac{1}{\%}\right]$ from Figure 3.21
F12	$(-1.4 \pm 0.2) \cdot 10^{-13}$	$(-2.1 \pm 2.4) \cdot 10^{-14}$	$\leq 0.7 \cdot 10^{-14}$
CO11-12	$(-8.5 \pm 0.8) \cdot 10^{-14}$	$(-1.8 \pm 0.9) \cdot 10^{-13}$	$(0.5 \pm 0.4) \cdot 10^{-14}$
CO10-11	$(-4.8 \pm 1.3) \cdot 10^{-14}$	$(-2.6 \pm 1.2) \cdot 10^{-14}$	$(1.1 \pm 1.2) \cdot 10^{-14}$
F23	$(1.2 \pm 0.4) \cdot 10^{-13}$	$(-2.3 \pm 1.9) \cdot 10^{-13}$	$(8.8 \pm 0.9) \cdot 10^{-14}$
CO22-23	$(4.7 \pm 1.7) \cdot 10^{-14}$	$(-5.3 \pm 1.4) \cdot 10^{-13}$	$(7.1 \pm 0.9) \cdot 10^{-14}$
CO21-23	$\leq 2.9 \cdot 10^{-14}$	$(-8.5 \pm 1.1) \cdot 10^{-13}$	$(5.3 \pm 0.8) \cdot 10^{-14}$

Table 3.6 – *Intensity light-shift (ILS) coefficients determined for three cases described by Figure 3.19, Figure 3.20 and Figure 3.21. The global ILS coefficients are determined at $P_{pump} = 11$ mW and $P_{det} = 93.5$ μW, the pump ILS coefficeints are determined at 11 mW and the detection ILS coefficients are determined at 93.5 μW.*

Laser locked on D_2-transition from ground-state	$\beta_{\text{global}}\left[\frac{1}{\text{MHz}}\right]$ from Figure 3.19	$\beta_{\text{pump}}\left[\frac{1}{\text{MHz}}\right]$ from Figure 3.20	$\beta_{\text{detection}}\left[\frac{1}{\text{MHz}}\right]$ from Figure 3.21
F = 1	$(1.07 \pm 0.03) \cdot 10^{-14}$	$(1.6 \pm 0.6) \cdot 10^{-14}$	$(1.3 \pm 0.4) \cdot 10^{-14}$
F = 2	$(-1.3 \pm 0.1) \cdot 10^{-13}$	$(-1.2 \pm 0.1) \cdot 10^{-13}$	$(-1.1 \pm 0.2) \cdot 10^{-13}$

Table 3.7 – *Global frequency light-shift coefficients determined from Figure 3.19, Figure 3.20 and Figure 3.21.*

3.2.2 Discussion of the pump and detection light-induced shift

Figure 3.20 and Figure 3.21 show that the clock frequency is sensitive to the pump and detection light optical power. From the AC-Stark theory [85] [87], we would expect that the LIS curves converge to a single value at zero light intensity. This is not the case for the pump and detection LIS curves of Figure 3.20 and Figure 3.21 or the global LIS curves.

The intensity LIS sensitivity coefficients (see Table 3.6) measured for the optical pump pulse are generally higher than the corresponding global intensity LIS coefficients for F=2 and are at the same order of magnitude or lower for F=1. The intensity LIS sensitivity coefficient for the optical-detection pulse is generally lower than the corresponding global intensity LIS coefficients.

3.2.2.1 Discussion of the pump light-induced shift

Concerning the pump LIS, as discussed in section 1.4.5.5, the coherence in the ground state is not correctly attenuated by the optical pumping. This could be due to insufficient optical power at the entrance of the PP or the inhomogeneity of the optical power inside the vapour cell. In the same section 1.4.5.5, the imaginary part of the residual coherence at the end of the pump pulse was shown to induce a clock frequency shift. Equation 1.36 describes how the coherence at the beginning of the optical pump pulse evolves during the pump pulse. The equation is composed of two parts: (1) a damping term $\exp(-(\gamma_2 + \frac{\Gamma_{R_i}}{1+\delta_0^2}) \cdot t_p)$ and (2) a LIS term $\exp(-i(\frac{\Gamma_{R_i}\delta_0}{1+\delta_0^2}) \cdot t_p)$. The first term describes the damping of the initial coherence via optical pumping. The second term describes how the initial coherence rotates in the Bloch sphere by an angle $\frac{\Gamma_{R_i}\delta_0}{1+\delta_0^2}\cdot t_p$. Both terms depend on the duration of the pump pulse duration t_p and the optical power via the optical pumping rate Γ_R. Therefore, the imaginary part of the coherence (equation 1.36) as a function of the optical pumping rate or the pump pulse duration is similar to a damped oscillation. If the pump LIS is a consequence of the coherence at the end of the pump pulse, then the hypothesis is that the pump LIS curve reproduces the same behaviour of a damped oscillation as a function of the optical pumping rate or the pump pulse duration.

In order to confirm this observation, we measured the clock frequency as a function of the pump pulse area—the product of the optical power ($\Gamma_R \propto P_{\text{pump}}$) and the pump pulse duration t_p—by varying both P_{pump} and t_p. The pump LIS measurement was repeated for two different pump pulse durations (0.2 ms and 0.8 ms) and the clock frequency was measured as a function of the pump pulse duration for a fixed light intensity. Figure 3.22 presents the clock frequency as a function of the pump pulse area ($P_{\text{pump}}\cdot t_p$) when the AOM-LH is frequency stabilised on F23. In order to extract the behaviour of the experimental data, the data are fitted with the following fit function:

$$f(x) = e^{-a_1\cdot x}\cdot\left(A\cdot\cos(a_2\cdot x) + B\cdot\sin(a_2\cdot x)\right) + a_3\cdot x + a_4 \tag{3.14}$$

where the first term, depending on a_1 and a_2, mimics the imaginary part of equation 1.36 and the second term, depending on a_3 and a_4, is a linear term. Using this fit function for the data in Figure 3.22, one obtains (for the black fit) $a_1 = 1.43\pm0.09$ [mW^{-1} ms^{-1}], $a_2 = 1.54\pm0.12$ [mW^{-1} ms^{-1}], $A = 1.36\pm0.19$ Hz, $B = -0.26\pm0.21$ Hz, $a_3 = -(5.3\pm0.9)\cdot10^{-3}$ [mW^{-1} ms^{-1}], and $a_4 = 4255.0\pm0.0009$ Hz. With the same data, the fit function 3.14 is applied without the linear term a_3, shown by the blue line. The comparison between the two fits shows that the data can be decomposed into two parts: (1) between 0 mW · ms up to ≈ 3 mW· ms, the data behave as the first term of equation 3.14; whereas (2) between 3 mW· ms and 10 mW · ms, the data shows a linear behaviour. This suggests that two phenomena are at the origin of the pump light where at least one could be the residual coherence.

An interesting feature of the data in Figure 3.22 is the presence of two local extrema: one at 1.5 mW· ms and another at 3 mW· ms. These points can be used to reduce the pump intensity LIS coefficients using a pump pulse duration of 0.1 ms and 0.2 ms for a pump optical power of 15 mW, for example.

However, to extend our analysis of these results and to obtain a more exact numerical calculation of the pump LS, it could be interesting to consider the optical pumping pulse and the optical-detection pulse in our numerical analysis described in the previous chapter. A complete numerical calculation of the POP scheme is reported in Micalizio et al. [88], where they have solved the differential equations describing the time evolution and the spatial distribution of the density matrix (similar to equation 1.33) and the light electric field distribution.

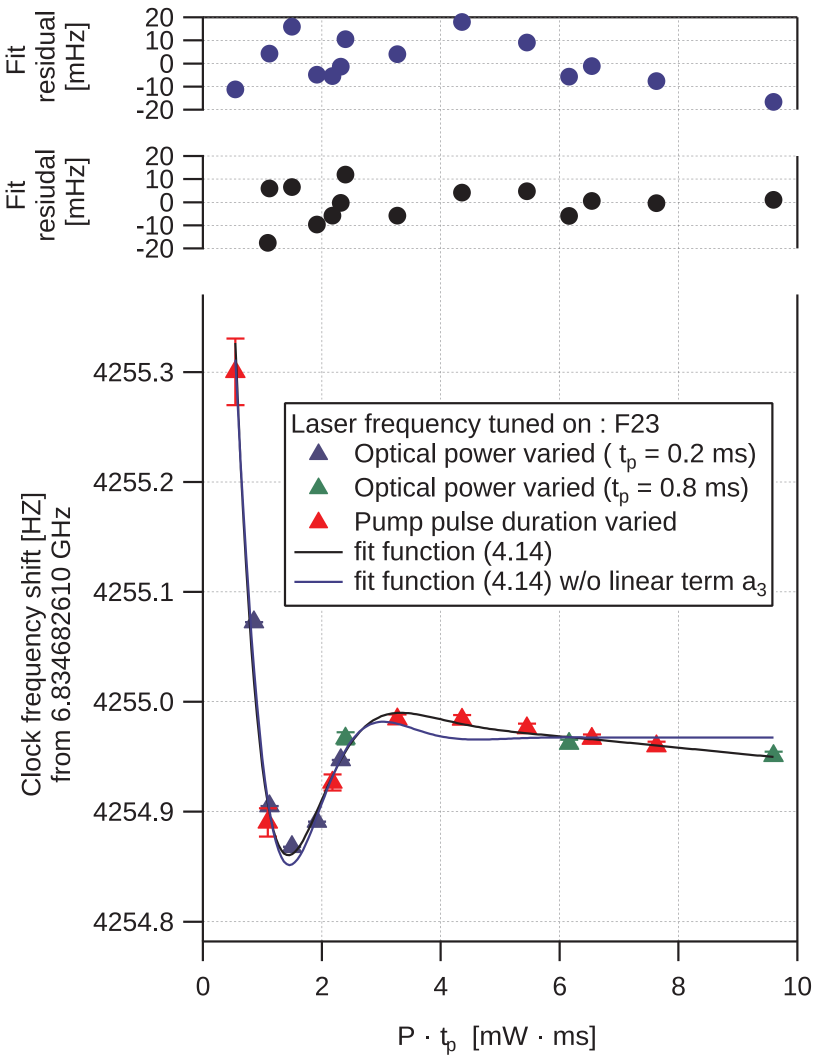

Figure 3.22 – *Pump LS. Bottom : clock frequency shift as a function of the pump pulse area. Three measurements were performed : pump optical power varied for a fixed pump pulse duration 0.2 ms (blue triange) and a pump pulse duration 0.8 ms (green triangle), fixed pump intensity 11 mW and pump pulse duration varied (red triangle). (black line) fit using the fit function 3.14 (see text for details). (blue line) fit using the fit function 3.14 without the linear term* a_3. *Top : fit residual.*

3.2.2.2 Discussion on the detection light-induced shift

The detection LIS is suspected of having two origins. The first origin is the impact of the inhomogeneity of the optical detection power inside the vapour cell. Similar to the origin of the MPS, the detection light acts as weighted average inside the vapour cell; the atoms close to the entrance of the vapour cell will contribute more to the atoms close to the cell's end. The second origin is the impact of optical pumping of the optical-detection pulse that adds to one of the pump pulses and thus has the same results illustrated in Figure 3.22.

3.2.3 Conclusion

This study demonstrates that, in addition to the residual LS effect shown by Gharavipour in his thesis [31], the global LIS is the result of at least two other phenomena: a pump LIS coming from a ground-state residual coherence and a detection LS. This study shows that the pump LIS shares similar features with the residual coherence at the end of the optical pump pulse when varying the pump pulse duration. However, the global LIS coefficients are the best coefficients for describing the clock frequency sensitivity to the laser intensity and frequency fluctuations, especially for the medium- to long-term analysis. Indeed, one can assume that during one complete POP cycle, the laser intensity and the laser frequency are constant and that these quantities do not vary significantly during one cycle but can vary over several cycles. This behaviour is reproduced correctly by our global LIS measurement, where the light intensity is varied with the same relative percentage over the entire cycle.

Considering an intensity fluctuation ≤ 0.3% (see Figure 2.6b), the intensity LIS of our clock prototype is estimated at the level of $1.5 \cdot 10^{-14}$ (for F=1) and at the level of $8.5 \cdot 10^{-15}$ (for F=2) at 10^4 s of integration time. Considering a frequency fluctuation ≤ 4 kHz (see Figure 2.6a), the frequency LIS of our clock prototype is estimated at the level of few 10^{-17} (for F=1) and at the level of few 10^{-16} (for F=2) at 10^4 s of integration time.

More generally, the LIS in a POP clock seems to be the consequence of several LIS phenomena. Two identified phenomena are the AC-Stark shift and the impact of the residual coherence at the end of the pump pulse. However, the next steps of this research involve identifying all the LIS phenomena and how the global LIS coefficients can be expressed as a function of separated LIS coefficients for each phenomenon. In parallel, it could be interesting to study how the separated LIS (pump LIS and detection LIS) change as functions of different clock parameters (pulses durations, microwave power, etc.). This study could lead to a new operation point that could minimise the impact of LSs on the clock frequency. In particular, it would be interesting to represent the global LIS as a function of the pump pulse area with the possibility to observe a local maximum as for the data of Figure 3.22.

3.3 Barometric-shift studies

In this section, the clock's sensitivity to the atmospheric pressure fluctuation is evaluated. The impact of atmospheric pressure variations on the clock's frequency—environmental pressure shifts—is the result of three mechanisms. The first mechanism is the temperature changes induced by changing conductive and convective heat flows that can modify the temperatures of all clocks parts [98], [90]. The second mechanism is the barometric effect: the external pressure variations deform the resonance cell's dimension and change the internal buffer-gas density thus changing the collision shift [98], [91]. The third mechanism is the change in the air dielectric constant that modifies the microwave-cavity resonance frequency and impacts the clock frequency through the cavity-pulling effect [92],[84].

This section focuses on the barometric effect. First, a simple model is used to estimate the clock's sensitivity to the change of the atmospheric pressure. Second, our POP-DR Rb clock is used to measure the coefficients with two types of measurement: correlation and a pressure-controlled chamber. Finally, the results are analysed and discussed.

3.3.1 Barometric effect

The frequency shift induced by the barometric effect is defined as the variation of the clock frequency due to a change in external pressure $\partial \nu_{clock}/\partial P_{out}$. Using the chain rule, the sensitivity coefficient can be written as:

$$\frac{\Delta \nu_{clock}}{\Delta P_{out}} = \frac{\Delta \nu_{clock}}{\Delta P_{BG}} \cdot \frac{\Delta P_{BG}}{\Delta P_{out}}, \tag{3.15}$$

where P_{BG} is the buffer-gas pressure and P_{out} is the pressure of the air surrounding the vapour cell. The first term of the right-hand side is the buffer-gas pressure shift $\Delta \nu_{clock}/\Delta P_{BG} \equiv \beta'$, see equation (1.77). The second term describes how internal pressure varies as a function of the external pressure. Considering the perfect gas law, the relative variation of the internal pressure equals the relative variation of the internal cell's volume V at T = const., i.e. $\Delta P_{BG}/P_{BG} = \Delta V/V$. One can therefore write:

$$\frac{\Delta \nu_{clock}}{\Delta P_{out}} = \beta' \cdot \frac{\Delta V}{V} \cdot \frac{P_{BG}}{\Delta P_{out}}. \tag{3.16}$$

The volume variation ΔV for our cylindrical cell is estimated to arise primarily from the cell's front and back windows, bending under the pressure difference across the glass [89] [120][5]. Considering clamped boundary conditions and an external pressure variation of $\Delta P_{out} = 1$ hPa, the deformation profile of the windows expressed in polar coordinates (radius r, angle θ) is given by [121]:

$$w(r,\theta) = \frac{1}{64D}(r_{cell}^2 - r^2)^2, \tag{3.17}$$

---

[5] in the case of a uniform pressure distribution around the vapour cell, the radial cell deformation is much smaller than the deformation of the cell windows. For simplicity, we consider that the volume variation is supposed to come from the cell's windows bending only. A more complete approach can be found in [91].

where r_{cell} is the cell's internal radius, D is the flexural rigidity defined as:

$$D = \left(\frac{E}{12(1-\sigma^2)}\right) \cdot t_{cell}^3 = D' \cdot t_{cell}^3, \tag{3.18}$$

where E is the glass's Young's modulus, t_{cell} the cell's window thickness, σ the Poisson's ratio, and D' a reduced rigidity depending on the cell material only. Our vapour cell is made of borosilicate glass with E = 64 kN/mm^2 = 64 $\cdot 10^8$ hPa and $\sigma = 0.2$. ΔV is obtained by integrating the deformation (3.17) over r and θ for the two cell windows:

$$\begin{aligned}
\frac{\Delta V}{V} &= \frac{2}{V}\int_0^{r_{cell}}\int_0^{2\pi} w(r,\theta)\, r dr d\theta \\
&= \frac{4\pi}{V}\cdot\frac{r_{cell}^6}{6}\cdot\frac{1}{64D} \\
&= \frac{1}{96D'}\cdot\frac{r_{cell}^4}{t_{cell}^3 l_{cell}},
\end{aligned} \tag{3.19}$$

where l_{cell} is the cell length. Based on equation (3.16), the impact of an external outside pressure change $\Delta P_{out} = 1$ hPa on the internal pressure is then given by:

$$\Delta P_{BG} = P_{BG}\cdot\frac{1}{96D'}\cdot\frac{r_{cell}^4}{t_{cell}^3 l_{cell}}. \tag{3.20}$$

Finally, the barometric coefficient is given by (using equations (3.15) and (3.20)):

$$\frac{\Delta\nu_{clock}}{\Delta P_{out}} = \beta'\cdot\frac{P_{BG}}{96D'}\cdot\frac{r_{cell}^4}{t_{cell}^3 l_{cell}}. \tag{3.21}$$

Table 3.8 presents the typical order of magnitude for ΔV, ΔP and $\frac{\Delta\nu_{clock}}{\Delta P_{out}}$ for the vapour cell presented in Chapter 3. Figure 3.23 presents the barometric coefficient given by equation (3.21) as a function of the cell dimensions and the glass's Young's modulus.

Internal cells dimensions	$\frac{\Delta V}{\Delta P_{out}}\left[\frac{\text{mm}^3}{\text{hPa}}\right]$	$\frac{\Delta P_{BG}}{\Delta P_{out}}\left[\frac{\text{hPa}}{\text{hPa}}\right]$	$\frac{\Delta\nu_{clock}}{\Delta P_{out}}\left[\frac{\text{Hz}}{\text{hPa}}\right]$	$\frac{\Delta(\nu_{clock}/\nu_0)}{\Delta P_{out}}\left[\frac{1}{\text{hPa}}\right]$
t = 1 mm, ∅ = 23 mm, l = 23 mm	$1.3\cdot10^{-3}$	$4.5\cdot10^{-6}$	$5.8\cdot10^{-4}$	$(8.5\pm2.7)\cdot10^{-14}$
t = 1 mm, ∅ = 12 mm, l = 12 mm	$2.8\cdot10^{-5}$	$6.6\cdot10^{-7}$	$8.7\cdot10^{-5}$	$(1.3\pm0.4)\cdot10^{-14}$

Table 3.8 – *Barometric effect on the vapour cell volume, the internal buffer gas pressure and the corresponding frequency clock sensitivities.*

3.3.2 Measurements

In order to highlight the barometric effect, our POP-DR Rb clock prototype is operated in conditions where all the instability contributions from other effects are of the order or below a few 10^{-14} at 10^4 s of integration time. First, operating the clock at the operating point that minimises the MPS (see section 3.1.1), the cavity-pulling shift sensitivity is reduced to $4.7\cdot10^{-17}$/hPa. Second, the clock

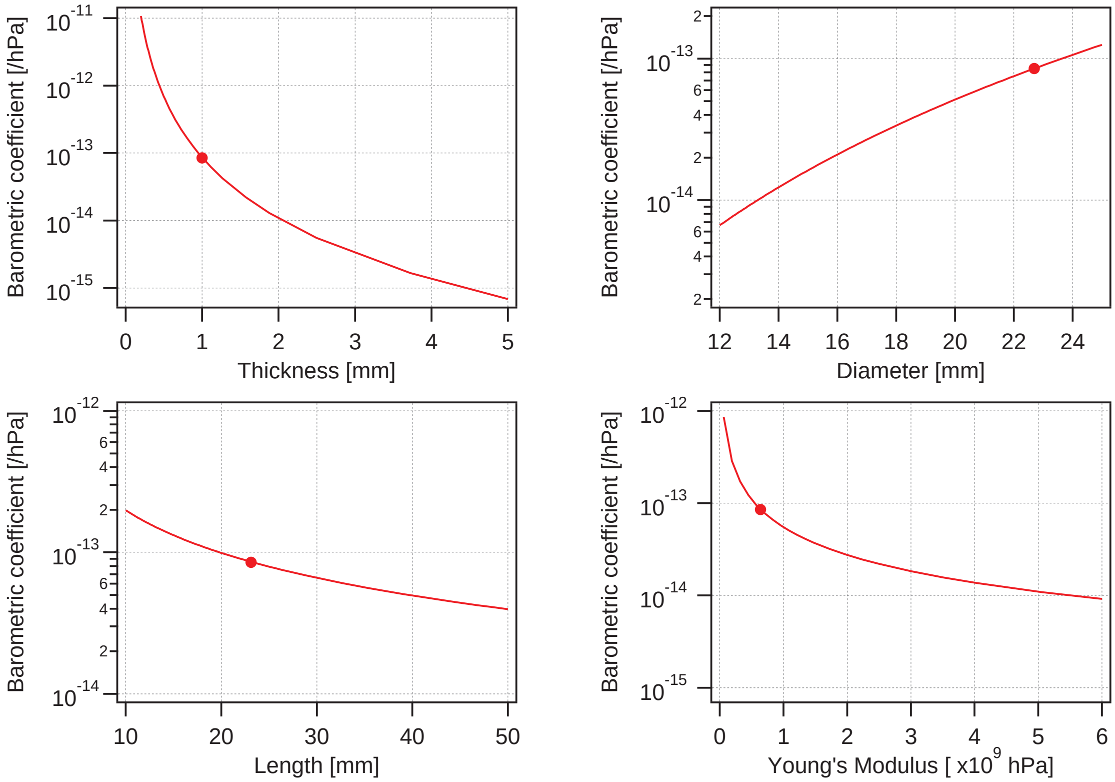

Figure 3.23 – *Barometric coefficient as a function of the cell's dimensions and Yougs modulus. The dots correspond to our cell's dimensions.*

vapour cell is operated at the temperature inversion point (see section 1.4.5.2). It guarantees that the clock frequency fluctuations due to cell-temperature changes contribute to the clock's relative frequency instabilities to 10^{-14} at 10^4 s of integration time.

3.3.2.1 Correlation measurement

The clock quartz is frequency stabilised on the central fringe of the Ramsey spectrum. The clock frequency is recorded simultaneously with the atmospheric pressure, temperature, and humidity. The atmospheric parameters are obtained from a national Swiss weather station situated close to the laboratory (longitude/latitude E6°57'/N47°00'). The duration of the measurement was 23 days. The clock frequency, the atmospheric pressure, humidity, and temperature are presented in Figure 3.24. Figure 3.24 shows a clear correlation between the atmospheric pressure and the clock frequency and does not show correlations with the atmospheric humidity or the atmospheric and laboratory temperatures. In order to extract an experimental barometric coefficient, Figure 3.25 presents the clock frequency is plotted against the atmospheric pressure. Due to the clear parallel lines in Figure 3.25, we conclude that the barometric effect is the main source of frequency instability. Moreover, multiple parallel lines are due to a clock frequency drift independent of the atmospheric pressure. The experimental barometric coefficient is obtained by a linear fit of the parallel lines in Figure 3.25, and an average experimental barometric coefficient of $(8.2 \pm 0.8) \cdot 10^{-14}$/hPa is obtained.

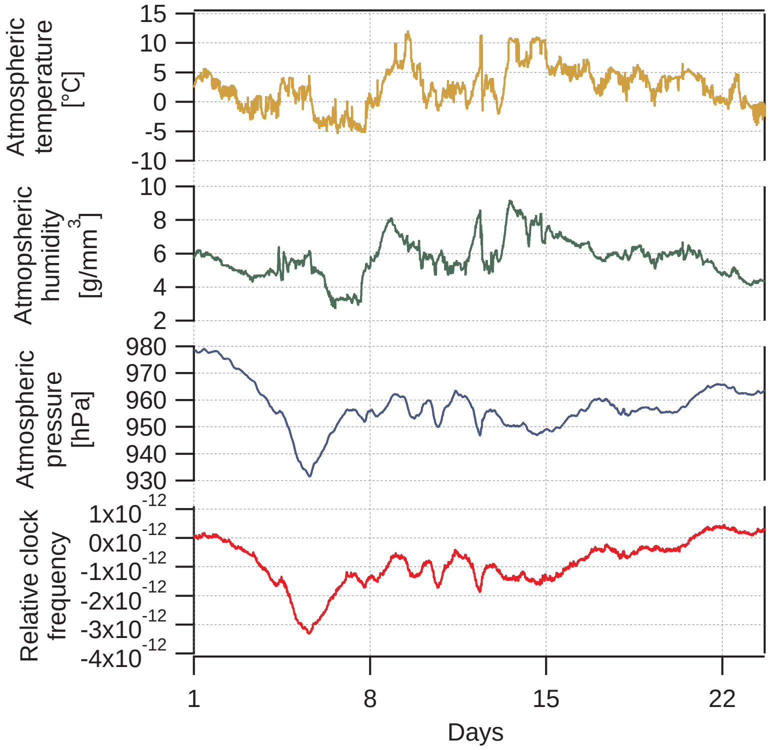

Figure 3.24 – *Time evolution of the clock frequency and the atmospheric parameters (pressure, humidity, temperature) measured at the Swiss weather station. Clock frequency is smoothed over 500 s.*

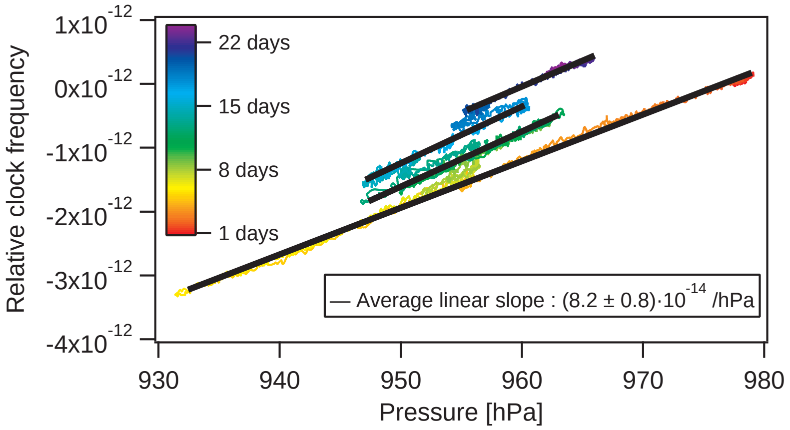

Figure 3.25 – *Relative clock frequency as a function of the atmospheric pressure. Dark lines: linear fit to subsets of data. Color scale: time scale with red day 1 and purple day 23. Measurement started on December 22, 2017. Figure adapted from [122].*

3.3.2.2 Pressure-controlled chamber

An additional measurement of the Barometric coefficient is performed by placing the clock PP inside a pressure-controlled (PC) chamber, see Figure 2.16. The chamber is used as a damper that reduces the atmospheric pressure fluctuation around the PP. Figure 3.26 shows the pressure measured inside the PC chamber and the atmospheric pressure. A reduction of the pressure fluctuation by one order of magnitude is obtained (from 1 hPa/hours without the PC chamber to 0.1 hPa/hours with the PC chamber, see Figure 3.27). Moreover, the pressure variations inside and outside the chamber are non-correlated. The pressure fluctuation inside the PC chamber is mainly dominated by the laboratory temperature fluctuation. The barometric coefficient is obtained by measuring the clock frequency as a function of the PC chamber pressure. The pressure inside the PC chamber is varied from 810 hPa to 960 hPa by steps of 20 hPa. The results are shown in Figure 3.28. An experimental barometric coefficient of $(7.9 \pm 0.6) \cdot 10^{-14}$/hPa is measured.

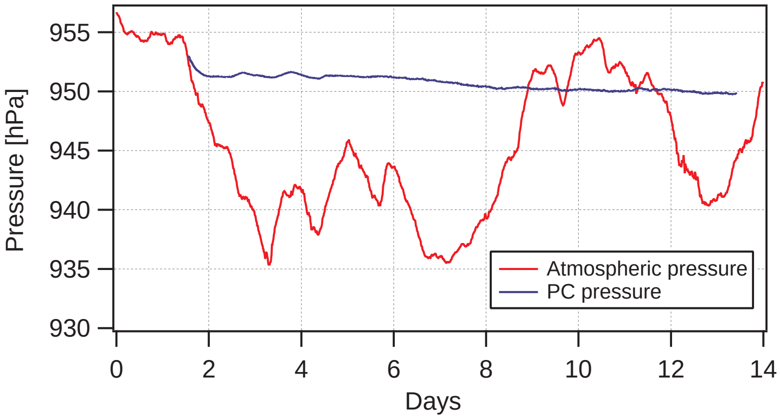

Figure 3.26 – *Impact of the PC chamber on the pressure around the physics-package.*

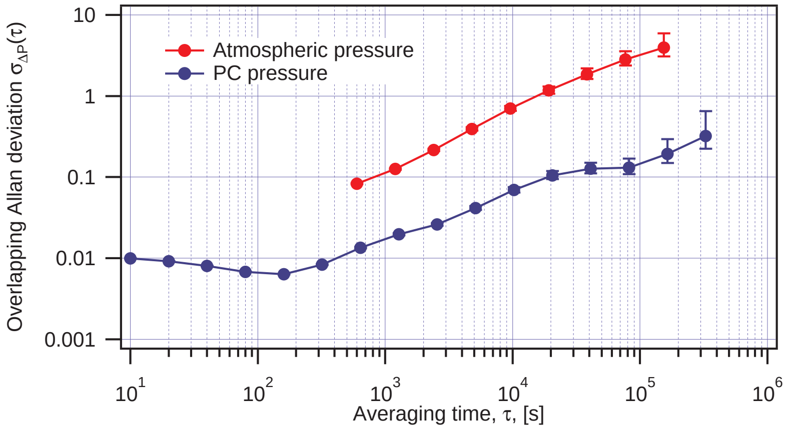

Figure 3.27 – *Overlapping Allan deviation of the atmospheric and PC pressures of Figure 3.26.*

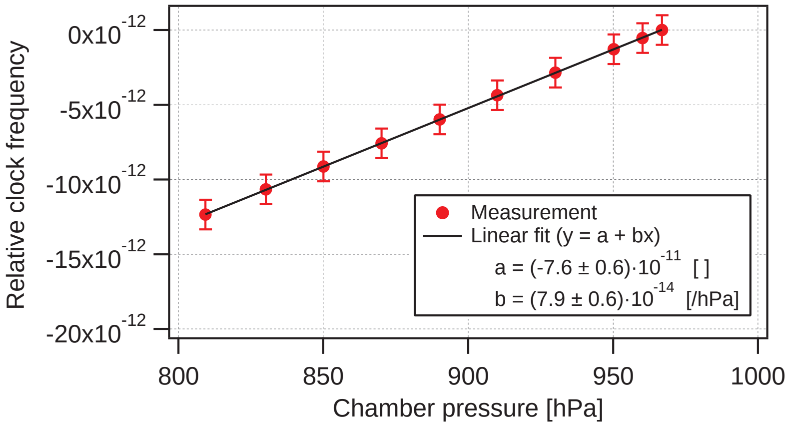

Figure 3.28 – *Barometric coefficient measurement using the PC chamber. Figure adapted from [119].*

3.3.3 Discussion and conclusion

Table 3.9 summarises the simulated and measured barometric coefficient. It confirms that the theoretical model presented in section 3.3.1 agrees with the experimental data. The barometric coefficients in Table 3.9 also agree with previously reported values [98]. The main consequence of the barometric coefficient is that, for typical daily atmospheric pressure fluctuation (1 hPa to tens of hPa), the clock relative frequency instabilities induced are about 10^{-12} to 10^{-13}. Moreover, for the transition from atmospheric pressure to vacuum, the clock relative frequency change should be about 10^{-11} to 10^{-10}. Such observations were reported for RAFS when the clock went from atmospheric pressure to vacuum [98][89][123].

Another physical effect that can deform the vapour cell is the cell's length thermal expansion. In the case of borosilicate glass, the linear thermal expansion coefficient is about $3.25 \cdot 10^{-6}$ /K. For a temperature change of 10 mK (see Table 1.9), it corresponds to a cell length variation of 0.8 nm. The relative volume change induced by the barometric effect (equation (3.19)) for an external pressure change of 1 hPa corresponds to a cell length variation of 3.4 nm. The impact of the linear thermal expansion coefficient is approximately 4.25 times lower than the volume change induced by the barometric effect.

Based on the experimental data presented in Figure 3.24, it is possible to estimate the relative frequency instability of our POP-DR Rb clock prototype free of the barometric effect. Figure 3.29 shows the relative clock frequency obtained by subtracting the barometric shift from the data of Figure 3.24 using the experimental barometric coefficient $(8.2 \pm 0.8) \cdot 10^{-14}$/hPa. Figure 3.30 presents the overlapping Allan deviation of the barometric effect–corrected clock frequency. The Rb clock prototype has an uncorrected relative frequency instability of $1 \cdot 10^{-13}$ at 10^4s of integration time. When the barometric effect is subtracted from the original data, a relative frequency instability of $2 \cdot 10^{-14}$ at 10^4s of integration time is estimated, which is an improvement by a factor of five compared to the original data.

Our analysis of the effect shows that a reduction of the barometric coefficient is possible. According to equation 3.21, the barometric coefficient depends on three main cell parameters: cell geometry and dimension, glass material, and the buffer-gas pressure shift. Figure 3.23 illustrates the barometric coefficient change with respect to the cell's dimension and the glass material. This suggests several possible ways of deducing the barometric coefficient. As demonstrated by Huang *et al.* [91],

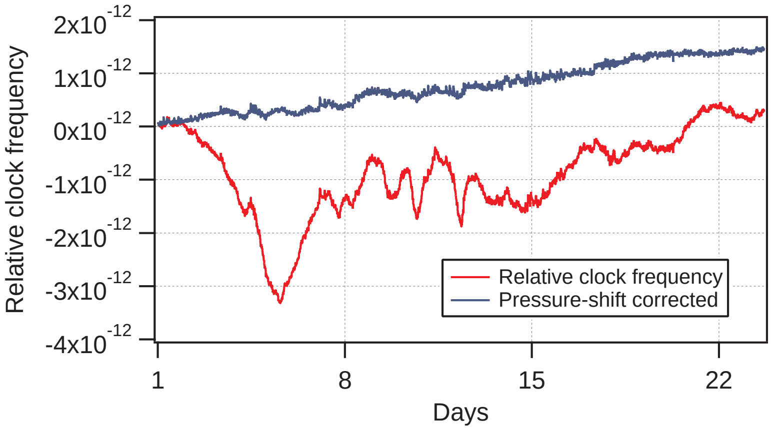

Figure 3.29 – *Relative clock frequency of the measurement of Figure 3.24. Red curve: orginal data. Blue curve: pressure-shift-corrected clock frequency using a coefficient* $(8.2 \pm 0.8) \cdot 10^{-14}$*/hPa. Figure adapted from [122].*

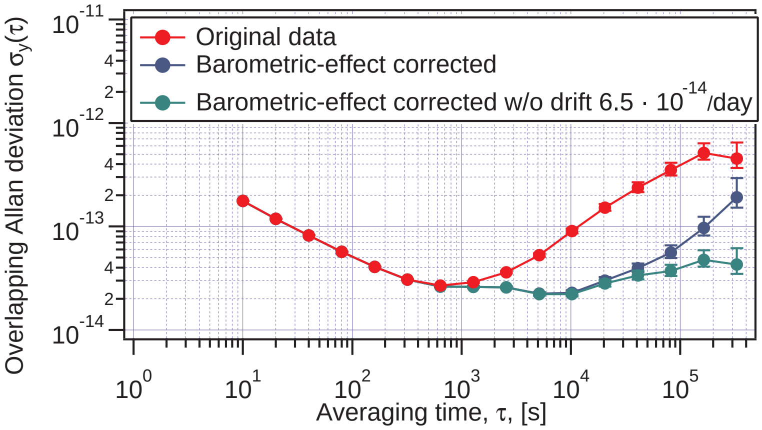

Figure 3.30 – *Overlapping Allan deviation of the data of Figure 3.29. Red curve: original data. Blue curve: barometric-effect-corrected clock frequency instabilities. Green curve: barometric-effect-corrected and drift removed clock frequency instabilities. Figure adapted from [122].*

doubling the vapour cell's wall thickness would reduce the barometric coefficient by one order of magnitude. Moreover, reducing the diameter by a factor of two would also reduce the barometric coefficient by one order of magnitude. Borosilicate glasses have Young's moduli that vary from $(50-70) \cdot 10^7$ hPa and Poisson's ratio from 0.19 to 0.21. Sapphire glass possesses a Young's modulus of $345 \cdot 10^7$ hPa, which would result in a barometric coefficient five times smaller with a sapphire glass cell with our cell's dimension [6]. Another solution is to reduce the buffer-gas pressure shift using a mixture of three BGs [82]. As shown by equation (1.77), the buffer-gas pressure coefficient is mainly dominated by β'. Calosso *et al.*[82] proposed a buffer-gas mixture of CH_4 (15.8 %), Ar (62.7 %) and N_2 (21.5 %), which could result in a negligible β'.

As a conclusion, the barometric effect coefficient is measured at about $(8.1 \pm 0.7) \cdot 10^{-14}$/hPa (see Table 3.9). Without any reduction of the atmospheric pressure fluctuation, the barometric effect induces relative frequency fluctuations at the order of few 10^{-13} at time scale of the day. It corresponds to the most important frequency instability source in our POP-DR Rb clock prototype. The PC chamber reduces the pressure fluctuation below 0.1 hPa. Using the PC chamber, the estimated contribution of the barometric effect on the medium- to long-term stability is approximately

---

[6] however sapphire glass presents birefringence which can be an important source of light perturbation.

$8 \cdot 10^{-15}$ at 10^4 seconds of integration time.

Methods	Barometric coefficient $\left[\frac{1}{\mathrm{hPa}}\right]$
Theory (equation (3.21))	$(8.5 \pm 2.7) \cdot 10^{-14}$
Measurement 1 (via correlation)	$(8.2 \pm 0.8) \cdot 10^{-14}$
Measurement 2 (via PC chamber)	$(7.9 \pm 0.6) \cdot 10^{-14}$
Average experimental coefficient	$(8.1 \pm 0.7) \cdot 10^{-14}$

Table 3.9 – *Barometric coefficients calculated and measured in this section.*

3.4 Other frequency shifts

3.4.1 Density shift

The temperature sensitivity of the clock frequency shift $\Delta\nu_{\text{clock}}$ is described in section 1.4.5.2. The measured temperature sensitivity of the clock frequency shift $\Delta\nu_{\text{clock}}$ (from the unperturbed ^{87}Rb ground-state resonant frequency) is presented in Figure 3.31. It was measured at a fixed stem temperature $T_{\text{stem}} = 59.2 \pm 0.2$ °C [7]. The data in Figure 3.31 is fitted with the following fit function [81]:

$$f(T) = c + b \cdot (T - T_0) + a \cdot (T - T_0)^2, \tag{3.22}$$

with $T_0 = 60$ °C. The inversion temperature is given by $T_{\text{inv}} = T_0 - \frac{b}{2a}$. Based on the fit parameters a, b, and c shown in Figure 3.31, one obtains an inversion temperature of $T_{\text{inv}} = 62.65 \pm 0.11$°C. The first-order cell-temperature coefficient is given by the derivative of equation (3.22) evaluated at $T = T_{\text{inv}}$. At this temperature, the first-order cell temperature is strongly reduced. However, due to the uncertainty coming from the fit parameters, the first-order coefficients are bound by $|\frac{\partial(\Delta\nu_{\text{clock}}/\nu_0)}{\partial T_{\text{cell}}}| \leq 1.06 \cdot 10^{-12}$/K (or 7.23 mHz/K at ν_0=6'834'682'610 Hz). Based on the fit parameter of Figure 3.31, the buffer-gas temperature coefficients β', δ', and γ' are calculated. Table 3.10 presents the experimental coefficients in comparison with the literature values [81][67]. A buffer-gas pressure of 32.6 hPa is assumed with a ratio of $P_{\text{Ar}}/P_{N_2} = 1.6$. An agreement between the coefficients derived from measurements and the literature is found, especially for β' and γ'. However, this method of coefficient measurement is limited by systematic biases like the LIS effects, static magnetic-field shift, or the effect of the stem. In theory, our measurements can be improved by mitigating these effects and can then access the "intrinsic" buffer-gas collisions coefficients.

The stem is operated at a lower temperature of 59.2 ± 0.2 °C compared to the core cell temperature. The temperature is kept lower such that the stem acts as a cold point, which avoids fluctuation of the Rb density in the vapour cell. The stem temperature-coefficient sensitivity [82] is $1.82 \cdot 10^{-12}$/K (or 12.4 mHz/K at ν_0=6'834'682'610 Hz), according to the measurements shown in Figure 3.32.

It is worth mentioning that the inversion temperature calculated from data in Figure 3.31 corresponds to the cell temperature that only suppresses the cell's temperature sensitivity coefficient and does not suppress the stem temperature sensitivity coefficient. This approach is different from the measurement method reported by Calosso et al.[82] where they determined an inversion temperature that cancels the cell-temperature sensitivity to common temperature fluctuation, by varying both T$_{\text{stem}}$ and T$_{\text{cell}}$ simultaneously.

---

[7] The temperature uncertainty of ±0.2 °C come from the uncertainty of the NTCs reported the datasheet.

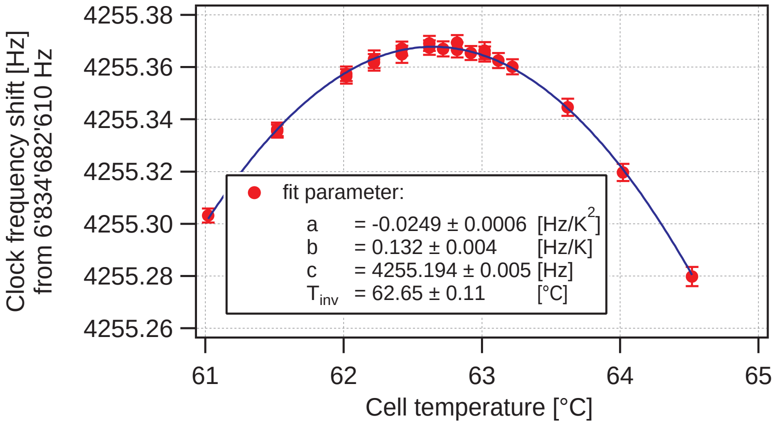

Figure 3.31 – *Clock frequency sensitivity to the vapour cell temperature. The data are fitted with the quadratic function 3.22.*

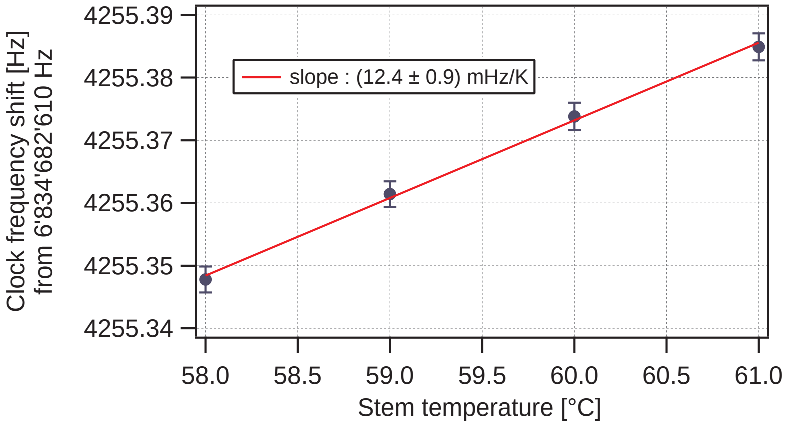

Figure 3.32 – *Clock frequency sensitivity to the stem temperature. The data are fitted with a linear function.*

	β' $\left[\frac{\mathrm{Hz}}{\mathrm{hPa}}\right]$	δ' $\left[\frac{\mathrm{Hz}}{\mathrm{hPa\,K}}\right]$	γ' $\left[\frac{\mathrm{Hz}}{\mathrm{hPa\,K^2}}\right]$
Measurement	$130.53 \pm 2 \cdot 10^{-4}$	$(0.41 \pm 0.02) \cdot 10^{-2}$	$(-7.65 \pm 0.19) \cdot 10^{-4}$
Literature [81]	130.49 ± 8.3 $^{a)}$	$(0.23 \pm 4.1) \cdot 10^{-2}$ $^{a)}$	$-5.37 \cdot 10^{-4}$ $^{a)}$
Literature [67]	130.21	$1.1 \cdot 10^{-2}$	$-6 \cdot 10^{-4}$

Table 3.10 – *Measured and calculated pressure shifts and temperature coefficients for our mixture of buffer gas Ar and N_2 at $T_0 = 60\,°\mathrm{C}$. a) uncertainty coming from the dispersion of the coefficients given in the Table 1 of ref [81].*

3.4.2 Second-order Zeeman shift

The impact of the fluctuation of the static magnetic field inside the vapour cell is characterised by measuring the sensitivity coefficient ($|\frac{\partial \nu_{\text{clock}}}{\partial B}|$) and the fluctuation of the static magnetic field $\sigma_B(\tau)$. The sensitivity coefficient is given by the variation of the clock frequency as a function of the static magnetic field generated by the coil surrounding the vapour cell (C-field). The C-field is varied by varying the coil's current. The calibration of the C-field as function of the coil's current is performed by measuring the Zeeman splitting of the ground state transition $|5^2S_{1/2}, F=1, m_F=1\rangle \leftrightarrow |5^2S_{1/2}, F=2, m_F=1\rangle$[31]. The clock frequency shift as function of the C-field is shown on Figure 3.33. Fitting the data with a quadratic function, a sensitivity coefficient of $1.77 \cdot 10^{-4}$/T is obtained at 10.7 μT (equivalent to a C-field current of 1.6 mA).

The magnetic shields inside the PP attenuate the environmental magnetic field. We denote B_r and B_n as the residual static magnetic field remaining and the noise field generated by the shields, respectively. The total fluctuation of the magnetic field $\sqrt{\sigma_{B_z}(\tau)^2 + \sigma_{B_n}(\tau)^2 + \sigma_{B_r}(\tau)^2}$ can be measured by frequency stabilising the clock quartz onto the $\pi_{\pm 1}$ transitions, see Figure 2.11a. These transitions are more sensitive to magnetic perturbation than the clock transition π_0. Frequency stabilising the clock quartz onto one $\pi_{\pm 1}$ transition allows the fluctuation of the static magnetic field inside the vapour cell to be measured directly using the sensitivity coefficient of the $\pi_{\pm 1}$ transitions ($\pm 1.4 \cdot 10^4$ MHz/T). Figure 3.34 presents the overlapping Allan deviation of the static magnetic field inside the vapour cell. At 10^4 s, the absolute fluctuation $\sigma_B(\tau)$ is about $5 \cdot 10^{-11}$ T. The static magnetic-field fluctuation induces a clock relative frequency fluctuation of few 10^{-15} at 1 s of integration time and $7 \cdot 10^{-15}$ at 10^4 of integration time.

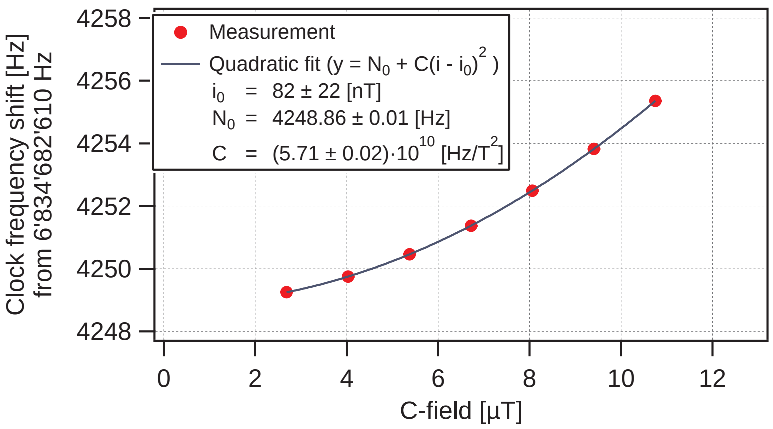

Figure 3.33 – *Clock frequency sensitivity to the static magnetic field inside the vapour cell. The clock is frequency stabilized onto the clock frequency (π_0 transition see Figure 2.11a)*

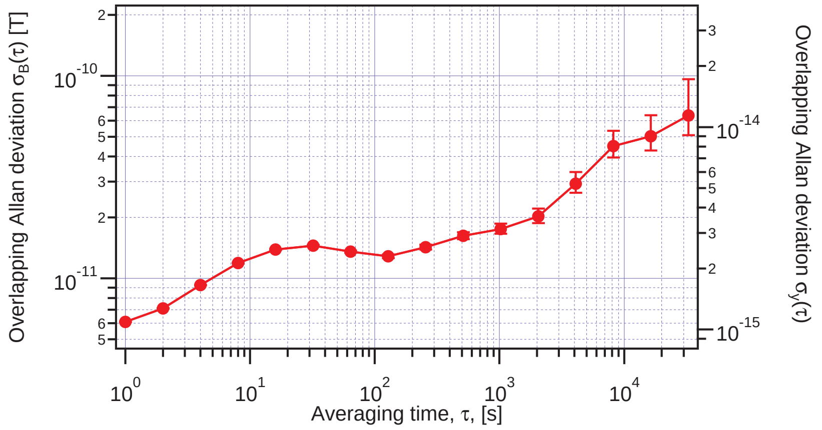

Figure 3.34 – *Total static magnetic field absolute fluctuation :* $\sigma_B(\tau) = \sqrt{\sigma_{B_z}(\tau)^2 + \sigma_{B_n}(\tau)^2 + \sigma_{B_r}(\tau)^2}$.

3.5 Frequency instability budgets and measurement

In the previous sections, the frequency sensitivity of our POP-DR Rb clock prototype was presented with an emphasis on the MPS, the LISs, and the barometric shift. For these three sensitivities, the approach of this study is to find operational points such that the sensitivity coefficients of the MPS, the LIS, and the barometric effect can be reduced compared to the previous situation described, for instance, in the thesis of Gharavipour [31]. In this section, we use the breadboard setup shown in see Figure 2.16. We demonstrate that the operating conditions found in this chapter lead to a frequency instability at the level of 10^{-14} in the medium- to long-term.

First, frequency instability budgets are presented for the short-term (1 to 100 s averaging time) and medium- to long-term (10^4s). These budgets are made in the operating conditions described in Table 3.11 that correspond to conditions of reduced sensitivity to the MPS, intensity LS, and the barometric effect frequency shift. Second, we present a typical frequency instability measurement of our POP-DR Rb clock prototype operated in these conditions.

Optical pumping	t_p = 0.4 ms	$P_{opt.}$ = 13 [mW]	Laser frequency	CO21-23
Microwave pulses	t_m = 0.3 ms	$P_{\mu w}$ = 20.1 [μW]	AOM frequency shift	-2 × (75 MHz)
Free evolution duration	t_R = 3 ms	-	LO modulation amplitude	80 Hz
Optical detection	t_d = 0.7 ms	$P_{opt.}$ = 120 [μW]	PC chamber	Yes (P = 950 hPa)
Total cycle time	t_d = 4.74 ms	-	T_{cell}, T_{stem}	62.65°C, 57.22°C
			C-field	10.7 μT

Table 3.11 – *Key clock parameters.*

3.5.1 Short-term budget

In this section, the short-term frequency instability is estimated using the analytical expressions presented in section 1.4.4. Figure 3.35a presents a typical optical-detection signal's RIN. It was measured for a continuous detection light of 120 μW of optical power. Figure 3.35b presents a typical central Ramsey fringe with an excellent contrast of ≈ 44 %. Table 3.12 presents the estimated short-term frequency instabilities induced by the shot noise (equation 1.64), the optical-detection noise (equation 1.65), and the LO phase noise via the Dick effect (equation 1.66). In addition, Table 3.12 also contains the short-term frequency instabilities induced by the intensity and frequency LS, the second-order Zeeman shift, and the MPS, which impact the short-term frequency instability below the shot-noise limit.

The total estimated short-term frequency instability is $4.8{\cdot}10^{-13}\ \tau^{-1/2}$. The main source of frequency instability is the optical-detection noise with a contribution of $4.5{\cdot}10^{-13}\ \tau^{-1/2}$. The optical-detection noise is composed of the shot noise, the AOM-LH AM noise, and the FM noise converted into AM noise inside the vapour cell. Detailed analysis and discussion of the optical-detection noise for a compact Rb clock with a design similar to the one used in this study can be found in [20] and [105][106][31].

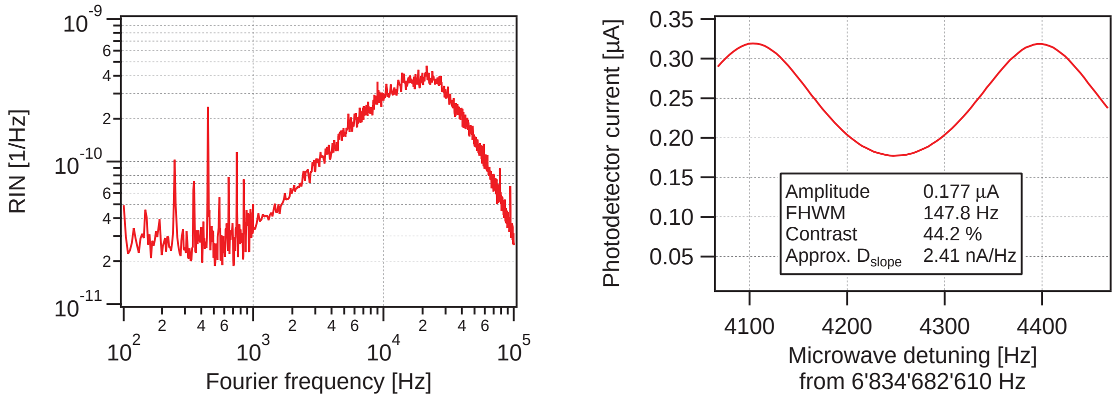

(a) **(b)**

Figure 3.35 – *(a) Typical optical detection signal's RIN measured for a continous detection light power of 120 μW. (b) Central Ramsey fringe measured in the condition of Table 3.11.*

Shot-Noise limit	$5.5 \cdot 10^{-14}\ \tau^{-1/2}$
Optical Detection	$4.5 \cdot 10^{-13}\ \tau^{-1/2}$
Dick Effect (LO)	$1.8 \cdot 10^{-13}\ \tau^{-1/2}$
Intensity LS	$3.7 \cdot 10^{-15}\ \tau^{-1/2}$
2^{nd}-order Zeeman	$9.8 \cdot 10^{-16}\ \tau^{-1/2}$
Frequency LS	$3.8 \cdot 10^{-16}\ \tau^{-1/2}$
Microwave PS	$7.4 \cdot 10^{-17}\ \tau^{-1/2}$
Total Estimated	$4.8 \cdot 10^{-13}\ \tau^{-1/2}$

Table 3.12 – *Estimated short-term frequency instability budget.*

3.5.2 Medium- to long-term budget

In this section, we review the frequency sensitivities mentioned above and in Chapter 1. Their impacts on the medium- to long-term clock frequency instability are summarised.

As already mentioned, the impact of the frequency sensitivities is quantified with a sensitivity coefficient to a clock parameter x, $\frac{\Delta f}{\Delta x}$, and the variance of the fluctuations of the clock parameter itself at 10^4 s, $\sigma_x(\tau = 10^4\ \text{s})$. The sensitivity coefficients and the fluctuation of the corresponding physical parameter were presented in Chapters 2 and 4. The fluctuation of the temperature of the vapour cell, the stem, and the microwave cavity was not measured in this study. For the establishment of the frequency instability budget, we consider the temperature fluctuations reported in the previous study [31]. Table 3.13 summarises the clock frequency sensitivity evaluated in this work and its impact on the medium- to long-term frequency instability of our POP-DR Rb clock prototype. When possible, the sensitivity coefficients are specified for two laser locking points: F=1 (CO10-11) and F=2 (CO21-23).

The estimated medium- to long-term frequency instability at 10^4 s is $2.2 \cdot 10^{-14}$ for F=1 and $1.7 \cdot 10^{-14}$ for F=2. For F=1, the main sources of frequency instability are the intensity LIS at $1.5 \cdot 10^{-14}$, the stem temperature sensitivity at $9.1 \cdot 10^{-15}$, and the second-order Zeeman effect at $8.2 \cdot 10^{-15}$. For F=2, the main sources of frequency instability are the intensity LIS at $1.5 \cdot 10^{-14}$, the stem temperature sensitivity at $9.1 \cdot 10^{-15}$ and the second-order Zeeman shift at $8.2 \cdot 10^{-15}$.

3.5.3 Frequency stability measurement

The Rb clock prototype is operated in the conditions summarised in Table 3.11. The clock's PP is placed inside a PC chamber, as mentioned in section 3.3.2.2, which guarantees a reduction of the external pressure fluctuation by one orders of magnitude (see Figure 3.27). The chamber pressure is set at ≈ 950 hPa, slightly lower than the atmospheric pressure at the time of the measurement. The clock frequency is recorded simultaneously with the atmospheric pressure, the pressure inside the vacuum chamber, the laboratory temperature, and the AOM-LH sub-Doppler photodetector voltage. The duration of the measurement is 10 days. The data is shown in Figure 3.38. The use of the PC chamber allows the impact of the barometric effect on the clock frequency to be reduced; indeed, frequency and pressure data of Figure 3.38 are no longer correlated. Moreover, the clock frequency is not correlated with the laboratory temperature. According to section 3.5.2, the clock frequency fluctuation is expected to be correlated with the static magnetic-field fluctuation.

The overlapping Allan deviation of the clock frequency is shown in Figure 3.36. A short-term frequency instability of $4.9 \cdot 10^{-13} \tau^{-1/2}$ is measured, in agreement with the estimated short-term stability in Table 3.12. The measured frequency instability averaged down as $\tau^{-1/2}$ up to $1 \cdot 10^{-14}$ at 10^4 s, slightly better than the estimated medium- to long-term stability of Table 3.13. The clock frequency drift is measured at the level of $+1.9 \cdot 10^{-14}$/day. It is interesting to note that the frequency drift does impact the medium-to-long term clock stability around 10^5 seconds. As can be seen in Table 3.13, the clock frequency instabilities arising due to the stem temperature sensitivity ($9.1 \cdot 10^{-15}$) and the second-order Zeeman shift ($8.2 \cdot 10^{-15}$) are the main limiting effects in the medium- to long-term. The cell-temperature sensitivity, the barometric effect, and the intensity LIS contribute at the level of $5 \cdot 10^{-15}$ each.

Figure 3.36 shows that the frequency instability of our clock presents a form of a plateau at 10^4 s of integration time. In order to verify that our clock frequency instabilities are not affected by any flicker noise, a selection of subset data (of 250'000 pts) is taken from data in Figure 3.36 between day 3 and day 4.5 of measurement. Figure 3.36 presents the Allan variance calculated over this selection of subset data using the Theo1 variance (short terminology for theoretical variance # 1). Figure 3.36 shows that the clock frequency is averaged down by $\tau^{-1/2}$ at the level of $2 \cdot 10^{-15}$ at $6 \cdot 10^4$ seconds of integration time. This shows that the clock frequency does not present any flicker noise at the level of 10^{-14}.

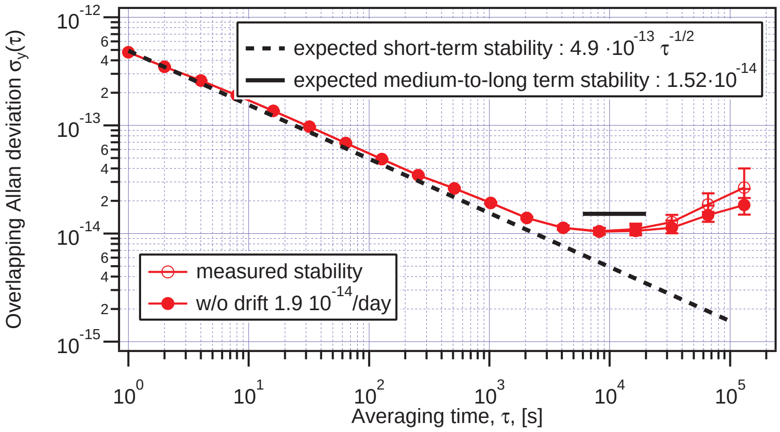

Figure 3.36 – *Overlapping Allan deviation of the clock frequency of Figure 3.38. Figure adapted from [119].*

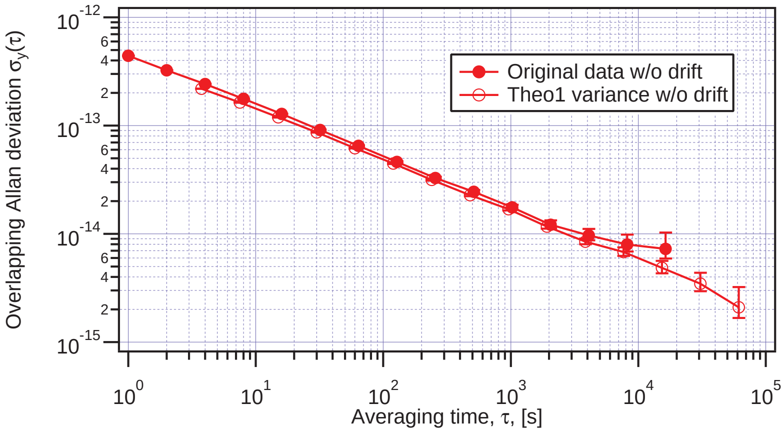

Figure 3.37 – *Theo1 Allan deviation of the clock frequency of Figure 3.38 over a selected period of time (day 3 to day 4.5) without drift.*

Physical effect		Physical parameter	Absolute coefficient	Relative coefficient	Physical fluctuation at 10^4 s	Frequency instability contribution at 10^4 s	
						F=1	F=2
Zeeman effect		C-field	1.21 MHz/T	$1.77\cdot10^{-4}$/T	$5\cdot10^{-11}$ T	$8.2\cdot10^{-15}$	$8.2\cdot10^{-15}$
Cell TC shift		T_{cell}	7.23 mHz/K	$1.06\cdot10^{-12}$/K	5 mK[31]	$5.3\cdot10^{-15}$	$5.3\cdot10^{-15}$
Stem TC shift		T_{stem}	12.4 mHz/K	$1.82\cdot10^{-12}$/K	5 mK[31]	$9.1\cdot10^{-15}$	$9.1\cdot10^{-15}$
Barometric effect		Pressure	0.56 mHz/hPa	$8.1\cdot10^{-14}$/hPa	0.06 hPa	$4.9\cdot10^{-15}$	$4.9\cdot10^{-15}$
Spin-Exchange$^{a)}$		T_{cell}	0.36 mHz/K	$5.27\cdot10^{-14}$/K	5 mK[31]	$2.7\cdot10^{-16}$	$2.7\cdot10^{-16}$
Light-shift	F=1	I_{Laser}	-0.33 mHz/%	$-4.9\cdot10^{-14}$/%	0.3 %	$1.5\cdot10^{-14}$	
	F=2		0.13 mHz/%	$2.9\cdot10^{-14}$/%			$8.5\cdot10^{-15}$
Light-shift	F=1	f_{Laser}	73.1 μHz/MHz	$1.1\cdot10^{-14}$/MHz	4 kHz	$4.3\cdot10^{-17}$	
	F=2		-832 μHz/MHz	$-1.3\cdot10^{-13}$/MHz			$4.9\cdot10^{-16}$
Microwave-shift	F=1	$P_{\mu W}$	20.8 mHz/μW	$3.05\cdot10^{-12}/\mu$W	2 nW	$6.1\cdot10^{-15}$	
	F=2		1.3 mHz/μW	$1.85\cdot10^{-13}/\mu$W			$3.7\cdot10^{-16}$
Cavity-pulling	F=1	$P_{\mu W}$ $^{b)}$	-0.31 mHz/μW	$4.5\cdot10^{-14}/\mu$W	2 nW	$9\cdot10^{-17}$	
	F=2		-0.2 mHz/μW	$-2.7\cdot10^{-14}/\mu$W			$1.9\cdot10^{-16}$
	F=1	T_{cav} $^{a)}$	-56.6 μHz/K	$-9\cdot10^{-15}$/K	5 mK	$5\cdot10^{-17}$	
	F=2		34.1 μHz/K	$5\cdot10^{-15}$/K			$2\cdot10^{-17}$
	F=1	Pressure $^{c)}$	-2.3 μHz/hPa	$-4\cdot10^{-16}$/hPa	0.06 hPa	$2\cdot10^{-17}$	
	F=2		1.4 μHz/hPa	$2\cdot10^{-16}$/hPa			$2\cdot10^{-16}$
	F=1	Humidity	-5.3 μHz/(g/m^3)	$-7.8\cdot10^{-15}$/(g/m^3)	0.2 g/m^3	$1.6\cdot10^{-15}$	
	F=2		32 μHz/(g/m^3)	$4.7\cdot10^{-15}$/(g/m^3)			$9.4\cdot10^{-16}$

Total estimated contribution at 10^4s	$2.2\cdot10^{-14}$	$1.7\cdot10^{-14}$

Table 3.13 – *Estimated frequency instabilities in our POP-DR Rb clock prototpye at 10^4 s of integration time. This table correpsonds to an updated version of the preliminary evaluation presented in [31]. a) this effect is included in the measured cell temperature coefficient. b) this effect is included in the measured microwave-power sensitivity coefficient. c) this effect is included in the measured barometric coefficient.*

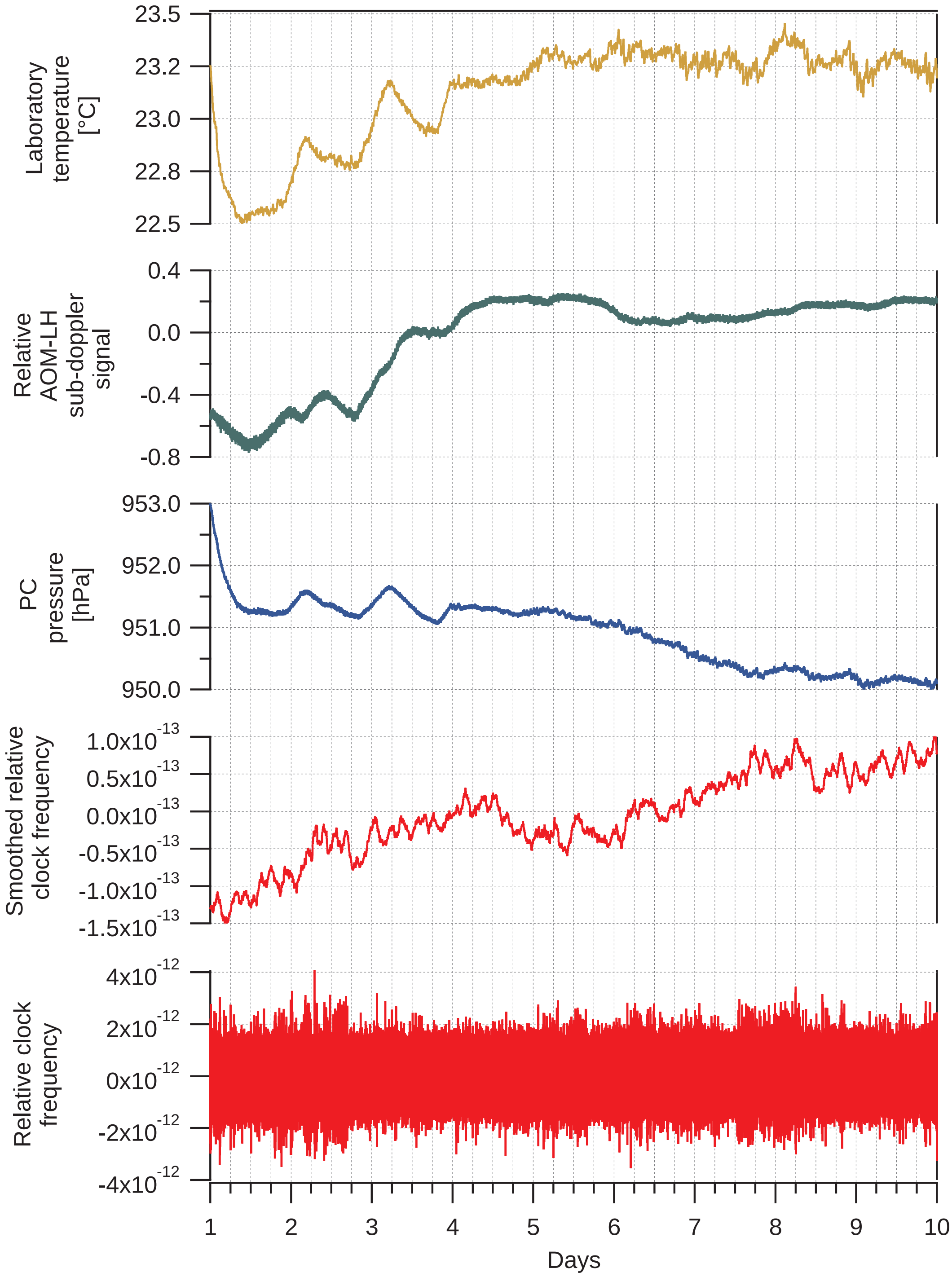

Figure 3.38 – *Time evolution of the laboratory temperature, the AOM-LH sub-Doppler signal, the PC chamber pressure, the smoothed relative clock frequency and the raw relative clock frequency. Temperature, AOM-LH signal and pressure data are smoothed over 10'000 s. The relative clock frequency is smoothed using a Box smoothing algorithm with 20'000 s.*

3.5.4 Discussion

The operating condition summarised in Table 3.11 allowed to reduce the impact of the MPS, the barometric effect, and the intensity LIS to reduce below 10^{-14}. The frequency instability measured in these conditions is now limited to 10^{-14} by another set of phenomena: the second-order Zeeman effect, the stem temperature sensitivity, and the intensity LS.

The impact of the second-order Zeeman shift can be reduced by operating the clock to at lower C-field amplitude. Indeed, it has been shown that the second-order Zeeman coefficient is proportional to the static magnetic field, see equation 1.71. As mentioned in Chapter 2, in our POP-DR Rb clock prototype, the C-field is generated by a coil surrounding the microwave cavity. Reducing the current sent to the coil by a factor of two would reduce the second-order Zeeman coefficient from 1.2 MHz/T to 0.6 MHz/T, which would result in a contribution of $4.1 \cdot 10^{-15}$ over the medium- to long-term time scale, i.e. also a reduction by a factor of two. A reduction of the amplitude of the C-field brings closer the neighbouring microwave transitions to the π_0 (the clock transition)(see Figure 2.11). It results in an overlapping between the clock transition (the Ramsey spectrum) with the envelope of the other Zeeman transitions. This in turn results in a frequency shift in the case of asymmetry between the envelopes of the neighbouring Zeeman transitions. This effect is refered to the Rabi pulling and is well-known for caesium-beam clocks [67][124]. In the condition of a large Zeeman splitting ϵ_Z compared to the microwave Rabi frequency b, the Rabi pulling shift is given by [67][124]:

$$\Delta\nu_{\mathrm{Rabi}} = \frac{15}{4\sin^2(bt_m)} \frac{b^2}{\epsilon_Z^3 T_R^2} \frac{n_1 - n_{-1}}{n_0} \tag{3.23}$$

where $\frac{n_1-n_{-1}}{n_0}$ is the relative atomic population asymmetry with n_m denoting the initial population of the F=1 Zeeman states (see Figure 2.11). In the case of compact caesium-beam frequency standard, a gross estimate of the relative frequency shift is at the level of 10^{-13} for a population asymmetry of 15% [67]. The population asymmetry is estimated at $\approx 3\%$ for our POP-DR Rb atomic clock by looking at the ratio between the transmission signal of the $\pi_{\pm 1}$ and the π_0 transitions of the Zeeman spectrum of Figure 2.11. Using equation 3.23 and the parameters of our atomic clock, one obtains a frequency shift at the order of 0.2 mHz and a sensitivity coefficient to the static magnetic field fluctuation at the order of -30 Hz/T. This sensitivity coefficient gives a contribution to the medium-to-long term frequency instability at the order of $5 \cdot 10^{-19}$ which is completely negligible for our clock. However, the associated coefficient scales with $1/B_z^3$ and with the microwave power b^2. In order to avoid any problem linked to an overlap of the neighbouring microwave transitions it is to keep the ratio $b/\epsilon_Z \gg 1$. The Ramsey pulling are induced the small circular components of the cavity microwave field [124] which results in residual σ transitions in the Zeeman spectrum (see Figure 2.11). According to the analysis reported in [124], the Ramsey-pulling is two order of magnitude higher than the Rabi-pulling, which is still negligible in our case. The evaluation of the Rabi- and Ramsey pulling presented here is quite a gross estimation of the impact of the neighbouring microwave transitions on the clock transitions. A better estimation can be obtained by using the approach described in [124] and using the calculation presented in chapter 1.

In the following of the discussion on the origin of the population asymmetry in the ground-state Zeeman level, on has to mention the impact of the light polarization. In our POP-DR Rb atomic clock, the LH-AOM output light is polarized linearly but perpendicular to the quantisation axis of the atoms (C-field direction), which predominantly induces sigma transitions. It means that after the pump pulse, we assume that the rubidium atoms are equi-distributed along the ground-state Zeeman level $n_{+1,0,-1} = 1/3$ when the laser is stabilized on F=2 and $n_{-2,-1,0,+1,+2} = 1/5$ when the laser is stabilized on F = 1. However, in the case of $\sigma^{\pm}$ polarisation light, the atoms are not equi-distributed in the ground-state Zeeman level after the pumping phase, see Figure 3.39. It results in a population imbalance between the initial F=1 or F=2 Zeeman states which induces an increase of the Rabi-pulling shift as mentioned before. The light polarisation has also an impact on the light-shift (AC-Stark shift) as discussed by Pellaton in his thesis [74]. However, we never observed any frequency shift originated from the light polarization at least that induces frequency instability contribution at the level of 10^{-14}. Moreover, the population imbalance in the ground state before the microwave interrogation would induce a reduction of the contrast of the central fringe. However, these aspects need to be further evaluated.

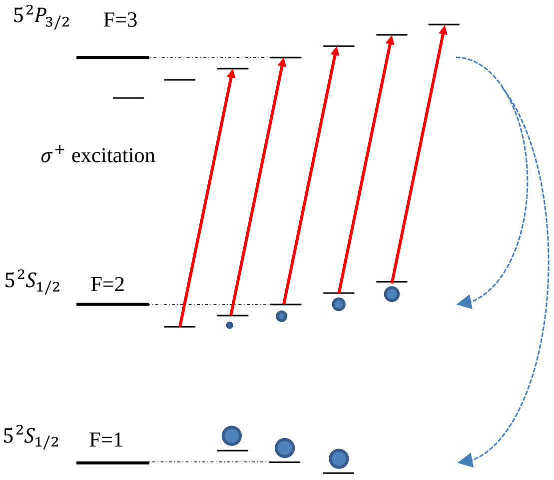

Figure 3.39 – *Schematic representation of the energy level scheme of the D_2 line showing the optical transition under σ^+ excitation. The size of the blue circle indicates the atomic population level.*

The reduction of the impact of the stem temperature sensitivity is more complicated. Two problems occur: (1) the stem temperature sensitivity coefficient cannot be minimised over the range of stem temperatures studied (see Figure 3.32), and (2) the temperature fluctuation in the stem and the cell is not well-known (the temperature fluctuation reported in Table 3.13 is an estimated upper limit). The temperature fluctuation of the stem and cell volume can be solved by improving the thermal control of these parts. Another solution would be to change the buffer-gas mixture. Indeed, as shown by equation 2.1, the stem temperature sensitivity is proportional to the stem volume and the buffer-gas pressure coefficient β'. At this point, we can kill two birds with one stone. Indeed, reducing the β' coefficient will not only significantly reduce the stem temperature sensitivity but also the barometric sensitivity of the vapour cell as discussed in section 3.3.3.

The two other limiting factors (barometric effect and intensity LS) are sensitive to long-term fluctuation of the laboratory temperature. Indeed, Figure 3.38 shows a correlation between the PC pressure and the AOM-LH sub-Doppler signal with changes in the long-term laboratory temperature. Better control of the thermal bath of the clock (which includes PP, PC, and AOM-LH) would allow a reduction of these two effects.

The signal-to-noise limit is degraded by a factor of three compared to the previously reported short-term frequency instability of our POP-DR Rb clock prototype [20][31]. This is due to the higher detection RIN measured in this thesis compared to the previously reported detection RIN [31][20]. The reasons behind the augmentation of the detection RIN were not investigated. A reduction of the detection RIN, and by consequence, the short-term frequency instability, while keeping the same level of medium- to long-term frequency instability could represent one of the major future improvements of our POP-DR Rb clock prototype.

3.6 Conclusion

In this chapter, the main physical effects that limit the medium- to long- term stability performance of our POP-DR Rb clock prototype are studied with an emphasis on the MPS, the LS, and the barometric effect. These studies resulted in an optimisation of the frequency stability of our POP-DR Rb clock prototype that demonstrated a medium- to long-term frequency stability of $1 \cdot 10^{-14}$.

Based on a numerical Bloch vector model, we can see that the MPS in our POP-DR Rb clock prototype arises from the combination of two inhomogeneities: Rb ground-state resonant-frequency shift distribution and microwave-field amplitude distribution. Experimental measurement of the MPS shows a particular behaviour when the laser is frequency tuned on F=2. An MPS coefficient at the level of $2 \cdot 10^{-13}/\mu$W is measured especially when the laser frequency is tuned on the CO21-23 transition and for $\theta_n = 0.57 \cdot \pi$ microwave pulse. This coefficient is one order of magnitude lower than the previously reported coefficient [86].

The frequency and intensity LIS sensitivity is a consequence of at least three phenomena: a pump LIS supposedly coming from a ground-state residual coherence, a detection LS, and a residual LS or AC-Stark shift. The experimental evaluation presented in section 1.4.5.5 opens the discussion on the origin of the LIS in POP-DR Rb clocks (few elements are presented in this chapter). However, an experimental global LIS coefficient includes all these LIS phenomena. This leads to an estimated impact of the intensity LIS on the long-term frequency instability of our POP-DR Rb clock prototype at the level $\leq 9 \cdot 10^{-15}$ when the AOM-LH is frequency stabilised onto CO21-23.

The barometric effect is found to be the most dominant source of long-term frequency instability for our POP-DR Rb atomic clock prototype in free atmosphere. The barometric effect coefficient is measured at about $(8.1 \pm 0.7) \cdot 10^{-14}$/hPa for our POP-DR Rb clock prototype. Without any reduction of the atmospheric pressure fluctuation, the barometric effect limits the frequency instability at the level of few 10^{-13}. Reducing the atmospheric pressure fluctuation around the PP, the contribution of the barometric effect to the medium- to long-term stability is reduced below $1 \cdot 10^{-14}$ at 10^4 seconds of integration time. The research presented in this chapter shows that the barometric effect is one of the most important sources of frequency instability for our atomic clock prototype, not only the one evaluated in this thesis but also for the previous realisation of atomic clock at LTF.

Finally, our POP-DR Rb clock prototype is operated in certain conditions (pulse durations, microwave power, light intensity, and PC chamber) such that the sensitivity coefficients are minimised (see Table 3.1). A medium- to long-term frequency instability at the level of $1 \cdot 10^{-14}$ at 10^4 s is measured, in agreement with the estimated medium- to long-term stability budget. According to the estimated frequency instability budget, the clock frequency instabilities arising due to the stem temperature sensitivity ($9.1 \cdot 10^{-15}$) and the second-order Zeeman effect ($8.2 \cdot 10^{-15}$) are expected to be the main limiting effect over the medium- to long-term. The impact of the second-order Zeeman effect can be further attenuated by reducing the amplitude of the C-field inside the vapour cell.

4 Additive manufactured microwave cavities

The previous chapter demonstrated that a high-performance vapour-cell frequency standard based on a compact magnetron-type cavity can achieve frequency instability performance comparable to state-of-the-art frequency stability when operated in the correct conditions. This chapter focuses on one of the critical parts of our POP-DR Rb clock prototype: the microwave cavity.

As mentioned in section 2.3.3, to obtain a strong clock signal, the microwave magnetic field H must be perfectly parallel to the static magnetic field B_{static} throughout the vapour cell. For most of the microwave cavities used in DR atomic clocks, a TE_{011}-like cavity mode is preferred. When H is parallel to B_{static}, the π-transitions are maximised, while the $\sigma\pm$ transitions are minimised (see Figure 2.11a). This aspect was addressed by Pellaton in his thesis [74]. Another requirement of H is that the microwave-field amplitude should be as homogeneous as possible throughout the cell such that a maximum number of atoms undergo an ideal $\pi/2$ pulse. Moreover, the microwave-field amplitude inhomogeneity impacts the microwave-power shift as evaluated numerically in section 3.1.2. As mentioned in Chapter 1, in a POP-DR Rb cell clock, one wants to avoid the generation of microwave photons during the Ramsey interrogation, which is at the origin of the cavity-pulling shift (see equation 1.84). In order to minimise the clock frequency fluctuation induced by cavity pulling, a low-quality factor (Q-factor) of the cavity ($Q \approx 100$) is needed. The low Q-factor of our microwave cavity is mainly due to the high dielectric loss induced by the glass cell [115]. Furthermore, the frequency detuning between the microwave-cavity frequency resonance and the Rb ground-state hyperfine clock frequency needs to be as small as possible. The microwave-cavity frequency resonance depends on the cavity geometry. Finally, the microwave cavity should be compact, lightweight, and easy to assemble.

Traditionally, atomic clock microwave cavities are generally manufactured by precision machining of bulk metals and assembly steps. In order to achieve the Rb ground-state frequency resonance and a homogeneous microwave-field orientation and amplitude, a precise positioning and alignment of the cavity components are required. The production of microwave-cavity prototypes is time-consuming and relies on expensive precision machining.

In the framework of the SERI/SSO-project, a consortium between the Microwave and Antennas Group (EPFL-MAG), Swissto12 SA and LTF evaluated the potential of AdM technologies (also called 3D-printing) to build AdM microwave cavities and their use in compact atomic clocks [109][125][126]. Two different manufacturing techniques were tested: a photopolymerisation process using stereolithography (SLA) and selective laser melting (SLM) of aluminium. These studies demonstrated a suitable approach for using AdM microwave cavities to build CW-DR Rb atomic clocks [125] and POP-DR Rb atomic clocks [109] with state-of-the-art short-term frequency instabilities.

Figure 4.1 – *Photography of the AdM microwave cavity manufactored using SLA technolgoy (metal-coated polymer). Figure adapted from [109].*

In this chapter, the implementation of AdM microwave cavity to build an POP-DR Rb atomic clock [109] is presented. The first part of the chapter presents the AdM cavity and its main characteristic. The second part of the chapter is dedicated to the POP-DR Rb clock based on the AdM microwave cavity. First, the Ramsey spectroscopy results are presented. Then the short-term clock frequency instabilities measurement is presented. A large part of the results presented in this chapter was published in [109] and [126].

4.1 3D-printed microwave cavities

4.1.1 Description

A description of the microwave cavities used in this thesis is presented in section 2.3.3. The microwave cavities used in this thesis are based on a so-called loop-gap structure, which allows the use of the TE011-like mode for clock operation. The manufactured AdM cavity cylinder is shown in Figure 4.1. Due to the AdM technology, the prototype cylinder is monolithic. The cylinder consists of a cylindrical shield and the electrode structure. The cavity is assembled with two cavity endcaps. One is equipped with the excitation loop, and the other supports the vapour cell. The AdM microwave cavity was built by SWISSto12 based on numerical calculations performed by EPFL-MAG [115]. The AdM cavity is made of a polymer by a photopolymerisation process that uses the SLA technology [127]. The SLA technology enables a manufacturing precision of $\approx 40\ \mu$m. In order to become RF-functional, the cylinder surface is coated with copper using SWISSto12's electroless plating process. The copper surface is passivated using a thin silver layer. The total volume of the cavity is 0.044 dm^3 with a mass of 60 g. The microwave-field orientation and the Q-factor of the cavity are first studied numerically by EPFL-MAG. A FOF of $\approx$ 0.9 and a typical Q $\approx$ 150 are obtained.

4.1.2 Characterisation

The return loss of the AdM cavity (the S11 parameter) is measured using a vector network analyser when the cavity is fully assembled with the endcaps and the vapour cell inside. Figure 4.2 presents the measured and simulated S11 parameter. It shows that the AdM microwave cavity meets the required 6.835 GHz frequency, as predicted by the simulation. Fine tuning of the microwave-

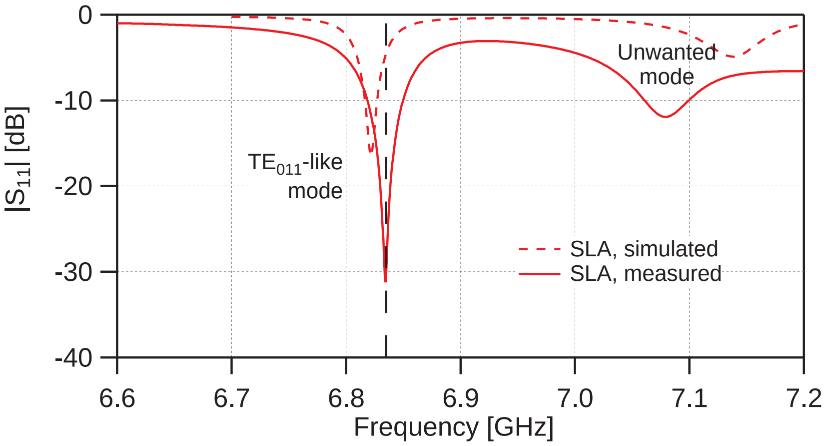

Figure 4.2 – *Return loss of the AdM cavity [109](solid line) measurement (dashed line) simulation. Figure adapted from [109].*

frequency resonance is achieved by two mechanisms [109]. The first mechanism is the use of a set of cavity prototypes with different gap sizes. The second mechanism is the adjustment of the cell position inside the cavity to change the dielectric loading of the cavity.

The measured Q-factor of the cavity is ≈ 60 for the SLA cavity. The difference of the predicted value (Q ≈ 150) is suspected of coming from manufacturing uncertainty on the vapour-cell tolerances and on the feeding loop, which increases the injection of the unwanted mode inside the cavity. The temperature sensitivity of the cavity detuning is measured $\partial\Delta\nu_{\mathrm{cav}}/\partial T = 250$ kHz/K. This value is higher than the typical temperature sensitivity of the CoM cavity of 40 kHz/K [31]. The impact on the cavity-pulling shift is still reasonable because the increase in the temperature sensitivity of the cavity is compensated by a reduction in the Q-factor of the cavity.

4.2 POP-DR Clock operation

In order to test the AdM cavity in an atomic clock, the fully assembled AdM cavity is placed inside a PP. The PP shares the same feature as the one described in section 2.3. The Rb vapour cell used in this PP possesses the same feature as the one described in section 2.3.2. The cell and cavity temperature is set at 63 °C and the stem temperature is set at 58 °C. No further optimisations of the cell and stem temperatures were carried out. The local oscillator used in this chapter is the same as the one described in section 2.3.4. A second AOM-LH identical to the one described in section 2.2.2 is used. Figure 4.3 shows the experimental breadboard.

Table
set at 7 mW, which corresponds to the maximum optical power achieved in this setup configuration. The microwave power is set at 9 μW, which corresponds to the first maximum of the Rabi oscillation. In our setup, a detection power of 435 μW achieved the higher central fringe contrast. The AOM-LH is frequency stabilised onto the F23 sub-Doppler transition, and the output optical frequency is frequency shifted by -150 MHz. Figure 4.4 compares the cell absorption spectrum obtained in the AOM-LH (bottom part) and in the PP (top part). In the next sections, the Zeeman spectrum, the Ramsey spectrum, and the Rabi oscillation are presented.

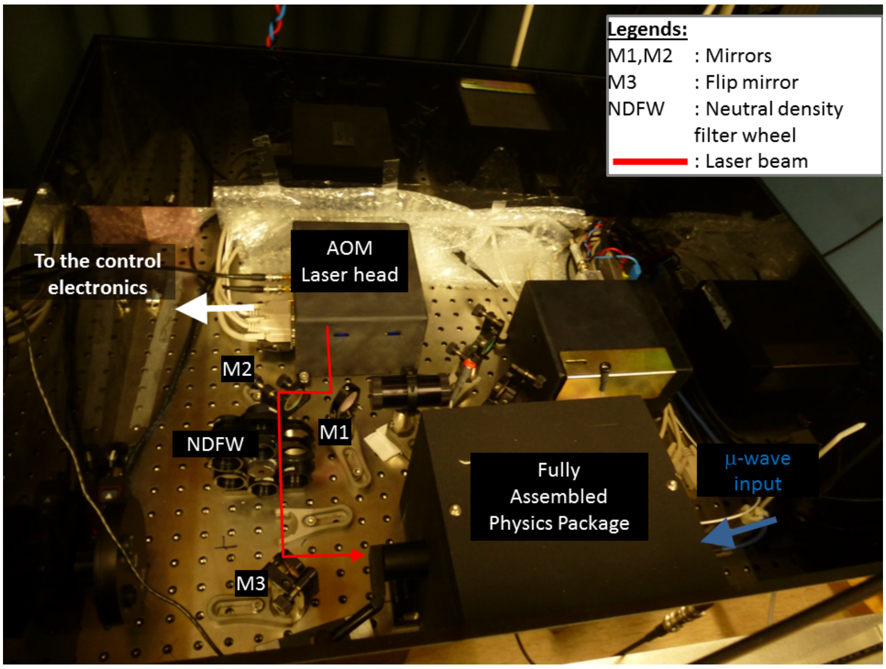

Figure 4.3 – *Experimental breadboard showing the Physics Package and the AOM laser head.*

Ramsey scheme	Duration [ms]	Input power
Optical pumping	$t_p = 0.4$	7 [mW]
Microwave pulses ($2 \times \pi/2$-pulses)	$t_m = 0.4$	9 [μW]
Ramsey time	$t_R = 3$	-
Optical detection	$t_d = 0.9$	435 [μW]

Table 4.1 – *Durations and input powers for three phases of optical pumping, microwave interrogation and optical detection used in this chapter.*

4.2.1 Ramsey spectroscopy results

The orientation of the microwave magnetic field parallel to the static magnetic field is evaluated by calculating the FOF (see equation 2.4). The Zeeman spectrum is measured in the DR-CW mode [109] with a microwave power of -29 dBm and a light intensity of 0.4 μW/mm^2. Figure 4.5 presents a typical Zeeman spectrum of the ground state. The Zeeman spectrum is composed of seven transitions of the ground states (see Figure 2.11). The sigma transitions are induced by the components of H perpendicular to the static magnetic field [74]. The strongly attenuated sigma transitions in Figure 4.5 confirm that the microwave magnetic field is parallel to the static magnetic field throughout the entire vapour cell. The experimental FOF is FOF = 0.98, which is larger than the one obtained for the CoM cavity (see Table 2.1).

As described in section 3.1, the measurement of the Rabi oscillation is a good indicator of the inhomogeneity of the microwave-field amplitude. Figure 4.6 compares the Rabi oscillation measured using the AdM cavity with the Rabi oscillation measured using the CoM cavity (see section 3.1). The Rabi oscillation measured with the AdM cavity shows slower damping that demonstrates a slightly better microwave-field amplitude homogeneity across the cell. The Ramsey spectrum is presented in Figure 4.7, the spectrum is measured in the condition described in Table 4.1. A central fringe contrast of 34% is achieved.

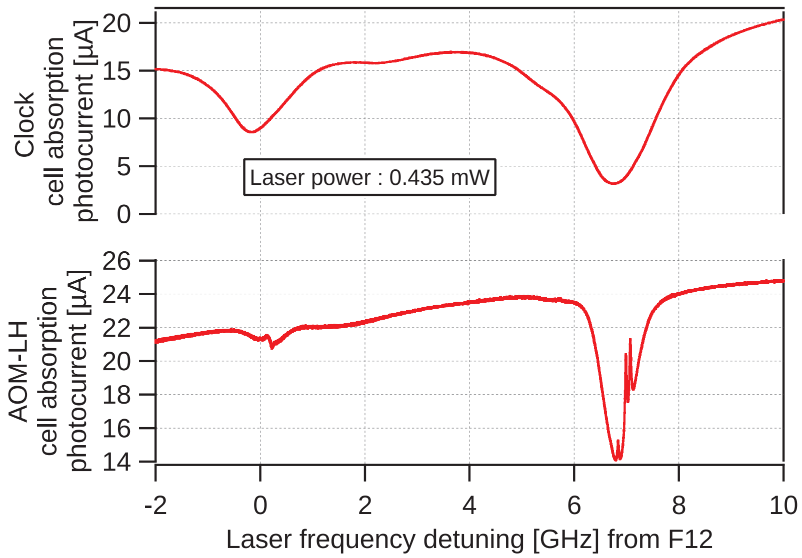

Figure 4.4 – *Top: clock cell absorption signal. Bottom: AOM-LH sub-Doppler absorption signal. The laser optical power is 0.435 mW.*

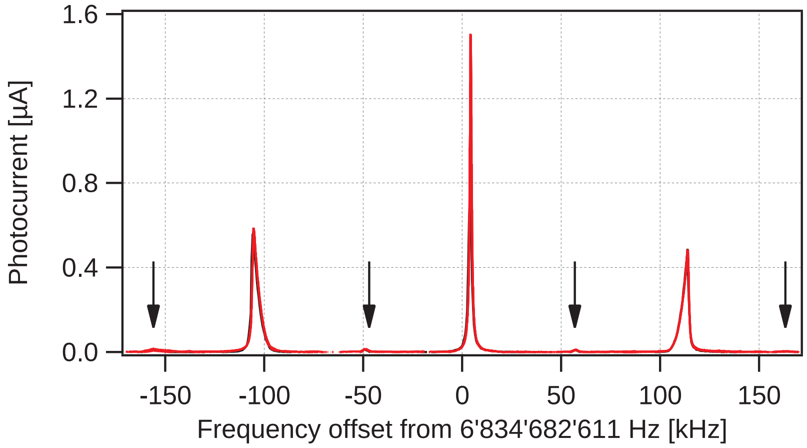

Figure 4.5 – *Measured Zeeman spectrum for the AdM cavity [109]. The sigma transitions are higlighted by arrows. Figure adapted from [109].*

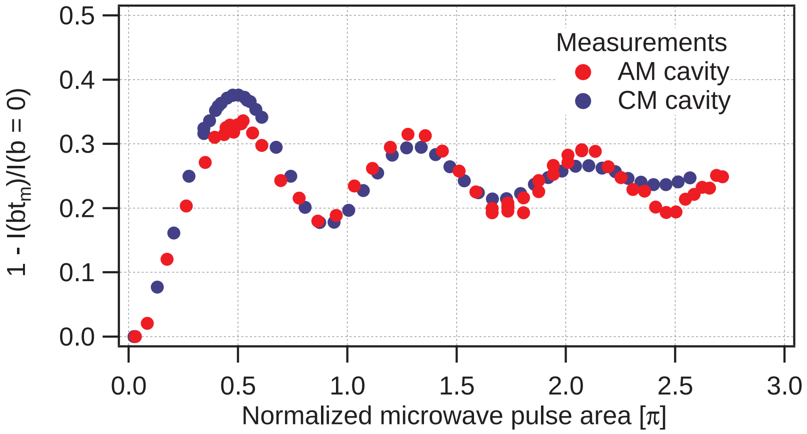

Figure 4.6 – *Measured Rabi oscillation (blue dots) with the CoM cavity see section 3.1 (red dots) with AdM cavity in the condition described in Table 4.1. Figure adapted from [109].*

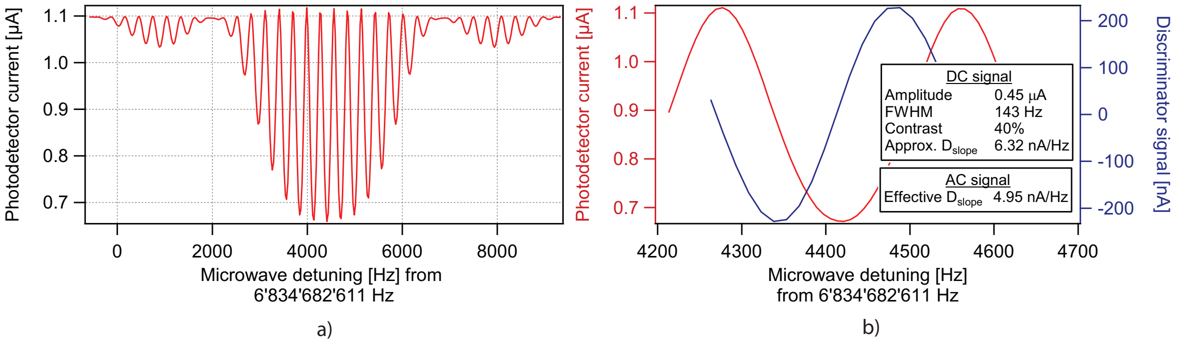

Figure 4.7 – *Ramsey signal with a) large span b) central fringe. The estimated discriminator slope is obtained using* $D_{approx} = 2A/FWHM$*. Figures adapted from [109].*

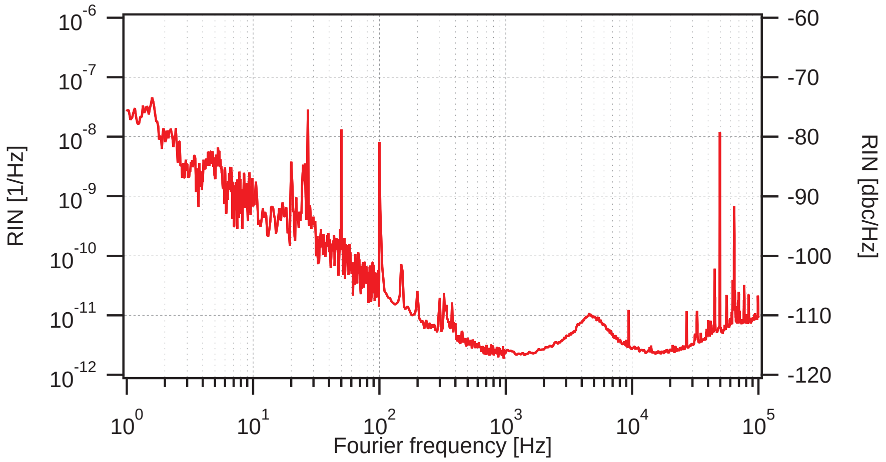

Figure 4.8 – *Typical optical detection signal's RIN measured for a continuous detection light power of 0.435 mW Figure adapted from [109].*

4.2.2 Clock performance

A good estimation of the short-term frequency instability is obtained using the analytical expressions presented in section 1.4.4. Figure 4.8 presents a typical optical-detection signal's RIN. It was measured for a continuous detection light of 435 μW of optical power. Table 4.2 presents the estimated short-term frequency instabilities induced by the shot noise (equation 1.64), the optical-detection noise (equation 1.65), and the LO phase noise via the Dick effect (equation 1.66). The total estimated short-term frequency instability is $2.5 \cdot 10^{-13}\ \tau^{-1/2}$ where the optical-detection noise with a contribution of $1.7 \cdot 10^{-13}\ \tau^{-1/2}$ and the Dick effect with a contribution of $1.8 \cdot 10^{-13}\ \tau^{-1/2}$ contribute equally.

The quartz is frequency stabilised on the central Ramsey fringe (see Figure 4.7b). The clock frequency is recorded over a period of one hour. The overlapping Allan deviation of the clock frequency is shown in Figure 4.9 as well as the relative clock frequency (inset). A short-term frequency instability of $2.5 \cdot 10^{-13}\ \tau^{-1/2}$ is measured in agreement with the estimated short-term stability of Table 4.2.

Shot-Noise limit	$2.7 \cdot 10^{-14}\ \tau^{-1/2}$
Optical Detection	$1.7 \cdot 10^{-13}\ \tau^{-1/2}$
Dick Effect (LO)	$1.8 \cdot 10^{-13}\ \tau^{-1/2}$
Total Estimated	$2.5 \cdot 10^{-13}\ \tau^{-1/2}$
Measured	$2.5 \cdot 10^{-13}\ \tau^{-1/2}$

Table 4.2 – *Estimated short-term frequency instability budget.*

The measured short-term frequency instability reported in this chapter (see Figure 4.9) is better by a factor of two rather than the one reported in Chapter 3. This is mainly due to the higher detection RIN reported in Chapter 3 and is better by a factor four compared to the frequency instabilities reported for the same SLA cavity by a factor four with the clock is operated in DR-CW [125]. The measured short-term frequency instability of Figure 4.9 is comparable to the state-of-the-art clock frequency instabilities reported for CW-DR Rb [26], POP-DR Rb [128], and Cs SABR-CPT [129].

The long-term frequency stability of the clock depends on many parameters, especially on the microwave-cavity ageing. Ageing studies of the AdM cavity were carried out [126] with a focus on the RF properties of the cavity. The ageing procedure consisted of thermal cycles; between each cycle, the cavity properties (dimensions, adhesions, analysis of the surface, and the RF performance) were measured. The results show that changes in the cavity properties are below the instruments uncertainties [126].

4.3 Conclusion

This chapter reviewed the detailed study of a compact loop-gap microwave resonator cavity realised by AdM techniques, in view of the of AdM microwave cavities applications to Rb DR atomic clocks [109][125].

The AdM cavity made by the vat photopolymerisation process using stereolithography (SLA) tech-

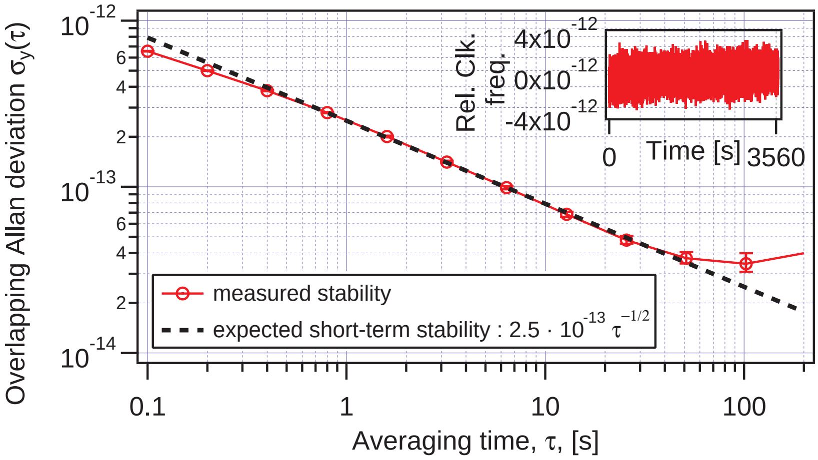

Figure 4.9 – *Overlapping Allan deviation of the clock frequency shown in the inset. Clock frequency shows a frequency drift of* $1.7 \cdot 10^{-11}$*/day. Figure adapted from [109].*

nology showed RF features similar to the conventional microwave cavity. A high FOF≈ 0.98 and the Rabi oscillations measured demonstrate a microwave-field amplitude uniformity and homogeneity at the same order as the CoM cavity studied in Chapter 3. The AdM cavity presents a low Q-factor (Q ≈ 60), which is ideal for the POP-DR Rb clock because it reduces the impact of a cavity-pulling shift.

The POP-DR Rb clock based on the AdM cavity demonstrated a short-term frequency instability at the state-of-the-art level with a short-term frequency instability of $2.5 \cdot 10^{-13}\ \tau^{-1/2}$ between 0.1 s to 100 s. In order to demonstrate a medium- to long-term frequency instability at the level of 10^{-14} at 10^4 seconds of integration time, the procedure described in Chapter 3 needs to be repeated. First, the cell temperature needs to be adjusted to cancel the cell-temperature sensitivity. This is followed by intensity LS and MP shift measurements. However, we would expect no significate difference with the operation conditions of the CoM cavity.

In this study, only the core cylindrical-structure of the microwave cavity was made using the AdM technique; the cavity endcaps (with the coupling loop) were made conventionally. Preliminary tests have demonstrated that the endcap with the coupling loop can be produced using the AdM technology. In particular, a prototype cavity cylinder with one endcap (containing the coupling loop) was realised monolithically using SLA (see Figure 4.10). Preliminary RF tests have shown that the Rb frequency resonance can be achieved with the prototype. This demonstrates that AdM technology can produce RF components with very low dimensions—for example, the mm-scale coupling loop—with control of the reproducibility and repeatability. Additive manufacturing technology can be applied to build cavities based on more complex geometry or cavities with mm-scale features. An additional benefit of the AdM microwave cavity is the mass reduction (≈ 30%) compared to conventional cavities.

Finally, this preliminary study shows that AdM technology, and AdM microwave cavities, in particular, demonstrate great potential for the next generation of compact and high-performance DR vapour-cell atomic clocks. The AdM cavity prototype fulfils the strict RF requirements. The reduced time and cost in the fabrication of AdM microwave cavities are of interest for industrial purposes and for the production of a moderate amount of cavity prototypes useful for prompt tests of novel cavity designs.

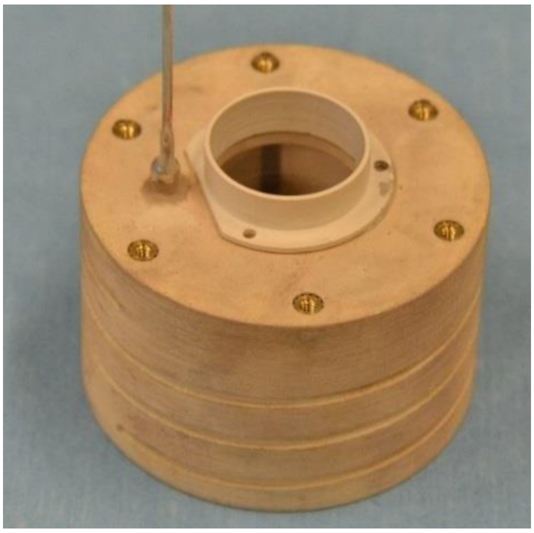

Figure 4.10 – *Photography of the AdM microwave cavity with one endcaps manufactored monolithically by SLA, courtesy to SwissTo12 (see also [130])*

5 Optical-frequency standard at 1.5 μm and 780 nm

The prediction of the rate of climate change during the 21st century is a major, growing field of research. The impact of these changes on our society could be very important and being able to anticipate them could be a necessity. The exact reason for the variation of the Earth's temperature is not a simple problem, and the active discussion in the scientific community shows the complexity of this problem.

Many observations since the 1950s show a warming of the world's climate [131]. Recent observations have been conducted using satellites, but older observations used paleoclimate reconstructions that provide records dating back millions of years. Together, these systems provide a long-term observation of the rate of climate change.

Three major gases of interest to climate scientists are carbon dioxide (CO_2), methane (CH_4), and nitrous oxide (N_2O). These are called greenhouse gases. A part of these gases comes from anthropogenic origins. Indeed, from 1750 to 2011, CO_2 emissions from human activity (such as fuel combustion, deforestation, and land use change) released 555 ± 85 PgC[1], corresponding to a total of 2035 ± 312 $PgCO_2$. Not all the CO_2 is injected into the atmosphere. A total of 240 ± 10 PgC have been accumulated in the atmosphere while 155 ± 30 PgC have been absorbed by the ocean and 160 ± 90 PgC have been stored into vegetation biomass and soils not affected by human activities [131]. These anthropogenic emissions have increased by 40% of the concentrations of carbon dioxide since the pre-industrial times.

As CO_2 gas is not static in the atmosphere but can interact with other gases, the ocean, or land, determining the impact of greenhouse gas requires understanding how these interactions take place. For this, a satellite provides more accurate measurements than a surface network of measurement because it covers a larger surface of measurement. However, the accuracy needed for this kind of measurement is difficult to achieve in space due to the many constraints of space.

Integrated-path differential absorption (IPDA) LIDAR is a technique that offers the advantage of eliminating the contribution of atmospheric scattering and can be used during daytime or night-time. This technique uses the laser light scattered back from the earth surface (see Figure 5.1). More exactly, two pulses of light at two different wavelengths are emitted through the atmosphere. The first wavelength, λ_{on}, is on or near the centre of one CO_2 absorption line, and the second wavelength, λ_{off}, is chosen such that the absorption from the CO_2 is less important. Then the quantity of interest is the difference between the two atmospheric transmissions. Investigations into the feasibility of a space instrument using the IPDA LIDAR technique were done by space agencies [34][132][133], including the European Space Agency (ESA) in the framework of the

---

[1] 1 PgC = 1 Gigatonne of carbon = 10^{15} gramme of carbon.

Advanced Space Carbon and Climate Observation of Planet Earth (A-SCOPE) [44][45]. Two wavelengths are envisaged for monitoring the CO_2 molecule: 1572 nm (called the B1 line) and 2051 nm (called the B2 line). The frequency stability and accuracy requirement on λ_{on} for both wavelengths were evaluated by Fix et al. [36] for such a space mission. In the case of a transmitter laser emitting at 1572 nm (B1) on the slope of one CO_2 absorption line, frequency fluctuation below 200 kHz ($<10^{-9}$ fractional frequency stability at 1572 nm) at 7 s averaging down below 20 kHz ($<10^{-10}$ fractional frequency stability at 1572 nm) for an integration time from 700 s to 3 years of mission operation time is targeted [36].

In the framework of a collaboration project between the Deutsches Zentrum für Luft- und Raumfahrt (DLR) and the LTF, a compact optical-frequency reference breadboard at 1572 nm (for the λ_{on} wavelength beam stabilisation) was designed at the LTF [64]. The frequency stabilisation was done using Rb since it has narrow sub-Doppler transition lines compared to CO_2. As the absorption wavelength of the Rb is around ≈ 780 nm, the stabilisation of the laser at 1.5 μm used frequency doubling and a compact optical-frequency comb generator (OFCG)[64][36]. The OFCG was used to transmit the frequency stability obtained using the Rb vapour cell to a slave laser emitting at 1572 nm. At LTF, preliminary frequency stability studies demonstrated that the frequency fluctuation of one line of the comb benefits from the high level of frequency stability obtained using the Rb vapour cell [64]. The work presented in this chapter concerns the frequency stability measurement of a 1572-nm slave laser offset locked to one line of the comb.

This chapter is decomposed in two parts.

- The first part of this chapter describes the laser system developed as an optical reference at 1572 nm. First, the laser system is described in section 5.1. Second, frequency instability measurements at 780 nm, 1560 nm, and 1572 nm are presented in section 5.2. A long-term frequency instability at the level of $4 \cdot 10^{-12}$ at $2 \cdot 10^5$ s of integration time is demonstrated. These results were published in a peer-reviewed article [37] and conference proceedings [65][134].
- The second part of this chapter presents additional studies on the Rb stabilisation of the laser system at 1560 nm and 780 nm. First, the reproducibility and repeatability of the frequency of the Rb-stabilised laser at 1560 nm and 780 nm are evaluated and presented in section 5.3. Second, the noise and spectral properties of the Rb-stabilised laser are analysed in section 5.4. The noise conversion through the frequency doubling is measured, and its impact on the laser linewidth and optical spectrum is presented. These studies were published in conference proceedings [65][134].

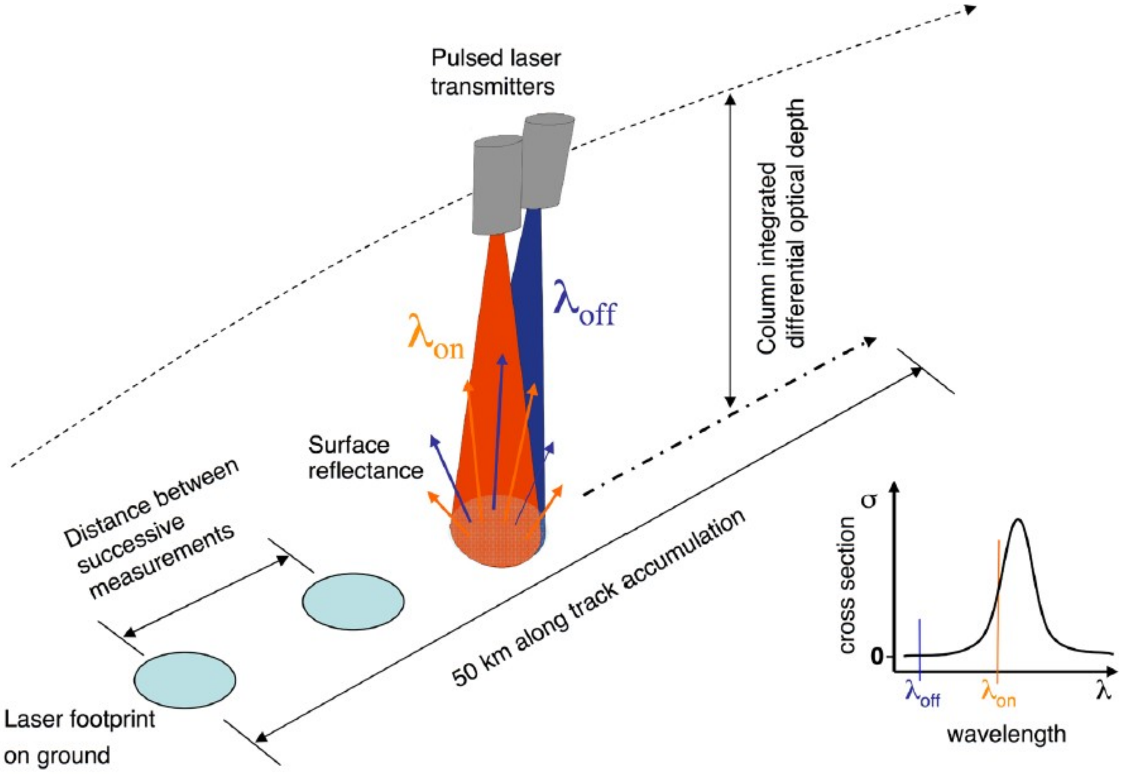

Figure 5.1 – *LIDAR principle and* λ_{on},λ_{off} *illustrations. Courtesy to Fix et al. [36].*

5.1 Experimental Setup

The laser system is presented in Figure 5.2. A DFB laser emitting at 1560 nm is used as a master laser. The master laser is frequency-doubled and frequency stabilised using the FRU (see section 2.2.1). The master laser is used to seed an OFCG, which generates an optical comb centred around the master laser frequency. A second DFB laser emitting at 1572 nm is used as a slave laser. The slave laser is offset-locked to one line of the optical comb. The optical system is fully fibred. The laser system possesses three different outputs (indicated in Figure 5.2): 780 nm, 1560 nm, and 1572 nm.

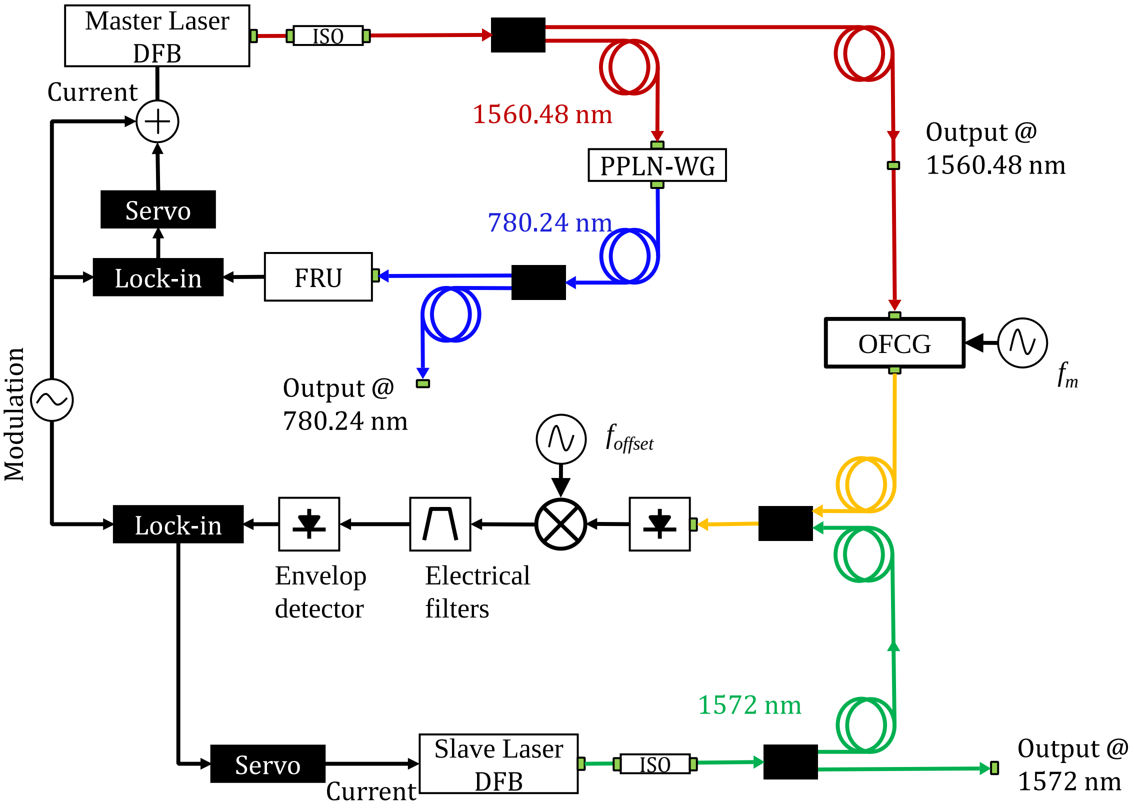

Figure 5.2 – *Fibered laser system. DFB : distributed feedback laser. PPLN-WG : periodically-poled lithium niobate waveguide. OFCG : optical frequency comb generator. ISO: fibered optical isolator. The black boxes are fibered beam splitter.*

5.1.1 Frequency-doubled Rb-stabilized 1560-nm laser

The master laser is a fibre-pigtailed DFB laser (Emcore) with 80 mW of output optical power at 1560 nm. The master laser is followed by a fibred optical isolator used to reduce the residual optical feedback. The master laser is split into two outputs using a 50/50 polarisation-maintaining fibre beam splitter (PM-BS). The first output is used to frequency stabilise the master laser and the second to generate the optical frequency spectrum (OFC).

The first output is frequency-doubled using a second harmonic generator (SHG) module made of a fibre-pigtailed 5 cm long periodically-poled lithium niobate (PPLN) waveguide (WG). The optimal operation temperature and the efficiency of the module is determined to be 50°C and 300 %/W (including the fibre coupling losses), respectively [64]. With 15 mW of incident optical power at 1560 nm, a maximum of 670 μW is generated at 780 nm [64]. The frequency-doubled light is then injected into the FRU (see section 2.2.1). The master laser is frequency stabilised on ^{87}Rb D_2 line at 780.24 nm using sub-Doppler spectroscopy. The 1560 nm laser is frequency-modulated with a modulation depth of ≈1 MHz by applying a 50 kHz sinusoidal signal to its injection current. An error signal is generated by demodulating the absorption signal at the modulation frequency using a lock-in amplifier. A feedback signal processed by a proportional-integrator servo-controller is applied to the laser injection current.

5.1.2 Optical frequency comb generator

The frequency-stabilised master laser is injected into the OFCG (OptoComb). The OFCG consists of an electro-optic modulator (EOM) enclosed in a waveguide Fabry-Perot cavity. The cavity finesse is 60, and its free spectral range is 2.5 GHz. The cavity is temperature stabilised at 45.2 °C. The EOM is driven by an RF signal f_m at 10 GHz [2] in resonance with the spectral-range fourth harmonic. The comb span can reach 30 to 40 nm centred at the master-laser frequency ν_{Master}. Figure 5.3 presents a typical optical-frequency comb generated for an input optical power of 12 mW, f_m = 10.0055 GHz (line spacing ≈ 0.08 nm) and a RF power of -2.8 dBm.

The n$^{\text{th}}$-order optical comb line frequency, ν_n, is simply obtained by $\nu_n = \nu_{\text{Master}} + \text{n}\cdot f_m$, where n is positive or negative integer value. The number of comb lines is approximately 500. The frequency fluctuation of the master laser is transmitted to all comb lines where the frequency fluctuation of the RF signal can reasonably be neglected. An important feature of the OFCG is that the 50-kHz FM applied to the master laser is also transferred to each comb line. The 50-kHz modulation present on each line comb is used as a modulation frequency for the offset locking of the slave laser to one line of the comb.

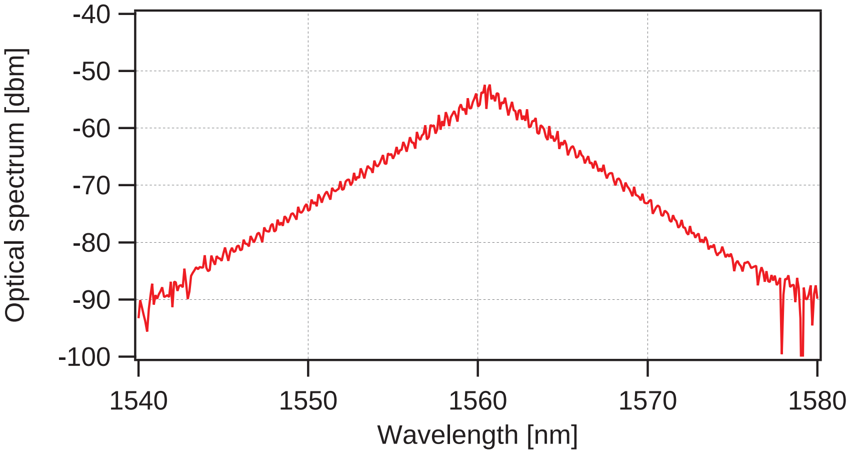

Figure 5.3 – *OFC spectral envelope.*

5.1.3 Offset-locked 1572 nm laser

The slave laser is a fibre-pigtailed DFB laser (Fitel) with 60 mW of output optical power at 1572 nm. The slave laser is followed by a fibred optical isolator used to reduce residual optical feedback.

---

[2] the synthesiser is referenced to a H-maser to guarantee good long-term frequency stability of the RF signal

The slave laser is split into two outputs using a 50/50 PM-BS. The first output is used to frequency stabilise the slave laser and the second as the laser system output.

The first output is used to frequency stabilise the slave laser on one line of the comb, using an offset-lock method [135]. First, the beat between the slave laser and the OFC is detected using a fast photodiode. Second, after a stage of amplification, the beat signal is down-converted by mixing with an external frequency f_{offset} generated from an external LO. The LO is also referenced to an H-maser. Third, the down-converted beat signal is filtered using a combination of high- and low-pass filters. Finally, the power of the down-converted beat signal is obtained using an envelope detector. The use of high- and low-pass filters and an envelope detector allows an absorption-like spectrum to be generated in the low-frequency electrical domain, which acts as a frequency discriminator [135]. First, a 11-MHz low-pass filter is used - when combined with a envelope detector - to detect the power of the down-converted beat signal between - 11 MHz and + 11 MHz. It results in a signal that is non zero for a down-converted beat frequency between -11 MHz and +11 MHz and zero for all the other frequencies and notably suppresses the beat notes with the other comb lines. A 1-MHz high-pass filter placed after the low-pass filter allows to create a dip-like feature with a FWHM of 2 MHz in the signal obtained from the envelope detector, see Figure 5.4. This narrow dip-like features is used for the frequency offset lock. The signal from the envelope detector is demodulated at the master-laser modulation frequency, which generates the error signal [135].

The error signal is obtained by demodulation at 50 kHz because the down-converted beat signal possesses the 50-kHz modulation of the master laser. An example of such a signal is shown in Figure 5.4. The frequency of the down-converted beat signal can be frequency stabilised to the centre of the envelope detector output (Figure 5.4) by acting on the injection current of the slave laser. The absence of FM on the slave-laser frequency implies that the laser system output is free of modulation.

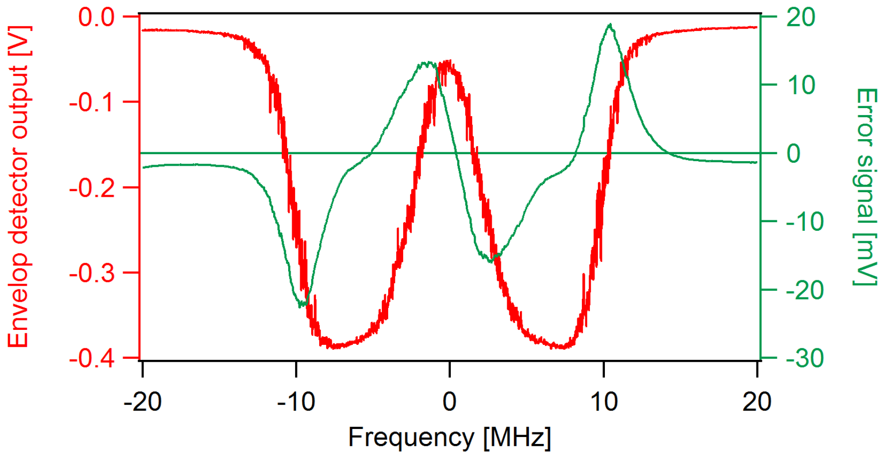

Figure 5.4 – *Envelope detector output (red curve) and the associated error signal (green curve).*

The slave-laser frequency is given by $\nu_{\text{Slave}} = \nu_{\text{Master}} + \text{n}\cdot f_m \pm f_{\text{offset}}$ and can be tuned by changing the comb spacing f_m and the offset frequency f_{offset}, which allows the slave-laser frequency to be frequency stabilised on the side of the CO_2 absorption profile. Figure 5.5 presents the CO_2 absorptions lines around 1572.5 nm (6360 cm^{-1}) obtained from the HITRAN database (edition 1986 [136]). From the reference absolute frequency of the CO_2 absorptions lines, it is possible to determine the comb line close to each CO_2 absorption line of Figure 5.5 by:

$$n = \frac{f_{\mathrm{R(x)}} - f_{\mathrm{Master}}}{f_m} \tag{5.1}$$

The optical frequency of the F23 transition of the ^{87}Rb D_2 line was precisely measured by Ye et al. [70]. The reference value of the F23 transition frequency is 384,228,115,203.2 kHz for the considered transition with an uncertainty of ± 11 kHz. Consequently, the reference value for the fundamental laser at 1560 nm corresponds to 194,114,057,601.6 kHz (± 6 kHz). Table 5.1 presents the comb lines associated with each CO_2 absorption line of Figure 5.5. The frequency difference between CO_2 transitions with the closest comb line is also presented in Table 5.1. For the demonstration of the laser system, the CO_2 R(20) transition is selected because, at the time of the measurement, the synthesiser used for the generation of f_{offset} was only able to generate an RF signal of frequency lower than 300 MHz.

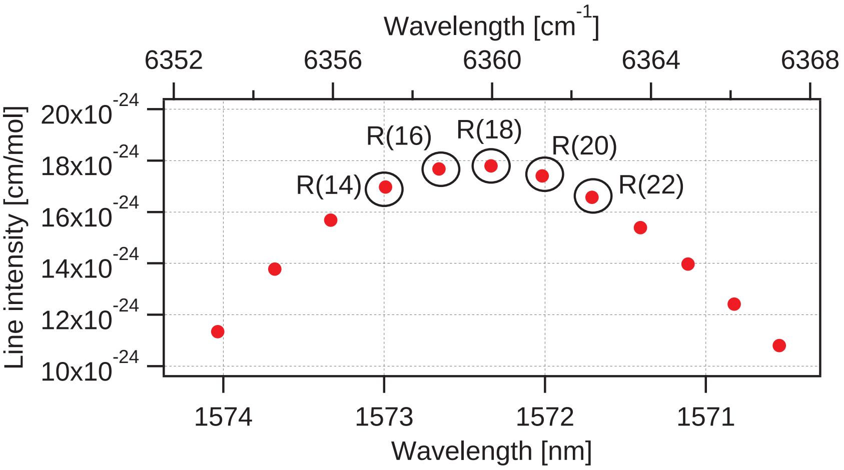

Figure 5.5 – *CO_2 absorption lines around 1572.5 nm (R(18) : 6360 cm^{-1}) [136].*

CO_2 R(x)	Comb line n	$f_{\mathrm{R(x)}} - f_n$ [MHz]
R(14)	-149	4’423
R(16)	-145	3’762
R(18)	-141	2’206
R(20)	-137	-240
R(22)	-133	-3’573

Table 5.1 – *Comb lines associated to each CO_2 transitions displayed on Figure 5.5 for f_m = 10.0055 GHz.*

Figure 5.6 presents the CO_2 absorption line R(20) (190’743’063’884’630 Hz [136]) and the offset-lock absorption-like signal obtained by varying the slave-laser frequency. The CO_2 absorption spectrum is obtained using a 15 cm long CO_2 vapour cell where the slave laser is reflected through it five times. The envelope detector output signal possess two absorption-like signals separated by a frequency interval of $2 \cdot f_{\mathrm{offset}} = 100$ MHz and centred around the comb line number n = -137. For the demonstration of the laser system, the slave laser is frequency stabilised on the right offset-lock absorption-like spectra at:

$$\nu_{\text{slave}} = \nu_{\text{master}} + n \cdot f_m + f_{\text{offset}}. \tag{5.2}$$

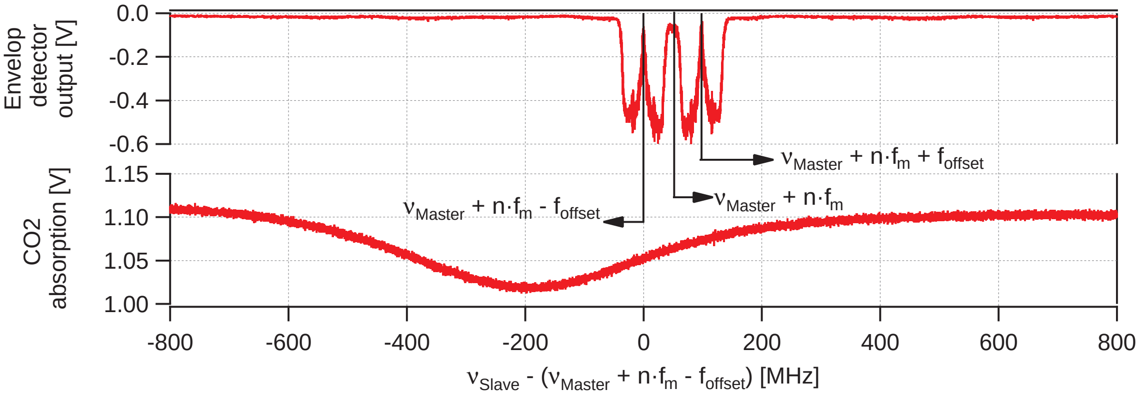

Figure 5.6 – *Top : Envelope detector output with* $f_{offset} = 50$ *MHz. Bottom : R(20)* CO_2 *absorption profle.*

5.1.4 Setup breadboard

A picture of the laser system breadboard is shown in Figure 5.7. The FRU temperatures (vapour cell temperature, baseplate temperature) are controlled by RCEs. The master and slave-laser temperature and injection currents are controlled by home-made electronics. The 10 GHz RF signal f_m is generated with a Hewlett-Packard synthesiser. The offset RF signal f_{offset} is generated with an SDI synthesiser. Both synthesisers are referenced to the same H-maser.

5.2 Frequency stability measurements

In this section, frequency stability is presented at three stages of the laser system: the master laser before (1560 nm) and after (780 nm) the frequency-doubling process and at the slave laser (1572 nm). The frequency instabilities achieved at 780 nm using the vapour cell are transferred without degradation to the laser system output at 1572 nm.

Previous evaluation of the frequency instability of the master laser was performed by Matthey et al. [64]. They demonstrated an identical relative frequency instability of the master laser at 1560 nm (before the PPLN-WG) and 780 nm (after the PPLN-WG). Moreover, the frequency instability of the master laser was shown to be transferred without additional frequency fluctuation of the OFC line [64]. In this section, an enhancement of the frequency instability of the master laser compared to previously reported results is presented [65][134]. Then the frequency instability of the slave-laser offset-lock to one line of the comb is presented [65][134].

5.2.1 Master-laser frequency instability measurement

The frequency stability of the master laser is evaluated from heterodyne beat measurements with external optical-frequency references. At 1560 nm, the fully-stabilised commercial Er:fibre comb (FC1500 from MenloSystems) referenced to an H-maser with a mode linewidth of ≈200 kHz (FWHM) was used as an optical reference. The 1560 nm laser was locked onto the F23 sub-Doppler transition.

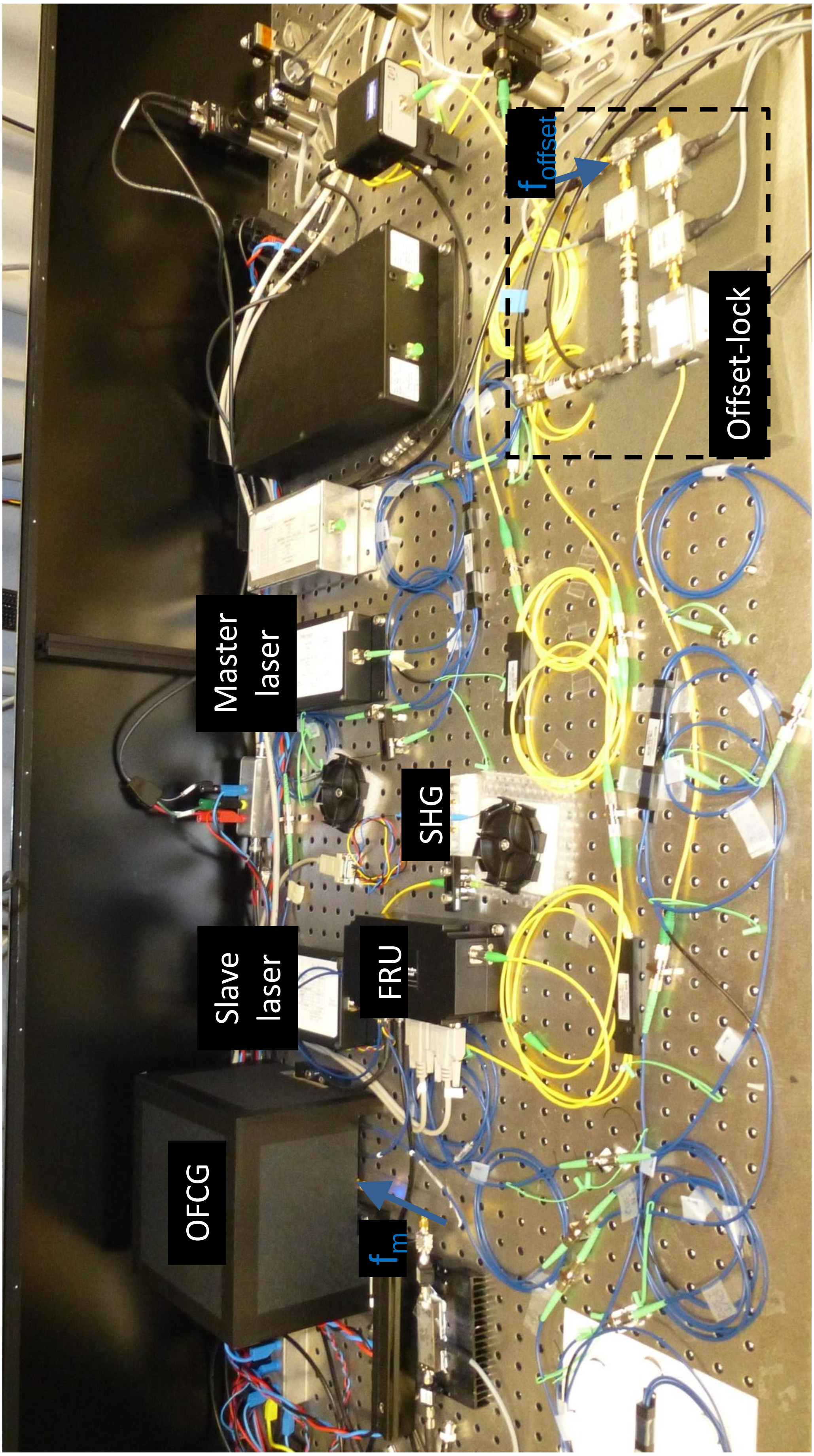

Figure 5.7 – *Experimental breadboard showing the laser system. This setup corresponds to the block scheme presented in Figure 5.2.*

A Std-LH (see Figure 2.3) locked onto the cross-over transition CO22-23 served as a frequency reference at 780 nm. The frequency stability of the master laser is simultaneously evaluated at 780 nm and 1560 nm.

The retrieved frequency stabilities are reported in Figure 5.8 in terms of overlapping Allan deviation. A fractional frequency instability of $5.2 \cdot 10^{-12}$ was obtained at 1560 nm for an integration time of 1 s, corresponding to absolute frequency variations of less than 1 kHz. It reached $2.7 \cdot 10^{-12}$ on the long-term (at 10^5 s). At 780 nm, the measurement of the short-term stability (below 10 s integration time) was limited by the resolution of the frequency counter, which was different from the counter employed in the measurement at 1560 nm. The long-term stability measured at 780 nm was limited by the frequency instability of the Std-LH used in the heterodyne beat. The measured frequency stability presents a bump that reaches $4 \cdot 10^{-11}$ at 100 s of integration time. However, the frequency instability performance fulfils the requirement (see Figure 5.8).

The main limitation in the mid-term stability of this laser arose from spurious reflections in the fibred system, which produced etalon fringes superimposed to the sub-Doppler absorption spectrum (see an example of etalon fringes in Figure 5.9). The laboratory temperature fluctuation (±1°C) results in the change in the etalon fringes, which leads to an increase in the frequency instability at integration times in the range of 100 s at both wavelengths.

The short-term frequency instability measured in this study is improved by one order of magnitude compared to the result reported by Matthey et al. [64]. This is because of the substitution of one damaged fibre PM-BS at 1560 nm at the output of the master laser. This PM-BS was responsible for frequency instabilities between 1 to 10 s of integration time probably by inducing reflections inside the fibre system.

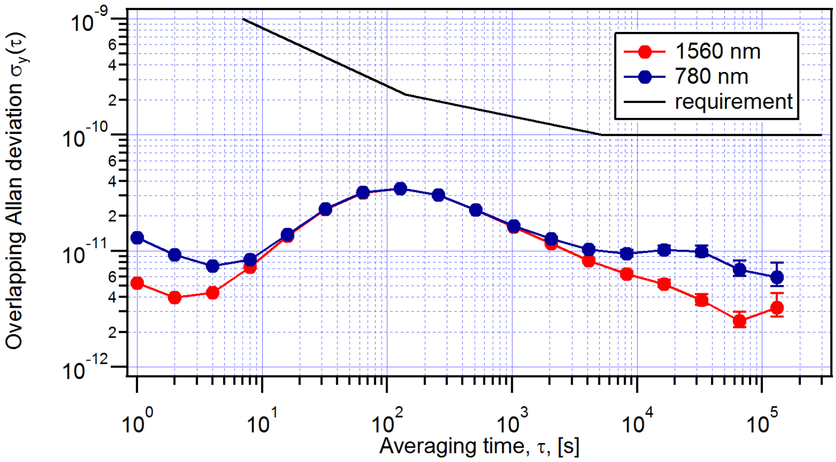

Figure 5.8 – *Relative frequency stability of the master laser. Red dots: beat note at 1560 nm of the master laser heterodyned with a fully-stabilized commercial Er-fiber frequency comb referenced to an H-maser. Blue squares: beat note at 780 nm of the frequency-doubled laser heterodyned with a reference 780-nm laser. Figure adapted from [65].*

Further improvements of the master-laser frequency instability were performed by N. Almat et al. [106][105]. A short-term frequency instability of about $2-5 \cdot 10^{-12}$ was demonstrated [105]. However, the etalon fringe still represents an important source of frequency instability in the medium term. A solution would be to subtract the signal at the entrance of the vapour cell from the sub-Doppler signal. An other possible solution is to subtract the Doppler background from the sub-Doppler

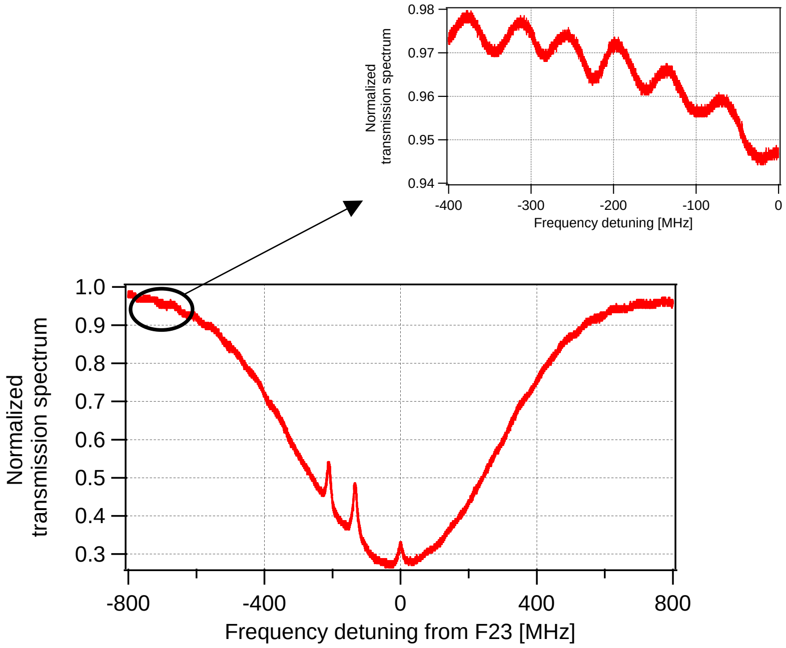

Figure 5.9 – *FRU absorption spectrum and highlight of etalon fringes.*

signal [68] [69]. In both manners, the signal used to frequency stabilise the laser contains only the information about the sub-Doppler signal and no other signals generated by the undesired optical cavity in the fibred system. This solution can be implemented because of the design of the FRU that contains one photodetector measuring the optical power at the entrance of the vapour cell and one photodetector after the vapour cell.

The use of the fully-stabilised Er:fibre comb allows the absolute frequency of the master laser at 1560 nm to be determined. The optical frequency is obtained from the measured frequencies of the comb repetition rate f_{rep} ($\approx$ 250 MHz), the carrier-envelope offset f_{CEO} ($\approx$ 20 MHz), and the beat signal f_{beat} between the laser and the comb:

$$\nu_{\text{laser}} = m \cdot f_{\text{rep}} + f_{\text{CEO}} - f_{\text{beat}}, \tag{5.3}$$

where m is the index of the comb mode (of the Er-fibre comb) involved in the beat signal. The sign of the beat signals f_{CEO} and f_{beat} was determined before the measurement. The Er-fibre comb mode $m = 767076$ was determined based on the reference F23 frequency [70]. An absolute master-laser frequency of (192’114’057’175 ± 10) kHz is measured.

5.2.2 Slave-laser frequency instability measurement

The frequency instability of the slave laser is evaluated from heterodyne beat measurements at 1572 nm with the fully-stabilised commercial Er-fibre comb referenced to an H-maser. The frequency instability measurement is performed for $f_{\text{offset}} = 50$ MHz and $f_m = 10.0055$ GHz so that the slave-laser frequency is lying in the CO_2 R(20) absorption line. The offset-lock absorption-like error signal is optimised by increasing the master-laser modulation amplitude. This consequently degrades the master-laser short-term frequency stability. The relative frequency instability of the slave laser is shown in Figure 5.10. The short-term frequency instability is $1 \cdot 10^{-11}$ at 1 s of integration time and is below $2.5 \cdot 10^{-11}$ for all integration times τ reaching $4 \cdot 10^{-12}$ on the long-term.

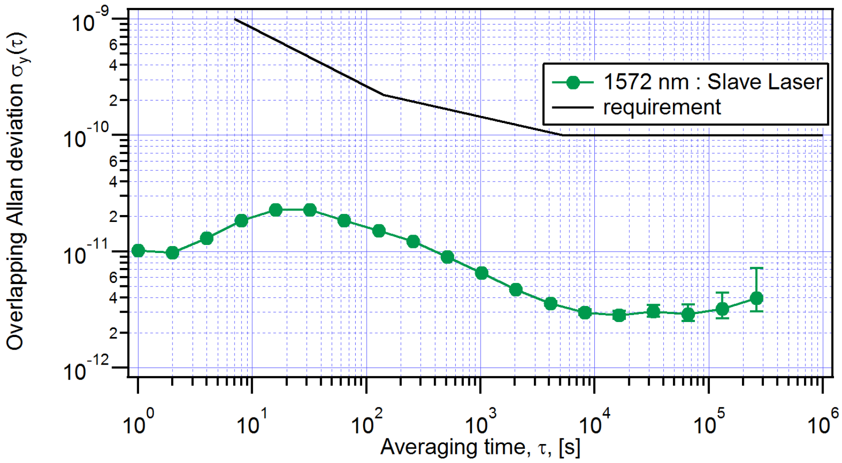

Figure 5.10 – *Relative frequency stability of the slave laser at 1572 nm. Figure adapted from [65].*

During this measurement, the laser system was less protected against rapid laboratory temperature changes (± 1°C) compared to the frequency instability measurement performed for the master laser. This resulted in a more severe impact of the frequency fluctuation induced by the etalon fringes, which shifted the frequency instability bump in the overlapping Allan deviation towards 30 s of integration time. Nevertheless, the demonstrated slave-laser frequency instability fulfils the requirement for atmospheric CO_2 monitoring at all time scales by two orders of magnitude. Moreover, the measured frequency instability of the slave laser is equivalent to the frequency instability of the master laser, demonstrating frequency transfer without the significant addition of frequency instability. The slave-laser frequency instability can be improved for all τ by reducing the impact of the etalon-fringes frequency fluctuation of the master-laser frequency stability. The frequency instability performances reported in this study are equivalent to the results reported using a compact 10-cm long multipass (optical pathlength of the order of 10 m) Herriott CO_2 cell by Numata et al. [35] and by Du et al. [137]. However, the long-term frequency instability presented in this study is one order of magnitude better than these two literature values for an integration time between 10’000 s and 100’000 s (see Figure 5.11).

The use of the fully-stabilised Er:fibre comb allows the absolute frequency of the slave laser to be determined. The optical frequency is obtained from the measured frequencies of the comb repetition rate f_{rep}, the carrier-envelope offset f_{CEO}, and the beat signal f_{beat} between the laser and the comb:

$$\nu_{\text{laser}} = m \cdot f_{\text{rep}} + f_{\text{CEO}} - f_{\text{beat}}, \tag{5.4}$$

where m is the index of the comb mode involved in the beat signal. The sign of the beat signals f_{CEO} and f_{beat} was determined before the measurement. The comb mode $m = 761603$ was determined based on the reference $f_{R(20)}$ frequency. An absolute slave-laser frequency of (190’743’357’072 ± 7) kHz is measured. The expected slave-laser frequency is given by equation 5.2 and is given by $f_{\text{slave}}^{\text{expected}}$ = (190’743’353’674 ± 10) kHz using the master-laser optical frequency measured in the previous section, f_m = 10.005 GHz and f_{offset} = 50 MHz. It leads to a frequency difference of ≈ -4 MHz between the expected value given by equation 5.2 and the measured optical frequency.

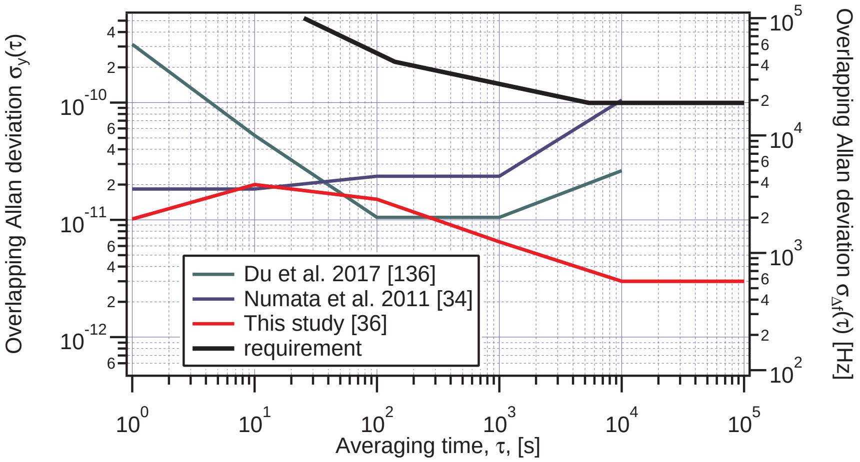

Figure 5.11 – *Relative and absolute frequency instability at 1572 nm of this study compared to litterature values.*

However, the origins of the frequency difference were not investigated. For the application of interest, such a frequency shift can be corrected for as long as its frequency value is known. The interest is to guarantee a 20 kHz stability of the slave laser optical frequency. The possible origins of the frequency shift may come from the master laser optical frequency or the offset-frequency in the offset lock.

5.3 Repeatability and reproducibility at 1560 nm and 780 nm

The frequency accuracy, the reproducibility, and the repeatability of a frequency-locked slave laser are quantities of interest for the IPDA LIDAR application. Moreover, these quantities are of interest if the laser system is replicated, e.g., for an industrial product. From equation 5.2, the slave-laser optical frequency is mainly dominated by the master-laser optical frequency. The repeatability and reproducibility of the optical frequency at 1560 nm and 780 nm are presented in the following section.

The optical frequency of the 1560 nm laser was determined from heterodyne beat measurements with the fully-stabilised commercial Er-fibre optical-frequency comb (Menlo Systems) referenced to an H-maser. The optical frequency is obtained from the measured frequencies of the comb repetition rate f_{rep}, the carrier-envelope offset f_{CEO}, and the beat signal f_{beat} between the laser and the comb (see equation 5.4). These frequencies were simultaneously recorded on a multi-channel counter with a 1 s gate time. The sign of the beat signals f_{CEO} and f_{beat} was determined before the measurement. The comb mode number m was assessed from the reference frequency of the considered F23 transition [70]. The repeatability of the laser locking point was estimated from nine consecutive measurements of the absolute frequency at 1560 nm. Each measurement had a duration of 15 min, and the laser was switched off for 15 minutes between measurements. The operating parameters (cell temperature, temperature and current of the laser, locking parameters, and free-space optics alignment) were kept unchanged among all measurements. The average optical frequency was determined for each measurement, and the measurements were repeated for one standard LH and two AOM-LH (details about these LHs can be found in section 2.2) at 780 nm (called Std-LH, AOM-LH v1 and AOM-LH v2). The design of AOM-LH v1 and v2 is the same architecture, but the AOM-LH v1 possesses a different Rb cell containing a higher ^{85}Rb/^{87}Rb isotopic ratio. The sub-Doppler spectroscopy setup of the 1560 nm laser and the three LHs at 780 nm was assembled and aligned following the same procedure. The three 780 nm lasers were locked to the same F23 transition, and their optical frequencies were measured using a heterodyne beat with the second harmonic component of the fully-stabilised commercial Er-fibre comb.

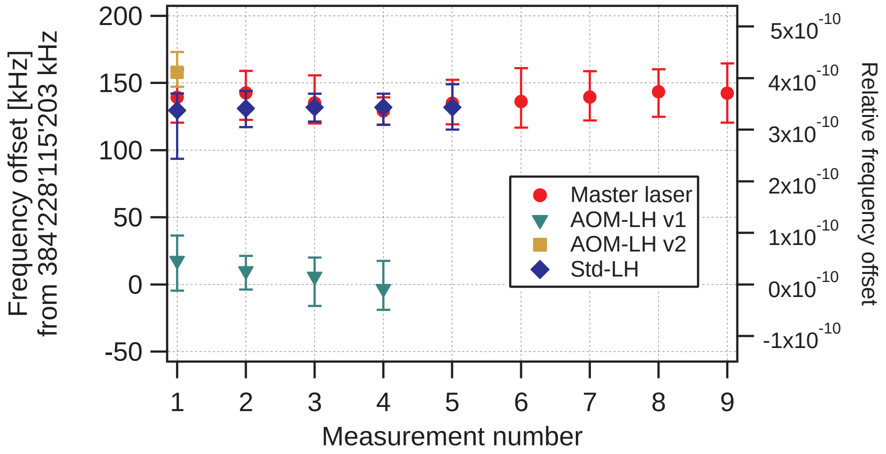

Figure 5.12 – *Relative frequency differences of the frequency-doubled 1560-nm laser optical frequency and of three Rb-stabilized 780-nm laser heads with respect to the reference value of the transition F23 [70]. Each measurement was separated by 15 min during which the laser was switched off. The error bars represent the standard deviation of each single relative frequency data time-series. Figure adapted from [65].*

The repeatability of the locking point of the Std-LH was determined in a similar way from several measurements of the same 15 min duration, without any change of its operating parameters. Only one measurement was realised with the AOM-LH v2; therefore, its repeatability was not evaluated. The relative difference between the measured optical frequency and the literature value [70] is shown in Figure 5.12. The nine measured values of the optical frequency of the 1560 nm laser present an average bias of +69 kHz with a repeatability of 2 kHz (corresponding to the standard deviation of the results) at 1560 nm, which translates into a bias of +138 kHz with a repeatability of 4 kHz at 780 nm. For the Std-LH, a bias of +131 kHz with a repeatability of 1 kHz was determined at 780 nm. A bias of +158 kHz was finally measured for the AOM-LH v2. The reproducibility of the simple sub-Doppler spectroscopy setup used in the 1560 nm laser, the Std-LH, and the AOM-LH v2 can be estimated by considering the complete set of measurements, indistinct from the laser source. An average bias of +142 kHz with a reproducibility of 14 kHz (standard deviation around the average of the average bias) is obtained for the F23 transition.

For the AOM-LH v1, a bias of 8 kHz with a repeatability of 9 kHz was determined at 780 nm. The reduction of the frequency bias by one order of magnitude is believed to result from the Doppler background, which is induced by the transition $|5^2S_{1/2}, F=3\rangle \leftrightarrow |5^2P_{3/2}, F=4\rangle$ of ^{85}Rb. This partially compensates for the slope of opposite sign, which is induced by the Doppler background of the transition $|5^2S_{1/2}, F=3\rangle \leftrightarrow |5^2P_{3/2}, F=1,2\rangle$ of ^{87}Rb. Therefore, a large contribution to the observed frequency bias for the all other LH is believed to result from the Doppler background. This effect could be more important to stabilising a laser to another sub-Doppler transition in the D2 line than the F23 transition considered in our case. The effect could be significantly suppressed by detecting the third harmonic of the modulation frequency (3f), which removes offsets resulting from linear backgrounds in the absorption spectrum from the error signal [138][69]. This technique strongly reduces the DC signal related to the Doppler background in the error signal [100].

5.4 Noise conversion through frequency doubling

In order to evaluate the noise budget of the short-term frequency stability, the possible contribution of the frequency-doubling unit was evaluated. The frequency noise power spectra density (FN-PSD) is multiplied by a factor 2^2 in an ideal (noiseless) frequency-doubling process. In order to assess the possible presence of extra noise induced in the PPLN-WG, the FN-PSD of the fundamental (1560 nm) and second harmonic (780 nm) components of the laser radiation were measured. This was realised by measuring the phase noise of the beat notes between the fundamental (or frequency-doubled) component of the 1560 nm DFB laser and the fundamental (second harmonic) component of the self-referenced frequency comb, using a phase noise analyser (FSWP from Rohde & Schwarz). The comb lines used in the beat signals have a much weaker frequency noise than the laser under test; therefore, these measurements assessed the frequency noise spectra of the laser properly. The FN-PSD was recorded with the laser in free-running mode and frequency stabilised onto the cross-over CO22-23 sub-Doppler transition. As displayed in Figure 5.13, the frequency noise spectrum of the locked laser presents two bumps, observed in both measurements at 1560 nm and 780 nm. The first bump around 100 Hz corresponds to the servo bump of the repetition rate stabilisation in the Er-fibre comb, while the second at 4 kHz corresponds to the bandwidth of the stabilisation loop of the 1560 nm laser. The average value of the ratio between the FN-PSD at 780 nm and at 1560 nm is 3.8 with a standard deviation of 0.6 for the free-running laser and 3.9 with a standard deviation of 0.4 for the frequency-locked laser, see Figure 5.15. Similar shape of the FN-PSDs with a ratio close to 2^2 indicate that no significant noise is added by the frequency-doubling process in the PPLN-WG.

The frequency-doubling process is a non-linear effect in which the generated output power is proportional to the square of the input power, i.e., $P_{\text{out}} = \eta \cdot P_{\text{in}}^2$. In the absence of excess noise, the optical-power fluctuations δP_{out} at the output of the PPLN waveguide are given by:

$$\delta P_{\text{out}} \approx 2 \cdot \eta \cdot P_{\text{in}} \cdot \delta P_{\text{in}}, \tag{5.5}$$

where δP_{in} represents the fluctuations of the laser power at the input of the frequency-doubling unit. It follows that the RIN - defined as $\delta P_{\text{out}}^2 / P_{\text{out}}^2$ - is multiplied by a factor 2^2 in an ideal frequency-doubling process. The RIN in our system was determined by analysing the signal of a photodetector at 1560 nm and 780 nm using a fast Fourier transform (FFT) spectrum analyser. Figure 5.14 shows the RIN measured for the fundamental and second harmonic components of the first 1560 nm DFB laser. The average value of the ratio between the RIN at 780 nm and at 1560 nm is 4.5 with a standard deviation of 1.4, see Figure 5.15. Similar RIN spectra (at 1560 nm and 780 nm) and a ratio close to 2^2 indicate that no supplementary amplitude noise is added by the PPLN-WG.

Precise determination of the noise generated by the PPLN-WG can be performed following the method used by Delehaye et al. [139]. Based on a Mach-Zehnder interferometer and a noise rejection technique, Delehaye et al. demonstrated that the phase noise added by the SHG module is bounded by -35 dBrad^2/Hz (equivalent to $6.3 \cdot 10^{-4}$ Hz^2/Hz at 1 Hz). For our master laser, such level of frequency noise contribution is negligible.

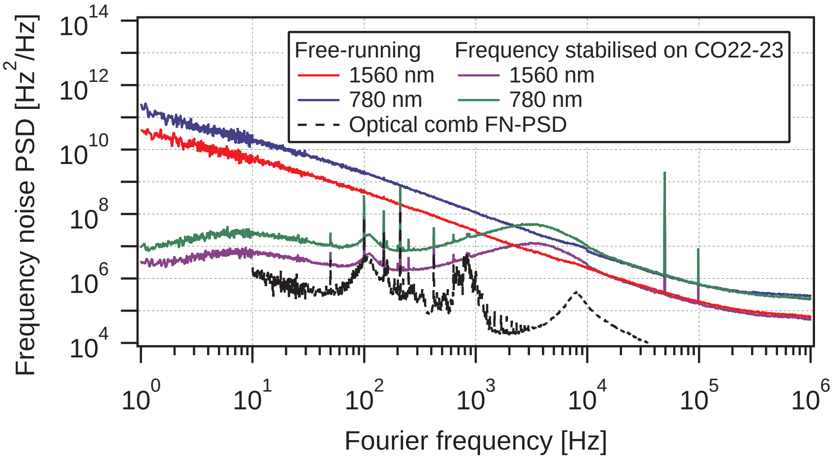

Figure 5.13 – *Frequency noise power spectral density (FN-PSD) of the fundamental and second harmonic components of the 1560-nm laser in free-running regime and frequency stabilised to the cross-over CO22-23 transition. The noise contribution of the comb mode at 1560 nm is also shown for comparison (black curve). Figure adapted from [65].*

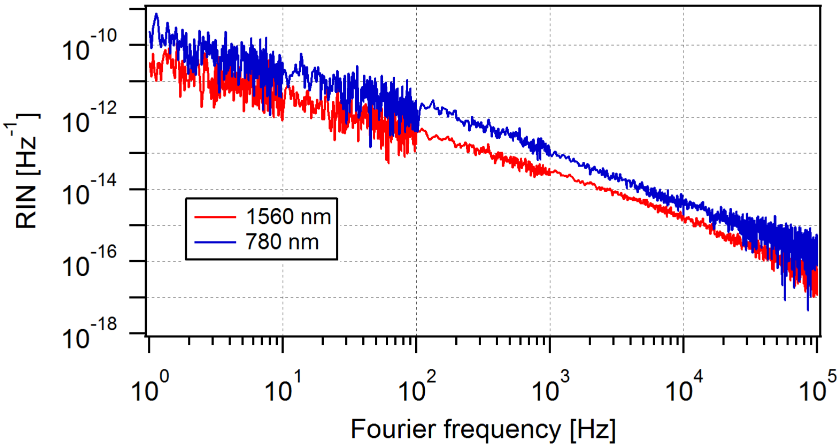

Figure 5.14 – *Relative intensity noise of the fundamental and second harmonic components of the free-running 1560-nm laser measured before and after the frequency-doubling module. Figure adapted from [65].*

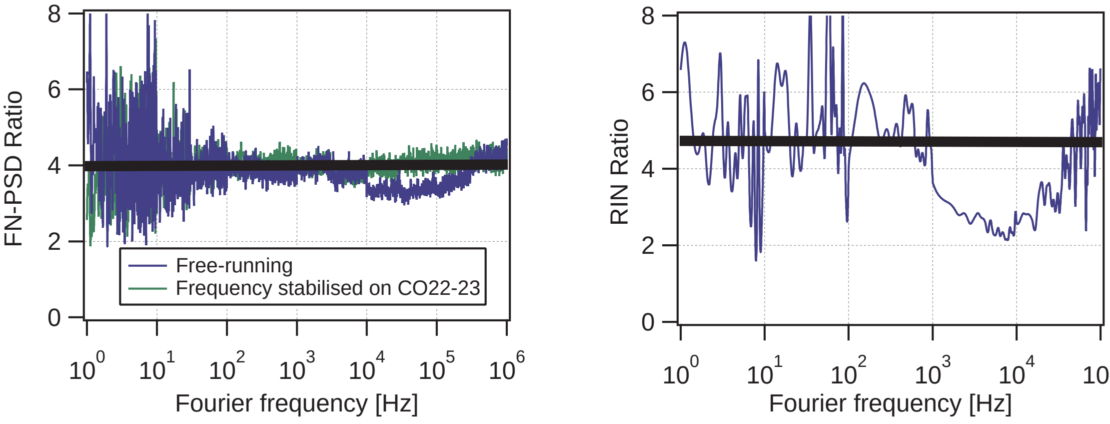

(a) *FN-PSD ratio.* **(b)** *RIN ratio.*

Figure 5.15 – ***(a)*** *Ratio between the fundamental and second harmonic components of the FN-PSD of the 1560-nm laser in free-running regime and frequency stabilised to the cross-over CO22-23 transition.* ***(b)*** *Ratio between the fundamental and second harmonic components of the RIN of the 1560-nm laser in free-running regime.*

5.4.1 Master laser linewidth

The master-laser FWHM linewidth is measured using two different techniques. The first technique is based on the β-separation line [135]. The master-laser FWHM is obtained from its measured frequency noise spectrum in free-running operation as a function of the observation time. Figure 5.16 presents the master-laser FWHM as a function of the observation frequency (the inverse of the observation time) obtained by applying the β-separation line method on the free-running frequency noise displayed in Figure 5.13. The master laser has an FWHM of (0.9± 0.1) MHz at 1560 nm and (1.8 ± 0.2) MHz at 780 for an observation time of 4 ms (250 Hz).

The second technique is based on the beat-note between the master laser and one line of the fully-stabilised Er-fibre comb. The latter has a mode linewidth ≈ 200 kHz (FWHM) at 1560 nm [79] and ≈ 400 kHz at 780 nm. The linewidth of the master laser is obtained from a Lorentzian fit applied to the beat-note between the master laser and one line of the comb observed in a bandwidth of 300 kHz. The measurement is repeated 20 times. The master-laser modulation amplitude is switched off, and the master is in free-running mode. A master-laser FWHM of (0.9 ± 0.4) MHz at 1560 nm and (1.6 ± 0.7) MHz at 780 is obtained. The error bars are the standard deviation. These values agree with the FWHM obtained using the β-line technique considering the error bars.

5.4.2 Master-laser optical spectrum

The optical spectrum of the fundamental and frequency-doubled components of the 1560 nm laser was finally measured using an optical spectrum analyser. At 1560 nm, a side-mode suppression ratio (SMSR) of 44 dB was measured (see Figure 5.17). Due to the quadratic intensity dependence of the frequency-doubling process, the side-modes of the 780 nm spectrum - after frequency doubling - were further attenuated below the noise floor of the spectrum analyser, resulting in an SMSR > 60 dB.

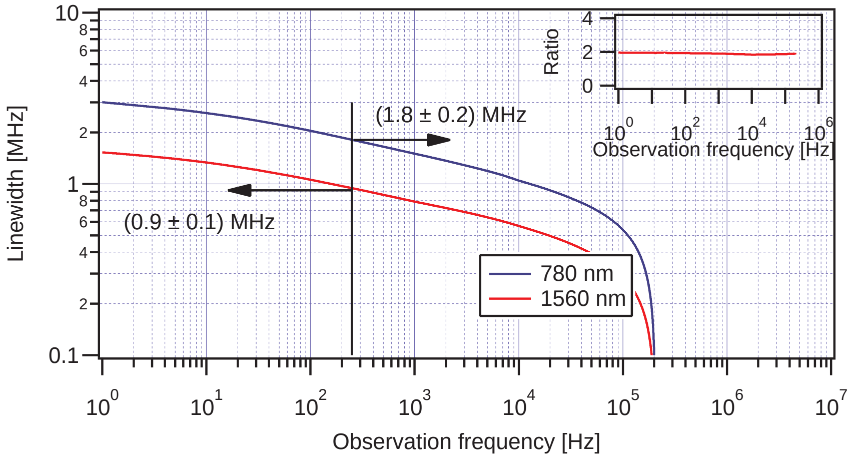

Figure 5.16 – *Master-laser FWHM as a function of the observation time obtained using the β-seperation line [135] method on the noise data of Figure 5.13. Inset : ratio between the blue and red curves.*

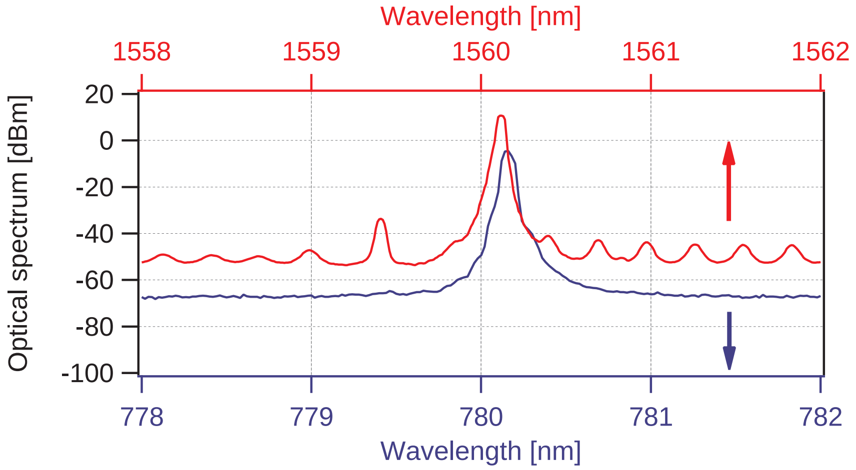

Figure 5.17 – *SMSR of the free-running 1560-nm laser before and after frequency doubling.*

5.5 Conclusion

In this chapter we presented a fibred Rb-stabilised laser system acting as an optical-frequency reference at 780 nm, 1560 nm, and 1572 nm. The heart of the laser system is a cm-scale Rb vapour cell used to frequency stabilise a 1560 nm frequency-doubled master laser on a Rb sub-Doppler absorption line. The frequency-stabilised master laser is used to produce an optical comb centred at 1560 nm using an OFCG. The optical comb covers a span of 40 nm around the master-laser optical frequency. Finally, a slave laser emitting at 1572 nm is offset-locked to one line of the comb. This study demonstrated that the laser system allows the frequency stability of the master laser to be transferred to the slave laser without significant degradation of the frequency stability.

A relative frequency instability between 0.5 and 1.3 $\cdot 10^{-11}$ at 1 s of integration time at 780 nm, 1560 nm, and 1572 nm is demonstrated. A long-term frequency instability between 3 and 6 $\cdot 10^{-12}$ at 10^5 s of integration time is measured. The demonstrated frequency instabilities fulfil the requirement for CO_2 monitoring for space by one order of magnitude. More generally, the laser system composed of the master-laser stabilisation loop and the OFCG can be used to transfer the frequency stability from 1560 nm to any frequency between 1540 nm and 1580 nm. Each comb line is expected to share the same frequency stability than the master laser frequency stability, in particular, for the comb line close to the other CO_2 absorption lines included between 1540 nm and 1580 nm.

The study presented in this chapter demonstrates that the slave-laser frequency stability is dominated by the master-laser frequency stability. The frequency performance of the slave laser is expected to be improved by the enhancement of the master-laser frequency stability. This can be done by reducing the impact of the frequency fluctuation, that is at the origin of a bump in the frequency instability at time scales between 10 s and 100 s. Another source of improvement is the choice of a low-frequency noise master laser. Indeed, the short-term frequency instability is proportional to the FN-PSD at the modulation frequency [100]. However, this study does not address the noise conversion from the master-laser frequency noise to the slave-laser frequency noise.

The laser system presented in this chapter can be reduced in complexity by omitting the offset frequency f_{offset} and the associated mixer. Indeed, by fine-tuning the repetition rate of the OFCG f_m, the beat-note between the comb line and the slave laser can be used to frequency stabilise the slave laser. For the comb line number n = -137 and a repetition rate of the OFCG f_m = 10.00511 GHz which gives a comb line optical frequency equal to the optical frequency of the slave laser measured in section 5.2.2. However, this simplification does not allow the slave laser to be frequency stabilised to any optical frequency within the 400 MHz large CO_2 absorption line because the repetition rate of the OFCG needs to be resonant with the 2.5 GHz free spectral range of our specific OFCG.

Preliminary measurement addressed the question of repeatability and reproducibility of the frequency stabilisation using the sub-Doppler spectroscopy on a cm-scale Rb vapour cell. The optical frequencies of four laser systems (three LH and the master laser) at 780 nm based on identical implementation of the sub-Doppler Rb spectroscopy scheme are measured using a fully-stabilised Er-fibre comb. The results show that the frequency-stabilised optical frequency presents a frequency offset of about 142 kHz with a reproducibility of 14 kHz when the laser is frequency stabilised on the F23 sub-Doppler transition. This study highlighted the case of a laser system having an Rb vapour cell with a higher isotopic ratio ^{85}Rb/^{87}Rb. In this case, the frequency offset is reduced by one order of magnitude. The frequency bias on the Rb-stabilised lasers is expected to be significantly reduced using the 3f modulation spectroscopy. This technique could be helpful in reducing the frequency bias of the laser due to Doppler background when it is frequency stabilised to a sub-Doppler transition other than the F23 transition.

Finally, the master laser acts as an optical-frequency reference at two wavelengths: 1560 nm and 780 nm. The master laser at 780 nm can be used as a light source for an Rb vapour-cell atomic clock. This approach allows a technological bridge to be created between the well-established and highly reliable commercial laser technology available at 1.5 μm and a high-performance Rb clock. In LTF and in the following of the work presented in this chapter, the use of a commercial 1.5-μm laser for a high-performance Rb atomic clock has been studied by Almat et al. [106][140]. In particular, they demonstrate the benefit of frequency low-noise 1.5-μm lasers in the reduction of short-term frequency instability via a reduction of the FM-to-AM noise conversion in the clock vapour cell [140]. However, they also show that the frequency-doubling unit used in their study (identical to the one used in this study) induces degradation of the optical power stability in the long-term (10^4 s of integration time) by one order of magnitude [106]. This impacts the long-term frequency instability of the Rb clock through the intensity LS. The relative optical-power fluctuations reported in Almat et al.'s study [106] is equivalent to the one measured for the AOM-LH (see Figure 2.6). However, the difference between the AOM-LH and Almat et al.'s fibred laser system is that the increase of the optical-power fluctuation is done by the AOM in the first case and by the frequency-doubling unit in the second case. One may expect that a fibred laser system composed of a frequency-doubling unit plus a fibred AOM would increase the optical-power fluctuation by at least one order of magnitude in the best case. Due to the important contribution of the intensity LS effect in the total frequency instability budget of our POP-DR Rb clock prototype ($\approx 0.5 - 1.5 \cdot 10^{-14}$ at 10^4 s of integration time see Table 3.13), it is expected to become mandatory to implement an intensity stabilisation of the laser source.

5.5.1 Discussion on the project trade-off

In order to achieve the stringent requirement imposed for atmospheric CO_2 monitoring, an absolute frequency reference is needed. Usually, frequency references are laser frequency stabilised using an atomic or molecular absorption line. The frequency reference at 1572 nm presented in this chapter is the results of a technological trade-off made by the LTF at the early beginning of the project. In the following, the trade-off made at that time is reviewed and updated with the conclusion of the study presented in this chapter.

Potential frequency references were identified for achieving the required laser frequency stabilisation: : the optical absorption lines of the CO_2 itself, Acetylene and rubidium. The CO_2 presents low absorptions signals (3.5% and 36% at 1.57 μm and 2.05 μm respectively) for a 1 m long cell filled with 10 mbar CO_2 at room temperature. Two solutions are well-known to increase the absorption performance. The first one is the use of a multipass cell. Numata et al. [35] have demonstrated relative frequency instability at 1572 nm of $3 \cdot 10^{-11}$ for integration time up to 1000 s using a 17-m pathlenght multipass cell. The second solution is the use of the sub-Doppler spectroscopy with noise-immune cavity enhanced optical heterodyne molecular spectroscopy (NICE-OHMS) [141] which are based on complex high-finesse cavities. The acetylene is a common molecule used for frequency standards in the 1550-nm region. It is worth to mention the frequency references developed at the Danish Fundamental Metrology (DFM) institute based on the sub-Doppler spectroscopy and a 50-cm long acetylene vapour cell. They achieved a relative frequency instability at the level 10^{-13} for integration times higher than 10'000 s [47]. Finally, rubidium vapour has been used to build frequency references in the 780-nm domain. At the LTF, the sub-Doppler spectroscopy in rubidium vapour cell can achieve high contrast with typically 200 μW of optical power and achieve excellent frequency stability (as discussed in chapter 2).

Different types of cell were envisaged : glass-blown cell, Rb MEMS cell, multipass cell and hollow-core photonic crystal fibres (HC-PCFs). The technology of glass-blown vapour cells with rubidium is a mature technology used for lamp-pumped Rb clocks. It has demonstrated an excellent long-life time (over than 10 years). Production of cm-scale vapour cell with and without buffer gas is mastered at the LTF (see Pellaton thesis [74] and chapter 2). Miniature rubidium vapour cells based on MEMS technology have been developed. The MEMS cells present a lower volume compare to cm-scale vapour cell and a pathlength of 0.5 mm. To obtain absorption levels equivalent to the one obtain with glass-blown cell, the MEMS cell are operated at higher temperature (80°C). This increase the pressure broadening of the absorption lines, but sub-Doppler spectroscopy is still possible. Multipass cells are a convenient way to increase the absorption. However, the physical dimension of such a cells are large : hundred of centimetre of lendght, volume up to 5 litres. Moreover, theses cells are subject to unwanted light scattering by the cell mirrors which creates etalon fringes on the absorption spectrum. HC-PCFs confine gas and light in tiny and periodically spaced air-holes of the fibre silica matrix. They present the advantage to propose a nearly perfect overlap between the optical field and the gas. An interesting type of HC-PCFs are based on a kagome structure [142].

These fibres present a larger core size which increases the molecular transit time and reduces the linewidth of the sub-Doppler absorption feature. However, HC-PCFs present important limitations due to random etalon effect and Fresnel reflections at the fibre connections. Nevertheless, a relative frequency stability at the level of $6 \cdot 10^{-12}$ at 1000 s was demonstrated [143]. Finally, HC-PCFs present a high-potential to build compact frequency references however the long-term frequency stabilities are limited by optical noises (etalons and reflections).

The optical frequency combs (OFCs) can be classed in two categories : active and passive optical comb. The first category concerns the self-referenced combs generated by an active lasing resonant cavity and the second concerns the optical comb generated from a continuous wave laser and a resonant cavity. The self-referenced combs that cover 1572 nm (B1 line) or 2051 nm (B2 line) are Er:fiber-, Cr:forsterite- or Er:Yb:glass-based lasers (see [144] for a complete review of self-referenced combs). The repetition rate is at the order of 100 MHz (up to 400 MHz)[144]. However, unambiguous determination of the comb line nearest to the slave laser could be difficult or impossible. Moreover, the electrical-to-optical efficiency [3] of these OFCs is at the order of 1-3%. Considering the additional power for control electronics and temperature control, a complete frequency comb could consume about 50 W, weigh 10 kg and fit a volume around 10-15 litres [144]. Two types of passive optical comb are considered. The first is the passive comb based on a Fabry-Perot EOM's - called OFCG, see section 5.1.2 - and the second is the passive comb based on microresonators (see [145] for a complete review of microresonators). The first difference between these two types of comb is that the OFCG is a commercial product for the 1.5-μm region whereas the microresonators are exclusively developed in research center. Reliability and stability in microresonators use and operation do not look adequate to the project keeping in mind long frequency stability tests. An other difference is about the light coupling. Coupling laser light in the OFCG is direct through optical fibre but it is done through evanescent waves via a tapered fibre or a prism for microresonator. In the latter case, the coupling is more sensitive to variations and mechanical instabilities. Concerning the dimensions, the microresonators have mm-cavity dimensions whereas the OFCG waveguide have cm-scale dimensions.

At the beginning of the project, the result of trade-off was (1) rubidium as frequency reference which gives a sufficiently marked absorption feature for small optical pathlength (2) a passive optical comb to fill the gap between the master laser and the CO_2 absorptions line (3) use an OFCG device because of its technological maturity.

Since the beginning of the project until now, stabilized laser system for CO_2 detection were developed in other laboratory. A compact laser system for the stabilisation at 2051 nm (B2 line) using a HC-PCF filled with pure CO_2 was developed by Schilt et al. [146], a relative frequency stability of $7 \cdot 10^{-10}$ is demonstrated for time scales ranging from 1 s up to 1000 s. More recently, a laser system based on NICE-OHMS instrumentation and frequency stabilisation on the acetylene 1531 nm and 1538 nm demonstrated relative frequency stability at the order of 10^{-11} at 1 seconds of integration time, averaging down as $1/\sqrt{\tau}$ up to $8 \cdot 10^{-13}$ at 240 s of integration time [147]. Finally, a laser system based on a frequency tripled Telecom laser diode at 1542 nm frequency stabilized to the narrow iodine hyperfine lines (at ≈ 514 nm) were reported by Philippe et al. [148]. They used a 20-cm long multipass iodine cell and they demonstrate a relative frequency instability of $4.8 \cdot 10^{-14}$ averaging down as $1/\sqrt{\tau}$ up to $6 \cdot 10^{-15}$ at 50 s. However, these two last publications do not present frequency stability at 1572 nm which result into a wavelength gap of 34 nm for [147] and 30 nm for [148]. Moreover, long-term frequency instability for integration times longer than one day for a

---

[3] ratio between output optical power and input electrical power

frequency stabilized laser at 1572 nm is absent to our knowledge. It confirms that the laser system presented in this chapter is an appropriate candidate. We also notice that all the authors reported limitation due to etalon effects and internal reflections which are the causes of medium-to-long term frequency instability. A good alternative to the laser system presented in this chapter is the used of a HC-PFC filled with pure CO_2. Preliminary results at 2.05 μm show promising performance for long-term frequency stability in a compact laser system [146].

Conclusion

This thesis identified the main sources of limitation of two compact and high-performance frequency references based on cm-scale Rb vapour cells: a microwave-frequency reference - pulsed optically pump double-resonance (POP-DR Rb) clock - and optical-frequency references (at 780 nm and 1.5 μm). The work presented in this thesis demonstrates frequency instabilities at the level of 10^{-14} for the POP-DR Rb clock and at the level of 10^{-11} for the optical reference for a setup volume of about few litre.

The POP-DR Rb clock

The results presented in this thesis represent an important step towards validating our POP-DR Rb clock prototype. The applications of interest for such an atomic clock include compact frequency reference for GNSS or communication systems. These applications impose limitations on atomic clocks: compact volume (< 3 litres), lightweight, low power consumption, simple production, extended lifetime, and low short- and long-term frequency instability. The research presented in this thesis presents solutions for several of these problems.

More precisely, the first research line of this thesis evaluates the medium- to long-term frequency stability of high-performance, compact POP atomic clocks. It evaluated the atomic clock's frequency sensitivity to relevant quantities: laser frequency and intensity fluctuations (light-induced shift effects), microwave power (microwave-power shift, MPS), and environmental effects (barometric effect, temperature).

The natural fluctuation of atmospheric pressure was found to be an important source of frequency instability for every vapour-cell atomic clock exposed to an open atmospheric environment. Moreover, it was the most dominant source of limitation for our Rb atomic clock prototype. It was measured that, for an atmospheric pressure fluctuation of 1 hPa, the relative clock frequency changes by $8 \cdot 10^{-14}$. Using a pressure-controlled chamber to control the pressure around the clock, the barometric effect was reduced such that it impacted the relative clock frequency at the level of $5 \cdot 10^{-15}$ at 10^4 s of integration time.

Several options for how to reduce the contribution of the barometric effect to the clock frequency instability without using a pressure-controlled chamber were discussed. First, the barometric sensitivity coefficients depend on the dimension and the materials of the vapour cell. By increasing the wall thickness by a factor of two, the barometric sensitivity coefficient is decreased by one order of magnitude. Another solution is to use a new buffer-gas mixture consisting of three buffer gases that cancels the buffer-gas pressure coefficient β'. Calosso et al. [82] have proposed a mixture of CH_4 (15.8%), Ar (62.7%), and N_2 (21.5%). However, a change to the vapour cell dimensions or component may change the microwave properties (amplitude, distribution, alignment) of the loaded microwave cavity. Therefore, it will result in a new production cycle of cells and microwave-cavity prototypes.

In addition, numerical simulation was carried out evaluating the impact of vapour cell inhomogeneity (temperature, light intensity, microwave power, and so forth) on the clock frequency. First, the numerical simulation, considering the microwave magnetic-field distribution of our cavity, reproduced the Ramsey fringes and its properties (Contrast and FWHM) in excellent agreement with the experimental signals. This first step confirmed the validity of the numerical simulations approach. The microwave-power shift also measured in our Rb atomic clock was reproduced by considering an Rb ground-state resonant-frequency shift inhomogeneity in addition to the microwave-field amplitude distribution of our convitonal manufactored cavity prototype. Consequently, the microwave-power shift measured in our POP-DR Rb prototype has a different physical origin than the microwave-power shift observed in other compact POP-DR Rb clock [19], which is a consequence of our low Q magnetron-type cavity. However, the results show that the model used in our numerical simulation failed to explain and reproduce the behaviour of the MPS of our POP-DR Rb prototype as a function of the laser frequency. Nevertheless, the experimental measurement of the microwave-power shift demonstrated that an operation point exists such that the MPS is minimised. For a laser frequency tuned on CO21-23 and for a microwave pulse area of $b \cdot t_m = 0.57 \cdot \pi$, the MPS is reduced to $2 \cdot 10^{-13} / \mu W$[4]. The MPS contribution to the relative frequency fluctuation of our Rb clock prototype is $4 \cdot 10^{-16}$ at 10^4 s of integration time. It is two orders of magnitude lower than the previous clock characterisation [31].

The evaluation of the intensity and frequency LSs shows that the frequency shift induced by the light frequency and intensity has contributions arising from each phase of the POP sequence. Experimentally, a pump and an intensity detection LS were demonstrated. The intensity LS is another important clock frequency stability limitation, whereas the frequency LS is negligible for our clock prototype. In this case, a solution could be to stabilise the optical intensity of the AOM-LH. As the intensity LS impacts the medium- to long-term frequency stability significantly, only long-term optical fluctuation needs to be corrected. The simplest solution would be to detect the optical-power fluctuation at the AOM-LH output and consequently change the AOM-LH diode temperature or the AOM drive power. An optical-power fluctuation below <0.1% for an integration time longer than 10^4s appear to be feasible.

Finally, the conclusion of this first research line was the demonstration of clock frequency instability to the level of 1×10^{-14} at 10^4 seconds of integration time. This level of medium- to long-term frequency stability is an important step for the establishment of the POP-DR Rb clock developed at the LTF for space applications. Figure 4 compares the frequency instability presented in this thesis with the performance of other compact vapour-cell atomic clocks reported by other laboratories.

3D-printing

The second research line of this thesis was the validation of 3D printing (additive manufacturing) for the fabrication of complex microwave cavities. The homogeneity and distribution of the microwave field inside the 3D-printed microwave cavity was characterised using the POP-DR Rb atomic clock. Short-term frequency stability at a state-of-the-art level was demonstrated.

The microwave cavity is one critical component of a compact atomic clock. Additive manufacturing technology is a promising technology for the production of microwave cavities. It allows new cavity designs to be quickly produced and tested. Moreover, the additive-manufactured magnetron-type cavities based on polymers can weigh less than conventional magnetron-type cavities, which is an

---

[4] in principle, there is no lower limit.

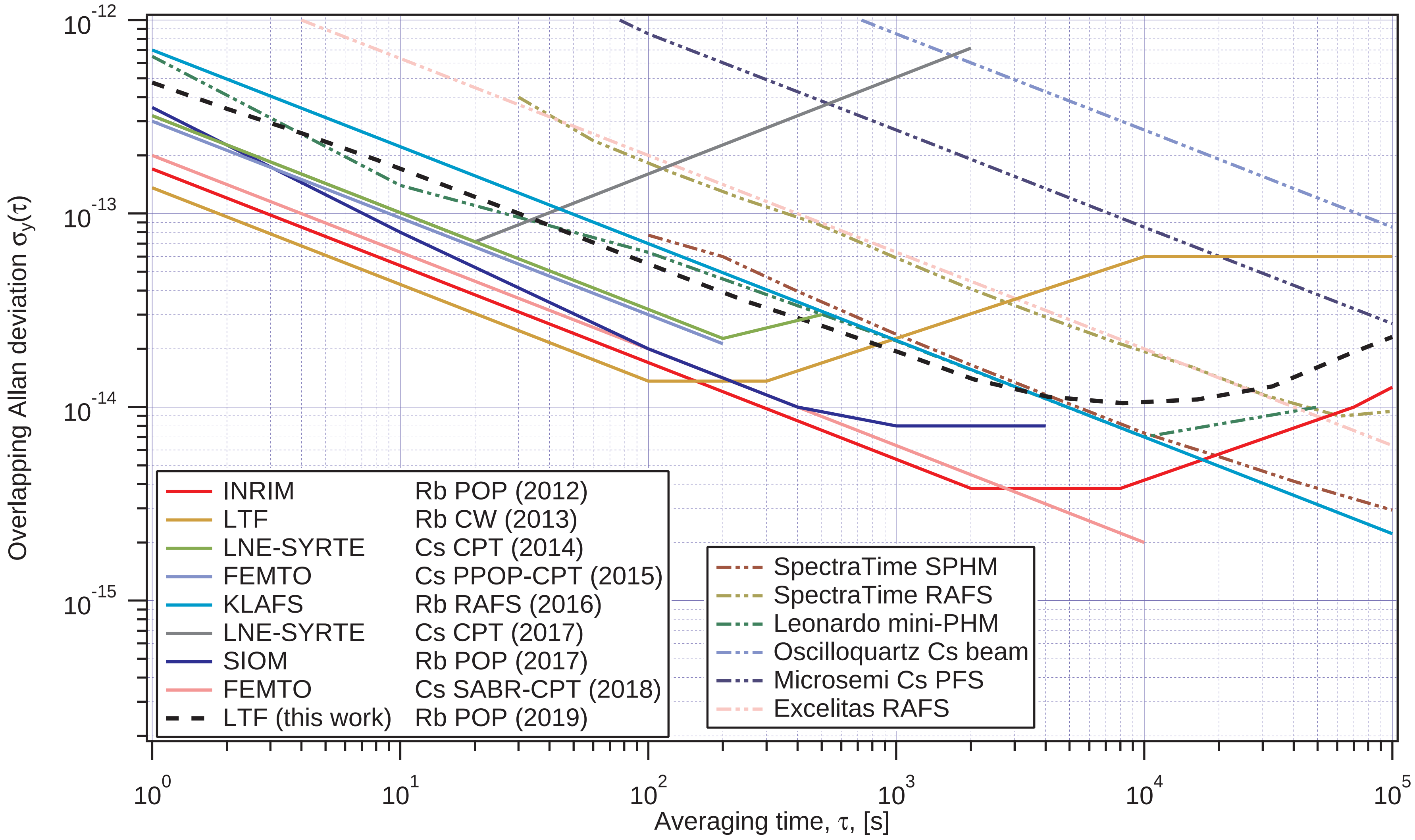

Figure 4 – *State of the art of laboratory compact atomic clocks in 2019 : INRIM Rb-POP [19]; UNINE Rb-CW [26]; LNE-SYRTE Cs CPT [27]; FEMTO PPOP Cs CPT [28]; KLAFS Rb RAFS [9]; KLAFS Rb RAFS [18]; LNE-SYRTE Cs CPT [24]; SIOM Rb-POP [21];FEMTO Cs SABR-CPT [11]; UNINE Rb-POP (This work). Industrial atomic clocks : SpectraTime SPHM [14] and RAFS [16]; Oscilloquartz Cs beam [12]; Leonardo mini-PHM [15]; Microsemi Cs PFS [29]; Excelitas RAFS [17].*

important feature for space applications. The long-term behaviour of the additive-manufactured microwave-cavity properties was assessed through an accelerating ageing test in [126], showing no evidence of long-term degradation of the microwave properties (Q-factor, resonant frequency, dimensions, etc.). A new POP-DR Rb clock prototype based on an additive-manufactured microwave cavity is envisaged to evaluate the impact of the AdM microwave cavity on the clock's long-term frequency stability.

Optical-frequency references at 1.5 μm

The third research line of this thesis is focused on a compact fibred laser system based on a single Rb vapour cell for the frequency stabilisation of lasers at 780 nm, 1560 nm, and 1572 nm. It was demonstrated that the frequency stability of light at 780 nm, 1560 nm, and 1572 nm is identical and comparable with the frequency stability of state-of-the-art optical-frequency reference LHs at 780 nm. Moreover, the measured frequency stability at 1572 nm represents state-of-the-art frequency stabilisation at 1572 nm. The main limitation of the frequency instability at 1572 nm comes from the frequency instability of the frequency-stabilised 1560 nm laser. Frequency fluctuation at a time scale of 100 s limits the frequency instability of the 1560 nm laser at the level of $4 \cdot 10^{-11}$. These fluctuations are thought to come from light reflections in the fibred system that produce etalon fringes on the sub-Doppler spectrum.

Subsequently, the frequency-stabilised lasers at 1560 nm and 780 nm were characterised in term of frequency accuracy and noise. Moreover, preliminary evaluations of the optical-frequency repeatability and reproducibility were performed. An average bias of the optical light frequency—more than three optical-frequency references were frequency stabilised using an identical sub-Doppler spectroscopy setup—of +142 kHz with a reproducibility of 14 kHz was measured when the lasers were frequency stabilised on the F23 transition. We believe that the main components of the frequency bias are (1) the Doppler background of the optical transition F21, F22, and F23; and (2) the Doppler background of the closest optical ^{85}Rb transitions. The frequency bias can be reduced using a 3f-modulation technique.

Future prospects

The results presented in this thesis show that it is possible to build a compact atomic clock with a relative frequency stability reaching 10^{-14} in the medium- to long-term using a compact magnetron-type microwave cavity and without the use of a vacuum chamber. New vapour cells with a mixture of three BGs and larger windows thickness are needed to achieve this demonstration.

According to the analysis of this thesis, the frequency instability of our POP-DR Rb clock prototype is dominated by a signal-to-noise limit from 1 s to 10^4 s of integration time. The high level of signal-to-noise is due to a higher detection RIN compared to the previously reported RIN [31][20]; its origins were not investigated in this thesis but the most probable sources of extra RIN noise are ground loops and damaged synthesizer.. An improvement in the short-term frequency instability without degrading the medium- to long-term frequency instability should be possible and constitutes an important next step.

The consequence of a lower short-term frequency instability is that it will be possible to achieve a relative frequency instability at the order of 10^{-14} for an integration time between 1000 s and 10'000 s. According to the frequency instability budget presented in this thesis, the identified parameters expected to limit the clock frequency stability are the intensity LS, the 2^{nd}-order Zeeman shift, and the stem temperature-coefficient shift.

The use of the POP-DR scheme instead of the DR-CW scheme significantly reduces the impact of the LS effects on the clock frequency. However, this study has shown that the LS effects (especially the intensity LS) are a dominant source of limitation on the clock's frequency stability. In order to overcome this source of limitation, it could be interesting to rework the laser source used in our clock prototype. The laser source is actually stabilised in frequency (using a reference vapour cell) but not in intensity. Two possible improvements are (1) to implement an additional control loop for laser intensity stabilisation in the AOM-LH, and (2) to design a new LH sharing similar feature with the actual AOM-LH but reducing the frequency stabilisation part (using Doppler stabilisation for example) and investing these resources into an intensity control loop.

The study of the impact of the light and microwave magnetic fields inhomogeneity on clock signals and frequency has opened a new prospective area for our POP-DR Rb clock prototype. This study has shown that the optical pump pulse may not be strong enough such that a residual coherence at the beginning of the microwave interaction may be present. The future next steps could be to determine the amplitude of this residual coherence experimentally and numerically. This will confirm that the MPS measured in this study originated from the residual coherence. Moreover, these results could add to a deeper understanding of the origin of the pump LS, which is suspected of having the same origin than the MPS.

Light sources are the most critical component of a compact atomic clock, especially in laser-pumped atomic clocks. Indeed, the atomic clocks presents in the GNSS are lamp-based atomic clocks because nowadays they represent the most reliable and robust light sources for space atomic clocks. The modern laboratory prototypes and the enthusiasm of the time and frequency community for the POP atomic clock make the laser-pump atomic clock a serious candidate for the second generation of compact atomic clocks. However, availability of reliable light sources emitting at 780 nm is limited. Frequency-doubled 1560 nm lasers present an interesting solution, allowing mature and high-reliability telecommunication optical components to be applied in laser-pump atomic clocks. The perspective of this solution is the demonstration of a compact laser system based on the SHG of 1.5-μm laser that achieves the same performance or better as the Rb LHs used in this work. This aspect has been recently investigated by Almat et al. [106][140].

A FWHM of the central fringe

In this section, the condition described by equation 1.49 is demonstrated. The demonstration makes use of the analytical expression of the central Ramsey fringe Δ=$\Delta(\Omega_m)$, which is the third component of the Bloch vector **R** deduced from the matrix product 1.43. Using the matrix 1.41 and 1.42 in equation 1.43 with $\mathbf{R} = [0, 0, \Delta_0]$, one obtains:

$$\begin{aligned}\Delta(\Omega_m) = \Delta_0 \Bigg[\quad & e^{-\gamma_1 T_r} \frac{\left(\Omega_m^2 + b^2 \cos(\xi t)\right)^2}{\xi^4} + e^{-\gamma_2 T_r} \frac{b^2 \Omega_m^2}{\xi^4} \left(1 - \cos(\xi t)\right)^2 \cos(\Omega_m T_r) \\ - \quad & e^{-\gamma_2 T_r} \frac{b^2}{\xi^2} \sin^2(\xi t) \cos(\Omega_m T_r) + e^{-\gamma_2 T_r} \frac{2 b^2 \Omega_m}{\xi^3} (1 - \cos(\xi t)) \sin(\xi t) \sin(\Omega_m T_r) \Bigg].\end{aligned} \tag{A.1}$$

Equation A.1 is identical to equation (5) provided by Micalizio et al. [75]. For simplicity, we applied the following changes of variable:

1. $m_{13} = -\frac{b}{\xi} \sin(\xi t_m)$,
2. $m_{23} = \frac{\Omega_m b}{\xi^2} (1 - \cos(\xi t))$,
3. $m_{33} = \frac{\Omega_m^2 + b^2 \cos(\xi t)}{\xi^2}$.

It is straightforward to show that $m_{13}^2 + m_{23}^2 + m_{33}^2 = 1$. Thus, equation A.1 transforms into:

$$\Delta(\Omega_m) = \Delta_0 \left[e^{-\gamma_1 T_r} m_{33}^2 + e^{-\gamma_2 T_r} \cos(\Omega_m T_r) \left(m_{23}^2 - m_{13}^2\right) + e^{-\gamma_2 T_r} \sin(\Omega_m T_r) \left(2 m_{13} m_{23}\right) \right]. \tag{A.2}$$

Using simple trigonometric relations, the later equation becomes:

$$\Delta(\Omega_m) \quad = \quad \Delta_0 \left[e^{-\gamma_1 T_r} m_{33}^2 - e^{-\gamma_2 T_r} A \cos\left(\Omega_m T_r - \phi\right) \right], \tag{A.3}$$

with $A = m_{13}^2 + m_{23}^2$ and $\phi = -2 \cdot \mathrm{atan}(m_{23}/m_{13})$. Let ω_{HWHM} be the half the FWHM of the central fringe $\omega_{\mathrm{FWHM}} = 2 \cdot \omega_{\mathrm{HWHM}}$. An important observation is that over the frequency range $-\omega_{\mathrm{HWHM}} \leq \omega \leq \omega_{\mathrm{HWHM}}$, the first term of equation A.3 is slowly varying in ω compared to the second term for all b. The first term can be considered as an offset of the signal. In fact, it corresponds to the Rabi pedestal, as discussed by Vanier et al. [67]. Using this observation, the condition on ω_{HWHM} is that the cosine term is zero meaning:

$$\cos\left(\omega_{\mathrm{HWHM}} T_R - \phi\right) = 0. \tag{A.4}$$

In the case of $\theta = \pi/2$, the latter condition is equivalent to $\Delta(\omega_{\mathrm{HWHM}}) = 0$ at the end of the second microwave pulse. Finally, the condition A.4 is transformed into a new condition on ω_{HWHM}:

$$\omega_{\mathrm{HWHM}} T_R + 2\,\mathrm{atan}\left(\frac{\omega_{\mathrm{HWHM}}}{\xi}\frac{1-\cos(\xi t)}{\sin(\xi t)}\right) = \frac{\pi}{2}, \tag{A.5}$$

which corresponds to equations (1.49) and (1.50).

B Environmental sensitivities of cavity frequency

In this section, the environmental sensitivities of the magnetron-type microwave-cavity frequency detuning $\Delta\nu_{\text{cav}}$ are presented. The calculations are performed following the calculation presented by Godone *et al.* [92]. The microwave-cavity resonance frequency is given by [26]:

$$\nu_{cavity} = \frac{1}{2\pi}\sqrt{\frac{n}{\pi r^2 \epsilon\mu}\frac{t}{W}}\sqrt{1+\frac{A_1}{A_2'}}\sqrt{\frac{1+\Delta Z/Z'}{1+\Delta W/W}}, \tag{B.1}$$

where n is the number of gaps with thickness t, and $\epsilon = \epsilon_r\epsilon_0$ and μ are electric permittivity and magnetic permeability of the free-space coupling between the electrode gaps, respectively. W is the electrode width with Δ W is the gap width extension due to the electric fringing fields, and Z is the physical length of the electrode with ΔZ the equivalent length extension due to the magnetic fringing field. $A_1 = \pi r^2$ is the cross-sectional area of the inner loop cylinder; $A_2' = \pi(R^2 - (r+W)^2) - nB$, is the area between the outer shield and the inner loop cylinder with B as the area of one support/slab holding an electrode.

We assume that the environmental parameter (pressure and humidity) impacts the microwave frequency by the change of the air dielectric constant. We can write:

$$\frac{\Delta\nu_c}{\nu_c} = -\frac{1}{2}\frac{\Delta\epsilon_r}{\epsilon_r}. \tag{B.2}$$

The expression of ϵ_r as a function of the environmental parameters is provided by the Clausius-Mossotti equation, which is given by:

$$\epsilon_r = 1 + 10^{-6}\left(1.57\frac{P_A}{T} + 1.35\frac{P_W}{T} + 7530\frac{P_W}{T^2}\right), \tag{B.3}$$

where P_W and P_A are the water and dry air partial pressures in Pa.

One wants to express humidity in unit of (g/m^3), one can use the perfect gas law in order to express the water partial pressure P_W [Pa] into the water air density h [g/m^3]. Indeed, it is straightforward to show that:

$$h = \frac{M_{\mathrm{H_2O}}}{R\cdot T}P, \tag{B.4}$$

where $M_{\mathrm{H_2O}} = 18$ [g/mol] is the water molar mass, $R = 8.3144598$[J/K mol] is the ideal gas constant, and T is the air temperature. For example, for an average humidity of 5.3 g/m^3, equation B.4 gives P_A = 8.22 hPa at the microwave-cavity temperature of T = 335.82 K. In the atmospheric conditions that prevailed during the measurement presented in section 3.5.3—an average atmospheric pressure of P$_A$ + P$_W$ = 977 hPa and an average humidity of 5.3 g/m^3—one obtains $\epsilon_r \approx 1 + 5.11 \cdot 10^{-7}$.

The microwave-cavity frequency detuning sensibility coefficients can be obtained using the derivative chain rules as follow:

$$\begin{aligned} \frac{\partial \nu_c}{\partial P_W} &= \Big(\frac{\partial \nu_c}{\partial \epsilon_r}\Big)\Big(\frac{\partial \epsilon_r}{\partial P_W}\Big), \\ \frac{\partial \nu_c}{\partial P_A} &= \Big(\frac{\partial \nu_c}{\partial \epsilon_r}\Big)\Big(\frac{\partial \epsilon_r}{\partial P_A}\Big). \end{aligned} \tag{B.5}$$

The first term $\frac{\partial \nu_c}{\partial \epsilon_r}$ can be calculated using equation B.2:

$$\frac{\partial \nu_c}{\partial \epsilon_r} = -3.42 \cdot 10^9 \Big[\mathrm{Hz}\Big]. \tag{B.6}$$

The second terms $\frac{\partial \epsilon_r}{\partial P_W}$ and $\frac{\partial \epsilon_r}{\partial P_A}$ are calculated using equation B.3 at the microwave-cavity temperature of T = 335.82 K:

$$\begin{aligned} \frac{\partial \epsilon_r}{\partial P_W} &= 10^{-6}\Big(1.35\frac{1}{T} + 7530\frac{1}{T^2}\Big) = 7.1 \cdot 10^{-8}\Big[\frac{1}{\mathrm{Pa}}\Big], \\ \frac{\partial \epsilon_r}{\partial P_A} &= 10^{-6}\Big(1.57\frac{1}{T}\Big) = 4.7 \cdot 10^{-9}\Big[\frac{1}{\mathrm{Pa}}\Big]. \end{aligned} \tag{B.7}$$

Finally, combining equations B.6 and B.7, the microwave-cavity frequency sensitivities are:

$$\begin{aligned} \frac{\partial \nu_c}{\partial P_W} &= -2.42 \cdot 10^2 \Big[\frac{\mathrm{Hz}}{\mathrm{Pa}}\Big], \\ \frac{\partial \nu_c}{\partial P_A} &= -16 \Big[\frac{\mathrm{Hz}}{\mathrm{Pa}}\Big] \end{aligned} \tag{B.8}$$

The first equation of (B.8) can be expressed in the unit of Hz/(g/m^3) using equation B.4:

$$\begin{aligned} \frac{\partial \nu_c}{\partial h} &= \frac{\partial \nu_c}{\partial P_W}\frac{\partial P_W}{\partial h} \\ &= \frac{\partial \nu_c}{\partial P_W}\frac{RT}{M_{\mathrm{H_2O}}} = -3.75 \cdot 10^4 \Big[\frac{\mathrm{Hz}}{(g/m^3)}\Big]. \end{aligned} \tag{B.9}$$

In standard atmospheric conditions, the variation of the atmospheric humidity is ≈ 0.2 g/m^3 and the variation of the atmospheric pressure is ≈ 2 hPa at time scale of 10^4s. These fluctuations induce a variation in the cavity frequency of $\Delta\nu_{\mathrm{cav}}\Big|_{\mathrm{humidity}}$ ≈ -7.5 kHz (equivalent to a relative frequency variation of $7.66 \cdot 10^{-7}$ at 6.8 GHz) because of the humidity fluctuation and $\Delta\nu_{\mathrm{cav}}\Big|_{\mathrm{pressure}}$ ≈ -3.2 kHz (equivalent to a relative frequency variation of $3.27 \cdot 10^{-7}$ at 6.8 GHz) because of the pressure fluctuation. These variations of the microwave cavity are lower than the cavity frequency detuning (the difference between the resonant microwave-cavity frequency and the Rb ground-state frequency difference, which is equal to 1.6 MHz for our CM cavity) by a factor of ≈ 200. The resulting change in the cavity-pulling shift is negligible.

C Barometric coefficient uncertainty calculus

The uncertainty given in the manuscript $(8.5 \pm 2.7) \cdot 10^{-14}$ [/hPa] is obtained considering a consolidated estimation of the uncertainty (see Table C.1).

	Value	Uncertainty [%]	$(df/dx_i)^2 \cdot u(x_i)^2$
Buffer-gas pressure-shift	$1.91 \cdot 10^{-8}$ [/hPa]	$3^{a)}$	$6.5 \cdot 10^{-30}$
P_{in}	32.5 [hPa]	$1^{a)}$	$7.2 \cdot 10^{-31}$
Internal radius	11.37 [mm]	$1^{b)}$	$1.2 \cdot 10^{-29}$
Internal length	23.11 [mma]	$1.3^{b)}$	$1.2 \cdot 10^{-30}$
Thickness	1 [mm]	$10^{c)}$	$6.5 \cdot 10^{-28}$
Young's Modulus E	$6.4 \cdot 10^{8}$ [hPa]	$10^{c)}$	$7.2 \cdot 10^{-29}$
Poisson's ratio σ	0.2	$10^{c)}$	$4.9 \cdot 10^{-31}$
Barometric Coefficient	$8.5 \cdot 10^{-14}$ [/hPa]	Uncertainty$^{d)}$	$2.7 \cdot 10^{-14}$[/hPa]

Table C.1 – *Uncertainty budget on the theoretical barometric coefficient.*

a) The uncertainty comes from the distribution of the buffer-gas coefficient given by Vanier et al. [81].
b) The uncertainty comes from the distribution of the dimensions of five nominally identical cells.
c) The uncertainty is unknown. An uncertainty of 10% is assumed.
d) Total uncertainty obtained using the definition given by [149].
If the uncertainty on the Young's modulus is 10% or does not have uncertainty, then the total uncertainty is respectively $\pm 2.7 \cdot 10^{-14}$/hPa or $\pm 2.6 \cdot 10^{-14}$/hPa. If the uncertainty of the Poisson's ratio is 10% or does not have uncertainty, then the total uncertainty varies by $1 \cdot 10^{-17}$/hPa, which is negligible. The main term in the uncertainty of the barometric effect is the uncertainty of the thickness.

D Ramsey spectrum enveloppe and normalisation

In this section, the Rabi envelopes of the Ramsey spectrum reported in this thesis are evaluated. Especially, the origin of the upper bump in the Ramsey spectrum that can show normalized transmission values larger than one (like in Figure 1.9) is discussed.

According to appendix A, the Ramsey spectrum is described by (see equation A.3) :

$$\Delta(\Omega_m) \quad = \quad \Delta_0\left[e^{-\gamma_1 T_R} m_{33}^2 - e^{-\gamma_2 T_R} A \cos\left(\Omega_m T_r - \phi\right)\right], \tag{D.1}$$

with $A = m_{13}^2 + m_{23}^2$ and $\phi = -2 \cdot \mathrm{atan}\, m_{23}/m_{13}$. Figure D.1 represents the calculated $\Delta(\Omega_m)$ according to equation D.1 in the following conditions : $\Delta_0 = 1$, $\theta = \pi/2$, $t_m = 0.3$ ms, $T_{\mathrm{Ramsey}} = 3$ ms, $\gamma_1 = 360$ s^{-1}, $\gamma_2 = 340$ s^{-1}.

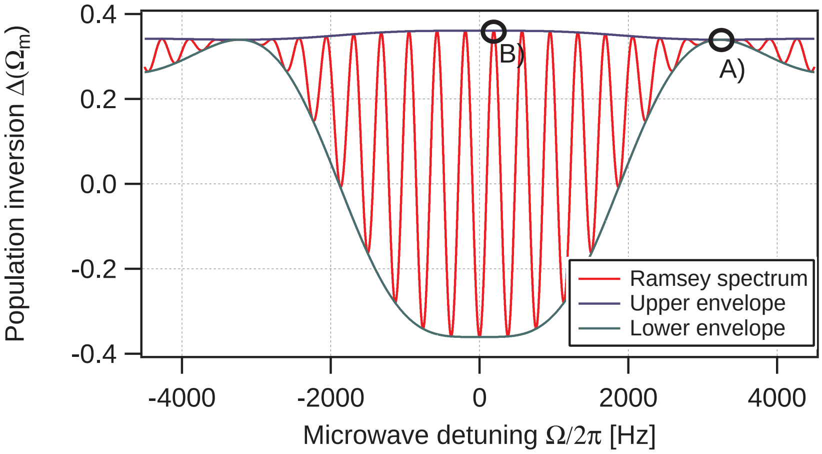

Figure D.1 – *Calculated Ramsey spectrum according to equation D.1 in the following conditions :* $\Delta_0 = 1$, $\theta = \pi/2$, $t_m = 0.3$ *ms,* $T_{ramsey} = 3$ *ms,* $\sigma_{13} = 1.3 \cdot 10^{-15} m^2$, $\gamma_1 = 360$ s^{-1} *and* $\gamma_2 = 340$ s^{-1}.

In equation D.1, the first term vary slowly with Ω_m whereas the second terms describes the Ramsey fringes. The analytical expression of the upper and the lower envelope of the Ramsey spectrum can be obtained considering the maximum and minimum value of the cosine term in equation D.1. Using $m_{13}^2 + m_{23}^2 + m_{33}^2 = 1$, one obtains :

$$\Delta(\Omega_m)^{\mathrm{u,l}} \quad = \quad \Delta_0 e^{-\gamma_1 T_R}\left[m_{33}(\Omega_m)^2 \pm e^{(\gamma_1-\gamma_2)T_R}(1 - m_{33}(\Omega_m)^2)\right], \tag{D.2}$$

where the plus sign corresponds to the upper envelope $\Delta(\Omega_m)^{\mathrm{u}}$ and the minus corresponds to the lower envelope $\Delta(\Omega_m)^{\mathrm{l}}$. The upper and lower envelope are shown on Figure D.1. It is interesting to note that the amplitude of the envelope depends on the difference between γ_1 and γ_2, as experimentally observed by Micalizio et al. [128][19]. In the case of $\gamma_1 = \gamma_2$, then the Ramsey spectrum presents a flat upper envelope.

We are interested in the atomic state corresponding to two particular points of the Ramsey spectrum, point A) and B) on Figure D.1. The point A) corresponds to a microwave detuning of $\Omega_m^A = 2\pi \cdot \frac{\sqrt{15}}{4t_m}$ (obtained from $\Delta(\Omega_m)^{\mathrm{u}} = \Delta(\Omega_m)^{\mathrm{l}}$) with $\Delta(\Omega_m^A) = \Delta_0 e^{-\gamma_1 T_R}$. For a microwave detuning of Ω_m^A, the microwave pulses do not affect the population inversion. Indeed, it is easy to see that the microwave pulse matrix M_m for $\Omega_m = \Omega_m^A$(see equation 1.41) is reduced to the identity matrix. It results that the inversion population at the end of the Ramsey scheme is equivalent to the inversion population obtained for a Ramsey scheme without microwave power, i.e $b = 0$. It means that the atomic state at the end of the Ramsey scheme is dominated only by population relaxation processes depending on γ_1 and T_R.

The point B) corresponds to a microwave detuning of $\Omega_m^B = \frac{2\pi}{T_R + \frac{4t_m}{\pi}}$ with $\Delta(\Omega_m^B) \approx \Delta_0 e^{-\gamma_2 T_R}$ (and corresponds to the Bloch sphere representation of Figure 1.8d). It means that the center of the upper envelope is dominated by the coherence relaxation γ_2 and T_R. This results from the fact that for $\theta = \pi/2$, $t_m \ll T_R$ and $\Omega_m \ll b$, the Bloch vector is projected quickly (at $t_m = 0.3$ ms and compared to the cycle time) to coherence plan after the first microwave pulse where it is less affected by population relaxation process but only by the coherence relaxation during the Ramsey time. It results that for $\Omega_m = \Omega_m^B$, the Bloch vector is less affected by population relaxation process but only by coherence relaxation process.

The conclusion is that - for the upper envelope - the center is dominated by coherence relaxation process whereas is dominated by population relaxation process at Ω_m^A and finally the form of the upper envelope depends on the difference between γ_1 and γ_2 (as described by the second term in equation D.2).

In this thesis, the Ramsey spectra are normalised to the light intensity at the end of the vapour cell for a Ramsey scheme without microwave power. It corresponds to an inversion population $\Delta_0 e^{-\gamma_1 T_R}$ and the light intensity at the point A) of the Ramsey spectrum. It means that the Ramsey spectra are normalized using a mixed states ($\Delta_0 e^{-\gamma_1 T_R}$) and not a pure state which explains why the normalised Ramsey spectra presented in this thesis can reach value higher than 1.

Bibliography

[1] CGPM, *Resolutions 1 of the 26 th CGPM*, https://www.bipm.org/en/CGPM/db/26/1/, 2018.

[2] P. J. Mohr, D. B. Newell, and B. N. Taylor, "CODATA recommended values of the fundamental physical constants: 2014", *Rev. Mod. Phys.*, vol. 88, p. 035 009, 3 2016. DOI: 10.1103/RevModPhys.88.035009.

[3] D. A. Steck, *Rubidium 87 D Line Data*, available online at https://steck.us/alkalidata/rubidium87numbers.pdf, (revision 2.1.5,13 January 2015).

[4] *Oxford dictionaries : time, oxford university press.* 2011.

[5] T. P. Heavner, E. A. Donley, F. Levi, G. Costanzo, T. E. Parker, J. H. Shirley, N. Ashby, S. Barlow, and S. R. Jefferts, "First accuracy evaluation of NIST-F2", *Metrologia*, vol. 51, no. 3, p. 174, 2014. DOI: 10.1088/0026-1394/51/3/174.

[6] F. Levi, D. Calonico, C. E. Calosso, A. Godone, S. Micalizio, and G. A. Costanzo, "Accuracy evaluation of ITCsF2: a nitrogen cooled caesium fountain", *Metrologia*, vol. 51, no. 3, p. 270, 2014. DOI: https://doi.org/10.1088/0026-1394/51/3/270.

[7] N. Huntemann, C. Sanner, B. Lipphardt, C. Tamm, and E. Peik, "Single-Ion Atomic Clock with 3 x 10^{-18} Systematic Uncertainty", *Phys. Rev. Lett.*, vol. 116, p. 063 001, 6 2016. DOI: 10.1103/PhysRevLett.116.063001.

[8] P. Gill, "Is the time right for a redefinition of the second by optical atomic clocks?", *Journal of Physics: Conference Series*, vol. 723, no. 1, p. 012 053, 2016. DOI: https://doi.org/10.1088/1742-6596/723/1/012053.

[9] G. Mei, D. Zhong, S. An, F. Zhao, F. Qi, F. Wang, G. Ming, W. Li, and P. Wang, "Main features of space rubidium atomic frequency standard for beidou satellites", in *2016 European Frequency and Time Forum (EFTF)*, 2016, pp. 1–4. DOI: 10.1109/EFTF.2016.7477803.

[10] T. Bandi, C. Affolderbach, C. Stefanucci, F. Merli, A. K. Skrivervik, and G. Mileti, "Compact, high-performance CW Double-Resonance rubidium Standard with $1.4 \times 10^{-13}\tau^{-1/2}$ Stability", *IEEE Trans. Ultrason., Ferroelectr., Freq. Control*, vol. 61, pp. 1769–1778, 11 2014. DOI: http://dx.doi.org/10.1109/TUFFC.2013.005955.

[11] M. Abdel Hafiz, G. Coget, M. Petersen, C. E. Calosso, S. Guérandel, E. de Clercq, and R. Boudot, "Symmetric autobalanced Ramsey interrogation for high-performance coherent-population-trapping vapor-cell atomic clock", *Applied Physics Letters*, vol. 112, no. 24, p. 244 102, 2018. DOI: 10.1063/1.5030009.

[12] Oscilloquartz, *OSA 3235B Cesium Clock*, 3235B specifications, 2018. [Online]. Available : https://www.oscilloquartz.com/en/products-and-services/cesium-clocks/osa-3230-series [Accessed March 27, 2019].

[13] Microsemi, *Cesium Clock and Frequency References specifications, 2018*, [Online]. Available : https://www.microsemi.com/product-directory/clocks-frequency-references/3832-cesium-frequency-references [Accessed March 27, 2019].

[14] F. Droz, P. Mosset, Q. Wang, P. Rochat, M. Belloni, M. Gioia, A. Resti, and P. Waller, "Space passive hydrogen maser - performances and lifetime data-", in *2009 IEEE International Frequency Control Symposium Joint with the 22nd European Frequency and Time forum*, 2009, pp. 393–398. DOI: 10.1109/FREQ.2009.5168208.

[15] Leonardo, *PHM Passive hydrogen maser*, PHM specifications, 2018. [Online]. Available : https://www.leonardocompany.com/documents/63265270/65648933/Passive_Hydrogen_Maser_LQ_mm07688_.pdf [Accessed March 27, 2019].

[16] Spectratime, *iSpace+™ Space-Qualified RAFS Spec*, RAFS specification, 2018. [Online]. Available : https://www.spectratime.com/uploads/documents/ispace/iSpace_RAFS_Spec.pdf [Accessed March 27, 2019].

[17] Excelitas, *Rubidium Atomic Frequency Standard, High-Performance Space-Qualified*, RAFS specification, 2018. [Online]. Available : http://www.excelitas.com/Downloads/DTS_Frequency_Standards_RAFS.pdf [Accessed March 27, 2019].

[18] Q. Hao, W. Li, S. He, J. Lv, P. Wang, and G. Mei, "A physics package for rubidium atomic frequency standard with a short-term stability of $2.4{\cdot}10^{-13}\tau^{-1/2}$", *Review of Scientific Instruments*, vol. 87, no. 12, p. 123 111, 2016. DOI: 10.1063/1.4972567.

[19] S. Micalizio, C. E. Calosso, A. Godone, and F. Levi, "Metrological characterization of the pulsed Rb clock with optical detection", *Metrologia*, vol. 49, no. 4, p. 425, 2012. DOI: 10.1088/0026-1394/49/4/425.

[20] S. Kang, M. Gharavipour, C. Affolderbach, F. Gruet, and G. Mileti, "Demonstration of a high-performance pulsed optically pumped Rb clock based on a compact magnetron-type microwave cavity", *J. Appl. Phys.*, vol. 117, no. 10, p. 104 510, 2015. DOI: 10.1063/1.4914493.

[21] G. Dong, J. Deng, J. Lin, S. Zhang, H. Lin, and Y. Wang, "Recent improvements on the pulsed optically pumped rubidium clock at SIOM", *Chin. Opt. Lett.*, vol. 15, no. 4, p. 040 201, 2017. DOI: 10.3788/COL201715.040201.

[22] N. Cyr, M. Tetu, and M. Breton, "All-optical microwave frequency standard: a proposal", *IEEE Transactions on Instrumentation and Measurement*, vol. 42, no. 2, pp. 640–649, 1993, ISSN: 0018-9456. DOI: 10.1109/19.278645.

[23] M. Abdel Hafiz, G. Coget, P. Yun, S. Guérandel, E. de Clercq, and R. Boudot, "A high-performance Raman-Ramsey Cs vapor cell atomic clock", *Journal of Applied Physics*, vol. 121, no. 10, p. 104 903, 2017. DOI: 10.1063/1.4977955.

[24] P. Yun, F. Tricot, C. E. Calosso, S. Micalizio, B. Francois, R. Boudot, S. Guerandel, and E. de Clercq, "High-Performance Coherent Population Trapping Clock with Polarization Modulation", *Phys. Rev. Applied*, vol. 7, p. 014 018, 1 2017. DOI: 10.1103/PhysRevApplied.7.014018.

[25] F.-X. Esnault, E. Blanshan, E. N. Ivanov, R. E. Scholten, J. Kitching, and E. A. Donley, "Cold-atom double-Λ coherent population trapping clock", *Phys. Rev. A*, vol. 88, p. 042 120, 4 2013. DOI: 10.1103/PhysRevA.88.042120.

[26] T. Bandi, "Double resonance studies on compact, high performance rubidium cell frequency standards", PhD thesis, University of Neuchâtel, 2013.

[27] S. Guerandel, J. Danet, P. Yun, and E. de Clercq, “High performance compact atomic clock based on coherent population trapping”, in *2014 IEEE International Frequency Control Symposium (FCS)*, 2014, pp. 1–5. DOI: 10.1109/FCS.2014.6859919.

[28] M. A. Hafiz, X. Liu, S. Guérandel, E. D. Clercq, and R. Boudot, “A CPT-based Cs vapor cell atomic clock with a short-term fractional frequency stability of $3 \times 10^{-13}\tau^{-1/2}$”, *Journal of Physics: Conference Series*, vol. 723, p. 012 013, 2016. DOI: 10.1088/1742-6596/723/1/012013.

[29] Microsemi, *5071A Primary Frequency Standard*, 5071A specification, 2018. [Online]. Available : https://www.leonardocompany.com/documents/63265270/65648933/Passive_Hydrogen_Maser_LQ_mm07688_.pdf [Accessed March 27, 2019].

[30] C. Stefanucci, T. Bandi, F. Merli, M. Pellaton, C. Affolderbach, G. Mileti, and A. K. Skrivervik, “Compact microwave cavity for high performance rubidium frequency standards”, *Rev. Sci. Instrum.*, vol. 83, no. 10, 104706, p. 104 706, 2012.

[31] M. Gharavipour, “Ramsey spectroscopy in a rubidium vapor cell and realization of an ultra-stable atomic clock”, PhD thesis, Laboratoire Temps-Fréquence (LTF), 2018.

[32] M. Nakazawa, “Recent progress on ultrafast/ultrashort/frequency-stabilized erbium-doped fiber lasers and their applications”, *Frontiers of Optoelectronics in China*, vol. 3, no. 1, pp. 38–44, 2010, ISSN: 1674-4594. DOI: 10.1007/s12200-009-0085-x.

[33] S. Masuda, E. Kanoh, A. Irisawa, and S. Niki, “Highly accurate michelson type wavelength meter that uses a rubidium stabilized 1560 nm diode laser as a wavelength reference”, *Appl. Opt.*, vol. 48, no. 22, pp. 4285–4290, 2009. DOI: 10.1364/AO.48.004285.

[34] G. Ehret, C. Kiemle, M. Wirth, A. Amediek, A. Fix, and S. Houweling, “Space-borne remote sensing of CO_2, CH_4, and N_2O by integrated path differential absorption lidar: a sensitivity analysis”, *Applied Physics B*, vol. 90, no. 3, pp. 593–608, 2008, ISSN: 1432-0649. DOI: 10.1007/s00340-007-2892-3.

[35] K. Numata, J. R. Chen, S. T. Wu, J. B. Abshire, and M. A. Krainak, “Frequency stabilization of distributed-feedback laser diodes at 1572 nm for lidar measurements of atmospheric carbon dioxide”, *Appl. Opt.*, vol. 50, no. 7, pp. 1047–1056, 2011. DOI: 10.1364/AO.50.001047.

[36] A. Fix, R. Matthey, A. Amediek, G. Ehret, F. Gruet, C. Kiemle, V. Klein, G. Mileti, J. P. do Carmo, and M. Quatrevalet, “Investigations on frequency and energy references for a space-borne integrated path differential absorption lidar”, in *Proc. SPIE 10563, International Conference on Space Optics — ICSO 2014,*, vol. 105630A, 2014. DOI: 10.1117/12.2304145.

[37] R. Matthey, W. Moreno, F. Gruet, P. Brochard, S. Schilt, and G. Mileti, “Rb-stabilized laser at 1572 nm for CO_2 monitoring”, *J. Phys. Conf. Ser.*, vol. 723, no. 1, p. 012 034, 2016. DOI: 10.1088/1742-6596/723/1/012034.

[38] J. F. Cliche and B. Shillue, “Applications of control precision timing control for radioastronomy maintaining femtosecond synchronization in the atacama large millimeter array”, *IEEE Control Systems Magazine*, vol. 26, no. 1, pp. 19–26, 2006, ISSN: 1066-033X. DOI: 10.1109/MCS.2006.1580149.

[39] G. Mileti, J. Deng, F. L. Walls, D. A. Jennings, and R. E. Drullinger, “Laser-pumped rubidium frequency standards: new analysis and progress”, *IEEE Journal of Quantum Electronics*, vol. 34, no. 2, pp. 233–237, 1998, ISSN: 0018-9197. DOI: 10.1109/3.658700.

[40] S. S. Sané, S. Bennetts, J. E. Debs, C. C. N. Kuhn, G. D. McDonald, P. A. Altin, J. D. Close, and N. P. Robins, "11 W narrow linewidth laser source at 780 nm for laser cooling and manipulation of Rubidium", *Opt. Express*, vol. 20, no. 8, pp. 8915–8919, 2012. DOI: 10.1364/OE.20.008915.

[41] T. Lévéque, L. Antoni-Micollier, B. Faure, and J. Berthon, "A laser setup for rubidium cooling dedicated to space applications", *Appl. Phys. B*, vol. 116, no. 4, pp. 997–1004, 2014. DOI: 10.1007/s00340-014-5788-z.

[42] Q. Wang, Z. Wang, Z. Fu, W. Liu, and Q. Lin, "A compact laser system for the cold atom gravimeter", *Opt. Commun.*, vol. 358, pp. 82–87, 2016. DOI: 10.1016/j.optcom.2015.09.001.

[43] V. Ménoret, R. Geiger, G. Stern, N. Zahzam, B. Battelier, A. Bresson, A. Landragin, and P. Bouyer, "Dual-wavelength laser source for onboard atom interferometry", *Opt. Lett.*, vol. 36, no. 21, pp. 4128–4130, 2011. DOI: 10.1364/OL.36.004128.

[44] ESA, *A-SCOPE - Advanced space carbon and climate observation of planet earth, Report for Assessment,SP-1313/1*. ESA-ESTEC, Noordwijk, The Netherlands, 2008, ISBN: 978-92-9221-406-7.

[45] F.-M. Bréon and P. Ciais, "Spaceborne remote sensing of greenhouse gas concentrations", *Comptes Rendus Geoscience*, vol. 342, no. 4, pp. 412 –424, 2010, Atmosphère vue de l'espace, ISSN: 1631-0713. DOI: https://doi.org/10.1016/j.crte.2009.09.012.

[46] K. Nakagawa, M. de Labachelerie, Y. Awaji, and M. Kourogi, "Accurate optical frequency atlas of the 1.5-μ bands of acetylene", *J. Opt. Soc. Am. B*, vol. 13, no. 12, pp. 2708–2714, 1996. DOI: 10.1364/JOSAB.13.002708.

[47] J. Hald, L. Nielsen, J. C. Petersen, P. Varming, and J. E. Pedersen, "Fiber laser optical frequency standard at 1.54 μm", *Opt. Express*, vol. 19, no. 3, pp. 2052–2063, 2011. DOI: 10.1364/OE.19.002052.

[48] F. Benabid, F. Couny, J. C. Knight, T. Briks, and P. S. J. Rusell, "Compact, stable and efficient all-fibre gas cells using hollow-core photonic crystal fibres", *Nature*, vol. 434, pp. 488–491, 2005. DOI: 10.1038/nature03349.

[49] M. Triches, A. Brusch, and J. Hald, "Portable optical frequency standard based on sealed gas-filled hollow-core fiber using a novel encapsulation technique", *Applied Physics B*, vol. 121, no. 3, pp. 251–258, 2015, ISSN: 1432-0649. DOI: 10.1007/s00340-015-6224-8.

[50] M. Triches, M. Michieletto, J. Hald, J. K. Lyngsø, J. Lægsgaard, and O. Bang, "Optical frequency standard using acetylene-filled hollow-core photonic crystal fibers", *Opt. Express*, vol. 23, no. 9, pp. 11 227–11 241, 2015. DOI: 10.1364/OE.23.011227.

[51] M. Poulin, C. Latrasse, N. Cyr, and M. Tetu, "An absolute frequency reference at 192.6 THz (1556 nm) based on a two-photon absorption line of rubidium at 778 nm for WDM communication systems", *IEEE Photonics Technology Letters*, vol. 9, no. 12, pp. 1631–1633, 1997, ISSN: 1041-1135. DOI: 10.1109/68.643293.

[52] M. Poulin, C. Latrasse, D. Touahri, and M. Têtu, "Frequency stability of an optical frequency standard at 192.6 thz based on a two-photon transition of rubidium atoms", *Optics Communications*, vol. 207, no. 1, pp. 233 –242, 2002, ISSN: 0030-4018. DOI: 10.1016/S0030-4018(02)01354-8.

[53] O. Terra and H. Hussein, “ An ultra-stable optical frequency standard for telecommunication purposes based upon the $^5S_{1/2} \rightarrow ^5 D_{5/2}$ two-photon transition in rubidium”, *Applied Physics B*, vol. 122, no. 2, p. 27, 2016, ISSN: 1432-0649. DOI: 10.1007/s00340-015-6309-4.

[54] J. Bernard, A. Madej, K. Siemsen, L. Marmet, C. Latrasse, D. Touahri, M. Poulin, M. Allard, and M. Têtu, “Absolute frequency measurement of a laser at 1556 nm locked to the $^5S_{1/2} \rightarrow ^5 D_{5/2}$ two-photon transition in ^{87}Rb”, *Optics Communications*, vol. 173, no. 1, pp. 357 –364, 2000, ISSN: 0030-4018. DOI: https://doi.org/10.1016/S0030-4018(99)00689-6.

[55] A. Onae, T. Ikegami, K. Sugiyama, F.-L. Hong, K. Minoshima, H. Matsumoto, K. Nakagawa, M. Yoshida, and S. Harada, “Optical frequency link between an acetylene stabilized laser at 1542 nm and an Rb stabilized laser at 778 nm using a two-color mode-locked fiber laser”, *Optics Communications*, vol. 183, no. 1, pp. 181 –187, 2000, ISSN: 0030-4018. DOI: 10.1016/S0030-4018(00)00854-3.

[56] V. Mahal, M. A. Arbore, M. M. Fejer, and A. Arie, “Quasi-phase-matched frequency doubling in a waveguide of a 1560-nm diode laser and locking to the rubidium D_2 absorption lines”, *Opt. Lett.*, vol. 21, no. 16, pp. 1217–1219, 1996. DOI: 10.1364/OL.21.001217.

[57] M. Poulin, N. Cyr, C. Latrasse, and M. Tetu, “Progress in the realization of a frequency standard at 192.1 THZ (1560.5 nm) using ^{87}Rb D_2-line and second harmonic generation”, *IEEE Trans. Instrum. Meas.*, vol. 46, no. 2, pp. 157–161, 1997. DOI: 10.1109/19.571801.

[58] A. Bruner, V. Mahal, I. Kiryuschev, A. Arie, M. A. Arbore, and M. M. Fejer, “Frequency stability at the kilohertz level of a rubidium-locked diode laser at 192.114 THz”, *Appl. Opt.*, vol. 37, no. 27, pp. 6410–6414, 1998. DOI: 10.1364/AO.37.006410.

[59] R. J. Thompson, M. Tu, D. C. Aveline, N. Lundblad, and L. Maleki, “High power single frequency 780 nm laser source generated from frequency doubling of a seeded fiber amplifier in a cascade of PPLN crystals”, *Opt. Express*, vol. 11, no. 14, pp. 1709–1713, 2003. DOI: 10.1364/OE.11.001709.

[60] S. Masuda, A. Seki, and S. Niki, “Optical frequency standard by using a 1560 nm diode laser locked to saturated absorption lines of rubidium vapor”, *Appl. Opt.*, vol. 46, no. 21, pp. 4780–4785, 2007. DOI: 10.1364/AO.46.004780.

[61] F. Lienhart, S. Boussen, O. Carraz, N. Zahzam, Y. Bidel, and A. Bresson, “Compact and robust laser system for rubidium laser cooling based on the frequency doubling of a fiber bench at 1560 nm”, English, *Applied Physics B*, vol. 89, no. 2-3, pp. 177–180, 2007, ISSN: 0946-2171. DOI: https://link.springer.com/article/10.1007/s00340-007-2775-7.

[62] F. Theron, O. Carraz, G. Renon, N. Zahzam, Y. Bidel, M. Cadoret, and A. Bresson, “Narrow linewidth single laser source system for onboard atom interferometry”, *Applied Physics B*, vol. 118, no. 1, pp. 1–5, 2015, ISSN: 1432-0649. DOI: 10.1007/s00340-014-5975-y.

[63] F. Theron, Y. Bidel, E. Dieu, N. Zahzam, M. Cadoret, and A. Bresson, “Frequency-doubled telecom fiber laser for a cold atom interferometer using optical lattices”, *Opt. Commun.*, vol. 393, no. Supplement C, pp. 152 –155, 2017. DOI: 10.1007/s00340-014-5975-y.

[64] R. Matthey, F. Gruet, S. Schilt, and G. Mileti, “Compact rubidium-stabilized multi-frequency reference source in the 1.55-μm region”, *Opt. Lett.*, vol. 40, no. 11, pp. 2576–2579, 2015. DOI: 10.1364/OL.40.002576.

[65] W. Moreno, R. Matthey, F. Gruet, P. Brochard, S. Schilt, and G. Mileti, “Rb-stabilized optical frequency reference at 1572 nm”, in *2016 European Frequency and Time Forum (EFTF)*, 2016, pp. 1–4. DOI: 10.1109/EFTF.2016.7477785.

[66] A. Godone, S. Micalizio, and F. Levi, “Pulsed optically pumped frequency standard”, *Phys. Rev. A*, vol. 70, p. 023 409, 2 2004. DOI: 10.1103/PhysRevA.70.023409.

[67] J. Vanier and C. Audoin, *The Quantum Physics of Atomic Frequency Standards.* Adam Hilger, 1989.

[68] D. W. Preston, “Doppler-free saturated absorption: laser spectroscopy”, *Am. J. Phys.*, vol. 64, no. 11, pp. 1432–1436, 1996. DOI: 10.1119/1.18457.

[69] W. Demtröder, *Laser Spectroscopy.* Springer, Berlin, Heidelberg, 2014. DOI: 10.1007/978-3-540-73418-5.

[70] J. Ye, S. Swartz, P. Jungner, and J. L. Hall, “Hyperfine structure and absolute frequency of the 87Rb 5P3/2 state”, *Opt. Lett.*, vol. 21, no. 16, pp. 1280–1282, 1996. DOI: 10.1364/OL.21.001280.

[71] A. Godone, F. Levi, and S. Micalizio, *Coherent Population Trapping Maser.* Torino, Italy: CLUT Editrice, 2002, p. 191, ISBN: 88-7992-166-5.

[72] G. Breit and I. I. Rabi, “Measurement of Nuclear Spin”, *Phys. Rev.*, vol. 38, pp. 2082–2083, 11 1931. DOI: 10.1103/PhysRev.38.2082.2.

[73] S. Bize, Y. Sortais, M. S. Santos, C. Mandache, A. Clairon, and C. Salomon, “High-accuracy measurement of the 87 rb ground-state hyperfine splitting in an atomic fountain”, *EPL (Europhysics Letters)*, vol. 45, no. 5, p. 558, 1999.

[74] M. Pellaton, “High-resolution spectroscopic studies in glass-blown and micro-fabricated cells for miniature rubidium atomic clocks”, PhD thesis, Laboratoire Temps-Fréquence (LTF), 2014.

[75] S. Micalizio, C. E. Calosso, F. Levi, and A. Godone, “Ramsey-fringe shape in an alkali-metal vapor cell with buffer gas”, *Phys. Rev. A*, vol. 88, p. 033 401, 3 2013. DOI: 10.1103/PhysRevA.88.033401.

[76] W. Riley and D. A. Howe, *Handbook of Frequency Stability Analysis.* NIST Spec. Pubs., 2008.

[77] G. Mileti and P. Thomann, “Study of the S/N performance of passive atomic clocks using a laser pumped vapour”, in *Proc. EFTF*, 1995, pp. 271–276.

[78] T4Science, *iMaser 3000 Smart active hydrogen maser clock*, iMaser3000 specifications, 2018. [Online]. Available : https://www.t4science.com/wp-content/uploads/2018/12/iMaser_Clock_Spec.pdf [Accessed March 7, 2019].

[79] V. Dolgovskiy, “All-optical microwave generation using frequency comb”, PhD thesis, Laboratoire Temps-Fréquence (LTF), 2012.

[80] G. Santarelli, C. Audoin, A. Makdissi, P. Laurent, G. J. Dick, and A. Clairon, “Frequency stability degradation of an oscillator slaved to a periodically interrogated atomic resonator”, *IEEE Transactions on Ultrasonics, Ferroelectrics, and Frequency Control*, vol. 45, no. 4, pp. 887–894, Jun. 14, 2018, ISSN: 0885-3010. DOI: 10.1109/58.710548.

[81] J. Vanier, R. Kunski, N. Cyr, J. Y. Savard, and M.Têtu, “On hyperfine frequency shifts caused by buffer gases: Application to the optically pumped passive rubidium frequency standard”, *J. Appl. Phys.*, vol. 53, no. 8, pp. 5387–5391, 1982. DOI: 10.1063/1.331467.

[82] C. E. Calosso, A. Godone, F. Levi, and S. Micalizio, "Enhanced temperature sensitivity in vapor-cell frequency standards", *IEEE Transactions on Ultrasonics, Ferroelectrics and Frequency Control*, vol. 59, no. 12, pp. 2646 –2654, 2012, ISSN: 0885-3010. DOI: 10.1109/TUFFC.2012.2505.

[83] S. Micalizio, A. Godone, F. Levi, and J. Vanier, "Spin-exchange frequency shift in alkali-metal-vapor cell frequency standards", *Phys. Rev. A*, vol. 73, p. 033 414, 3 2006. DOI: 10.1103/PhysRevA.73.033414.

[84] S. Micalizio, A. Godone, F. Levi, and C. Calosso, "Medium-long term frequency stability of pulsed vapor cell clocks", *IEEE Transactions on Ultrasonics, Ferroelectrics, and Frequency Control*, vol. 57, no. 7, pp. 1524–1534, 2010, ISSN: 0885-3010. DOI: 10.1109/TUFFC.2010.1583.

[85] C. Cohen-Tannoudji, "Théorie quantique du cycle de pompage optique. vérification expérimentale des nouveaux effets prévus", PhD thesis, Faculté des sciences de l'université de Paris, 1962.

[86] M. Gharavipour, C. Affolderbach, S. Kang, T. Bandi, F. Gruet, M. Pellaton, and G. Mileti, "High performance vapour-cell frequency standards", *J. Phys. Conf. Ser.*, vol. 723, no. 1, p. 012 006, 2016. DOI: 10.1088/1742-6596/723/1/012006.

[87] B. S. Mathur, H. Tang, and W. Happer, "Light Shifts in the Alkali Atoms", *Phys. Rev.*, vol. 171, pp. 11–19, 1 1968. DOI: 10.1103/PhysRev.171.11.

[88] S. Micalizio, A. Godone, F. Levi, and C. Calosso, "Pulsed optically pumped ^{87}Rb vapor cell frequency standard: A multilevel approach", *Phys. Rev. A*, vol. 79, p. 013 403, 1 2009. DOI: 10.1103/PhysRevA.79.013403.

[89] W. Riley, *Rubidum Frequency Standard Primer*, Second Edition, H. T. Services, Ed. Oct. 25, 2014, p. 163.

[90] G. Iyanu, H. Wang, and J. Camparo, "Pressure sensitivity of the vapor-cell atomic clock", *IEEE Transactions on Ultrasonics, Ferroelectrics, and Frequency Control*, vol. 56, no. 6, pp. 1139–1144, 2009, ISSN: 0885-3010. DOI: 10.1109/TUFFC.2009.1155.

[91] M. Huang, C. M. Klimcak, and J. C. Camparo, "Vapor-cell clock frequency and environmental pressure: resonance-cell volume changes", in *2010 IEEE International Frequency Control Symposium*, 2010, pp. 208–211. DOI: 10.1109/FREQ.2010.5556344.

[92] A. Godone, S. Micalizio, F. Levi, and C. Calosso, "Microwave cavities for vapor cell frequency standards", *Rev. Sci. Instrum.*, vol. 82, no. 7, pp. 074 703–1–15, 2011, ISSN: 00346748. DOI: DOI:10.1063/1.3606641.

[93] W. J. Riley, "A rubidium clock for GPS", in *13th Annual Precise Time and Time Interval (PTTI) Meeting*.

[94] A. Risley and G. Busca, "Effect of Line Inhomogeneity on the Frequency of Passive Rb 87 Frequency Standards", in *32nd Annual Symposium on Frequency Control*, 1978, pp. 506–513. DOI: 10.1109/FREQ.1978.200282.

[95] T. C. English, E. Jechart, and T. M. Kwon, "Elimination of the light shift in rubidium gas cell frequency standards using pulsed optical pumping", in *Tenth Annual Precise Time and Time Interval (PTTI) Applications and Planning Meeting*, 1979 [Online]. Available : https://ntrs.nasa.gov/search.jsp?R=19790016568 [Accessed March 27, 2019].

[96] A. Risley, S. Jarvis, and J. Vanier, “The Dependence of Frequency Upon Microwave Power of Wall-coated and Buffer-gas-filled Gas Cell Rb^{87} Frequency Standards”, *J. Appl. Phys.*, vol. 51, no. 9, pp. 4571–4576, 1980. DOI: 10.1063/1.328348.

[97] G. Mileti, I. Ruedi, and H. Schweda, “Line inhomogeneity effects and power shift in miniaturized rubidium frequency standard”, in *Proc. EFTF 1992*, 1992.

[98] W. J. Riley, “The physics of the environmental sensitivity of rubidium gas cell atomic frequency standards”, *IEEE Trans. Ultrason., Ferroelectr., Freq. Control*, vol. 39, no. 2, pp. 232–240, 1992. DOI: 10.1109/58.139119.

[99] C. Affolderbach and G. Mileti, “Tuneable, stabilised diode lasers for compact atomic frequency standards and precision wavelength references”, *Optics and Lasers in Engin.*, vol. 43, pp. 291–302, 2004. DOI: 10.1016/j.optlaseng.2004.02.009.

[100] C. Affolderbach and G. Mileti, “A compact laser head with high-frequency stability for rb atomic clocks and optical instrumentation”, *Rev. Sci. Instrum.*, vol. 76, no. 7, 073108, p. 073 108, 2005. DOI: 10.1063/1.1979493.

[101] F. Gruet, M. Pellaton, C. Affolderbach, T. Bandi, R. Matthey, and G. Mileti, “Compact and frequency stabilised laser heads for rubidium atomic clocks”, in *Proc. ICSO*, Ajaccio, Corse, France, 2012. DOI: 10.1117/12.2309135.

[102] D. Miletic, “Light-shift and temperature–shift studies in atomic clocks based on coherent population trapping”, PhD thesis, Université de Neuchâtel, 2013.

[103] S. Kang, M. Gharavipour, F. Gruet, C. Affolderbach, and G. Mileti, “Compact and high-performance rb clock based on pulsed optical pumping for industrial application”, in *2015 Joint Conference of the IEEE International Frequency Control Symposium the European Frequency and Time Forum*, 2015, pp. 800–803. DOI: 10.1109/FCS.2015.7138962.

[104] J. C. Camparo, “Conversion of laser phase noise to amplitude noise in an optically thick vapor”, *J. Opt. Soc. Am. B*, vol. 15, no. 3, pp. 1177–1186, 1998. DOI: 10.1364/JOSAB.15.001177.

[105] N. Almat, W. Moreno, M. Pellaton, M. Gharavipour, F. Gruet, C. Affolderbach, and G. Mileti, “Cell-based stabilized laser sources and light-shifts in pulsed rb atomic clocks”, in *2017 Joint Conference of the European Frequency and Time Forum and IEEE International Frequency Control Symposium (EFTF/IFCS)*, 2017, pp. 63–65. DOI: 10.1109/FCS.2017.8088801.

[106] N. Almat, W. Moreno, M. Pellaton, F. Gruet, C. Affolderbach, and G. Mileti, “Characterization of frequency-doubled 1.5- mu m lasers for high-performance rb clocks”, *IEEE Transactions on Ultrasonics, Ferroelectrics, and Frequency Control*, vol. 65, no. 6, pp. 919–926, 2018, ISSN: 0885-3010. DOI: 10.1109/TUFFC.2018.2793419.

[107] C. E. Calosso, S. Micalizio, A. Godone, E. K. Bertacco, and F. Levi, “Electronics for the Pulsed Rubidium Clock: Design and Characterization”, *IEEE Transactions on Ultrasonics, Ferroelectrics, and Frequency Control*, vol. 54, no. 9, pp. 1731–1740, 2007, ISSN: 0885-3010. DOI: 10.1109/TUFFC.2007.458.

[108] W. Froncisz and J. S. Hyde, “The Loop-Gap Resonator: A New Microwave Lumped Circuit ESR Sample Structure”, *Journal of magnetic resonance*, vol. 47, pp. 515–521, 1982. DOI: 10.1016/0022-2364(82)90221-9.

[109] C. Affolderbach, W. Moreno, A. E. Ivanov, T. Debogovic, M. Pellaton, A. K. Skrivervik, E. de Rijk, and G. Mileti, “Study of additive manufactured microwave cavities for pulsed optically pumped atomic clock applications”, *Appl. Phys. Lett.*, vol. 112, no. 11, p. 113 502, 2018. DOI: 10.1063/1.5019444.

[110] C. Audoin, N Dimarcq, V Giordano, and J Viennet, “Physical origin of the frequency shifts in cesium beam frequency standards: related environmental sensitivity”, in *22nd Annual Precise Time and Time Interval (PTTI) Applications and Planning Meeting*, 1990.

[111] R. Li and K. Gibble, “Phase variations in microwave cavities for atomic clocks”, *Metrologia*, vol. 41, no. 6, pp. 376–386, 2004. DOI: 10.1088/0026-1394/41/6/004.

[112] J. Guena and M. Abgrall and D. Rovera and P. Laurent and B. Chupin and M. Lours and G. Santarelli and P. Rosenbusch and M. E. Tobar and R. Li and K. Gibble and A. Clairon and S. Bize, “Progress in atomic fountains at LNE-SYRTE”, *IEEE Transactions on Ultrasonics, Ferroelectrics, and Frequency Control*, vol. 59, no. 3, pp. 391–409, 2012, ISSN: 0885-3010. DOI: 10.1109/TUFFC.2012.2208.

[113] A Jallageas, L Devenoges, M Petersen, J Morel, L. G. Bernier, D Schenker, P Thomann, and T Südmeyer, “First uncertainty evaluation of the focs-2 primary frequency standard”, *Metrologia*, vol. 55, no. 3, p. 366, 2018. DOI: https://doi.org/10.1088/1681-7575/aab3fa.

[114] C. Affolderbach, G. Du, T. Bandi, A. Horsley, P. Treutlein, and G. Mileti, “Imaging Microwave and DC Magnetic Fields in a Vapor-Cell Rb Atomic Clock”, *IEEE Transactions on Instrumentation and Measurement*, vol. 64, no. 12, pp. 3629–3637, 2015, ISSN: 0018-9456. DOI: 10.1109/TIM.2015.2444261.

[115] A. E. Ivanov, “Resonant structures for vapor-cell atomic clocks”, PhD thesis, IEL, Lausanne, 2017, p. 175. DOI: 10.5075/epfl-thesis-7859.

[116] A. Godone and S. Micalizio, *Phase-shift in vapor cell and compact cold-atom frequency standards*, 2017.

[117] W. Moreno, M. Pellaton, C. Affolderbach, N. Almat, M. Gharavipour, F. Gruet, and G. Mileti, “Impact of microwave-field inhomogeneity in an alkali vapour cell using Ramsey double-resonance spectroscopy”, *Quantum Electronics*, vol. 49, no. 3, pp. 293–297, 2019. DOI: 10.1070/QEL16883.

[118] A. Hudson and J. Camparo, “Mesoscopic physics in vapor-phase atomic systems: collision-shift gradients and the 0-0 hyperfine transition”, *Phys. Rev. A*, vol. 98, p. 042 510, 4 2018. DOI: 10.1103/PhysRevA.98.042510.

[119] C. Affolderbach, N. Almat, M. Gharavipour, F. Gruet, W. Moreno, M. Pellaton, and G. Mileti, “Selected studies on high performance laser-pumped rubidium atomic clocks”, in *2018 IEEE International Frequency Control Symposium (IFCS)*, 2018, pp. 1–6. DOI: 10.1109/FCS.2018.8597452.

[120] S. Karlen, J. Gobet, T. Overstolz, J. Haesler, and S. Lecomte, “Quantitative micro-raman spectroscopy for partial pressure measurement in small volumes”, *Applied Spectroscopy*, vol. 71, no. 12, pp. 2707–2713, 2017. DOI: 10.1177/0003702817724410.

[121] S. Timoshenko and S. Woinowsky-Krieger, *Theory of plates and shells*, ser. Engineering societies monographs. McGraw-Hill, 1959.

[122] W. Moreno, M. Pellaton, C. Affolderbach, and G. Mileti, “Barometric effect in vapor cell atomic clocks”, *IEEE Transactions on Ultrasonics, Ferroelectrics, and Frequency Control*, vol. 65, no. 8, pp. 1500–1503, 2018, ISSN: 0885-3010. DOI: 10.1109/TUFFC.2018.2844020.

[123] T. Lynch and W. Riley, *Tactical Rubidium Frequency Standard (TRFS)*. Rome Air Development Center, Air Force Systems Command, 1987, vol. 1, [Online] Available : https://apps.dtic.mil/dtic/tr/fulltext/u2/a192981.pdf [Accessed March 27, 2019].

[124] H. Seong Lee, T. Yong Kwon, H.-S. Kang, Y.-H. Park, C.-H. Oh, S. Eon Park, H. Cho, and V Minogin, “Comparison of the Rabi and Ramsey pulling in an optically pumped caesium-beam standard”, *Metrologia*, vol. 40, p. 224, Sep. 2003. DOI: 10.1088/0026-1394/40/5/303.

[125] M. Pellaton, C. Affolderbach, A. Skrivervik, A. Ivanov, T. Debogovic, E. de Rijk, and G. Mileti, “3D printed microwave cavity for atomic clock applications: proof of concept”, English, *Electron. Lett.*, vol. 54, pp. 691–693, 11 2018, ISSN: 0013-5194. DOI: 10.1049/el.2017.4176.

[126] W. Moreno, C. Affolderbach, M. Pellaton, G. Mileti, A. E. Ivanov, A. Skrivervik, T. Debogovic, S. Capdevila, D. Hoerni, and E. deRijk, “Ramsey-mode rb cell clock demonstration with a 3d-printed microwave cavity”, in *2018 European Frequency and Time Forum (EFTF)*, 2018, pp. 75–79. DOI: 10.1109/EFTF.2018.8409001.

[127] F. Calignano, D. Manfredi, E. P. Ambrosio, S. Biamino, M. Lombardi, E. Atzeni, A. Salmi, P. Minetola, L. Iuliano, and P. Fino, “Overview on additive manufacturing technologies”, in *Proc. IEEE*, vol. 105, 2017, pp. 593–612. DOI: 10.1109/JPROC.2016.2625098.

[128] S. Micalizio, A. Godone, C. Calosso, F. Levi, C. Affolderbach, and F. Gruet, “Pulsed optically pumped rubidium clock with high frequency-stability performance”, *IEEE Trans. Ultrason., Ferroelect., Freq. Control*, vol. 59, no. 3, pp. 457 –462, 2012, ISSN: 0885-3010. DOI: 10.1109/TUFFC.2012.2215.

[129] M. Abdel Hafiz, G. Coget, M. Petersen, C. Rocher, S. Guérandel, T. Zanon-Willette, E. de Clercq, and R. Boudot, “Toward a High-Stability Coherent Population Trapping Cs Vapor-Cell Atomic Clock Using Autobalanced Ramsey Spectroscopy”, *Phys. Rev. Applied*, vol. 9, p. 064 002, 6 2018. DOI: 10.1103/PhysRevApplied.9.064002.

[130] S. S. Center, *Space Technologies Studies 2016: Results*, EPFL, Lausanne, Switzerland, 2018. [Online]. Available : https://www.spacecenter.ch/wp-content/uploads/2018/02/mdp-2016-full-abstract-book.pdf [Accessed Mai 15, 2019].

[131] P. Ciais, C. Sabine, G. Bala, L. Bopp, V. Brovkin, J. Canadell, A. Chhabra, R. DeFries, J. Galloway, M. Heimann, C. Jones, C. L. Quéré, R. B. Myneni, S. Piao, and P. Thornton, *Carbon and Other Biogeochemical Cycles. In: Climate Change 2013: The Physical Science Basis. Contribution of Working Group I to the Fifth Assessment Report of the Intergovernmental Panel on Climate Change [Stocker, T.F., D. Qin, G.-K. Plattner, M. Tignor, S.K. Allen, J. Boschung, A. Nauels, Y. Xia, V. Bex and P.M. Midgley (eds.)]* U. K. Cambridge University Press Cambridge and U. New York NY, Eds. 2013.

[132] R. T. Menzies and D. M. Tratt, “Differential laser absorption spectrometry for global profiling of tropospheric carbon dioxide: selection of optimum sounding frequencies for high-precision measurements”, *Appl. Opt.*, vol. 42, no. 33, pp. 6569–6577, 2003. DOI: 10.1364/AO.42.006569.

[133] J. Caron and Y. Durand, "Operating wavelengths optimization for a spaceborne lidar measuring atmospheric CO_2", *Appl. Opt.*, vol. 48, no. 28, pp. 5413–5422, 2009. DOI: 10.1364/AO.48.005413.

[134] W. Moreno, R. Matthey, F. Gruet, P. Brochard, S. Schilt, and G. Mileti, "Rb-stabilized compact optical frequency comb acting as a versatile wavelength reference", in *2016 Conference on Lasers and Electro-Optics (CLEO)*, San Jose, California, 2016, SM2H.5.

[135] S. Schilt, R. Matthey, D. Kauffmann-Werner, C. Affolderbach, G. Mileti, and L. Thévenaz, "Laser offset-frequency locking up to 20 GHz using a low-frequency electrical filter technique", *Appl. Opt.*, vol. 47, no. 24, pp. 4336–4344, 2008. DOI: 10.1364/AO.47.004336.

[136] L. S. Rothman, R. R. Gamache, A. Goldman, L. R. Brown, R. A. Toth, H. M. Pickett, R. L. Poynter, J.-M. Flaud, C. Camy-Peyret, A. Barbe, N. Husson, C. P. Rinsland, and M. A. H. Smith, "The hitran database: 1986 edition", *Appl. Opt.*, vol. 26, no. 19, pp. 4058–4097, 1987. DOI: 10.1364/AO.26.004058.

[137] J. Du, Y. Sun, D. Chen, Y. Mu, M. Huang, Z. Yang, J. Liu, D. Bi, X. Hou, and W. Chen, "Frequency-stabilized laser system at 1572 nm for space-borne CO_2 detection LIDAR", *Chin. Opt. Lett.*, vol. 15, no. 3, p. 031 401, 2017. DOI: doi:10.3788/COL201715.031401.

[138] J. M. Supplee, E. A. Whittaker, and W. Lenth, "Theoretical description of frequency modulation and wavelengthmodulation spectroscopy", *Appl. Opt.*, vol. 33, no. 27, pp. 6294–6302, 1994. DOI: 10.1364/AO.33.006294.

[139] M. Delehaye, J. Millo, P. Y. Bourgeois, L. Groult, R. Boudot, E. Rubiola, E. Bigler, Y. Kersalé, and C. Lacroûte, "Residual phase noise measurement of optical second harmonic generation in ppln waveguides", *IEEE Photonics Technology Letters*, vol. 29, no. 19, pp. 1639–1642, 2017, ISSN: 1041-1135. DOI: 10.1109/LPT.2017.2741667.

[140] N. Almat, M. Pellaton, W. Moreno, F. Gruet, C. Affolderbach, and G. Mileti, "Rb vapor-cell clock demonstration with a frequency-doubled telecom laser", *Appl. Opt.*, vol. 57, no. 16, pp. 4707–4713, 2018. DOI: 10.1364/AO.57.004707.

[141] J. Ye, L.-S. Ma, and J. L. Hall, "Ultrasensitive detections in atomic and molecular physics: demonstration in molecular overtone spectroscopy", *J. Opt. Soc. Am. B*, vol. 15, no. 1, pp. 6–15, 1998. DOI: 10.1364/JOSAB.15.000006.

[142] F. Couny, F. Benabid, and P. S. Light, "Large-pitch kagome-structured hollow-core photonic crystal fiber", *Opt. Lett.*, vol. 31, no. 24, pp. 3574–3576, 2006. DOI: 10.1364/OL.31.003574.

[143] K. Knabe, S. Wu, J. Lim, K. A. Tillman, P. S. Light, F. Couny, N. Wheeler, R. Thapa, A. M. Jones, J. W. Nicholson, B. R. Washburn, F. Benabid, and K. L. Corwin, "10 kHz accuracy of an optical frequency reference based on 12C2H2-filled large-core kagome photonic crystal fibers", *Opt. Express*, vol. 17, no. 18, pp. 16 017–16 026, 2009. DOI: 10.1364/OE.17.016017.

[144] S. A. Diddams, "The evolving optical frequency comb [Invited]", *J. Opt. Soc. Am. B*, vol. 27, no. 11, B51–B62, 2010. DOI: 10.1364/JOSAB.27.000B51.

[145] T. J. Kippenberg, R. Holzwarth, and S. A. Diddams, "Microresonator-based optical frequency combs", *Science*, vol. 332, no. 6029, pp. 555–559, 2011, ISSN: 0036-8075. DOI: 10.1126/science.1193968. eprint: https://science.sciencemag.org/content/332/6029/555.full.pdf.

[146] S. Schilt, R. Matthey, K. Hey Tow, L. Thevenaz, and T. Sudmeyer, "All-fiber versatile laser frequency reference at 2 μm for CO2 space-borne lidar applications", *CEAS Space Journal*, 2017. DOI: 10.1007/s12567-017-0164-6.

[147] Y. Zhou, J. Liu, S. Guo, G. Zhao, W. Ma, Z. Cao, L. Dong, L. Zhang, W. Yin, Y. Wu, L. Xiao, O. Axner, and S. Jia, “Laser frequency stabilization based on a universal sub-doppler nice-ohms instrumentation for the potential application in atmospheric lidar”, *Atmospheric Measurement Techniques*, vol. 12, no. 3, pp. 1807–1814, 2019. DOI: 10.5194/amt-12-1807-2019.

[148] C. Philippe, D. Holleville, R. L. Targat, P. Wolf, T. Leveque, R. L. Goff, E. Martaud, and O. Acef, “A compact frequency stabilized telecom laser diode for space applications”, vol. 10562, 2017. DOI: 10.1117/12.2296121.

[149] JCGM, *Evaluation of measurement data — Guide to the expression of uncertainty in measurement*, https://www.bipm.org/utils/common/documents/jcgm/JCGM_100_2008_E.pdf, First edition September 2008, 2008.

William MORENO

william.moreno@alumni.epfl.ch
Nationality : Swiss, Spanish
OrcID: 0000-0001-5502-2475

Education

University of Neuchâtel,Time and Frequency Laboratory, Switzerland

FEB 2015 - JUNE 2019 PhD in Physics

- PhD's thesis "*Rubidium Vapour-cell Frequency Standards : Metrology of Optical and Microwave Frequency References*"
- Thesis Director: Prof. Gaetano Mileti

EPFL,Swiss Federal Institute of Technology in Lausanne, Switzerland

SEPT. 2012 – FEB. 2014 Master of Science in Physics

- Master's thesis: *Studies of SU(n) quantum chains*, Advisor: Prof. Frédéric Mila
- Several semesters in theoretical and numerical projects carried out in condensed matter theory

SEPT. 2008 – JULY. 2012 Bachelor in Physics

OCT. 2006 – JULY. 2008 Preparation school Cours Mathématique Special (CMS)

Gymnase de Burier, la Tour-de-Peilz, Switzerland

OCT. 2003 – JULY 2006 High school general culture certificate in paramedical science

Work experience

University of Neuchâtel, Time and Frequency Laboratory, Switzerland

FEB 2015 - JUNE 2019 PhD student :

- Laser, microwave, and Ramsey spectroscopy of alkali-metals vapour
- Metrology of the medium-to-long term sources of frequency instabilities of double-resonance atomic clocks
- Study and reduction of vapour-cell atomic-clock barometric effect
- Numerical simulation of light and microwave fields inhomogeneity impact on the atom-light interaction inside the clock vapour cell
- Test and characterization of 3D-printed microwave cavities for Pulsed Optically Pumped compact atomic clocks
- Studies on frequency-doubled Rubidium-stabilized 1560-nm laser for on-board compact CO_2 spectroscopy at 1572 nm

Teaching activities

- Supervision of student : Timothé Schlüssel, "Characterization of a commercial external-cavity laser with narrow linewidth", September 2016, high school semester project (maturity project). Carried out supervision in the laboratory and of the writing of the student manuscript.

- Scientific expertise for science festivals in Neuchâtel (FestiScience 2016, Microcity 2016, FestiScience 2018) and for the International Clock Museum (www.mih.ch)
- During the PhD: teaching laboratories for first-year medicine and pharmacy, experimental demonstrations for theoretical complements for General Physics I and II, and presentation of satellite-based LIDAR as physics lecture for Physics for the Natural System (2nd year student), collaboration in physics lectures for HEP-BEJUNE continuous education.
- During Maser's and Bachelor's degrees: assistant for General Physics III & IV, assistant for Analysis II for CMS, assistant for Physics I for first-year medicine.

Awards

- Winner of the academic International Physicists' Tournament 2013, web http://ipt.epfl.ch/2013/

Personal skills

- Linguistic competences: English (fluent, equivalent to C1), French (mother tongue), Spanish (basic knowledge), German (basic knowledge)
- Software skills: Matlab (data analysis, theoretical simulations, and programming), Igor Pro (data analysis and programming), Stable32 (data analysis), C++ (basic knowledge), Latex and Microsoft Office (document editing)